

LARGE EDDY SIMULATION/TRANSPORTED PROBABILITY DENSITY  
FUNCTION MODELING OF TURBULENT COMBUSTION: MODEL  
ADVANCEMENT AND APPLICATIONS

A Dissertation

Submitted to the Faculty

of

Purdue University

by

Pei Zhang

In Partial Fulfillment of the

Requirements for the Degree

of

Doctor of Philosophy

August 2019

Purdue University

West Lafayette, Indiana

**THE PURDUE UNIVERSITY GRADUATE SCHOOL**  
**STATEMENT OF DISSERTATION APPROVAL**

Dr. Gregory A. Blaisdell

School of Aeronautics and Astronautics

Dr. Stephen D. Heister

School of Aeronautics and Astronautics

Dr. Li Qiao

School of Aeronautics and Astronautics

Dr. Haifeng Wang, Chair

School of Aeronautics and Astronautics

**Approved by:**

Dr. Weinong (Wayne) Chen

Head of the School Graduate Program

*To my parents*

## ACKNOWLEDGMENTS

Firstly, I would like to express my sincere gratitude to my advisor Professor Haifeng Wang for his constant support and guidance. His commitment and dedication to work has been a great motivation to me in my Ph.D. study. He inspires me and his other students to conduct rigorous and innovative research with critical thinking, and he has always been there for us with all the assistance in our work. In addition to my advisor, I would also like to thank my other thesis committee members, Professor Gregory Blaisdell, Professor Li Qiao, and Professor Stephen Heister. I have benefited greatly from their insightful comments on my research work as well as the advice and support on my career development.

I want to thank my fellow labmates in Purdue Computational Energy and Propulsion Lab (CEPL), for the cheerful discussions in our weekly group meeting and all the fun we have had together in the past few years, among them Dr. Chao Han, Tejas Pant, Tianfang Xie, Dr. Harshad Lalit, Dr. Meng Xia, Jie Tao, Utsav Jain, Shashank Kashyap, and Abhinand Ayyaswamy. I am very grateful to Dr. Jacqueline H. Chen and Dr. Hemanth Kolla from Sandia National Labs for the collaborations, and for sharing their valuable research experience and career advice with me. I want to also thank all my dear friends for their companionship and support in my life.

Last but not least, I would like to thank my parents Fang and Hao, my little brother Xiaole for their constant love and support. They are my rock. I would also like to specially thank Chao for his companionship during all the years. His encouragement and support make my work and life much easier and enjoyable.

My research is mainly funded by the National Science Foundation (NSF). The dissertation would have not been possible without the support from the Bilslund Dissertation Fellowship. I am grateful to the School of Aeronautics and Astronautics for the Koerner Scholarship, the College of Engineering for conference travel grant support, and the ITaP Research Computing (RCAC) for providing the computational resources in my research.

## TABLE OF CONTENTS

	Page
LIST OF TABLES . . . . .	viii
LIST OF FIGURES . . . . .	ix
NOMENCLATURE . . . . .	xv
ABSTRACT . . . . .	xix
1 INTRODUCTION . . . . .	1
1.1 Background . . . . .	1
1.2 Turbulent combustion regimes . . . . .	2
1.3 Single-regime turbulent combustion . . . . .	5
1.3.1 Overview . . . . .	5
1.3.2 Turbulent non-premixed combustion . . . . .	8
1.3.3 Turbulent premixed combustion . . . . .	10
1.3.4 Turbulent partially premixed combustion . . . . .	13
1.4 Multi-regime turbulent combustion . . . . .	15
1.4.1 Challenges in turbulent combustion modeling . . . . .	15
1.4.2 Current progress . . . . .	20
1.5 Objectives and outline . . . . .	22
2 STUDIES OF A TURBULENT PULSED JET FLAME USING LES/PDF . . . . .	25
2.1 Introduction . . . . .	26
2.2 Experimental conditions of Sydney turbulent pulsed jet flame . . . . .	30
2.3 Modelling approaches . . . . .	31
2.3.1 LES method . . . . .	32
2.3.2 PDF method . . . . .	33
2.3.3 Coupling algorithm and other numerical details . . . . .	35
2.4 Model assessment for statistically transient flames . . . . .	36
2.4.1 General considerations . . . . .	36
2.4.2 Strategies for averaging to estimate statistics . . . . .	39
2.4.3 Constructing confidence intervals . . . . .	41
2.5 Results and discussion . . . . .	43
2.5.1 Effect of inflow turbulence intensity . . . . .	43
2.5.2 Specification of the pulsed inflow boundary condition . . . . .	46
2.5.3 Sensitivity to model and numerical parameters . . . . .	50
2.5.4 Experimental validation of the predictions of the flow and turbulence fields . . . . .	55

	Page
2.5.5	Experimental validation of combustion field . . . . . 60
2.6	Conclusions . . . . . 65
3	A UNIFIED VIEW OF PILOT STABILIZED TURBULENT JET FLAMES FOR MODEL ASSESSMENT ACROSS DIFFERENT COMBUSTION REGIMES . . . 68
3.1	Introduction . . . . . 68
3.2	A unified view of piloted turbulent jet flames . . . . . 70
3.2.1	Global characterization of piloted turbulent jet flames . . . . . 70
3.2.2	Parameterization and regime diagram of piloted turbulent jet flames 71
3.2.3	Examination of unified piloted turbulent jet flames . . . . . 75
3.3	Assessment of LES/PDF in unified piloted turbulent jet flames . . . . . 78
3.3.1	LES/PDF modeling approach . . . . . 79
3.3.2	Model assessment across different combustion regimes . . . . . 80
3.4	Conclusions . . . . . 87
4	VARIANCE CONSISTENT MEAN SHIFT PARTICLE MODEL FOR TREAT- ING DIFFERENTIAL MOLECULAR DIFFUSION IN TRANSPORTED PDF METHODS FOR TURBULENT REACTIVE FLOWS . . . . . 89
4.1	Introduction . . . . . 90
4.2	Transported PDF methods and molecular diffusion models . . . . . 93
4.2.1	Transported PDF methods and Monte Carlo solution method . . . . . 93
4.2.2	Random walk model for equal-diffusivity problems . . . . . 96
4.2.3	Mean shift particle model for differential molecular diffusion . . . . . 98
4.2.4	Boundedness preservation and correction algorithm . . . . . 99
4.3	Variance consistent mean shift particle model for molecular diffusion . . . . . 102
4.3.1	VCMS model for a single scalar diffusion system . . . . . 102
4.3.2	Boundedness correction for single-scalar VCMS model . . . . . 103
4.3.3	VCMS model for a multiple-scalar diffusion system . . . . . 109
4.3.4	Boundedness correction for multiple-scalar VCMS model . . . . . 112
4.4	Examination and validation of variance consistent mean shift particle models 117
4.4.1	A turbulent mixing layer test case . . . . . 118
4.4.2	Single scalar without boundedness correction . . . . . 122
4.4.3	Single scalar with boundedness correction . . . . . 128
4.4.4	Multiple scalars without boundedness correction . . . . . 133
4.4.5	Multiple scalars with boundedness correction . . . . . 138
4.4.6	Effect of different mixing models . . . . . 146
4.4.7	Comparison of computational cost . . . . . 147
4.4.8	Model performance under real turbulence conditions . . . . . 148
4.5	Conclusions . . . . . 152
5	AN A PRIORI EXAMINATION OF A POWER-LAW MIXING TIME SCALE MODEL FOR TRANSPORTED PDF METHOD IN A HIGH-KARLOVITZ NUM- BER TURBULENT PREMIXED DNS FLAME . . . . . 156
5.1	Introduction . . . . . 156

	Page
5.2 LES/PDF modeling of turbulent combustion . . . . .	162
5.2.1 LES/PDF method . . . . .	162
5.2.2 Mixing models for conditional molecular diffusion . . . . .	164
5.2.3 Models for sub-filter scale mixing frequency . . . . .	165
5.3 Examination of sub-filter scale mixing frequency modeling in DNS flames .	167
5.3.1 A high-Ka turbulent premixed DNS jet flame . . . . .	167
5.3.2 Examination of sub-filter scale mixing frequency . . . . .	171
5.3.3 Assessment of sub-filter scale mixing frequency models . . . . .	178
5.4 Conclusions . . . . .	182
6 CONCLUSIONS AND FUTURE WORK . . . . .	186
REFERENCES . . . . .	190

## LIST OF TABLES

Table	Page
3.1 Summary of piloted turbulent jet flames. . . . .	72
3.2 Sydney/Sandia inhomogeneous inlet piloted turbulent jet flames [25]. Volume flow rate ratios of air to fuel $\text{CH}_4$ for all the four cases are 2:1. . . . .	72
3.3 The computational domain and the number of grids in the axial, radial, and azimuthal directions, respectively, used in the LES/PDF simulations of the piloted turbulent jet flames. . . . .	79
4.1 Mixing layer parameters and their specifications . . . . .	119
4.2 The values of errors $ C_{e1} $ for $\tilde{\xi}$ and $\xi_{RMS}$ corresponding to $n_{pc} \rightarrow \infty$ in equation (4.79) from the simulations of the single-scalar turbulent mixing layer with the different models (RW, MS, and VCMS) and the different boundedness correction algorithms at $x/l_m = 0$ (or 0.6). . . . .	127
4.3 The values of errors $ C_{e1} $ for $\tilde{\Phi}$ and $\Phi_{RMS}$ corresponding to $n_{pc} \rightarrow \infty$ in equation (4.79) from the simulations of the multi-scalar turbulent mixing layer with the different models (RW, MS, and VCMS) without boundedness correction at $x/l_m = 0$ (or 0.6). . . . .	137
4.4 The values of errors $ C_{e1} $ for $\tilde{\Phi}$ and $\Phi_{RMS}$ corresponding to $n_{pc} \rightarrow \infty$ in equation (4.79) from the simulations of the multi-scalar turbulent mixing layer with the multi-scalar VCMS model and with the different boundedness correction algorithms (MP, LDF, CSB, or CMP) at $x/l_m = 0, 0.6,$ or $-0.6$ . . . . .	143
4.5 Estimated range of turbulent $Re_t$ in a few laboratory-scale experiments or DNS.	150

## LIST OF FIGURES

Figure	Page
1.1 Different combustion regimes in turbulent combustion. . . . .	3
1.2 A sketch of a laminar opposed jet non-premixed flame. . . . .	8
1.3 A sketch of a laminar fuel-lean premixed flame. . . . .	10
1.4 Regime diagram for turbulent premixed combustion [71,72]. . . . .	11
2.1 A schematic illustration of the turbulent pulsed jet flame. (Colour online) . . .	26
2.2 An example of the measured time history of the centerline axial velocity at the jet inlet in the pulsed jet flame. . . . .	31
2.3 Mean and rms axial inflow velocity normalized by the inflow jet bulk velocity $U_{bL} = 41$ m/s in flame L. . . . .	44
2.4 Radial profiles of the predicted (lines) and measured (symbols) mean axial velocity $\langle \tilde{u} \rangle$ , rms axial velocity $u'$ , mean mixture fraction $\langle \tilde{\xi} \rangle$ , mean temperature $\langle \tilde{T} \rangle$ and mean mass fraction $\langle \tilde{Y}_{CO_2} \rangle$ at the axial locations of $x/D_f = 10, 20,$ and $30$ in Flame L. . . . .	45
2.5 The pulse function $f(t)$ estimated from the measurements at the different radial locations at the jet inlet of the turbulent pulsed jet flame. . . . .	48
2.6 Time series of the relative turbulence intensity at the different radial locations at the jet inlet of the pulse jet flame. The shaded region indicates the pulse. . . . .	49
2.7 Time series of the predicted mean and rms axial velocity at the different axial and radial locations in the pulsed jet flame with the different values of $C_\phi$ . . . . .	51
2.8 Time series of the predicted mean and rms axial velocity at the different axial and radial locations in the pulsed jet flame with three different grid resolutions. . . . .	52
2.9 Time series of the predicted mean and rms axial velocity at the different axial and radial locations in the pulsed jet flame with three different values of the inflow turbulence intensity parameter $\vartheta = 0.5, 1.0$ and $2.0$ . . . . .	54
2.10 Direct comparison of the predicted mean axial velocity (left) and rms velocity (right) with 20 simulation realisations (x-axis) and 10 simulation realisations (y-axis). The error bars are the 95% confidence intervals. . . . .	55

Figure	Page
2.11 Direct comparison of the predicted (y-axis) and measured (x-axis) mean axial velocity. The shaded region is $\pm 30\%$ deviation from the diagonal. The error bars are the 95% confidence intervals. . . . .	56
2.12 Direct comparison of the predicted (y-axis) and measured (x-axis) rms axial velocity. The shaded region is $\pm 30\%$ deviation from the diagonal. The error bars are the 95% confidence intervals. . . . .	56
2.13 Time series of the predicted (dark red lines) and measured (grey lines with circles) mean axial velocity at the different axial and radial locations in the pulsed jet flame. The error bars are the 95% confidence intervals. . . . .	58
2.14 Time series of the predicted (dark red solid lines) and measured (grey lines with circles) rms axial velocity at the different axial and radial locations in the pulsed jet flame. The error bars are the 95% confidence intervals. . . . .	59
2.15 Time series of the measured PLIF-OH images [15] at the selected times, $t = [11, 13, 19, 21, 23, 25, 27, 40]$ ms. . . . .	61
2.16 Time series of the measured PLIF-OH images (left) [15] and the predicted OH mass fraction contours (right) at the selected times, $t = [11, 13, 19, 21, 23, 25, 27, 40]$ ms. . . . .	62
2.17 PDF profiles of conditional temperature, $T _{0.02 < \xi < 0.1}$ , and OH mass fraction, $\phi_{OH} _{0.02 < \xi < 0.1}$ , at three locations, $x/D = [10, 20, 30]$ . . . . .	64
2.18 Contours of PDF of conditional temperature, $T _{0.02 < \xi < 0.1}$ , and OH mass fraction, $\phi_{OH} _{0.02 < \xi < 0.1}$ , at three locations, $x/D = 10, 20, 30$ . The dashed magenta lines indicate the corresponding extinction duration from measurement [15]. . . . .	64
3.1 The Sydney pilot flame burner [9, 152]. Two concentric tubes are used, the fuel jet tube ( $D_f$ ) and the pilot tube ( $D_p$ ), to separate the fuel jet, the hot pilot flow, and the coflow air. The central tube ( $D_c$ ) is a recent addition to the burner [24–26] to produce different stratifications in composition at the fuel jet exit with varying recession distance $L$ . More information about the geometric parameters can be found in Tables 3.1 and 3.2. . . . .	71
3.2 A regime diagram for pilot stabilized turbulent jet flames. (The diagram is not to scale.) . . . . .	74
3.3 The measured conditional mean temperature $\langle T \xi \rangle$ (K) and conditional PDF of temperature $f(T 0.02 < \xi < 0.1)$ against $\xi$ at $x/D_f = 20$ in flames L, B, and M [9, 118], and at $x/D_f = 15$ in flames D, E, and F [88], and flames I1-I4 [25]. (More results are shown in the Supplementary Materials.) . . . . .	76

Figure	Page
3.4 The measured radial profiles of the mean temperature $\langle T \rangle$ (K) at $x/D_f = 20$ in flames L, B, and M [9, 118], at $x/D_f = 8.5$ in flames F1, F2, and F3 [83], and at $x/D_f = 15$ in flames D, E, and F [88], and flames I1-I4 [25]. (More results are shown in the Supplementary Materials.) . . . . .	78
3.5 Radial profiles of the predicted (lines) and measured (symbols) mean and rms mixture fractions $\langle \xi \rangle$ , $\langle \xi \epsilon \rangle$ at $x/D_f = 1$ in flames I1-I4 [25]. . . . .	81
3.6 Predicted (left) and measured (right) scatter plot of temperature against mixture fractions at $x/D_f = 1$ in flames I1-I4 [25]. The diamond symbols correspond to the pilot condition, and the circle symbols indicate the theoretically fully mixed condition of the fuel jet. . . . .	82
3.7 Radial profiles of the predicted (lines) and measured (symbols) mean and rms mixture fractions $\langle \xi \rangle$ , $\langle \xi \epsilon \rangle$ at $x/D_f = 20$ in flame L, at $x/D_f = 8.5$ in flame F1, at $x/D_f = 15$ in flame E, and in flames I1-I4. (More results are shown in the Supplementary Materials.) . . . . .	84
3.8 Predicted (lines) and measured (symbols) conditional mean temperature $\langle T   \xi \rangle$ (K) against $\xi$ at $x/D_f = 20$ in flame L, at $x/D_f = 15$ in flame E, and in flames I1-I4. (More results are shown in the Supplementary Materials.) . . . . .	85
3.9 Radial profiles of the predicted (lines) and measured (symbols) mean temperature $\langle T \rangle$ (K) at $x/D_f = 20$ in flame L, at $x/D_f = 8.5$ in flame F1, at $x/D_f = 15$ in flame E, and in flames I1-I4. (More results are shown in the Supplementary Materials.)	86
4.1 Illustration of the clipping with paired-mixing (CPM) correction algorithm . . . . .	107
4.2 A turbulent mixing layer in forced homogeneous isotropic turbulence . . . . .	118
4.3 The profiles of the scalar mean $\tilde{\xi}$ , the scalar RMS $\xi_{RMS}$ , and their errors $E_{\tilde{\xi}}$ and $E_{\xi_{RMS}}$ against $x/l_m$ in the single-scalar turbulent mixing layer with the RW, MS, and VCMS models (without boundedness correction). The error bars are the 95% confidence intervals estimated from multi-trial simulations. . . . .	123
4.4 The convergence of the PDF particle prediction errors for the scalar mean $E_{\tilde{\xi}}$ and RMS $E_{\xi_{RMS}}$ at $x/l_m = 0$ against $n_{pc}$ in the single-scalar turbulent mixing layer with the RW, MS, and VCMS models (without boundedness correction). The error bars are the 95% confidence intervals estimated from multi-trial simulations. The solid lines are the curve fits by using the model equation (4.79). . . . .	125
4.5 The particle scalar values $\xi^*$ against $x/l_m$ in the single-scalar turbulent mixing layer predicted by the VCMS model without boundedness correction. (Circles: the particle scalar values $\xi^*$ ; solid line: the scalar mean $\tilde{\xi}$ ; dashed lines: the scalar upper and lower bounds.) . . . . .	127

Figure	Page
4.6 The particle scalar values $\xi^*$ against $x/l_m$ in the single-scalar turbulent mixing layer predicted by the VCMS model with the four different boundedness correction algorithms, MP, LDF, CSB, and CPM. (Circles: the particle scalar values $\xi^*$ ; solid line: the scalar mean $\tilde{\xi}$ ; dashed lines: the scalar upper and lower bounds.) . . .	129
4.7 The profiles of the scalar mean $\tilde{\xi}$ , the scalar RMS $\xi_{RMS}$ , and their errors $E_{\tilde{\xi}}$ and $E_{\xi_{RMS}}$ against $x/l_m$ in the single-scalar turbulent mixing layer with the VCMS model and the four different boundedness correction algorithms (MP, LDF, CSB, and CPM). The error bars are the 95% confidence intervals estimated from multi-trial simulations. . . . .	130
4.8 The convergence of the PDF particle prediction errors for the scalar mean $E_{\tilde{\xi}}$ and RMS $E_{\xi_{RMS}}$ at $x/l_m = 0$ against $n_{pc}$ in the single-scalar turbulent mixing layer with the VCMS model and the different correction algorithms (MP, LDF, CSB, and CPM). The error bars are the 95% confidence intervals estimated from multi-trial simulations. The solid lines are the curve fits by using the model equation (4.79). The errors are evaluated at the mixing layer center $x/l_m = 0$ except $E_{\tilde{\xi}}$ with the CSB correction which is evaluated at $x/l_m = 0.6$ (for $E_{\tilde{\xi}}$ , only the results from CSB are shown). . . . .	131
4.9 The percentage $\eta_{BV}$ of the number of particles that violate the scalar bounds among the total number of particles used in the simulations of the single-scalar turbulent mixing layer by using the VCMS model and with or without boundedness correction. The error bars are the 95% confidence intervals estimated from multi-trial simulations. . . . .	132
4.10 The profiles of the scalar mean $\tilde{\Phi}$ (vector), the scalar RMS $\Phi_{RMS}$ , and their errors $E_{\tilde{\Phi}}$ and $E_{\Phi_{RMS}}$ against $x/l_m$ for the different scalars in the multi-scalar turbulent mixing layer with the RW, MS, and VCMS models (without boundedness correction). The error bars are the 95% confidence intervals estimated from multi-trial simulations. 134	134
4.11 The convergence of the PDF particle prediction errors for the mean $E_{\tilde{\Phi}}$ and RMS $E_{\Phi_{RMS}}$ against $n_{pc}$ for the different scalars in the multi-scalar turbulent mixing layer with the RW, MS, and VCMS models (without boundedness correction). The error bars are the 95% confidence intervals estimated from multi-trial simulations. The solid lines are the curve fits by using the model equation (4.79). The errors are evaluated at the mixing layer center $x/l_m = 0$ except $E_{\tilde{\Phi}}$ with the RW model which is evaluated at $x/l_m = 0.6$ . . . . .	136
4.12 The particle scalar values $\Phi^*$ against $x/l_m$ in the multi-scalar turbulent mixing layer predicted by the VCMS model with the four different boundedness correction algorithms, MP, LDF, CSB, and CPM. (Circles: the particle scalar values $\Phi^*$ ; solid line: the scalar mean $\tilde{\Phi}$ ; dashed lines: the scalar upper and lower bounds.) . . .	139

Figure	Page
4.13 The particle values in the scalar space shown in a triangular coordinate system. (The scalars $\phi_3$ and $\phi_4$ are combined to show the four-scalar particles on the triangular coordinate. First subplot shows the initial particles, second subplot shows the updated particles at $t = t_e$ without boundedness correction, and all the other subplots show the updated particles with the different correction algorithms.) . . . . .	140
4.14 The profiles of the scalar mean $\tilde{\Phi}$ (vector), the scalar RMS $\Phi_{RMS}$ , and their errors $E_{\tilde{\Phi}}$ and $E_{\Phi_{RMS}}$ against $x/l_m$ for the different scalars in the multi-scalar turbulent mixing layer with the VCMS model and the different boundedness correction algorithms (MP, LDF, CSB, and CPM). The error bars are the 95% confidence intervals estimated from multi-trial simulations. . . . .	141
4.15 The convergence of the PDF particle prediction errors for the mean $E_{\tilde{\Phi}}$ and RMS $E_{\Phi_{RMS}}$ against $n_{pc}$ for the different scalars in the multi-scalar turbulent mixing layer with the VCMS model and the different correction algorithms (MP, LDF, CSB, and CPM). The error bars are the 95% confidence intervals estimated from multi-trial simulations. The solid lines are the curve fits by using the model equation (4.79). The errors are evaluated at the mixing layer center $x/l_m = 0$ except $E_{\tilde{\Phi}}$ with the CSB correction which is evaluated at $x/l_m = 0.6$ or $-0.6$ . . . . .	142
4.16 The percentage $\eta_{BV}$ of the number of particles that violate the scalar bounds among the total number of particles used in the simulations of the multi-scalar turbulent mixing layer by using the VCMS model and with or without boundedness correction. The error bars are the 95% confidence intervals estimated from multi-trial simulations. . . . .	144
4.17 The errors $ C_{e1} $ involved in the different correction algorithms (MP, LDF, CSB, and CPM) combined with the multi-scalar VCMS model for the predictions of the scalar mean $\tilde{\Phi}$ (left) and the scalar RMS $\Phi_{RMS}$ (right) in the multi-scalar turbulent mixing layer. . . . .	144
4.18 The particle scalar values $\Phi^*$ against $x/l_m$ in the multi-scalar turbulent mixing layer predicted by the VCMS model with the CPM correction and with the MCurl mixing model (the first row) and the EMST mixing model (the second row). The profiles of the scalar mean $\tilde{\Phi}$ against $x/l_m$ with the different mixing models are shown in the third row, and the profiles of the scalar RMS $\Phi_{RMS}$ in the last row. The error bars are the 95% confidence intervals estimated from multi-trial simulations. . . . .	147
4.19 The predicted maximum error of $\xi_{RMS}$ , $\max(E_{\xi_{RMS}})/\xi_{RMS,0}$ , against $Re_t$ in the single-scalar turbulent mixing layer test case with the RW model, the MS model and the VCMS model, and three boundedness correction options: without correction, with the MP correction, and with the CPM correction. The error bars are the estimated 95% confidence intervals estimated from multi-trial simulations. . . . .	148

Figure	Page
4.20 Updated particle values $\xi_p^{n+1}$ against the initial particles $\xi_p^n$ after one particle time step for the three different cases with different values of $[\xi_s, \xi_e]$ to illustrate the overcorrection caused by the MP correction algorithm. . . . .	154
5.1 Laminar flame thermal thickness and laminar flame speed, $\delta_{th}$ and $S_L$ , of CH <sub>4</sub> /air mixtures at different equivalence ratios $\Phi$ and at $T = 300$ K and $P = 1$ atm. . .	168
5.2 Contours of instantaneous temperature $T$ , Ka and $-\log(\text{Da})$ in the DNS flame, and the location of the DNS flame in the Borghi diagram. . . . .	168
5.3 Contours of the filtered temperature, the sub-filter scale RMS temperature $\sqrt{T''^2}$ , the sub-filter scale scalar dissipation rate $\chi_T$ , and the sub-filter scale mixing time scale $\Omega_T$ in the DNS flame at a filter size $\Delta = 21\Delta_{DNS}$ . . . . .	170
5.4 Sub-filter scale mixing scaling factor for temperature $F_T$ from a global view (left), and a local view (right) at $x/D = 28$ , $r/D = 0.75$ . . . . .	172
5.5 Sub-filter scale mixing scaling factor for temperature $F_T$ at multiple spatial points (symbols: DNS data; lines: power-law fitting curves). . . . .	174
5.6 Sub-filter scale mixing scaling factor for multiple scalars at multiple spatial points (symbols: DNS data; lines: power-law based fitting curves $1 + [\Delta/(b\delta_{th})]^a$ ). . .	175
5.7 Radial profiles of the fitting parameter $a$ at four axial locations $x/D = [4, 16, 28, 40]$ for multiple scalars. . . . .	176
5.8 Radial profiles of the fitting parameter $b$ at four axial locations $x/D = [4, 16, 28, 40]$ for multiple scalars. . . . .	177
5.9 Radial profiles of the mean equivalence ratio $\Phi$ , mean temperature $\langle T \rangle_{\theta,t}$ , and local flame length scale $\delta_{th}(\Phi)$ , at four axial locations $x/D = [4, 16, 28, 40]$ . . . . .	177
5.10 Comparisons of the sub-filter scale mixing scaling factor for temperature from DNS data and models. . . . .	179
5.11 Radial profiles of the sub-filter scale mixing scaling factor for temperature from DNS data and models at $\Delta = 21\Delta_{DNS}$ at four axial locations $x/D = [4, 16, 28, 40]$ . .	180
5.12 Radial profiles of mean mixing frequency $\Omega_T$ for temperature from DNS data and models. . . . .	183
5.13 Comparison of mean mixing frequency $\langle \Omega_\alpha \rangle_{\theta,t}$ from DNS and from LER-B model with $a = 1.5$ and $b$ from fitting for multiple scalars at four axial locations $x/D = [4, 16, 28, 40]$ . . . . .	184
5.14 Comparison of instantaneous mixing frequency $\Omega_\alpha$ from DNS and from LER-B model with $a = 1.5$ and $b$ from fitting for multiple scalars at four axial locations $x/D = [4, 16, 28, 40]$ . . . . .	185

## NOMENCLATURE

$\mathbf{A}$	matrix defined in equation (4.61)
$\mathbf{B}$	vector defined in equation (4.61)
$c$	decay-factor $c(\Delta t) = 1 - \exp(-\Omega\Delta t)$
$\check{c}$	decay-factor for the boundedness correction in a multi-scalar system
$c^+$	modified decay-factor for a single-scalar system, $c^+(\Delta t) = 1 - \exp[-(\Omega + \omega)\Delta t]$
$\hat{c}_\alpha$	decay-factor for a multi-scalar system due to $\hat{\omega}_\alpha$ , $\hat{c}_\alpha(\Delta t) = 1 - \exp(-\hat{\omega}_\alpha\Delta t)$
$C_\alpha$	conservation correction for the mixture-averaged molecular diffusion term (equation (4.3))
$\hat{C}_\alpha$	conservation correction for the mixture-averaged molecular diffusion term (equation (4.9))
$C_{e1}$	model constant for the model of error in equation (4.79)
$C_{e2}$	model constant for the model of error in equation (4.79)
$C_\phi$	model constant of the mixing frequency $\Omega$ model
$Da$	Damk $\cong$ hler number
$e_{Y,k}$	error involved in the particle results $Y$ from the $k$ th simulation trial
$E_{tr}$	numerical truncation error due to the use of a finite number of grids and time step sizes
$E_Y$	bias-free estimate of error in $Y$ from multiple simulation trials (equation (4.77))
$f$	probability density function (PDF)
$F$	a function defined in equation (4.47)
$k$	turbulent kinetic energy
$Ka$	Karlovitz number

$Le_\alpha$	Lewis number for the $\alpha$ th scalar
$l_t$	integral length scale
$l_m$	turbulent mixing layer length scale
$n_{pc}$	number of particles per grid cell
$n_t$	number of particle simulation trials
$n_\phi$	number of scalars
$\mathcal{O}$	order of magnitude
$p, q$	particle index
$Pr$	Prandtl number
$Q$	queue
$Re$	Reynolds number
$S_L$	laminar premixed flame speed
$S_\alpha$	chemical reaction source term of $\alpha$ th scalar
$Sc_t$	turbulent Schmidt number
$\mathbf{S}$	chemical reaction source term vector $\mathbf{S} = (S_1, \dots, S_{n_\phi})$
$t$	time
$t_0$	a reference time
$t_e$	end time of a simulation
$\mathbf{u}$	velocity vector
$u'$	integral velocity
$\mathbf{W}$	isotropic vector-valued Wiener process
$\mathbf{x}$	physical location vector
$\mathbf{X}$	particle location vector
$\alpha, \beta$	scalar index
$\chi$	scalar dissipation rate
$\Gamma_\alpha$	molecular diffusivity of $\alpha$ th scalar
$\Gamma$	molecular diffusivity of a single scalar (or equal molecular diffusivity for all scalars)
$\Gamma_t$	turbulent eddy diffusivity

$\delta_L$	laminar premixed flame thickness
$\delta_R$	reaction zone thickness of laminar premixed flame
$\Delta$	LES filter size
$\Delta t$	time step size
$\Delta\tilde{\phi}_\alpha$	mean shift of scalar $\tilde{\phi}_\alpha$ (equation (4.32))
$\Delta\hat{\phi}_{\alpha,p}$	modified scalar shift (equation (4.64))
$\Delta\tilde{\xi}$	mean shift of scalar $\tilde{\xi}$
$\varepsilon$	turbulent kinetic energy dissipation rate
$\eta$	Kolmogorov length scale
$\eta_{BV}$	percentage of the number of particles with the scalar boundedness violation among the total number of particles
$\theta$	mixing parameter in the CPM correction algorithm in equation (4.71)
$\nu$	kinematic viscosity
$\nu_t$	turbulent eddy viscosity
$\tau_\eta$	Kolmogorov time scale
$\tau_t$	integral time scale
$\tau_C$	chemical time scale
$\tau_m$	mixing time scale
$\xi$	a single conserved scalar
$\xi_{min}$	lower bound of scalar $\xi$
$\xi_{max}$	upper bound of scalar $\xi$
$\rho$	density
$\sigma_Y$	standard deviation of $Y$
$\phi_\alpha$	value of $\alpha$ th scalar
$\phi_{\alpha,min}$	lower bound of scalar $\phi_\alpha$
$\phi_{\alpha,max}$	upper bound of scalar $\phi_\alpha$
$\Phi$	scalar vector $\Phi = (\phi_1, \phi_2, \dots, \phi_{n_\phi})$
$\Psi$	sample space variable for random variable $\Phi$ , $\Psi = (\psi_1, \psi_2, \dots, \psi_{n_\phi})$
$\Omega$	turbulent mixing frequency (equation (4.11))

$\omega$	single-scalar frequency correction for variance consistency (equation (4.41))
$\omega_\alpha$	multi-scalar frequency correction for variance consistency (equation (4.53))
$\hat{\omega}_\alpha$	modified multi-scalar frequency correction for variance consistency (equation (4.59))
$\hat{\Omega}$	vector formed by $\hat{\omega}_\alpha$ , $\hat{\Omega} = (\hat{\omega}_1, \hat{\omega}_2, \dots, \hat{\omega}_{n_\phi})$
$\overline{\square}$	Reynolds average
$\tilde{\square}$	Favre average
$\square''$	fluctuation
$\langle \square   \square \rangle$	conditional average
$\langle \square \rangle_t$	average from different particle simulation trials
$\square^n$	quantity at the $n$ th time step $t = t^n$
$\square^{\hat{n}}$	a predictor of quantity at the $(n + 1)$ th time step $t = t^{n+1}$
$\square^*$	quantity evaluated at the particle location $\mathbf{X}_p^*$
$\square_{PT}$	quantities obtained from the PDF particle method
$\square_{FV}$	quantities obtained from the finite volume method
$\square_L$	values at the left boundary of the computational domain
$\square_R$	values at the right boundary of the computational domain
$\square_{RMS}$	root mean square

## ABSTRACT

Zhang, Pei PhD, Purdue University, August 2019. Large Eddy Simulation/Transported Probability Density Function Modeling of Turbulent Combustion: Model Advancement and Applications. Major Professor: Haifeng Wang.

Studies of turbulent combustion in the past mainly focus on problems with single-regime combustion. In practical combustion systems, however, combustion rarely occurs in a single regime, and different regimes of combustion can be observed in the same system. This creates a significant gap between our existing knowledge of combustion in single regime and the practical need in multi-regime combustion. In this work, we aim to extend the traditional single-regime combustion models to problems involving different regimes of combustion. Among the existing modeling methods, Transported Probability Density Function (PDF) method is attractive for its intrinsic closure of treating detailed chemical kinetics and has been demonstrated to be promising in predicting low-probability but practically important combustion events like local extinction and re-ignition. In this work, we focus on the model assessment and advancement of the Large Eddy Simulation (LES)/ PDF method in predicting turbulent multi-regime combustion.

Two combustion benchmark problems are considered for the model assessment. One is a recently designed turbulent piloted jet flame that features statistically transient processes, the Sydney turbulent pulsed piloted jet flame. A direct comparison of the predicted and measured time series of the axial velocity demonstrates a satisfactory prediction of the flow and turbulence fields of the pulsed jet flame by the employed LES/PDF modeling method. A comparison of the PLIF-OH images and the predicted OH mass fraction contours at a few selected times shows that the method captures the different combustion stages including healthy burning, significant extinction, and the re-establishment of healthy burning, in the statistically transient process. The temporal history of the conditional PDF of OH mass fraction/temperature at around stoichiometric conditions at different axial locations

suggests that the method predicts the extinction and re-establishment timings accurately at upstream locations but less accurately at downstream locations with a delay of burning re-establishment. The other test case is a unified series of existing turbulent piloted flames. To facilitate model assessment across different combustion regimes, we develop a model validation framework by unifying several existing pilot stabilized turbulent jet flames in different combustion regimes. The characteristic similarity and difference of the employed piloted flames are examined, including the Sydney piloted flames L, B, and M, the Sandia piloted flames D, E, and F, a series of piloted premixed Bunsen flames, and the Sydney/Sandia inhomogeneous inlet piloted jet flames. Proper parameterization and a regime diagram are introduced to characterize the pilot stabilized flames covering non-premixed, partially premixed, and premixed flames. A preliminary model assessment is carried out to examine the simultaneous model performance of the LES/PDF method for the piloted jet flames across different combustion regimes.

With the assessment work in the above two test cases, it is found that the LES/PDF method can predict the statistically transient combustion and multi-regime combustion reasonably well but some modeling limitations are also identified. Thus, further model advancement is needed for the LES/PDF method. In this work, we focus on two model advancement studies related to the molecular diffusion and sub-filter scale mixing processes in turbulent combustion. The first study is to deal with differential molecular diffusion (DMD) among different species. The importance of the DMD effects on combustion has been found in many applications. However, in most previous combustion models equal molecular diffusivity is assumed. To incorporate the DMD effects accurately, we develop a model called Variance Consistent Mean Shift (VCMS) model. The second model advancement focuses on the sub-filter scale mixing in high-Karlovitz ( $Ka$ ) number turbulent combustion. We analyze the DNS data of a Sandia high- $Ka$  premixed jet flame to gain insights into the modeling of sub-filter scale mixing. A sub-filter scale mixing time scale is analyzed with respect to the filter size to examine the validity of a power-law scaling model for the mixing time scale.

# 1. INTRODUCTION

## 1.1 Background

Combustion has always been a crucial part of our life. The first application of combustion can be traced back to the Stone Age, when people used heat and light from combustion of organic plants for cooking, warmth, and lighting. In the 21st century, combustion has been widely employed in transportation, industrial, residential and commercial areas. In the year 2014, about 74% of residential and commercial energy supply was from combustion of fossil fuels including liquid petroleum, natural gas, and coals, as reported by International Energy Outlook 2017 [1]. The percentages were even larger in the other two areas, industry and transportation. In total, more than 83% of global energy supply was provided by combustion of fossil fuels in 2014 and the projected number for 2050 is as large as 77%. Combustion of fossil fuels has been and will continue to be the dominant way of global energy supply in the 21st century and in the foreseeable future.

There are two well-recognized concerns about fossil fuels combustion as the primary energy source. One concern is the gradual depletion of fossil fuels. Since it requires millions of years to form fossil fuels which are generally viewed as non-renewable, consumption of fossil fuels is much faster than formation. At the current consumption and formation rates, the fossil fuels will eventually be exhausted in about hundreds of years. Efforts have been made to find new types of energy sources, such as nuclear power and renewable energy sources. An increasing proportion of nuclear and renewable energy is projected by International Energy Outlook 2017 [1]. However, despite the projected increase of nuclear and renewable energy supply, in this century, fossil fuels are expected to be still the primary energy source. Scientists are trying to improve combustion efficiency of fossil fuels with the hope that they can last longer, while striving for finding alternative energy sources. The other concern is combustion emissions. Fossil fuels consist of carbon, hydrogen, oxygen,

nitrogen, and sulfur. They release  $\text{H}_2\text{O}$ ,  $\text{CO}_2$ ,  $\text{CO}$ ,  $\text{NO}_x$ ,  $\text{SO}_2$ , soot, and unburned hydrocarbons (UHCs), when burned with air. Some of the products cause serious environmental and health issues. For example,  $\text{CO}_2$ ,  $\text{N}_2\text{O}$ , and unburned  $\text{CH}_4$  are greenhouse gases that directly contribute to the global warming effect, and other products, such as  $\text{CO}$ , soot, UHCs, and  $\text{NO}_x$ , are toxic gases which impose great threats to the health of living lives on earth. Thus, combustion systems with low emissions are targeted. The movement toward this target is typically driven by government regulations on emissions.

In summary, combustion of fossil fuels is and will continue to be the primary way to acquire energy in the 21st century. An improved combustion system with high efficiency and low emissions will continuously be sought. To aid the improvement, we need to develop a thorough understanding of combustion physics. The goal of the current study focuses on this direction to advance our understanding of real combustion processes.

## 1.2 Turbulent combustion regimes

Combustion of fossil fuels is an extremely complicated process, which encompasses strongly coupled multi-scale multi-physical sub-processes including multi-phase flow, turbulence, molecular transport, and chemical reactions. This work focuses on turbulent combustion problems of gaseous fuels and oxidizers. Based on the mixing status of fuel and oxidizer streams before entering chemical reaction region, combustion problems are generally categorized into three combustion regimes, *i.e.*, non-premixed, premixed, and partially premixed combustion, as shown in Figure 1.1. Non-premixed combustion is at the one extreme among all combustion problems where the fuel and oxidizer streams enter the chemical reaction region separately. The mixing between the fuel and oxidizer occurs at the flame front and at a much slower rate than chemical reaction, which makes non-premixed combustion typically a mixing controlled process. Examples of non-premixed combustion include simple flames such as a candle flame, and complicated ones such as the combustion inside diesel engines. The opposite extreme of non-premixed combustion is premixed combustion, where the fuel and oxidizer are perfectly mixed before entering reaction region. In premixed

combustion, the flame front is located between the fresh reactants and combustion products, and propagates toward the fresh reactants. Examples of premixed combustion include simple flames such as the Bunsen flame, and complicated ones such as the combustion inside gasoline engines. In addition to non-premixed combustion and premixed combustion, there is another combustion regime called partially premixed combustion, which is much more complicated than the previous two regimes. A detailed discussion about partially premixed combustion is provided later in Section 1.3.4.

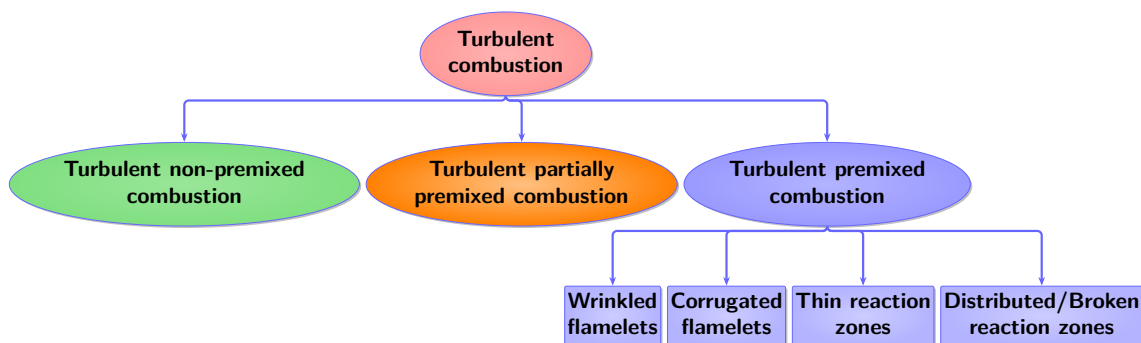


Figure 1.1. Different combustion regimes in turbulent combustion.

Combustion in the above three different regimes is fundamentally different. First, the dominant or limiting physical process is different for each combustion mode. Non-premixed combustion is typically mixing controlled while the case in premixed combustion is much more complicated, where the chemical process could be slow compared to mixing depending on the specific combustion sub-regimes in Figure 1.1. (In the rest of the thesis, we call it regime instead of sub-regime, for simplicity.) A few dimensionless parameters have been used to characterize turbulent premixed combustion regimes, about which more discussions can be found in Section 1.3.3. Second, in non-premixed combustion, chemical reaction most likely occurs at the stoichiometric condition ( $\phi = 1$ ), while in premixed combustion, it depends on the equivalence ratio  $\phi$  of the reactants and very fuel-lean combustion is possible. Fuel-lean combustion, which has lower temperature and therefore depresses  $\text{NO}_x$  formation, is a desired operating condition in modern engines, driven by the regulations and environ-

mental concerns. Also, premixed combustion has the property of flame front propagation while non-premixed combustion does not; the thickness of reaction zone is generally much thinner in premixed combustion than non-premixed combustion. These regime-dependent characteristics help characterize combustion problems and also serve as guidelines for the design of combustion systems.

Single-regime combustion problems have been the focus of previous combustion studies, especially non-premixed combustion and premixed combustion. Many collaborative efforts have been organized at the national and international levels to tackle the problems. Examples of the joint efforts are the International Workshop on Measurement and Computation of Turbulent Nonpremixed Flames (TNF) [2] and the International Workshop on Premixed Turbulent Flames (PTF) [3]. Extensive experimental and numerical studies have been conducted, facilitated by the collaborations in the TNF and PTF workshops. Sitting between non-premixed and premixed combustion, partially premixed combustion has a much wider coverage of combustion problems. It can appear as both a desired and undesired operating condition in practical combustion systems. For example, inhomogeneity in composition is intentionally designed in stratified charge engines to improve the engine performance with increased efficiency and reduced emissions, while partial premixing occurs in a premixed burner as undesired due to inadequate mixing. Compared to non-premixed and premixed combustion, partially premixed combustion has not received the same level of attention in scientific research. Fundamentally, it is difficult to precisely define “partially premixed combustion”, and also difficult to develop elementary flames for studying partially premixed combustion. Nevertheless, we view partially premixed combustion as a single-regime combustion.

All of the above single-regime combustion can coexist in real-world combustion problems. One example is the combustion inside diesel spray engines. In diesel engines, fuel droplets are injected directly into the compressed high temperature air, evaporate, mix with air, and auto-ignite. A lifted non-premixed flame is formed after auto-ignition. The dominant combustion in diesel engines is non-premixed combustion; there exists, however, a rich premixed combustion zone at the end of the flame lift-off region near the centerline [4],

which helps stabilize the flame. Apparently, combustion of practical interest can exhibit multiple regimes of combustion simultaneously in the same combustion system. Despite the significance of the practically relevant combustion scenarios, studies of multi-regime combustion are yet very limited. Thus, it is imperative to conduct multi-regime combustion studies to provide the knowledge base.

This dissertation work builds upon existing knowledge of single-regime combustion and extends it for multi-regime combustion. In the following, we review existing studies on single-regime combustion in Section 1.3, and discuss the challenges in extending the studies to multi-regime combustion in Section 1.4.

### **1.3 Single-regime turbulent combustion**

The main goal of turbulent combustion study is an accurate and thorough understanding of combustion physics which facilitates practical combustion system design. Significant progress toward the goal has been made in the past, both experimentally and computationally. In this section, we first provide a brief overview of the progress in 1.3.1, and further present the characteristics of turbulent combustion and a background survey of previous modeling studies from the view of combustion regimes in 1.3.2, 1.3.3, and 1.3.4.

#### **1.3.1 Overview**

The progress of experimental studies is mainly along with the applications of laser diagnostics to turbulent combustion problems. Turbulent combustion fields can be represented by a few critical quantities including velocities, species mass fractions, and temperature. Laser techniques have been applied to measure these quantities, such as Laser Doppler velocimetry (LDV) pointwise measurement for velocity [5, 6], Raman/Rayleigh Scattering/Laser-induced fluorescence (LIF) for temperature and major species [5, 7–9], and Planar LIF (PLIF) for minor species [10]. The acquired measurement data are extremely valuable for model validation as well as for interrogating physics inside turbulent combustion fields. Recent advancement of high-speed laser diagnostics has moved toward

spatially and temporally resolved measurements, enabling detailed examinations of predictive capabilities of models such as large eddy simulation (LES) and better illustration of turbulence-flame interactions. Currently, the temporal resolution can reach up to the order of MHz [11, 12]. Radicals inside flame fronts including OH [13–16], CH [17, 18], and CH<sub>2</sub>O [19], have been measured by using PLIF at 5-10 kHz. In [14, 15], 2D OH-PLIF images are collected at 5 kHz in a statistically transient flame, *i.e.*, Sydney turbulent pulsed piloted jet flame. The pulsed jet flame exhibits different regimes of combustion characteristics and hence is selected as one of the target flames in this work, as reported in detail in Chapter 2. The measurements start to cover partially premixed combustion recently, e.g., the TU Darmstadt stratified burner [20, 21], the Cambridge stratified swirl burner [22, 23], and the Sydney piloted burner with inhomogeneous inlets [16, 24–26]. Predictive studies of the Sydney inhomogeneous inlets turbulent piloted flame series [16, 24–26] consisting of flames from non-premixed combustion regime to partially premixed combustion regime, are reported in Chapter 3.

Along with the experimental progress, significant advancement has been made in turbulent combustion modeling studies. Turbulent combustion is a highly nonlinear problem consisting of multiple physical processes, such as turbulence, molecular transport, and chemical reaction, occurring at different time and length scales. A simulation that resolves all the relevant multi-scale processes is a direct numerical simulation (DNS). The scales in turbulence range from the integral length scale,  $l_t$ , which is comparable to the geometric configuration size of the flow field, to the smallest Kolmogorov scale,  $\eta$ , the ratio of which is  $l_t/\eta \sim \text{Re}^{3/4}$ . It is computationally demanding to resolve all the turbulent structures and the situation is even worse in turbulent combustion where exist additional flame structures coupled with turbulent structures. Limited by the computational resource, only DNS studies of combustion problems with simple configurations at small or moderate Reynolds (Re) number are affordable [27–37]. Recently, Wang et al. [38–41] reported DNS studies of a turbulent premixed jet flame at  $\text{Re}=10,500$ , more discussions on which are reported in Chapter 5. The DNS studies are very useful for the understanding of combustion physics; however, when it comes to the engineering problems in real applications, less costly approaches,

such as Reynolds-averaged Navier-Stokes (RANS) and LES, are needed. RANS method is widely used in industrial problems and early modeling studies [6, 42, 43]. In RANS, only time-averaged flow and flame structures are resolved, making it less attractive to study the detailed physics in turbulent combustion problems. LES method, though more expensive than RANS, can capture time-dependent combustion dynamics and large-scale fluctuating flow and flame structures. The LES studies of turbulent single-regime combustion have been reported for non-premixed combustion [44–46], premixed combustion [47–49], and partially premixed combustion [50–52]. In these studies, LES method has shown its superiority in capturing instantaneous large-scale flow and flame interactions. In this work, LES method is employed to study the combustion physics in multi-regime turbulent combustion.

In LES method, only large-scale structures are resolved; hence a turbulent combustion model is required to describe the interactions between the unresolved flow and flame structures. There exist three major categories of turbulent combustion models to treat the unresolved flow-flame interactions, *i.e.*, the flamelet models [53], the conditional moment closure (CMC) method [54], and the transported probability density function (PDF) method [55]. The flamelet models and CMC are originally developed for turbulent non-premixed combustion, and hence they are strongly regime-dependent. Significant changes are required when the modeling ideas are adopted for modeling combustion in a different combustion regime. The transported PDF method does not have the strongly embedded regime assumptions compared to the other two methods in the first place, and it has been widely examined in turbulent non-premixed combustion [46, 56–59] and premixed combustion [49, 60–62]. It has the potential to treat multiple regimes of combustion simultaneously; however, the method's performance in multi-regime combustion has rarely been tested. In this work, we systematically assess, for the first time, the performance of the transported PDF method in multi-regime turbulent combustion.

### 1.3.2 Turbulent non-premixed combustion

Non-premixed combustion exists in many practical applications, such as the combustion inside jet engines, diesel engines, and gas furnaces. A simple example of laminar non-premixed combustion is shown in Figure 1.2, which is a schematic illustration of a laminar opposed jet non-premixed flame. The fuel and oxidizer streams come from the opposite directions, mix via diffusion and convection at the flame front, and then are consumed by chemical reaction occurring around the stoichiometric condition ( $\phi = 1.0$ ). For the mixing and chemical reaction processes, two time scales are involved, namely the chemical time scale  $\tau_c$  and the mixing time scale  $\tau_m$ . Typically, chemical reaction is much faster than mixing in non-premixed combustion, *i.e.*, the Damköhler number  $Da = \tau_m/\tau_c \gg 1$ . That is to say, mixing is the bottleneck process while the chemical reaction process is much faster; non-premixed combustion is then a mixing controlled process. Compared to laminar non-premixed combustion, the mixing rate in turbulent non-premixed combustion is enhanced significantly by turbulence. Intense turbulence is often desired in practical applications to allow sufficient mixing before chemical reaction. If, however, the mixing is too fast such that  $Da \sim 1$ , the heat release from chemical reaction is very limited, which can potentially lead to undesirable phenomena, such as local and global extinction.

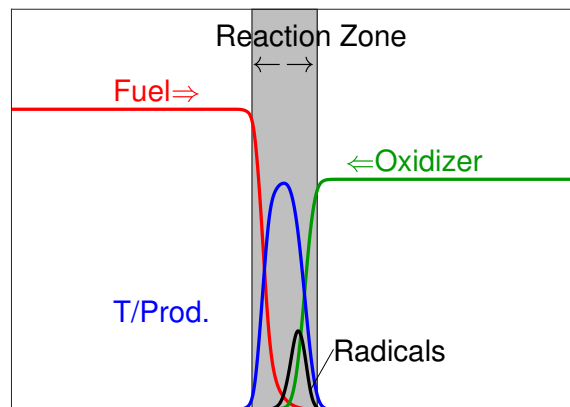


Figure 1.2. A sketch of a laminar opposed jet non-premixed flame.

Turbulent non-premixed combustion has been extensively studied in the past. A conserved scalar, mixture fraction  $\xi$ , is typically introduced to describe the mixing between fuel and oxidizer. Several combustion models adopt the mixture fraction concept, including the flamelet model [53] and CMC [54]. The basic idea of flamelet models is to treat the local flame structures of a turbulent flame as a statistical ensemble of one-dimensional laminar flame structures, which can be represented by mixture fraction  $\xi$  and the local strain rate or scalar dissipation rate  $\chi_\xi$ . The interactions between chemistry and turbulence are modeled by a presumed joint PDF of  $\xi$  and  $\chi_\xi$ . The CMC model is based on the observation that in turbulent combustion scalar fluctuations in mixture fraction  $\xi$  space are much smaller than those in physical space. This makes the averaged (or filtered) highly nonlinear chemical reaction source term for a conditional mean (or filtered) scalar on mixture fraction much easier to model. In this method, transport equations of conditional scalars on mixture fraction are solved. These  $\xi$ -based models have shown the capability in predicting turbulent non-premixed flames near equilibrium state, such as the DLR  $\text{CH}_4/\text{H}_2/\text{N}_2$  jet flame [10] in [63, 64] and the Sydney bluff body flame [65] in [66–68]. However, issues occur when turbulent combustion moves away from equilibrium state and local extinction happens, *i.e.*,  $Da \gg 1$  is not valid. The prediction of local extinction is viewed as an important criterion of a reliable model for turbulent non-premixed combustion. Over the years, the transported PDF method is found to be the most suitable model for predicting local extinction. In the transported PDF method, the transport equation of the joint PDF of random turbulent combustion fields is solved directly. As discussed in detail in later sections, the transported PDF method has natural advantages in dealing with the highly nonlinear chemical source term hence turbulence-chemistry interactions. The prediction success of local extinction by the transported PDF method has been demonstrated in a variety of flames, such as the Sandia piloted flames E and F [59], the Sydney piloted flames B and M [69], and the Sydney turbulent pulsed piloted flame [14].

In summary, significant progress has been made in turbulent non-premixed combustion modeling. The transported PDF model, which is employed in this work, has shown its su-

priority in predicting non-premixed combustion at varying burning conditions from steady burning [46, 56–58] to local extinction [14, 59, 69, 70].

### 1.3.3 Turbulent premixed combustion

Premixed combustion, like non-premixed combustion, is also widely observed in industrial applications, such as the combustion inside gasoline engines and gas turbine engines. Different from non-premixed combustion, in premixed combustion, the fuel and oxidizer are well mixed before chemical reaction. The flame front is located at the interface of the fresh reactants mixture and high temperature combustion products, and propagates toward the fresh reactants. An illustrative sketch of a laminar fuel-lean premixed flame structure is shown in Figure 1.3. As shown in the figure, a laminar premixed flame structure can be divided into three zones, *i.e.*, the preheat zone, the reaction zone, and the recombination zone. Major reactions occur in the reaction zone. The heat released from the reaction zone diffuses into the preheat zone to pre-heat the fresh reactants before reaction. The reaction zone is in general much thinner than the preheat zone. For hydrocarbon flames, typically the laminar flame thickness,  $\delta_L$ , is about 10 times as large as the thickness of the reaction zone,  $\delta_R$ .

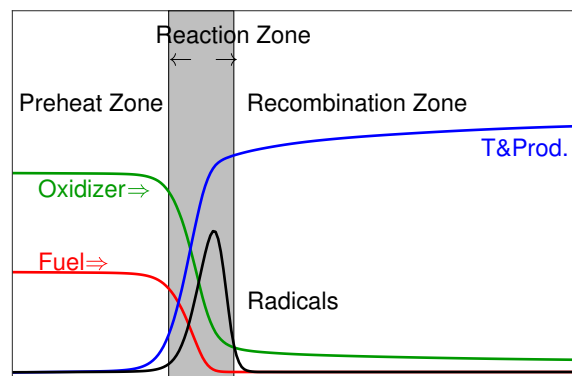


Figure 1.3. A sketch of a laminar fuel-lean premixed flame.

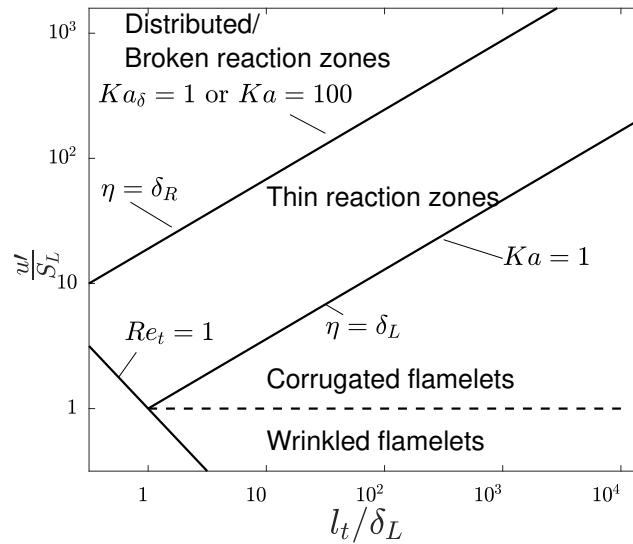


Figure 1.4. Regime diagram for turbulent premixed combustion [71, 72].

Compared to the laminar premixed flame structure in Figure 1.3, the flame structure of a turbulent premixed flame is much more complicated due to the existence of turbulent eddies at sizes varying from Kolmogorov scales to integral scales. Depending on the relative magnitudes of flame scales and turbulence scales, the turbulent premixed flame structure is affected by turbulent structures at different levels. Typically representative flame scales include the laminar flame thickness  $\delta_L$ , the reaction zone thickness  $\delta_R$ , and the chemical time scale  $\tau_C = \delta_L/S_L$  with  $S_L$  being the laminar flame speed; turbulent scales include the two length scales,  $l_t$  and  $\eta$ , and the corresponding time scales, *i.e.*, the Kolmogorov time scale  $\tau_\eta$  and the integral time scale  $\tau_t$ . A few dimensionless parameters have been used to describe the interactions, which are turbulent Reynolds number,  $Re_t = u'l_t/\nu$ , Damköhler number,  $Da = \tau_t/\tau_C$ , and Karlovitz number,  $Ka = \tau_C/\tau_\eta$ . Here,  $u'$  is the turbulent velocity and  $\nu$  is the kinematic molecular viscosity. A regime diagram for turbulent premixed combustion has been proposed by Borghi [71] and Peters [72], as shown in Figure 1.4, based on these scales, where several premixed combustion regimes are introduced. At one extreme where the laminar premixed flame thickness  $\delta_L$  is smaller than the Kolmogorov length scale  $\eta$ ,  $\delta_L < \eta$ , the inner structures of a premixed flame are not affected by turbulence and turbulent

eddies only distort and stretch the thin flame fronts. This regime is called the flamelet regime. At the other extreme where the smallest eddies are smaller than the thickness of inner reaction zone, *i.e.*,  $\eta < \delta_R = 1/10\delta_L$ , turbulent eddies can potentially penetrate the reaction zone. In this case, chemical reaction is affected by turbulence; as a result, local extinction or distributed reaction zone can happen. This regime is called the broken reaction zones or distributed reaction zones with  $Ka > 100$ . Also shown in Figure 1.4, between the broken reaction zones regime and the flamelet regimes, there locates the thin reaction zone regime. In this regime, Kolmogorov scale  $\eta$  is larger than the reaction zone thickness  $\delta_R$  but smaller than the laminar flame thickness  $\delta_L$ ,  $\delta_R < \eta < \delta_L$ . Small turbulent eddies can penetrate preheat zone but cannot penetrate reaction zone. This implies that for flames in this regime, the thin reaction zone is unaffected and the preheat zone is thickened/broadened due to turbulent mixing. Turbulent premixed combustion condition in modern power systems has been driven toward extreme turbulence and ultra fuel-lean combustion featuring high  $Ka$  numbers,  $Ka > 100$ . In Chapter 5, we present our work on the High- $Ka$  turbulent combustion modeling.

These regime characteristics are very useful for turbulent premixed combustion modeling and different regime-dependent models have been proposed. For combustion problems in the flamelet regime or thin reaction zone regime, the grids in modeling studies typically cannot resolve the thin reaction layers limited by the computational cost. Several approaches have been proposed to address this issue. One is the artificially thickened flame (ATF) approach [73, 74], in which the flame front is artificially broadened to a computational resolvable scale by introducing a factor to the diffusion and chemical reaction terms. Another approach is the flame front tracking approach [75]. In this approach, the flame front position is represented by the iso-surface of a level set function  $G = G_0$  and an equation, G-equation, is solved. The two approaches dealing with the thin flame front combined with different chemistry models have been successfully employed to turbulent premixed flames. For example, the ATF approach combined with Flamelet Generated Manifolds (FGM) tabulated chemistry was applied to premixed combustion in [76–78].

The transported PDF studies of turbulent premixed combustion in the RANS context [79, 80] and in the LES context [49, 60–62, 81] have been reported. In [79], the joint composition PDF with the modified Curl model [82] was adopted to solve turbulent premixed flames F1 and F3 [83]. The same flame F3 was calculated in [80] using a hybrid RANS/joint composition PDF. The study was focused on the performance of different mixing models and scalar mixing time scale models. It was found that the Euclidean Minimum Spanning Tree (EMST) model [84] predicted the best results, while the Interaction by Exchange with the Mean (IEM) model [85] and the modified Curl model [82] predicted unrealistic PDF shapes. In [62], a combined LES/PDF method [86] with Eulerian stochastic fields numerical solution was employed to solve a premixed propane turbulent bluff body flame. Recently, a different LES/PDF method with Lagrangian particle numerical solution [46] was used to study the turbulent premixed counterflow flames [87] in [49]. These studies demonstrate the capability of the transported PDF method in predicting turbulent premixed combustion. However, the aforementioned studies are the direct applications of mixing models that are originally developed for non-premixed combustion. Further model assessment and development work is needed for turbulent premixed combustion. More discussions can be found in Chapter 5.

### **1.3.4 Turbulent partially premixed combustion**

Compared to non-premixed and premixed combustion, partially premixed combustion has a much wider coverage in practical applications. Combustion that is neither purely non-premixed combustion nor purely premixed combustion is defined as partially premixed combustion. In this case, the combustion scenarios are much more complicated. Based on the partial premixing level between the fuel and oxidizer, it can be further classified into different categories. If the partial premixing level, usually represented by the equivalence ratio  $\phi$ , is out of the flammable range, it extinguishes or burns with another fuel/oxidizer stream exhibiting the characteristics of non-premixed combustion, such as the Sandia turbulent piloted flames D, E and F [88]. If the equivalence ratio  $\phi$  is non-uniformly distributed inside

the flammable range, the combustion here is stratified premixed combustion. Depending on the gradient of the equivalence ratio  $\phi$ , there are two types of stratified combustion, back-supported and front-supported [89]. In the back-supported stratified flame, the flame front propagates from stoichiometric to lean fresh mixture and the radicals and heat from reaction zones are transported to the lean side to facilitate the reactions. This type of combustion has been applied in stratified charge engines. In this way, much leaner stable combustion is enabled with high efficiency and low emissions. Since combustion in the first category is similar to non-premixed combustion, which has been well studied as presented in Section 1.3.2, the following review of previous studies focuses on the stratified premixed combustion.

Compared to studies in non-premixed and premixed combustion, there are fewer existing studies in stratified combustion. It is one of the relatively new topics in the TNF workshop [2]. Several new burners are designed in recent years to study turbulent stratified combustion dynamics, such as the TU Darmstadt stratified burner [20, 21], and the Cambridge stratified swirl burner [22, 23]. A few modeling studies have been reported on these stratified flames, such as [90–94] for TU Darmstadt stratified burner and [95–98] for Cambridge stratified burner. In most of the modeling studies, turbulent stratified combustion is treated as turbulent premixed combustion and the same modeling methods of turbulent premixed combustion in Section 1.3.3 are used. This modeling strategy has proved to be successful in the above two burners. For example, good predictions of stratified Cambridge flames using the Filtered TABulated Chemistry for LES (F-TACLES) were reported in [97]. In [90], LES predictions with five different premixed combustion models, which are ATF with FGM, the F-TACLES, the flame surface density function, G equation with the flamelet/progress variable approach, and a LES on a very fine grid with combustion chemistry directly treated, are reported for TU Darmstadt flame series. It was concluded that the modeling strategy, which uses turbulent premixed combustion models to predict turbulent stratified combustion, is well suitable in combustion with mild stratification, and its performance in the flames with stronger stratification needs to be validated. A LES/PDF study of partially premixed combustion was conducted [98], in which the LES/PDF predictions of two nonreacting and

four reacting cases based on the Cambridge stratified swirl burner are reported and have been shown in good agreement with the measurements.

Recently, a series of new partially premixed flames, *i.e.*, Sydney piloted burner with inhomogeneous inlets [16,24–26], were designed. With varying inlet conditions, the flame series shows both non-premixed and stratified combustion regimes. In our work, multi-regime combustion dynamics are studied in a few turbulent piloted jet flames including this new flame series using the LES/PDF method, as shown in Chapter 3.

## **1.4 Multi-regime turbulent combustion**

Though significant progress has been made in turbulent combustion studies, they mainly focus on single-regime combustion. In practical applications, combustion can rarely be in a single regime. The study of multi-regime combustion represents a critical need in practical combustion applications and is expected to be an emerging research area in the coming years. When studying multi-regime turbulent combustion, we face a lot of challenges, some of which are shared for all turbulent combustion regimes while others are specially associated with multi-regime combustion. We discuss these modeling challenges in Section 1.4.1, and summarize the existing modeling work on multi-regime combustion in Section 1.4.2.

### **1.4.1 Challenges in turbulent combustion modeling**

Turbulent combustion is a challenging problem to solve from both theoretical and computational perspectives. It is a complex multi-scale multi-physics system consisting of physical processes including chemical reaction/molecular transport/turbulence, on some of which we do not have an accurate predictive theory and are still actively working. Turbulence, for example, is a well-known unresolved mathematical and physical problem [99]. And yet in turbulent combustion, these processes are coupled together, which makes it even more challenging and requires additional research efforts to develop an accurate theory for turbulent combustion. Furthermore, the physical processes are associated with a large variety of scales; solving turbulent combustion means solving the multi-scale processes si-

multaneously, which is a hard task in terms of theory as well as computational cost. The relevant scales in turbulent combustion range from the largest scales related to the geometry size, to the smallest scales related to the Kolmogorov scales or the chemical scales. To capture the large-scale spatial and temporal physics, an adequately large computational domain and long computational time are required, and to resolve the smallest scales, extremely high temporal and spatial resolutions are required. Simulations, *i.e.*, DNS, that satisfy these requirements are prohibitively expensive, especially for turbulent combustion in real applications.

For turbulent combustion in real applications, less expensive statistical approaches like RANS and LES are typically used. In this work, we are interested in LES approach. In LES, large-scale flame and flow structures are resolved with a relatively low grid and time resolution compared to DNS; consequently, physics occurring at small scales, or say sub-filter scales are not solved and require modeling. The small scale/sub-filter scale physics requiring modeling include chemical reaction, molecular diffusion, sub-filter scale turbulent transport, as well as the couplings between them. The challenges of modeling these small-scale physics are discussed as follows.

**Chemical reaction** — Chemical reaction plays a crucial role in turbulent combustion, via which the chemical energy in fossil fuels is transferred into thermal energy in power systems. Hence, it is critically important to have an accurate prediction of chemical reaction. The prediction of chemical reaction, however, is quite challenging, mainly due to the fact that it is a highly nonlinear complicated multi-scale multi-species process, as illustrated below.

- (1) Combustion of hydrocarbon fuels is a very complex process involving many species and elementary reactions. Challenges are caused by the complexity of the detailed chemical reaction kinetics/mechanisms, which describes the reaction rates of elementary reactions. In detailed chemical mechanisms of hydrocarbon fuels, typically 50 ~ 3000 species and 300 ~ 8500 elementary reactions are involved [100]. The first difficulty caused by the large number of species

and elementary reactions is the unbearably high computational cost; as a result, dimension reduction techniques are constantly being sought [101]. The second one is the determination of chemical kinetics parameters for the elementary reaction rates, which is a nontrivial task considering the large number. The chemical kinetics parameters are typically determined by using experimental or computational methods. The process involves large uncertainties, which cause deviations in combustion predictions hence are important to be quantified. Uncertainty quantification (UQ) has been an active research topic in chemical kinetics and a detailed review can be found in [102].

- (2) In addition to the complexity of chemistry itself, another major challenge in turbulent combustion modeling comes from the interactions between chemistry and turbulence. Chemical reaction rate  $\mathcal{S}(T, \phi)$  is a highly nonlinear function of temperature  $T$  and species mass fractions  $\phi$ , which appears as a filtered term,  $\tilde{\mathcal{S}}$ , in LES and requires modeling. The high nonlinearity of the term causes large deviations in modeling by using the resolved quantities as  $\mathcal{S}(\tilde{T}, \tilde{\phi})$ . The modeling of sub-filter scale chemistry and turbulence interactions is very challenging and has been the major target of turbulent combustion models. Besides, the interactions between turbulence and chemistry are strongly regime-dependent as discussed in section 1.3, and therefore it is even more challenging to develop a general model. Fortunately, this is not a problem in the transported PDF method, in which the filtered chemical source term  $\tilde{\mathcal{S}}$  is closed.

**Molecular diffusion** — Molecular diffusion is another critically important process in turbulent combustion, which mixes together fuel and oxidizer molecules and transports away the product molecules from the flame front so that the chemical reaction can proceed. It occurs at the smallest scales hence requires modeling in LES. There are mainly two modeling challenges related to molecular diffusion process.

- (1) The first one is the modeling of differential/preferential molecular diffusion (DMD). There are many species involved in turbulent combustion, and they diffuse at dif-

ferent molecular rates. Lewis number, *i.e.*,  $Le_\alpha = \Gamma_T/\Gamma_\alpha$ , is typically used to characterize the differential molecular transport. Here,  $\Gamma_T$  is the thermal diffusivity and  $\Gamma_\alpha$  is the molecular diffusivity of specie  $\alpha$ . In a typical methane flame, the Lewis number ranges from  $Le_H = 0.18$  for H to  $Le_{CH_2CO} = 1.51$  for  $CH_2CO$ , suggesting nearly ten times difference in molecular diffusion rates. The importance of DMD effects on turbulent combustion has been reported in many studies [103–109]. However, equal diffusion is typically assumed in current models hence additional efforts are required to advance the DMD modeling in turbulent combustion. In Chapter 4, we report our efforts on DMD modeling in the transported PDF method for turbulent combustion.

- (2) Another modeling challenge is scalar mixing, which represents the small/sub-filter scale molecular transport effects. In the transport equation of sub-filter scale scalar variance, it appears in the form of the scalar dissipation rate  $\chi_\alpha$ , standing for the decaying rate of turbulent scalar fluctuations due to small/sub-filter scale molecular diffusion. It is a critical quantity in turbulent combustion problems and appears in all combustion models as a critical parameter [110]. Also, the coupling of this term with turbulence and chemistry makes it combustion regime-dependent and brings additional challenges. The modeling study of this quantity is still ongoing and an accurate model for this quantity to fully describe mixing is not expected to appear in the near future. Our work in Chapter 5 contributes toward this direction.

**Sub-filter scale turbulent transport** — Turbulence is a multi-scale process, in which the scales range from Kolmogorov scales,  $\eta$  and  $\tau_\eta$ , to integral scales,  $l_t$  and  $\tau_t$ . In LES, the grid resolution  $\Delta$  is typically much larger than  $\eta$  hence models are required to describe the sub-filter scale turbulence effects. The related modeling challenges can be illustrated from two aspects,

- (1) One is the coupling of unresolved turbulence with the other two processes. Turbulence produces scalar fluctuations which bring in additional modeling chal-

lenges for the highly nonlinear chemical source term, as well as the molecular mixing process by increasing mixing rate, as discussed above.

- (2) The other one is the sub-filter scale transport, in the form of sub-filter scale convection term. Generally, a gradient-diffusion model is used to represent this term with a sub-filter scale turbulent diffusivity  $\Gamma_t$ . However, there exists experimental evidence showing deviations from the model, as discussed in [99]. Thus, new models are required. Besides, though the coupling between chemistry and turbulence is two-way, currently the chemistry effects on sub-filter scale turbulent transport have not been properly treated, which also requires additional modeling work.

The challenges aforementioned are general challenges existing in all combustion problems, both idealized single-regime combustion and real-world multi-regime combustion. Modeling of multi-regime combustion is much more challenging than single-regime combustion. In the following, we discuss the characteristic challenges of multi-regime combustion modeling.

An issue related to multi-regime combustion is how to precisely define “multi-regime combustion”. There is not a clear definition of this term yet. Generally, there are two different views about multi-regime combustion. One views multi-regime combustion as a blended mixture of single-regime combustion. The other view is to treat multi-regime combustion as a new combustion regime that is in parallel to the existing regimes. All the different regimes are the solutions of the underlying governing equations for the respective problems. In our opinion, neither view is adequate to describe multi-regime combustion. Perhaps at this stage, the best view of multi-regime combustion is to take both the above views, which is adopted in this work.

Regarding the modeling, multi-regime combustion inherits all the challenges from single-regime combustion. Characteristics of the challenges, e.g., chemistry-turbulence interactions and small scale molecular mixing, are strongly combustion regime dependent. As a result, a general model, suitable for all the combustion regimes, is desired for multi-regime combustion. However, most of the current combustion models are strongly regime-

dependent, which are developed for a specific combustion regime and significant efforts are required to extend the model to a different combustion regime; even more efforts are required to develop a general model capable of turbulent combustion at different regimes. Besides, the interactions of regions with different combustion regimes in the same combustion fields represent additional challenges to combustion modeling, as well as the transitions between different combustion regimes. Furthermore, a thorough understanding of multi-regime combustion relies heavily on the accurate detection of the different regimes of combustion. In the past, flame index [111] has been proposed for this purpose. Development of accurate detection techniques of different combustion regimes still remains a great challenge.

#### **1.4.2 Current progress**

There have been some efforts on multi-regime combustion modeling. In the existing work, a typically used modeling framework is based on the regime-dependent models, such as flamelet models [112–114], where a regime detector is applied to detect the combustion regime locally. Once the local combustion regime is determined, the corresponding single-regime combustion model is used to solve combustion dynamics at that location. For the regime-dependent studies, an unavoidable challenge is the definition of the regime detector. Several existing detectors [111, 112, 114–116] have been discussed in [113]. Generally there are two types of detectors. One is the widely used flame index [111] or its improved version [115]. The other is based on the transformations of flamelet equations, such as [112, 116]. The studies on defining an accurate and general regime detector are still ongoing. For the treatment of transition between non-premixed and premixed regimes, typically a blending parameter is defined to represent the contributions from the two regimes. In this case, partially premixed combustion is treated as an ensemble of non-premixed and premixed combustion instead of a fundamental combustion pattern. In [113], this blending method is found to perform reasonably well in a 2-D laminar triple flame and a 2-D laminar

opposed non-premixed flame. The accuracy of the method in turbulent flames needs to be further verified.

As a general model without regime-dependent assumptions on turbulence-chemistry interactions, LES/PDF method suffers less from the above issues. It is potentially applicable to multi-regime combustion without additional regime-dependent adjustments. However, this has not been verified yet. Besides, it has modeling issues related to molecular transport, the characteristics of which are regime-dependent. In this work, we aim to assess the LES/PDF method performance and improve the sub-models of the method, *i.e.*, molecular transport modeling, in predicting multi-regime combustion.

In Sections 1.3.2-1.3.4, the capability of the transported PDF method has been shown from previous individual studies of combustion in different regimes. However, the conclusion of model performance in different regimes gathered from these independent studies is not fair enough, since these studies were performed independently, where different PDF closure methods, chemistry mechanisms, and grids were used. In the current work, the modeling details are carefully designed so that we can get a systematic assessment of LES/PDF performance in a unified series of several existing piloted turbulent flames across different regimes. Furthermore, the fact that a model can accurately predict combustion in different regimes individually does not necessarily mean that it is capable of predicting multi-regime combustion since, in multi-regime combustion, the interaction and transition between different regimes need to be considered. So in this work, the LES/PDF performance is also assessed in a single flame, the Sydney turbulent pulsed piloted jet flame, which exhibits multi-regime combustion dynamics simultaneously.

From the model development perspective, the molecular transport related sub-models in LES/PDF method are originally developed for non-premixed combustion. The PDF studies of premixed/partially turbulent combustion are mostly the direct applications of the models for non-premixed combustion. The molecular transport related sub-models suitable for premixed/partially premixed single-regime and multi-regime combustion are missing. Thus, in the dissertation, we report our work on advancing molecular transport modeling in

LES/PDF methods, with a focus on DMD modeling and the sub-filter scale mixing modeling in turbulent premixed combustion.

## 1.5 Objectives and outline

So far, a review of combustion characteristics and existing modeling studies has been presented. In the review, we have shown the challenges and the potential of LES/PDF method in turbulent multi-regime combustion. In this work, we aim to *assess* and *improve* the performance of the LES/PDF method in predicting turbulent multi-regime combustion. This research is valuable for the development of more general combustion models for real-world combustion problems.

To assess the method performance, two benchmark combustion problems are studied. One is the Sydney turbulent pulsed piloted jet flame [14,15], which is a statistically transient flame, featuring bimodal and multi-regime combustion dynamics simultaneously. The other is a unified series of existing turbulent piloted flames across different combustion regimes covering non-premixed, partially premixed, and premixed regimes. The specific objectives based on the two benchmark problems are listed as follows:

1. Assess the LES/PDF method's performance in a turbulent pulsed jet flame exhibiting statistically transient bimodal and multi-regime combustion dynamics;
2. Assess the LES/PDF method's performance across different regimes of combustion in the unified series of turbulent piloted flames.

LES/PDF studies of the turbulent pulsed flame and the unified series of several existing turbulent piloted flames are reported in Chapters 2 and 3, respectively. In Chapter 2, a validation framework for statistically transient problems with several averaging strategies and with a bootstrap method for constructing confidence intervals is established. Following this framework, predictive results of the turbulent pulsed jet flame focusing on the turbulence and flow fields are compared with measurements. In Chapter 3, the flames studied range from non-premixed combustion, to partially premixed combustion, and to premixed combustion. A systematic model assessment framework across different combustion regimes

is established. The framework is based on a unified view of the different piloted flames via proper parameterization. A regime diagram of turbulent piloted flames is proposed as a guideline for a thorough model validation over different combustion regimes. Following this framework, a preliminary model assessment is performed.

The second goal of this dissertation work is to improve the performance of the LES/PDF method. To achieve this goal, we work from two aspects, *i.e.*, DMD modeling and sub-filter scale mixing modeling. The specific objectives are,

1. Develop a model for treating the DMD effects accurately and consistently in the transported PDF method;
2. Examine the sub-filter scale mixing time scale in a high-Ka turbulent premixed DNS jet flame and provide guidance for future mixing modeling development.

The importance of DMD in turbulent combustion modeling has been reported, however, it has not been treated properly in existing combustion models. In Chapter 4, we present our work on improving the DMD treatment in the transported PDF method. In particular, we propose a new model called variance consistent mean shift (VCMS) model which is able to, for the first time, consider the DMD effects accurately in both the scalar mean and variance level. The model performance is thoroughly validated in a mixing layer test case.

In Chapter 5, we report our work on sub-filter scale mixing time scale modeling in a high-Ka turbulent premixed DNS jet flame. The DNS flame features an intense interaction between the turbulence and flame structures in the distributed/broken reaction zone regime as suggested by the DNS dimensionless parameters. In this work, the sub-filter scale mixing time scale is analyzed with respect to the filter size to examine the validity of a power-law scaling model for the mixing time scale in LES/PDF.

Finally, in Chapter 6, we summarize the major conclusions of the dissertation work and propose potential future work.

The major accomplishments of this work are summarized as follows:

- Extend a model validation framework from statistically stationary combustion problems to statistically transient combustion problems;

- Establish a systematic evaluation framework for model performance in combustion across different combustion regimes;
- Propose a regime diagram as a guide for future studies of multi-regime combustion;
- Demonstrate the LES/PDF method's capability in predicting statistically transient combustion process involving bimodal combustion dynamics, as well as its capability in capturing different combustion regimes;
- Develop a new model for consistent molecular diffusion modeling in the transported PDF method;
- Validate a power-law scaling for sub-filter mixing time scale in a high-Ka turbulent premixed DNS jet flame, and propose a new model based on the DNS observations.

## 2. STUDIES OF A TURBULENT PULSED JET FLAME USING LES/PDF

A turbulent piloted jet flame subject to a rapid velocity pulse in its fuel jet inflow is proposed as a new benchmark case for the study of turbulent combustion models. In this work, we perform modelling studies of this turbulent pulsed jet flame and focus on the predictions of its flow, turbulence and combustion fields. An advanced modelling strategy combining the large eddy simulation (LES) and the probability density function (PDF) methods is employed to model the turbulent pulsed jet flame. Characteristics of the velocity measurements are analysed to produce a time-dependent inflow condition that can be fed into the simulations. The effect of the uncertainty in the inflow turbulence intensity is investigated and is found to be very small. A method of specifying the inflow turbulence boundary condition for the simulations of the pulsed jet flame is assessed. The strategies for validating LES of statistically transient flames are discussed, and a new framework is developed consisting of different averaging strategies and a bootstrap method for constructing confidence intervals. Parametric studies are performed to examine the sensitivity of the predictions of the flow and turbulence fields to model and numerical parameters. A direct comparison of the predicted and measured time series of the axial velocity demonstrates a satisfactory prediction of the flow and turbulence fields of the pulsed jet flame by the employed modelling methods. In addition to the flow and turbulence fields, the performance of the LES/PDF methods in predicting the statistically transient combustion field is also reported. It is found that the current methods capture the different stages in the statistically transient *bimodal* combustion process with a qualitative comparison of the time series of PLIF-OH images and the contour plots of the predicted OH mass fraction. The time history of PDFs of temperature and OH

---

<sup>1</sup>The majority of this chapter is from the paper [117] — P. Zhang, A.R. Masri, H. Wang. Studies of the flow and turbulence fields in a turbulent pulsed jet flame using LES/PDF. *Combustion Theory and Modelling*, 2017, 21(5): 897-927.

mass fraction shows that the method predicts the extinction and burning re-establishment timings accurately at upstream locations but less accurately at downstream locations with a delay of the burning re-establishment.

## 2.1 Introduction

Almost all canonical laboratory flames, especially those found in the International Workshop on Measurement and Computation of turbulent nonpremixed flames (TNF) [2], are statistically stationary. Statistically transient flames have received little attention except in the area of reciprocating engines. In gas turbine engines and other applications, the operation condition is typically statistically stationary. Occasionally, however, the operation conditions vary in time, e.g. due to a change in the fuel injection. Such a change can significantly influence the flow and combustion processes and can potentially cause undesirable phenomena such as local and global extinction and combustion instability. Studying and understanding the dynamics of statistically transient flames are therefore important to the design and control of practical combustion processes.

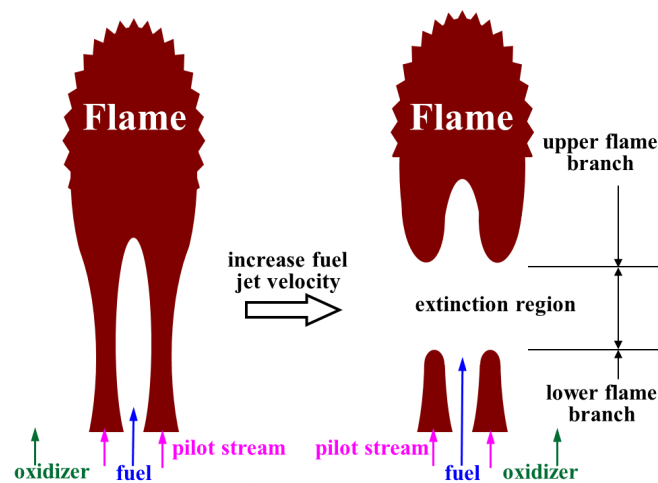


Figure 2.1. A schematic illustration of the turbulent pulsed jet flame. (Colour online)

Motivated by the above, Wang et al. [14] introduced a new class of statistically transient jet flames stabilised on the Sydney piloted burner [9, 118] but now using a short velocity pulse to supply the fuel. The quantity of fuel supplied and the supply duration is well controlled so that the jet transitions from stable to unstable within a very short time. Subject to this velocity pulse, the flame exhibits a complicated dynamic response. As shown in Figure 2.1, the flame is broken into an upper branch and a lower branch due to the increased flow stretching caused by the velocity pulse. Preliminary studies of the pulsed jet flame are reported in [14] by using a high-speed planar laser-induced fluorescence (PLIF-OH) imaging and an advanced modelling with the combined large-eddy simulation (LES)/probability density function (PDF) methods [46]. The preliminary results in [14] successfully replicated the measured timing and duration of extinction in this flame.

The turbulent pulsed jet flame is based on the Sydney piloted flames L, B, and M. The modelling studies of the Sydney flames L, B, and M [9, 118] have been reported in several previous studies. The modelling method used in this work is based on the transported PDF method [46, 55, 99] and earlier efforts to model the flames using the same approach are surveyed here. Chen et al. [119] performed a Reynolds averaged Navier-Stokes (RANS)/PDF study of flames L and B with two simple chemical reaction mechanisms for methane oxidation, a reduced mechanism with five scalars and four-step reactions [120] and a constrained equilibrium mechanism with four scalars, and with a modified coalescence/dispersion (CD) mixing model [121] (or modified Curl model [82]). In order to ignite the flame, it was found to be necessary to insert particles with burned stoichiometric gas mixture into the fuel jet at the downstream of the jet exit. Masri and Pope [122] studied flames K, L, and M using the velocity-composition joint PDF method [55] with an improved stochastic mixing model by Pope [123]. Two thermochemistry models were applied, with one assuming that the particle density was a prescribed piece-wise function of the mixture fraction, and the other obtaining density from a pre-calculated laminar flamelet table of an opposed jet flame with the stretch rate  $a = 100\text{s}^{-1}$ . It was found that simple treatment of chemistry was in general inadequate, and detailed chemistry was necessary for an accurate prediction of the chemical kinetics and its interaction with turbulence in these flames. Incorporating detailed

chemical reaction mechanism in the PDF modelling was enabled by the invention of in situ adaptive tabulation (ISAT) [124]. Saxena and Pope [56, 125] used a skeletal C1 mechanism with 16 species [126] in the joint PDF modelling of velocity, turbulence frequency, and composition in flame L by employing the ISAT method. In this study, it was found that with a skeletal mechanism the compositions were captured more accurately, including the intermediate species CO and H<sub>2</sub>. Two mixing models, the interaction by exchange with the mean (IEM) model [85] (or the linear mean-square estimation (LMSE) model [127] and the Euclidean minimum spanning tree (EMST) model [84], were employed. It was reported that the IEM model was unable to yield a burning flame, while the EMST model can yield burning flames without any difficulty. Jones and Kakhi [128] compared the performance of two mixing models, the CD model [121] and the IEM model [85], in flames L and B using an Eulerian joint-scalar PDF method [129]. In their study, the difficulty of yielding burning flames was not observed by using the IEM model, and it was concluded that the IEM model captured local extinction well but not re-ignition, while the CD model failed to predict local extinction. The performance differences of the IEM model reported in [56, 125, 128], and the CD model in [119, 128], are possibly due to the difference in their modelling approaches, reaction mechanisms or PDF closures. Juddoo et al. [130] reported that the EMST model failed to reproduce flame B using the composition PDF method. This failure, however, was not reproduced in a different study by using a joint velocity-frequency-composition PDF method [131]. The exact reason for the performance difference of the EMST model in these studies is also unknown and is possibly due to the difference in the chemical reaction mechanisms and PDF closures. LES/PDF studies of flames L, B, and M that successfully capture local extinction and re-ignition have been reported in Wang et al. [14] and in Prasad et al. [69]. Overall the latest transported PDF method combined with RANS or LES is reported to be capable of reproducing the Sydney flames L, B, and M reasonably well. The combined LES/PDF method is adopted here to model the modified flame L, the Sydney turbulent pulsed jet flame.

Although the pulsed jet flame in Figure 2.1 is a small modification to the statistically stationary flame L, the effect of this modification is not expected to be small. Flame L is

a purely non-premixed turbulent flame, for which the modelling is quite successful after several decades of model development and validation for turbulent non-premixed combustion. The turbulent pulsed jet flame, however, exhibits distinctive combustion dynamics. Firstly, two extreme combustion behaviours are embedded in the same flame, healthy burning and full extinction. This bimodal combustion behaviour creates a challenging case for modelling since models in the past were usually validated against cases with moderate extinction [69, 130, 132, 133]. Secondly, the exact nature of combustion in the pulsed jet flame is not fully known at this stage, and it is speculated that, in addition to non-premixed combustion, another regime of combustion such as premixed and partially premixed is possibly involved in the same flame, especially near the edge of the extinction region shown in Figure 2.1. It is extremely challenging for existing models to predict multi-regime combustion processes simultaneously.

Following the preliminary LES/PDF study of the pulsed jet flame in [14], we continue a detailed modelling study of this flame. The focus here will be put on the predictions of the flow and turbulence fields as well as the combustion field in the flame. This study is enabled by recently available new measurements of the velocity data and the high-speed PLIF-OH images in the pulsed jet flame using the joint OH-PLIF/OH\* chemiluminescence/laser Doppler velocimetry (LDV) [15] at the University of Sydney. An intriguing issue with all LES practice is how to rigorously validate LES. LES simulations are inherently unsteady and a true representation of the unsteady flow and combustion phenomena by using the model is critical to the development of sound LES models. The new Sydney LDV velocity data and PLIF-OH images for the pulsed jet flame enables us to examine the model's capability to represent physically unsteady processes in turbulent combustion.

The rest of the paper is organised as follows. Section 2.2 summarises the experimental conditions and Section 2.3 discusses the modelling approaches. Section 2.4 discusses general model assessment for LES of statistically transient flames and develops a model assessment framework consisting of different averaging strategies and the bootstrap resampling [134] for constructing confidence intervals. The results are reported in Section 2.5. The effect of the uncertainty in the inflow turbulence intensity is investigated in Section

2.5.1. The specification of the pulsed inflow turbulence boundary condition is validated with the available experimental data in Section 2.5.2. The sensitivity of modelling results to model and numerical parameters is examined in Section 2.5.3. A direct comparison of the temporal evolution of the flow and turbulence statistics in the pulsed jet flame is carefully conducted from the simulations and the measurements in Section 2.5.4. The temporal evolution of the combustion field is examined in Section 2.5.5. The conclusions are drawn in Section 2.6.

## 2.2 Experimental conditions of Sydney turbulent pulsed jet flame

The flame burner used for the pulsed jet flame is identical to the one that is used in the statistically-stationary Sydney piloted jet flames L, B, and M in [9, 118], which is also used in the widely studied Sandia piloted jet flames D, E, and F [88]. The flame burner has a central jet tube with a diameter  $D = 7.2$  mm and with  $\text{CH}_4$  as the fuel. The jet is surrounded by a pilot stream composed of combustion products from a stoichiometric mixture of  $\text{C}_2\text{H}_2$ ,  $\text{H}_2$ , and air at the same C/H mole ratio as  $\text{CH}_4$ . The bulk velocity of the unburnt pilot pre-mixture is 3 m/s. A co-flow of air with a speed of 15 m/s is supplied around the burner. The central fuel jet bulk velocity  $U_b(t)$  varies in time. Initially the flame is at the condition of Flame L [9, 118] with the fuel jet bulk velocity of  $U_{bL} = 41$  m/s. A rapid velocity pulse is then superimposed to the constant bulk velocity of the fuel jet. (The pilot and the air co-flow remain unchanged.) A small CNG tank independent from the main fuel stream is used to supply the fuel pulse [14, 15]. The flow of this extra supplied fuel is controlled by solenoid valves. Different shapes of the pulses can be obtained by specifying the pressure of the supplied fuel with a pressure regulator.

An example of the measured time history of the centerline axial velocity  $u_{exp}(0, 0, 0, t)$  at the jet inlet is shown in Figure 2.2, where  $u_{exp}(x, r, \theta, t)$  denotes the measured axial velocity at location  $(x, r, \theta)$  and time  $t$ , and  $(x, r, \theta)$  is the cylindrical coordinate. The pulse duration  $\tau_p$  is about  $\tau_p = 10$  ms. The added velocity pulse yields the maximum inflow velocity above the extinction threshold [14]. A joint OH-PLIF/OH\* chemiluminescence/LDV

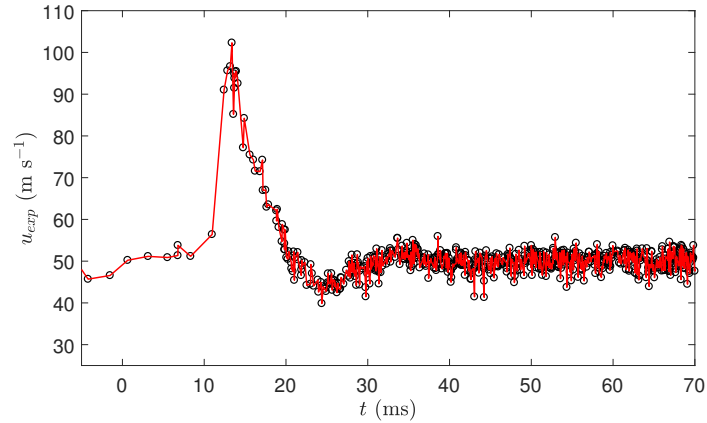


Figure 2.2. An example of the measured time history of the centerline axial velocity at the jet inlet in the pulsed jet flame.

system is used to measure simultaneously OH planar images and axial and radial velocities at various locations [15]. The OH images with an effective area ( $36\text{mm high} \times 36\text{ mm wide}$ ; equivalently  $5D \times 5D$ ) are captured by a high speed camera at 5 kHz, LaVision High-speed Speed-Star 6 (HSS6) CMOS camera. Axial and radial velocities at selected spatial locations are measured simultaneously with the OH-PLIF using a commercial LDV system (TSI Model FSA 3500/4000). The experiment and the measurements are repeated multiple times in order to produce statistics that are useful for model validation. More than 20 repeated experiments are conducted. More details about this experiment can be found in [15].

### 2.3 Modelling approaches

A combined LES/PDF method [46] is employed to model the turbulent pulsed jet flame. Three dimensional and time-dependent resolved velocity fields  $\tilde{\mathbf{u}}(x, r, \theta, t)$  are solved by using the LES method [135]. The combustion fields are modelled by the composition PDF method [46, 55, 99, 136] which features an exact treatment of the effect of detailed chemical kinetics on the evolution of the combustion fields. A hybrid finite volume/Monte Carlo

particle method [14, 46] is applied to solve the closed governing equations. The detailed description of the combined LES/PDF approach is given in this section.

### 2.3.1 LES method

In LES, the large-scale turbulent motions are solved directly and the residual scale effect is modelled. To achieve this, a spatial filter  $G(\mathbf{x}, \Delta\mathbf{x})$  is applied to the Navier-Stokes equations, i.e.,  $\overline{f}(\mathbf{x}, t) = \int f(\mathbf{x}', t)G(\mathbf{x}, \mathbf{x}' - \mathbf{x})d\mathbf{x}'$ . The Favre filtered continuity and momentum equations are:

$$\frac{\partial \overline{\rho}}{\partial t} + \frac{\partial \overline{\rho u}_j}{\partial x_j} = 0, \quad (2.1)$$

$$\frac{\partial \overline{\rho u}_i}{\partial t} + \frac{\partial \overline{\rho u}_i \tilde{u}_j}{\partial x_j} = -\frac{\partial \overline{P}}{\partial x_i} + \frac{\partial}{\partial x_j} (2\mu \tilde{S}_{ij}) + \frac{\partial T_{ij}}{\partial x_j}, \quad (2.2)$$

where the tilde “~” denotes Favre filtering, and  $\tilde{S}_{ij} = (\partial \tilde{u}_i / \partial x_j + \partial \tilde{u}_j / \partial x_i) / 2 - \delta_{ij} \partial \tilde{u}_k / \partial x_k / 3$  is the trace-less strain rate tensor. In the last term of Equation (2.2),  $T_{ij} = \overline{\rho \tilde{u}_i \tilde{u}_j} - \overline{\rho u}_i \overline{u}_j$  is the residual turbulent stress which is unclosed and needs modelling. The eddy viscosity model [99] is used to close this term:

$$T_{ij} = \overline{\rho \tilde{u}_i \tilde{u}_j} - \overline{\rho u}_i \overline{u}_j = 2\mu_t \tilde{S}_{ij} + \frac{1}{3} T_{kk} \delta_{ij}, \quad (2.3)$$

where the residual turbulent eddy viscosity  $\mu_t$  is modeled through the Smagorinsky model [137]  $\mu_t = C_\mu \overline{\rho} \Delta^2 |\tilde{\mathbf{S}}|$  with the model constant  $C_\mu$  determined by the dynamic procedure [138]. The turbulence resolution scale  $\Delta$  is specified to be the same as the local grid size. To reduce the computational cost of evaluating transport properties, we follow previous studies [46] to approximate the molecular viscosity as:

$$\mu = \rho v_0 \left( \frac{\tilde{T}}{T_0} \right)^\alpha, \quad (2.4)$$

where  $v_0 = 1.613 \times 10^{-5} \text{ m}^2/\text{s}$ ,  $T_0 = 300.0 \text{ K}$ ,  $\alpha = 1.721$ .

The closed continuity and momentum equations are cast in the cylindrical system for the current turbulent pulsed jet flame and are solved using a finite volume method. Second order conservative schemes are used to discretise the LES equations. The time advancement

is done by using a semi-implicit iterative solution procedure. More details about the LES solution method can be found in [135, 139].

### 2.3.2 PDF method

In the composition PDF method, the density-weighted joint composition  $\tilde{f}(\boldsymbol{\psi}; \mathbf{x}, t)$  is employed to represent the sub-filter scale distribution of the random combustion fields at the spatial location  $\mathbf{x}$  and time  $t$ , where  $\boldsymbol{\psi}$  is the composition sample space vector corresponding to the composition vector  $\boldsymbol{\phi} = \{\phi_\alpha, \alpha = 1, \dots, n_\phi\}$  consisting of all the species mass fractions and enthalpy. The transport equation of the joint composition PDF  $\tilde{f}(\boldsymbol{\psi}; \mathbf{x}, t)$  of all the species mass fractions and enthalpy [136] is:

$$\begin{aligned} \frac{\partial \bar{\rho} \tilde{f}}{\partial t} + \frac{\partial}{\partial x_j} (\bar{\rho} \tilde{u}_j \tilde{f}) + \frac{\partial}{\partial \psi_\alpha} [\bar{\rho} \tilde{f} S_\alpha(\boldsymbol{\psi})] - \frac{\partial}{\partial x_j} \left( \bar{\rho} \Gamma \frac{\partial \tilde{f}}{\partial x_j} \right) = \\ - \frac{\partial}{\partial x_j} \left( \bar{\rho} \tilde{f} \widetilde{u_j''} | \boldsymbol{\psi} \right) - \frac{\partial^2}{\partial \psi_\alpha \psi_\beta} \left[ \tilde{f} \left( \overline{\rho \Gamma \frac{\partial \phi_\alpha}{\partial x_j} \frac{\partial \phi_\beta}{\partial x_j} | \boldsymbol{\psi}} \right) \right], \end{aligned} \quad (2.5)$$

where  $\tilde{u}_j$  is the resolved velocity and  $\Gamma$  is the molecular diffusivity. A similar form to the molecular viscosity  $\mu$  in Equation (2.4) is used here to calculate the molecular diffusivity:

$$\Gamma = \Gamma_0 \left( \frac{\tilde{T}}{T_0} \right)^\alpha, \quad (2.6)$$

where  $\Gamma_0 = \nu_0 / Sc = 2.293 \times 10^{-5} \text{ m}^2/\text{s}$ ,  $T_0 = 300.0 \text{ K}$ ,  $\alpha = 1.660$ . In this study equal molecular diffusivity and unity Lewis number are assumed following common practice [46, 55].

The terms on the left hand side of Equation (2.5) are closed, including the chemical reaction source term. The fact that the chemical reaction can be treated exactly is the major advantage of the transported PDF method. The two terms on the right hand side are unclosed. The first term is the spatial flux due to the residual velocity and is usually modelled by the gradient diffusion hypothesis [55]:

$$- \frac{\partial}{\partial x_j} \left( \bar{\rho} \tilde{f} \widetilde{u_j''} | \boldsymbol{\psi} \right) = \frac{\partial}{\partial x_j} \left( \bar{\rho} \Gamma_t \frac{\partial \tilde{f}}{\partial x_j} \right), \quad (2.7)$$

where  $\Gamma_t$  is the residual turbulent eddy diffusivity. It is obtained from  $\bar{\rho} \Gamma_t = \mu_t / Sc_t$  with the Schmidt number  $Sc_t = 0.4$ . The second term on the right hand side of Equation (2.5)

represents the molecular mixing in the composition space due to the conditional scalar dissipation. The closure of this term has been one of the main focuses of the PDF studies in the past. Several mixing models have been developed, e.g. the IEM model [85], the Modified Curl model [82], and the EMST model [84]. In the present study, the EMST model [84] is used. Both IEM and modified Curl models have difficulty yielding extinction correctly due to the known shortcoming of non-localness in mixing [20,36] [84, 140], and they are not suitable for the current study of the pulsed jet flame which involves significant extinction.

With all the unclosed terms modelled, the transport equation for the composition PDF is solved numerically by using the Monte Carlo particle method [55] that is implemented in a research code named HPDF [46]. The method uses an equivalent particle system to represent the joint composition PDF. Each particle has its location  $\mathbf{X}^*(t)$ , compositions  $\boldsymbol{\phi}^*(t)$ , mass  $m^*$ , and other properties, e.g. velocity  $\tilde{\mathbf{u}}^*(t)$ , diffusivities  $\Gamma^*$  and  $\Gamma_t^*$ , and mixing frequencies  $\Omega^*$  that can be obtained from the field data with interpolation, at time  $t$ . In this work, the mixing frequency is approximated as:

$$\Omega = \frac{C_\phi(\Gamma + \Gamma_t)}{2\Delta^2}, \quad (2.8)$$

with the model constant  $C_\phi=3.0$ . Different values of  $C_\phi$  combined with EMST have been examined in the flame L, and it is found that this value of 3.0 yields overall the best agreement with the experimental data of flame L [9, 118]. The same value is adopted here for the turbulent piloted flame. Sensitivity studies of the predictions of the flow and turbulence fields in the pulsed jet flame to the different values of  $C_\phi$  will be further examined in Section 2.5.3. The governing equations for the particles are the following stochastic differential equations (SDE):

$$d\mathbf{X}^*(t) = \left[ \tilde{\mathbf{u}} + \frac{\nabla [\bar{\rho}(\Gamma + \Gamma_t)]}{\bar{\rho}} \right]^* dt + [2(\Gamma + \Gamma_t)^*]^{1/2} d\mathbf{W}, \quad (2.9)$$

$$d\boldsymbol{\phi}^*(t) = \mathbf{M}(\boldsymbol{\phi}^*, \Omega^*)dt + \mathbf{S}(\boldsymbol{\phi}^*)dt, \quad (2.10)$$

where  $d\mathbf{W}$  is the incremental Wiener process.  $\mathbf{M}(\boldsymbol{\phi}^*, \Omega^*)$  stands for mixing and  $\mathbf{S}(\boldsymbol{\phi}^*)$  is the chemical reaction source term. The superscript "\*" represents the quantity at the particle location  $(\mathbf{X}^*(t), t)$ .

Both first order and second order time-splitting schemes [46] are available to solve the above SDE. The difference of using the different schemes is negligibly small when they are used in the simulations of turbulent jet flames [46]. In this work, the first order time-splitting scheme,  $\mathbb{T}\mathbb{M}\mathbb{R}$  [46], is used to integrate the SDEs, where  $\mathbb{T}$  represents the substep of transport of particles in the physical space following Equation 2.9,  $\mathbb{M}$  represents the substep of mixing in the composition space, and  $\mathbb{R}$  denotes the substep of chemical reaction. The first order explicit Euler scheme is used to integrate Equation 2.9. The EMST model is employed to model the mixing process. A reduced chemical mechanism DRM19 [141] consisting of 19 species is used to describe the oxidation of  $\text{CH}_4$ . The DRM19 is derived from GRI-Mech 1.2 [142,143] and is found to be able to replicate the detailed GRI-Mech 1.2 with reasonable accuracy based on our parametric studies of flame L (results are not shown). Pure  $\text{CH}_4$  is used in the simulations to replace CNG that was used in the experiment. The difference between CNG and  $\text{CH}_4$  is due to the ethylene content which causes a slight change in the stability limit. For example, the measured blow-out velocity for a turbulent jet flame with CNG and  $\text{CH}_4$  as fuel is 113.1 m/s and 105.0 m/s [25], respectively, with the relative difference about 7%. Thus, some difference in extinction behaviour is expected when  $\text{CH}_4$  is used to replace CNG in the current simulations. ISAT [124] is applied to accelerate the calculation of the integration of chemical reactions with an ISAT error tolerance of  $10^{-4}$ . Smaller ISAT error tolerance has been tested and yields little difference in the predictions while increasing the computational cost significantly.

### 2.3.3 Coupling algorithm and other numerical details

The LES and PDF methods are fully coupled by using an algorithm that is consistent at both the model and numerical levels. The equivalent enthalpy approach proposed by Muradoglu et al. [144] is used to couple the flow fields and particle properties.

The same grid in the LES solver is used in the particle method to track the locations of particles and to estimate the statistics from the cell particles. For a given cell with  $N_{pc}$  particles, the  $n$ th moment of a composition variable  $\phi$  can be calculated as:

$$\widetilde{\phi}^n = \frac{\sum_{i=1}^{N_{pc}} m_i^* \phi_i^{*n}}{\sum_{i=1}^{N_{pc}} m_i^*}, \quad (2.11)$$

where  $m_i^*$  is the mass and  $\phi_i^*$  is the composition value of the  $i$ th particle. A particle number control technique including cloning and annihilation is employed at every time step after the particle transport to ensure the particle number in each cell approximately constant. For the current simulations, we set the number of particles per cell to be  $N_{pc}=30$  following [14]. The domain size is chosen to be  $[0, 60D] \times [0, 20D] \times [0, 2\pi]$  in the axial  $x$ , radial  $r$ , and azimuthal  $\theta$  directions, respectively. The domain is partitioned into  $256 \times 108 \times 48$  non-uniform grid cells in the respective directions. The inflow turbulence boundary condition is generated from a separate three dimensional fully developed turbulent pipe flow simulation. The generated inflow boundary condition is statistically stationary and is scaled according to the measured velocity pulse to produce a consistent boundary condition for the pulsed jet flame. A simple scaling approach by defining a spatially independent pulse function is used [14]. This simple scaling approach makes two assumptions about the inflow turbulence boundary condition for the simulations. First, the relative turbulence intensity (turbulence intensity normalized by the local mean velocity) is the same throughout the pulse at the jet inlet. Second, the scaling is independent of the spatial locations at the inlet. We will evaluate the validity of these assumptions by using the recent LDV velocity measurements [15] in Section 2.5.2. For more details of the current modelling approaches, the readers are referred to [14,46].

## 2.4 Model assessment for statistically transient flames

### 2.4.1 General considerations

Past LES modeling focuses mostly on statistically stationary flames, and the model assessment is often based on time averaged statistics. Two important issues emerge recently

from this practice of LES model assessment. Firstly, the model validation based on time-averaged statistics is unable to examine the model's capacity to truly represent the temporal evolution of turbulence and combustion fields in LES since it smoothes out all the temporal fluctuations. It is desired that the LES model can capture an accurate temporal evolution of large-scale turbulence structures. The importance to resolve large turbulence length scales accurately in LES has been emphasised significantly in the past. It is equally important to resolve large turbulence timescales accurately in order to capture the temporal evolution of large scale turbulence in LES. This issue is particularly important for LES of turbulent combustion since flame structures are embedded in turbulent flows. The modeling of the evolution of the flame structures directly affects the prediction quality of turbulent combustion fields. The second issue is that the time-averaging technique is not directly applicable to statistically transient problems like the pulsed jet flame studied in this work. New model assessment approaches are thus needed. With the availability of more and more temporally resolved experimental data for turbulent flames, due to the significant advancement of laser diagnostic techniques in the past few years, using those data for a rigorous model validation becomes a particularly pressing issue. This paper presents an important attempt to address the model validation for LES to represent the temporal evolution of turbulence and combustion.

In general, there are several approaches that we can use for comparing the temporal evolution of LES model predictions with temporally resolved measurements.

1. A direct comparison between LES model predictions and measurements can be made, e.g., a comparison of the predicted and measured temperature at a selected location. This comparison is easy and, to some extent, informative, but it is qualitative in nature at most. There are also two conceptual issues involved in this direct comparison. The first one is that the LES predicted and measured temporal fields are different realizations from a turbulent flow problem. A direct comparison between them is more or less meaningless since the difference between them does not indicate the same level of disagreement between the model predictions and measurements. The second issue is that the LES predictions are filtered fields of the underlying turbulence fields,

while the measurements may represent the true underlying fields if the measurement resolution is high enough, or represent filtered fields as well but with a different filter width depending on the measurement resolution. This difference of the representation of the predicted and measured fields causes the direct comparison problematic as well.

2. The characteristics of the temporal evolution of the predicted and measured combustion fields can be compared, such as the integral time scales and frequency spectrum. This is a more rigorous comparison and provides a more quantitative measure of how the LES models capture the temporal correlation of the turbulence and combustion fields. A limitation of this comparison is that it is typically applicable only to statistically stationary problems.
3. Modal analysis can be used to compare the model predictions and measurements, such as the Proper Orthogonal Decomposition (POD) [145] and the Dynamic Mode Decomposition (DMD) [146]. Such an analysis can provide information of the models' representation of spatial and temporal coherent structures of the turbulence and combustion fields. This analysis is also generally only applicable to statistically stationary processes.
4. For statistically repeatable processes, like the turbulent pulsed jet flame, multiple realizations can be conducted in both experiments and simulations. Time dependent statistics can then be extracted from the realizations for the model comparison. This is a relatively easy approach with solid basis for validating models in statistically transient problems. Just like any other statistical approach, the statistics requires a lot of realizations to converge, which leads to costly simulations and/or measurements.
5. Although in general time-averaging cannot be used in statistically transient problems, a locally defined time-averaging can still be useful in model validation for computing statistics. A local time averaging time scale  $h$  can be defined to average the instantaneous fields in the time interval  $[t, t + h]$ . Any high frequency component can be filtered by this local time averaging. The results contain low frequency component

(large time-scale), which can be useful for model validation. It is noted that the results of local time average of a stochastic process are random and hence cannot be used for model comparison directly. Nevertheless, the random fluctuations in the locally time averaged results are smaller than the instantaneous fields, which makes the comparison less problematic compared to the direct comparison.

6. Certain problems feature statistical homogeneity, such as the circumferential direction in the turbulent pulsed jet flame. For these problems, spatial averaging in the homogeneous direction can be used to extract statistics for model comparison.

All of the above methods have their advantages and disadvantages. There is no single method that is adequate for LES model validation, due to the limitation of the method or its computational and measurement cost. In this work, we aim to combine several of the above methods to provide a feasible framework for validating LES model predictions for the temporal evolution of the flow and turbulence fields in the turbulent pulsed jet flame. Viewing the measurements and model predictions of the turbulence fields in the pulsed jet flame as individual realizations from the same turbulent problem, we need a sufficiently large number of realizations which are statistically independent and identically distributed (IID) to computing statistics in order to ensure statistical convergence. The challenge is how to obtain a sufficiently large number of IID realizations with reasonable cost. In the following, we layout an approach combining a few of the above methods to gain as many statistical samples as possible for computing statistics without incurring prohibitive cost. Meanwhile, an approach to estimate the uncertainty of the computed statistics is discussed.

#### **2.4.2 Strategies for averaging to estimate statistics**

For the current turbulent pulsed jet flame, we combine three averaging strategies — sample averaging from different realizations, spatial averaging from the homogeneous circumferential direction, and a local time averaging with a small time interval — to obtain statistics from LES of the statistically transient problem for the comparison with the experimental data. Each of the averaging strategies is defined below.

For a random process  $g(\mathbf{X}, t)$  which can represent the LES solutions at a particular location  $\mathbf{X}$  or a point-wise measurement at  $\mathbf{X}$ . We can repeat simulations and measurements for  $M$  times and obtain observations as  $g_m(\mathbf{X}, t) (m = 1, \dots, M)$ . All these observations are assumed to be IID. A sample averaging over the observations can be defined as:

$$\langle g(\mathbf{X}, t) \rangle_m = \frac{1}{M} \sum_{m=1}^M g(\mathbf{X}, t), \quad (2.12)$$

where  $\langle \cdot \rangle_m$  denotes the sample averaging. Typically the number of observations  $M$  that can be obtained in the simulations or the experiments is limited, and additional averaging is needed to obtain statistics with reduced statistical errors.

A local time-averaging over a small time interval can be introduced as:

$$\langle g(\mathbf{X}, t) \rangle_h = \frac{1}{h} \int_{t-\frac{h}{2}}^{t+\frac{h}{2}} g(\mathbf{X}, s) ds, \quad (2.13)$$

where  $\langle \cdot \rangle_h$  denotes the local time-averaging, and  $h$  is the time-averaging interval. The value of  $h$  needs to be carefully chosen and typically is required to be smaller than the characteristic time scale associated with  $g(\mathbf{X}, t)$ . For the turbulent pulsed jet flame studied in this work,  $h$  needs to be much smaller than the pulse duration  $\tau_p$ . Meanwhile, the value of  $h$  also needs to be as large as possible since the data within the time interval are not IID. A large value of  $h$  is helpful to alleviate the strong correlation of the data within  $h$ .

For statistically homogeneous problems, a spatial averaging along the homogeneous direction can be introduced as:

$$\langle g(\mathbf{X}, t) \rangle_D = \frac{1}{H_D} \int_0^{H_D} g(\mathbf{X}, t) dx_D, \quad (2.14)$$

where  $\langle \cdot \rangle_D$  is the spatial averaging along the  $Dth$  direction, and  $H_D$  is the domain size in the  $Dth$  direction. For the turbulent pulsed jet flame, the spatial averaging can be used along the  $\theta$  (azimuthal) direction to obtain  $\langle g(\mathbf{X}, t) \rangle_\theta$  since the flame is statistically axisymmetric. Similar to the specification of the time interval  $h$  for the local time averaging, the domain size  $H_D$  for the spatial averaging needs to be large enough since the data inside the domain are not IID.

The above defined averaging strategies can be stacked together for producing better statistics in the statistically transient problems than using any single of them. For example, we can use a notation like  $\langle \cdot \rangle_{m,h,\theta}$  to denote a statistics obtained by taking the sample averaging in Equation 2.12 first, the local time-averaging in Equation 2.13 next, and then the spatial averaging in Equation 2.14. These combined averaging strategies can produce statistics with reduced statistical error so that a more rigorous LES model validation can be performed for statistically transient problems.

### 2.4.3 Constructing confidence intervals

With the above combined averaging strategies, we expect to have reduced statistical errors in the results compared to those with only single averaging. The statistical error which is unknown at this point can still yield significant uncertainty in the computed statistics that can hinder an informative comparison between the modeling results and the experiments. To provide an estimated level of uncertainty of the computed statistics, we outline below a simple yet general method to construct the confidence intervals for the statistics obtained based on the averaging strategies in Section 2.4.2.

For a random variable  $Y$ , we make a set of  $N_m$  observations denoted as  $\hat{y} = \{y_m, m = 1, \dots, N_m\}$ . These observations are IID. In many problems, a quantity  $Q$  as a function of the set of observations  $Q(\hat{y})$  is sought. A typical example is that  $Q$  is the sample average of  $\hat{y}$ ,  $Q = \langle y \rangle_m$ . To construct the confidence interval of the estimated  $Q$ , we need to find the underlying probability distribution of  $Q$ . If  $Q = \langle y \rangle_m$ , this distribution is well known and it is approximately a normal distribution according to the central limit theorem [147]. The 95% confidence interval can be easily constructed to be  $\left[ \langle y \rangle_m - 1.96 (\sigma^2(y)/N_m)^{1/2}, \langle y \rangle_m + 1.96 (\sigma^2(y)/N_m)^{1/2} \right]$ , where  $\sigma^2(y)$  is the variance of  $y$ . In general, however,  $Q$  can be more complicated than simple sample averaging, and it may not be formulated to fit the central limit theorem, e.g.,  $Q = \langle y \rangle_m^a$  where  $a$  is a constant ( $a \neq 1$ ). Thus we need a more general approach to construct the confidence interval for evaluating  $Q$ . A simple approach based on the bootstrap resampling [134] is outlined below.

Based on only one set of observations  $\hat{y}$ , we can only evaluate one sample value of  $Q$ . In order to get the probability distribution information of  $Q$ , we have to generate more samples for  $Q$ . More new samples typically are not feasible in many problems. In this case, bootstrap resampling [134] becomes a useful method. A new set of observations can be obtained by resampling the original set of observations  $\hat{y}$  with replacement. We denote the new set of observation as  $\hat{y}_n = \{y_{nm}, m = 1, \dots, N_m\}$  with the new set the same size as the original set. The resampling is done with replacement so the elements in  $\hat{y}_n$  may contain repeated elements of  $\hat{y}$ . From this new set of observations we can compute a new value of  $Q_n = Q(\hat{y}_n)$ . The bootstrap resampling can then be repeated many times to get a set of samples  $\hat{Q} = \{Q_n, n = 1, \dots, N_s\}$  where  $N_s$  is the number of times that the original set has been resampled. This set of samples  $\hat{Q}$  provides an estimate of the probability distribution of  $Q$ . Following the basic bootstrap method [134], the 95% confidence interval can be constructed from the bootstrapped sample set as  $[Q_{2.5}^*, Q_{97.5}^*]$  where  $Q_\alpha^*$  is the  $\alpha$ th percentile of the sample distribution. This confidence interval provides a measure of the level of uncertainty involved in the estimate of  $\langle Q \rangle$ .

We now show an example to demonstrate the above bootstrap method for constructing the confidence intervals. We take  $y$  as a uniformly distributed random variable between  $[0, 1]$ , and obtain  $N_m = 10$  random samples as  $\hat{y} = [0.81, 0.91, 0.13, 0.91, 0.63, 0.1, 0.28, 0.55, 0.96, 0.96]$ . We perform the bootstrap resampling for  $N_s = 1000$  times to obtain the different sets of observations  $\hat{y}_n$ . We define  $Q$  to be the sample average,  $Q = \langle y \rangle_m$ . From the different set of observations  $\hat{y}_n$ , we can compute the function  $Q_n$ . From the set of samples  $\hat{Q}$ , we can estimate the 2.5th percentile  $Q_{2.5}^*$  to be 0.42, i.e., the probability  $Prob(Q < Q_{2.5}^*) = 2.5\%$ . Similarly we can find  $Q_{97.5}^* = 0.81$ . Thus the 95% confidence interval for estimating the sample average  $\langle y \rangle_m$  is  $[0.42, 0.81]$  based on the bootstrap method. For comparison, we construct the confidence interval based on the central limit theorem since the sample mean is sought here. Based on the sample mean (0.62) and variance (0.12) of the original set of observation  $\hat{y}$ , we can construct the 95% confidence interval as  $[0.41, 0.83]$ . We can see that the confidence interval from the bootstrap method is close to that obtained from the central limit theorem expectedly when computing sample averaging. The bootstrap method,

however, represents a more general approach than the central limit theorem for constructing confidence intervals for estimating functions that is are not limited to simple averaging of the samples.

The above averaging strategies together with the constructed confidence intervals are used in the following discussions for comparing the simulation results and the measurements of the turbulent pulsed jet flame, in order to provide a rigorous validation of the LES method for statistically transient problems.

## **2.5 Results and discussion**

Multiple IID simulations of the turbulent pulsed jet flame with the LES/PDF methods are performed, and the results are discussed in the following. The effect of the uncertainty in the inflow turbulence intensity is investigated in Flame L first in Section 2.5.1. The method of specifying the turbulence inflow boundary condition for the simulations of the pulsed jet flame is examined in Section 2.5.2. The sensitivity of the model predictions to model and numerical parameters is studied in 2.5.3. The comparison of the predicted and measured velocity statistics is done in Section 2.5.4. The temporal evolution of the combustion field is presented in Section 2.5.5.

### **2.5.1 Effect of inflow turbulence intensity**

In the simulations, the inflow turbulence boundary condition of the fuel jet is time-dependent and is generated from a separate fully-developed pipe flow simulation. A numerical forcing is added to the pipe flow simulation to yield the pipe flow statistics (mean and variance) in agreement with the experimental data for flame L [9, 118]. Measurement uncertainty exists in the experimental data that are used for the numerical forcing. Here we examine the effect of this uncertainty in the inflow turbulence intensity on the flame simulations. The statistically stationary case, flame L, is used as the test case. The same effect will also be examined in the turbulent pulsed jet flame later in Section 2.5.3.

Figure 2.3 shows the radial profiles (lines) of the inflow mean axial velocity  $\langle \tilde{u} \rangle$  and the root mean square (rms) axial velocity  $u' = \langle \tilde{u}^2 - \langle \tilde{u} \rangle^2 \rangle^{1/2}$  obtained from the generated inflow boundary condition, where  $\tilde{u}$  is the resolved axial velocity, and  $\langle \cdot \rangle$  denotes the mean (or mathematical expectation) estimated from time-averaging over a long period of time (about 2.5 flow through times based on the fuel jet velocity). In the figure, the measurements that were obtained in the 1980s [148] are shown as cycles and are denoted as the old measurements. Good agreement between the simulation and the measurement is observed, indicating the effectiveness of the numerical forcing.

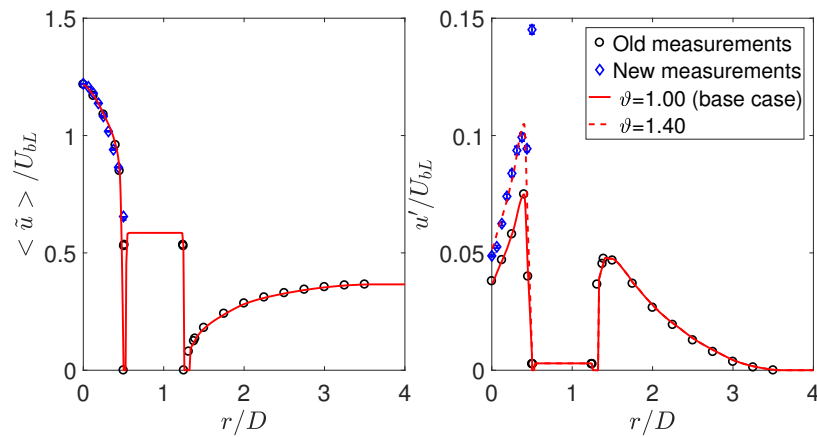


Figure 2.3. Mean and rms axial inflow velocity normalized by the inflow jet bulk velocity  $U_{bL} = 41$  m/s in flame L.

From the recent measurements of the velocity data in the turbulent pulse jet flames [15], we can extract the same inflow statistics. One measured time series of the axial velocity is shown in Figure 2.2. By averaging the measured time series, excluding the pulse, we can obtain a new measurement for  $\langle u_{exp} \rangle$  and  $u'_{exp}$  for flame L. The new measurement data are shown in Figure 2.3 as diamonds. The error bars on the new measurements are the 95% confidence intervals  $\left[ -1.96\sigma / \sqrt{N_m}, 1.96\sigma / \sqrt{N_m} \right]$  with  $\sigma^2$  the variance of the computed time-averages estimated from about 20 repeated measurements and  $N_m$  is the number of samples. Comparing the old measurements (cycles) [148] and the new measurements (diamonds) [15], we can see that the difference in the mean axial velocity is small (relative

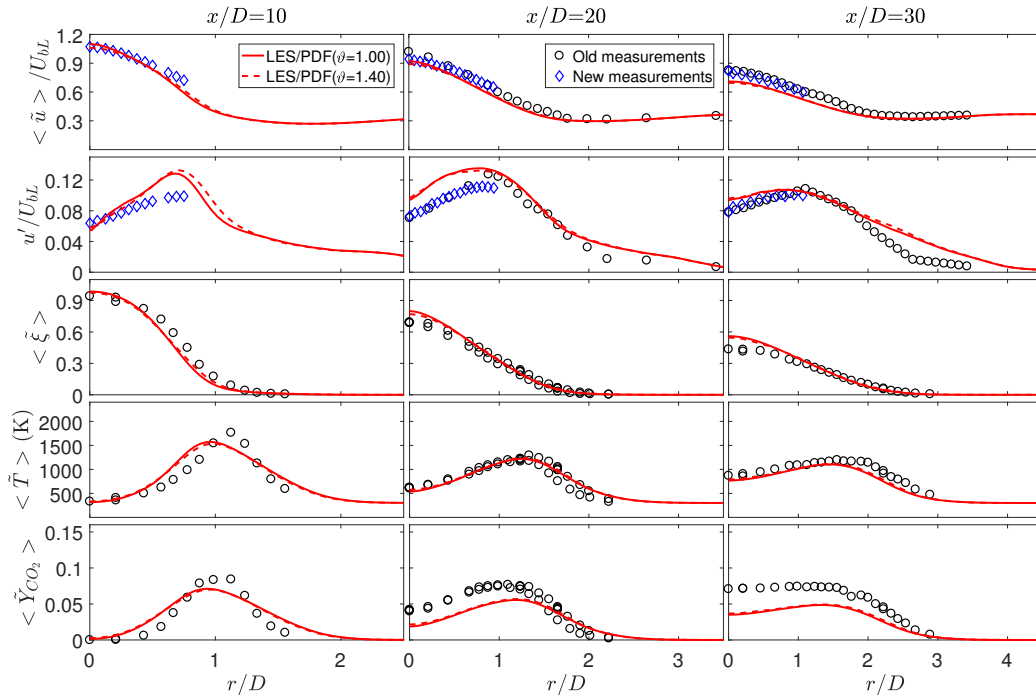


Figure 2.4. Radial profiles of the predicted (lines) and measured (symbols) mean axial velocity  $\langle \tilde{u} \rangle$ , rms axial velocity  $u'$ , mean mixture fraction  $\langle \tilde{\xi} \rangle$ , mean temperature  $\langle \tilde{T} \rangle$  and mean mass fraction  $\langle \tilde{Y}_{CO_2} \rangle$  at the axial locations of  $x/D_f = 10, 20,$  and  $30$  in Flame L.

difference within 5%), and the rms axial velocity from the new measured data is about 40% higher than the old measurements. The difference in the two sets of measurements, mainly in the rms axial velocity, is a reasonable indication of the measurement uncertainty. Such uncertainty in the measurements causes the same level of uncertainty in the specification of the inflow boundary condition for the simulations. Next we examine the effect of such uncertainty on the model predictions.

We select the inflow turbulence time series  $\tilde{u}(0, r, \theta, t)$  generated from a fully developed pipe flow simulation forced by the old measurements [148] as the base case. The base case is scaled according to the following equation so that the mean velocity is not altered and different turbulence intensity can be obtained in the inflow boundary condition:

$$\tilde{u}(0, r, \theta, t) = \langle \tilde{u}_{base} \rangle + (\tilde{u}_{base}(0, r, \theta, t) - \langle \tilde{u}_{base} \rangle) \cdot \vartheta, \quad (2.15)$$

where  $\tilde{u}(0, r, \theta, t)$  is the base case, and  $\vartheta$  is a scaling factor. Two values of  $\vartheta$ , 1.0 and 1.4, are evaluated as shown in Figure 2.3 as lines. The value of  $\vartheta=1.0$  (solid line in Figure 2.3) yields the inflow rms axial velocity in good agreement with the old measurements (cycles), and the value of  $\vartheta=1.4$  (dashed line in Figure 2.3) yields the inflow rms axial velocity in good agreement with the new measurements (diamonds).

The effect of the scaling factor  $\vartheta$  in the boundary condition on the prediction of Flame L is examined in Figure 2.4 where the radial profiles are shown of the mean axial velocity  $\langle \tilde{u} \rangle$ , rms axial velocity  $u'$ , mean mixture fraction  $\langle \tilde{\xi} \rangle$ , mean temperature  $\langle \tilde{T} \rangle$ , and mean mass fraction of  $\text{CO}_2$   $\langle \tilde{Y}_{\text{CO}_2} \rangle$  at the axial locations of  $x/D_f = 10, 20, \text{ and } 30$ . The symbols are the old (cycles) and new (diamonds) measurements. The lines are the simulation results obtained with the different inflow turbulence boundary conditions scaled according to Equation (2.15) with the scaling factor  $\vartheta=1.0$  (base case, solid lines in Figure 2.4) and  $\vartheta=1.4$  (dashed lines in Figure 2.4). The two scaling factors  $\vartheta$  have 40% relative difference, but they result in negligible difference (relative difference less than 5%) consistently in all the results downstream. Therefore, in spite of the large uncertainty in the inflow boundary condition for the turbulence intensity, the effect of such uncertainty is found to be very small in flame L. This is a useful conclusion for specifying reliable inflow boundary conditions for flame L. The extensibility of this conclusion to pulsed jet flame is also confirmed [117] (not presented in the thesis). The base case with  $\vartheta=1$  is used for all the later discussions if not stated explicitly.

## 2.5.2 Specification of the pulsed inflow boundary condition

To model the turbulent pulsed jet flame, a detailed time-dependent inflow turbulence boundary condition is required to describe both the turbulent fluctuations and the pulse. To generate such a boundary condition, Wang et al. [14] defined a pulse function  $f(t)$  and specified the required boundary condition according to:

$$\tilde{u}(0, r, \theta, t) = \tilde{u}_{base}(0, r, \theta, t) \cdot (1 + f(t)), \quad (2.16)$$

where  $\tilde{u}_{base}(0, r, \theta, t)$  is the inflow velocity of the base case discussed in Section 2.5.1. Taking the mean (or mathematical expectation) of Equation (2.16), we obtain:

$$\langle \tilde{u}(0, r, \theta, t) \rangle = \langle \tilde{u}_{base}(0, r, \theta, t) \rangle \cdot (1 + f(t)). \quad (2.17)$$

Similarly, we can obtain the rms velocity  $u'$  from Equation (2.16) as:

$$u'(0, r, \theta, t) = u'_{base}(0, r, \theta, t) \cdot (1 + f(t)). \quad (2.18)$$

The pulse function  $f(t)$  is a function of time only, and can be estimated from the axial velocity at the jet inlet based on Equation (2.17). For the estimate, the centerline axial velocity ( $r = 0, \theta = 0$ ) is used and from Equation (2.17), we obtain:

$$f(t) = \frac{\langle \tilde{u}(0, 0, 0, t) \rangle}{\langle \tilde{u}_{base}(0, 0, 0, t) \rangle} - 1, \quad (2.19)$$

in which  $\langle \tilde{u}_{base}(0, 0, 0, t) \rangle$  is the mean centerline axial velocity  $U_{0L}$  of Flame L, and  $\langle \tilde{u}(0, 0, 0, t) \rangle$  can be estimated from the measurements  $\langle u_{exp}(0, 0, 0, t) \rangle_{m,h}$  by performing the sample averaging in Equation (2.12) over the repeated measurements and the local time averaging in Equation (2.13) on the experimental data at the centerline and at the jet exit. The local time-averaging interval  $h$  is chosen to be much smaller than the pulse duration  $\tau_p$ ,  $h = \tau_p/20$ . The factor of 1/20 is specified based on the trade-off discussed in Section 2.4.2. The time scale associated with the duration of extinction in the pulsed jet flame is estimated to be about the same order of magnitude as the pulse  $\tau_p$  according to the OH-PLIF measurements [15]. Thus, the time averaging with the specified  $h$  ( $h \ll \tau_p$ ) is expected to be able to retain large extinction events in the pulsed jet flame. The resulted pulse function  $f(t)$  by using the centerline velocity measurement data at the jet exit is shown in the left subplot of Figure 2.5. The error bars in the figure are the 95% confidence interval computed following the method discussed in Section 2.4.3.

The specification of the inflow turbulence boundary condition in Equation (2.15) implies two assumptions as discussed in Section 2.3.3. The first one is that the pulse functions  $f(t)$  at the different radial locations at the jet inlet are the same since we use the single pulse function acquired at the centerline for the entire cross section of the fuel jet inflow. The

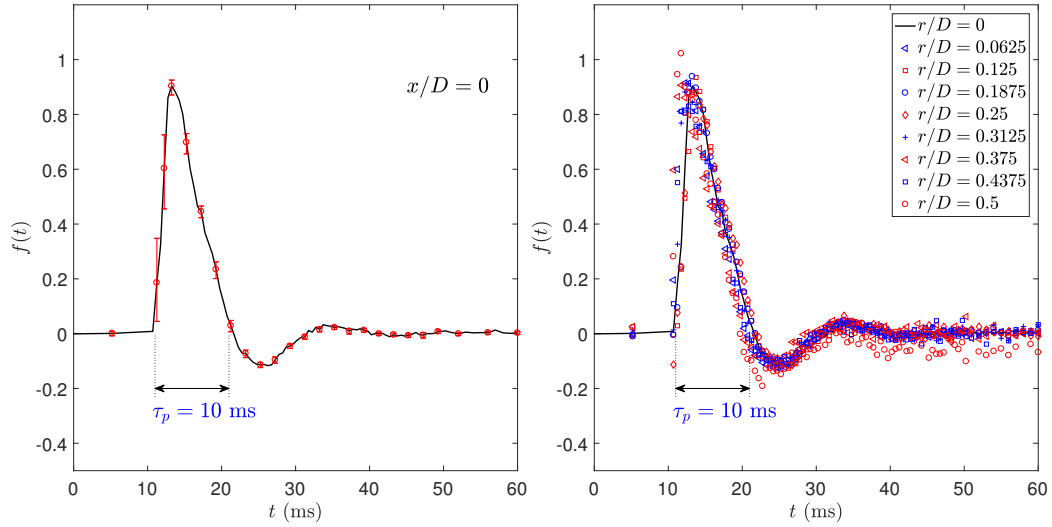


Figure 2.5. The pulse function  $f(t)$  estimated from the measurements at the different radial locations at the jet inlet of the turbulent pulsed jet flame.

second one is that the relative fluctuation, i.e. the ratio of turbulence intensity to the local mean velocity, keeps approximately constant during the pulse (as can be seen from Equation (2.20) in the later discussion). Next, we examine the validity of these two assumptions.

Following the same procedure for determining  $f(t)$  from the centerline axial velocity at the jet exit outlined above, we can determine  $f(t)$  from other radial measurement locations at the jet inlet. Figure 2.5 (right subplot) shows the different pulse functions  $f(t)$  computed from the measurements at the different radial locations at the jet inlet. The shapes of the pulse functions at the different radial locations are very similar to each other, which provides the basis for the assumption that the pulse function is, to a large extent, independent of the radial locations at the jet inlet. This validates the first assumption implied in the specification for the inflow turbulence boundary condition of the pulsed jet flame.

Combining Equations (2.17) and (2.18), we can obtain the following relation:

$$\frac{u'}{\langle \tilde{u}(0, r, \theta, t) \rangle} = \frac{u'_{base}}{\langle \tilde{u}_{base}(0, r, \theta, t) \rangle}. \quad (2.20)$$

The relation shows that the relative turbulence intensity in the specified inflow of the pulsed jet flame obtained from Equation (2.15) is the same as the relative turbulence intensity in

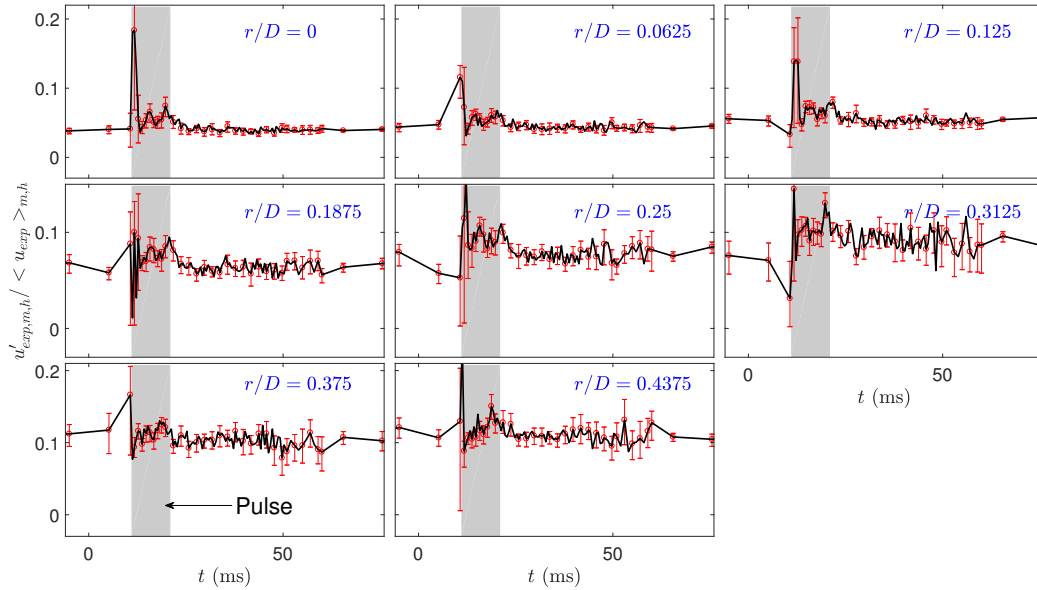


Figure 2.6. Time series of the relative turbulence intensity at the different radial locations at the jet inlet of the pulse jet flame. The shaded region indicates the pulse.

flame L and hence is independent of time, which is the second assumption mentioned above. We can test the validity of this assumption by examining the experimental data. By using the experimental data, we can estimate  $u'$  from  $u'_{exp,m,h} = (\langle u_{exp}^2 \rangle_{m,h} - \langle u_{exp} \rangle_{m,h}^2)^{1/2}$  by employing the sample averaging and the local time averaging over the experimental data. Similarly, we can estimate  $u'_{base}$ ,  $\langle \tilde{u}(0, r, \theta, t) \rangle$ , and  $\langle \tilde{u}_{base}(0, r, \theta, t) \rangle$  from the experimental data. Figure 2.6 shows the relative turbulence intensity calculated from the measurements at the jet inlet and at the different radial locations. The error bars are the 95% confidence intervals, which indicate the uncertainty of the measured relative turbulence intensity. Within the experimental uncertainty, the relative turbulence intensity at the different radial locations is approximately constant throughout the time, except at the very beginning of the pulse. At that time, the relative turbulence intensity shoots up accompanied by large confidence intervals. This can be attributed to the sparse data at the beginning and before the pulse from the experimental measurements as indicated in Figure 2.2. For the rest of the time in-

cluding most of the pulse, the relative turbulence intensity is approximately constant, which supports the second assumption for defining the pulse function,  $f(t)$ .

To summarize, we analyze the available LDV velocity measurement data at the jet inlet to examine the validity of the scaling approach in Equation (2.15) that was used to generate the time-dependent inflow turbulence boundary conditions for the simulations of the turbulent pulsed jet flame. The results support that the two assumptions involved in Equation (2.15) are valid for generating the inflow turbulence boundary condition that matches the first two moments with the measurements. More complicated approaches are possible to generate a more accurate inflow boundary condition.

### 2.5.3 Sensitivity to model and numerical parameters

The sensitivity of the model predictions of the pulsed jet flame to the model and numerical parameters is investigated in this sub-section, including the sensitivity to the mixing model constant  $C_\phi$  in Equation (2.8), to the grid resolution, to the uncertainty in the inflow turbulence intensity, and to the number of IID realisations for estimating statistics in Section 2.4.2. In the simulations, multiple IID simulations are performed to generate the statistics and to estimate the simulation uncertainty. The IID simulations are obtained by feeding different inflow boundary condition database from separate fully developed pipe flow simulations and by using different random seeds in the Monte Carlo particle simulations. The time history of the mean axial velocity from the simulations is calculated based on a three-way averaging  $\langle \tilde{u} \rangle_{h,\theta,m}$ , i.e., averaging inside the time-interval  $h$  in Equation (2.13), averaging in the azimuthal direction  $\theta$  in Equation (2.14), and averaging over the multiple simulations in Equation (2.12). The rms velocity  $u'$  is estimated as follows:

$$u' \approx u'_{h,\theta,m} = \left( \langle \tilde{u}^2 \rangle_{h,\theta,m} - \langle \tilde{u} \rangle_{h,\theta,m}^2 \right)^{1/2} \quad (2.21)$$

The bootstrap method discussed in Section 2.4.3 is used to construct the confidence intervals for estimating  $\langle \tilde{u} \rangle_{h,\theta,m}$  and  $u' \approx u'_{h,\theta,m}$ , by resampling from the different simulation realizations to form new samples.

### Mixing model parameter $C_\phi$

The mixing model parameter  $C_\phi$  determines the rate of mixing in the EMST mixing model used in this study. It is widely known that the value of  $C_\phi$  affects significantly the model calculations, especially the predictions of local extinction [132]. The flow and turbulence fields are, however, insensitive to the values of  $C_\phi$ . The focus of this work is placed on the predictions of the flow and turbulence fields in the turbulent pulsed jet flames. Here we confirm this insensitivity by examining the effect of different values of  $C_\phi$  (1.0, 2.0, and 3.0) on the predictions of the mean and rms axial velocity. The sensitivity results are reported in Figure 2.7. In these results, only one realisation is performed for each value of  $C_\phi$  and hence the results fluctuate significantly. The grid used for the testing is  $144 \times 108 \times 48$ . The statistical difference of the results with the different values of  $C_\phi$  is seen to be small with the predicted velocity pulse occurring at about the same time at the different locations. This confirms that the impact of the different values of  $C_\phi$  on the predictions of the velocity and turbulence fields is small, and a single value of  $C_\phi = 3.0$  which is used for later discussions is deemed to be adequate.

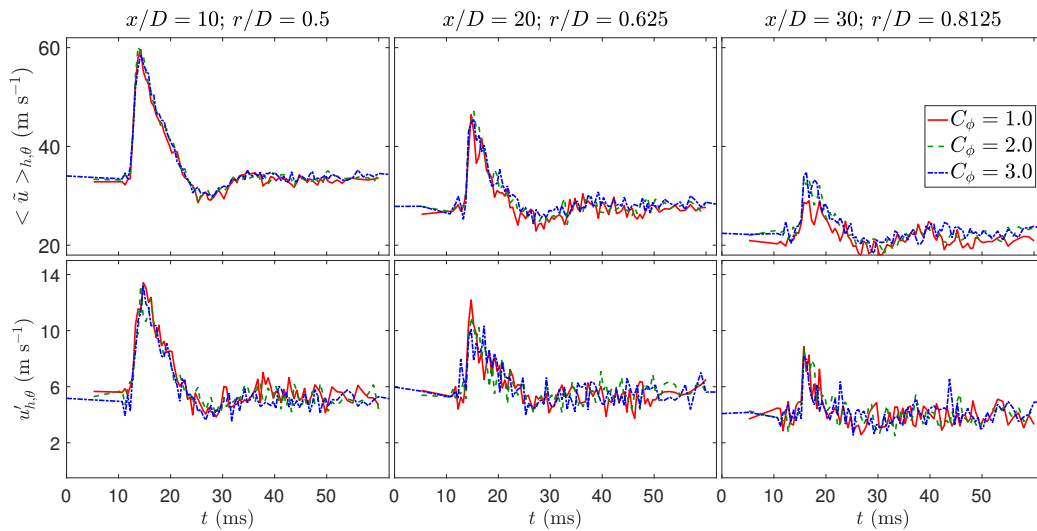


Figure 2.7. Time series of the predicted mean and rms axial velocity at the different axial and radial locations in the pulsed jet flame with the different values of  $C_\phi$ .

## Grid sensitivity

A grid with the resolution of  $256 \times 108 \times 48$  in the axial, radial and azimuthal directions, respectively, is used for most of the discussions in this paper. To confirm the suitability of this grid for the purpose of the study, we examine the sensitivity of the LES/PDF predictions of the velocity and turbulence fields in the pulsed jet flame to the variation of grid resolution in this sub-section. Two more grids with  $144 \times 108 \times 48$  and  $512 \times 192 \times 96$  are used in addition to the grid of  $256 \times 108 \times 48$  for the sensitivity analysis. The sensitivity results are shown in Figure 2.8. For the grid of  $256 \times 108 \times 48$ , 20 IID simulations are available, and hence the results are smoother and the 95% confidence interval is available by using the approach outlined in Section 2.4.3, while for the other two grids, only one simulation is conducted. From the figure, we can see that the difference of the results from the three different grids is insignificant and the grid with  $256 \times 108 \times 48$  captures accurately the transient history of the mean and rms axial velocity when compared to the refined grid. For the rest of the paper, the grid of  $256 \times 108 \times 48$  will be used for the discussions.

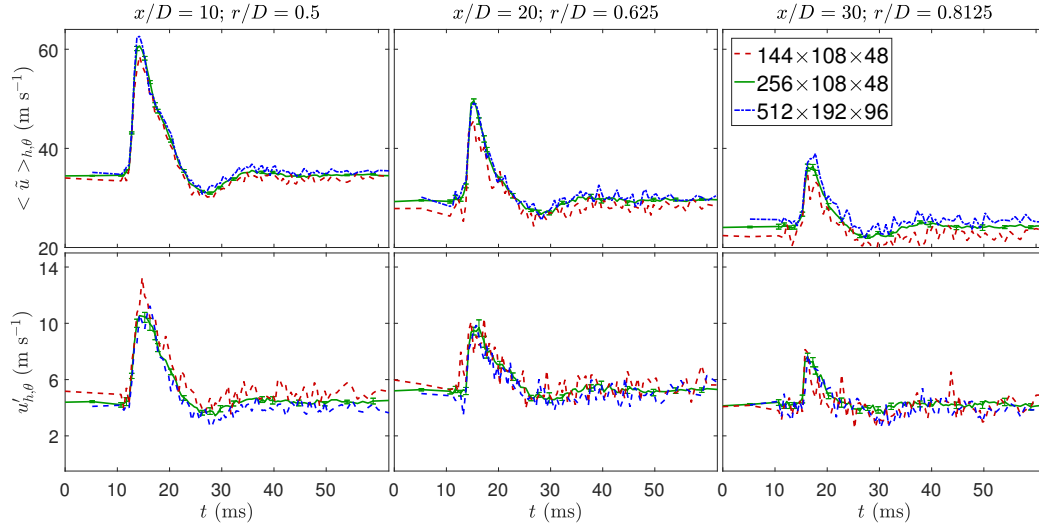


Figure 2.8. Time series of the predicted mean and rms axial velocity at the different axial and radial locations in the pulsed jet flame with three different grid resolutions.

### Inflow turbulence intensity

The uncertainty involved in the specification of the inflow turbulence intensity has been examined in Section 2.5.1 for flame L. It is found that the effect of the uncertainty fades very quickly towards downstream in flame L. The same effect is examined here for the turbulent pulsed jet flame to check whether the same observations in flame L can be made in the pulsed jet flame. Following Equation (2.16) and replacing  $\tilde{u}_{base}(0, r, \theta, t)$  in the equation by Equation (2.15), we obtain:

$$\tilde{u}(0, r, \theta, t) = [\langle \tilde{u}_{base} \rangle + (\tilde{u}_{base}(0, r, \theta, t) - \langle \tilde{u}_{base} \rangle) \cdot \vartheta] \cdot (1 + f(t)), \quad (2.22)$$

which can be used for specifying the inflow boundary condition in the pulsed jet flame to examine the effect of the inflow turbulence intensity by varying  $\vartheta$ . Two values of  $\vartheta = 1.0$  and  $1.4$  have been examined in Section 2.5.1 for the predictions of flame L based on two different sets of experimental data for flame L. For the pulsed jet flame, we further examine the effect of three values of  $\vartheta = 0.5, 1.0,$  and  $2.0$  on the predictions of the pulsed jet flame. The sensitivity results for the different values of  $\vartheta$  are shown in Figure 2.9. For the case of  $\vartheta = 1.0$ , 20 IID simulations are available, and hence the results in Figure 2.9 are smoother and the 95% confidence interval is available by using the approach outlined in Section 2.4.3, while for the other two values of  $\vartheta = 0.5$  and  $2.0$ , only one simulation is conducted. From the figure, we can clearly see the effect of the different values of  $\vartheta$  on the specification of the inflow turbulence intensity at  $x/D = 0$ . At downstream locations ( $x/D > 10$ ), however, we see very little difference among the different results with the different values of  $\vartheta$  other than the statistical fluctuations, which supports the fact that the effect of the inflow turbulence intensity in the pulsed jet flame is similar to that observed in flame L in Section 2.5.1. In the following discussions, the value of  $\vartheta = 1.0$  is used.

### Number of IID simulation realisations

The estimated statistics by using the approach in Section 2.4.2 heavily rely on the number of IID simulation realisations. A large number of IID realisations are needed in order

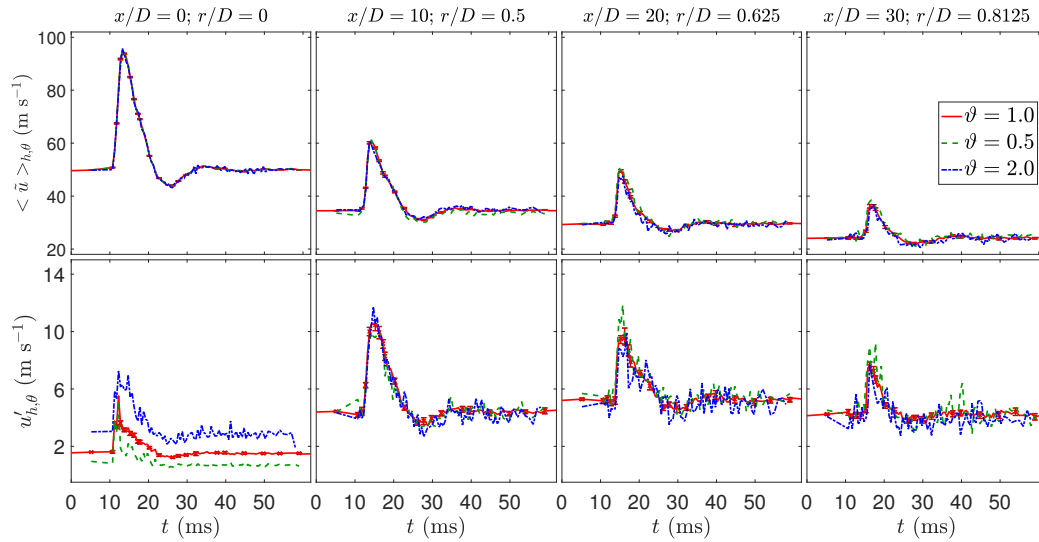


Figure 2.9. Time series of the predicted mean and rms axial velocity at the different axial and radial locations in the pulsed jet flame with three different values of the inflow turbulence intensity parameter  $\vartheta = 0.5, 1.0$  and  $2.0$ .

to have a sufficient number of realisations to cover possible random samples and to ensure statistical convergence and accuracy. In the following, we examine the effect of the number of IID simulation realisations on the estimated statistics. A total of 20 realisations are performed for estimating the statistics. Two sets of statistics are obtained, with one using all 20 realisations and the other using only half of the realisations. The obtained results from the different number of realisations are plotted against each other as shown in Figure 2.10 for the mean and rms axial velocity. The horizontal and vertical error bars are the 95% confidence intervals, obtained by using the approach discussed in Section 2.4.3. From the figure, we can see that the results lie close to the diagonal line which is mostly inside the error bars. This strongly indicates that there is only little difference between the statistics obtained by using 10 realisations and 20 realisations. The number of realisations used in this study appears to be adequate to provide accurate statistics for the discussions, and further increasing the number of realisations is not expected to alter the current results significantly.

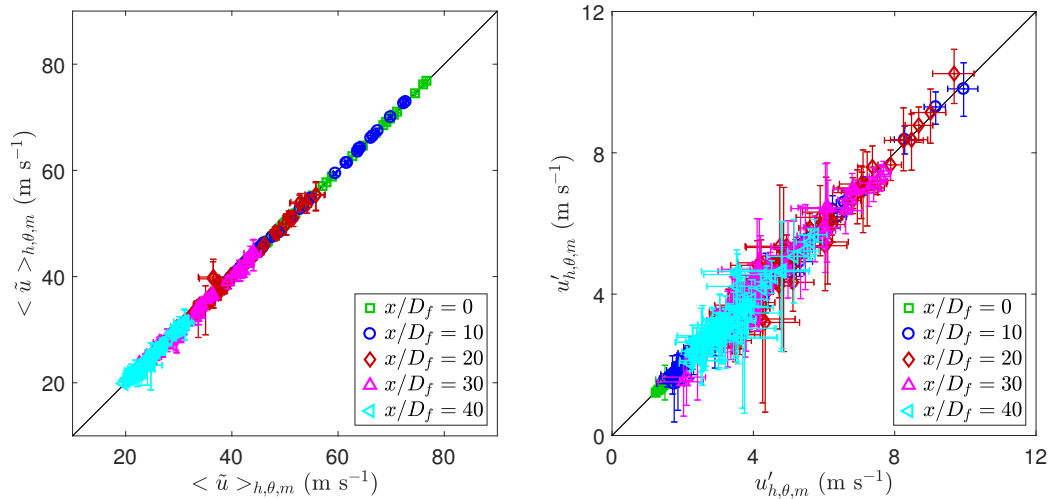


Figure 2.10. Direct comparison of the predicted mean axial velocity (left) and rms velocity (right) with 20 simulation realisations (x-axis) and 10 simulation realisations (y-axis). The error bars are the 95% confidence intervals.

#### 2.5.4 Experimental validation of the predictions of the flow and turbulence fields

In this section, we compare, as directly as possible, the model predictions and the measurements of the temporal evolution of the flow and turbulence fields in the pulsed jet flame. In the simulations, 20 IID simulations are performed to generate the statistics and to estimate the simulation uncertainty. The procedure mentioned in Section 2.4.2 is used to estimate the mean velocity  $\langle \tilde{u} \rangle_{h,\theta,m}$  and rms velocity  $u'_{h,\theta,m}$  from the simulations. The calculations of  $\langle u_{exp} \rangle$  and  $u'_{exp}$  from the measurements are similar excepting no averaging along the  $\theta$  direction since only point-wise data are available,  $\langle u_{exp} \rangle \approx \langle u_{exp} \rangle_{h,m}$  and  $u'_{exp} \approx u'_{exp,h,m}$ . About 20-40 realisations (depending on the different measurement locations) are available from the experiments for calculating the statistics.

With the time being synchronised in the simulations and in the measurements, the predicted and measured mean and rms axial velocities are plotted against each other in Figures 2.11 and 2.12, at a few selected axial and radial locations within  $0 \leq x/D \leq 40$  and  $0 \leq r/D \leq 0.8125$ . The horizontal and vertical error bars on the plots for the mean and rms velocity show the 95% confidence intervals in the measurements and in the simulations, re-

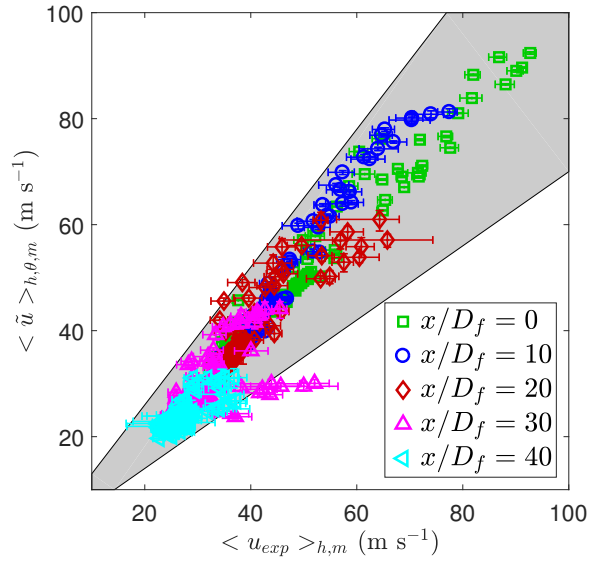


Figure 2.11. Direct comparison of the predicted (y-axis) and measured (x-axis) mean axial velocity. The shaded region is  $\pm 30\%$  deviation from the diagonal. The error bars are the 95% confidence intervals.

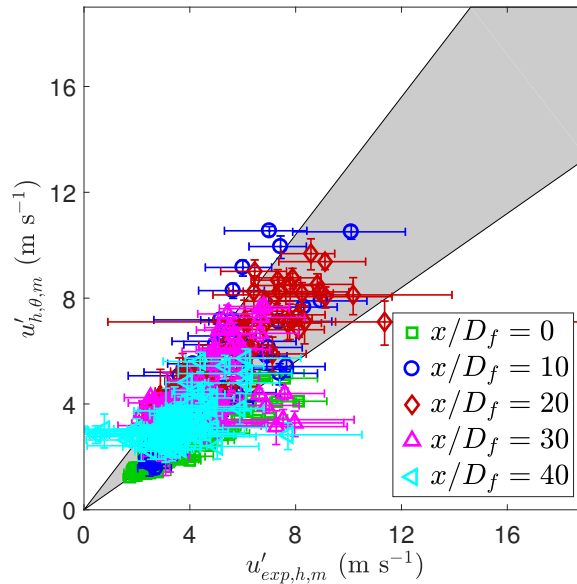


Figure 2.12. Direct comparison of the predicted (y-axis) and measured (x-axis) rms axial velocity. The shaded region is  $\pm 30\%$  deviation from the diagonal. The error bars are the 95% confidence intervals.

spectively. The shaded region is defined as  $\pm 30\%$  deviation from the diagonal. Any result that falls in this region is within 30% relative difference between the simulations and the measurements.

For the mean axial velocity in Figure 2.11, the correlation between the LES simulation results and the measurements is much stronger than the instantaneous axial velocity. The 95% confidence intervals are shown as the horizontal error bars for the measurements and the vertical error bars for the LES simulations. The uncertainty in the measurements indicated by the error bars is much larger than that in the simulations. There are two reasons for this difference of the uncertainty levels in the simulations and in the measurements. Firstly, a very small number of samples are available in the measurements at the beginning period of the pulse [15] to compute the statistics. Secondly, the spatial averaging along the azimuthal direction is used in the simulations while there is no spatial averaging in the measurements, resulting in much reduced statistical errors in the simulations. From the comparison of the predicted and measured mean axial velocity in Figure 2.11, we see that most data points examined lie within the  $\pm 30\%$  region, with a few exceptions on the lower-right corner (mostly for data at  $x/D = 30$  with the relative error about 45%) where the model predictions are much lower than the measurements. Theoretically, an ideal LES model yields the identical results as the measurements, i.e. all data lying along the diagonal line (with the uncertainty in the measurements neglected). The deviation from this ideal case indicates the level of errors in both the LES simulations and in the measurements. In LES simulations, the errors include both the model error and the numerical error. The numerical error includes both deterministic errors such as the numerical discretisation error and random errors due to an inadequate sampling for computing the statistics. The confidence intervals for the LES results in the figure measure the random error approximately. Detailed error analysis and error isolation in a rigorous model comparison are very difficult. From the current comparison, we can estimate that the overall relative difference between the measurements and simulations for the mean axial velocity in the turbulent pulsed jet flame is within 30% at most of the examined locations.

The comparison of the rms axial velocity is shown in Figure 2.12. The confidence intervals for computing the rms axial velocity are much larger than those for the mean shown in Figure 2.11. The confidence intervals from the measurements are also much larger than those from the simulations for the same two reasons explained above. The rms data show larger deviation from the ideal case in comparison to the mean data shown in Figure 2.11. Given the larger uncertainty in computing the rms velocity in Figure 2.12, it is not clear currently whether larger errors are involved in computing the rms than the mean. With the 95% confidence intervals, it seems that the overall relative difference between the measurements and simulations for the rms axial velocity is also within 30% statistically with a few exceptions.

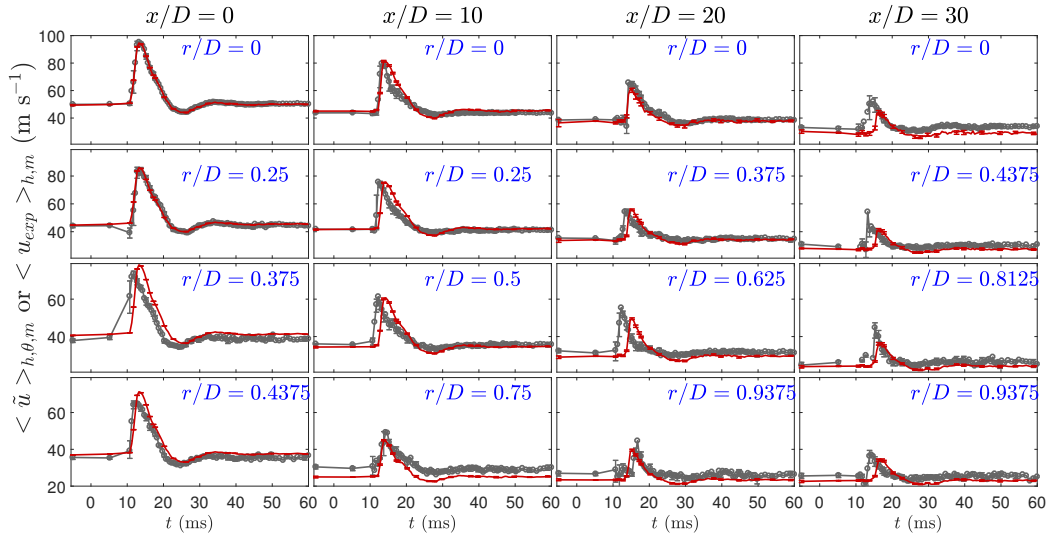


Figure 2.13. Time series of the predicted (dark red lines) and measured (grey lines with circles) mean axial velocity at the different axial and radial locations in the pulsed jet flame. The error bars are the 95% confidence intervals.

The time series of the mean axial velocity at the different axial and radial locations are compared directly in Figure 2.13, where the measurements are denoted as the grey circles and the LES/PDF predictions are red solid lines. The error bars are the 95% confidence intervals. The models are able to capture the transient process of the mean flow fields with reasonable accuracy, including the magnitude of the velocity and the timing and duration of

the pulse. Some small discrepancy between the model predictions and the measurements is observed. For example, at  $(x/D, r/D) = (20, 0.625)$ , the predicted velocity pulse response is about 3 ms late compared to the measurements. The observed discrepancy can be explained by at least three factors: the model uncertainty, measurement uncertainty, and the uncertainty in the inflow boundary condition. It is noted that the pulse function obtained from the centreline axial velocity at the jet inlet in Equation (2.19) causes some discrepancy between the measurements and the specification of the inflow boundary condition away from the centreline at the jet inlet. This discrepancy in the inflow in the simulations is expected to propagate downstream and causes the discrepancy downstream as observed in the figure. It is also noted that the measurement uncertainty before and at the beginning of the pulse is quite large due to a limited number of samples, which is expected to cause the major discrepancy between the predictions and the measurements at that time. Overall the temporal evolution of the mean axial velocity in the pulsed jet flame is captured by the current LES/PDF methods satisfactorily.

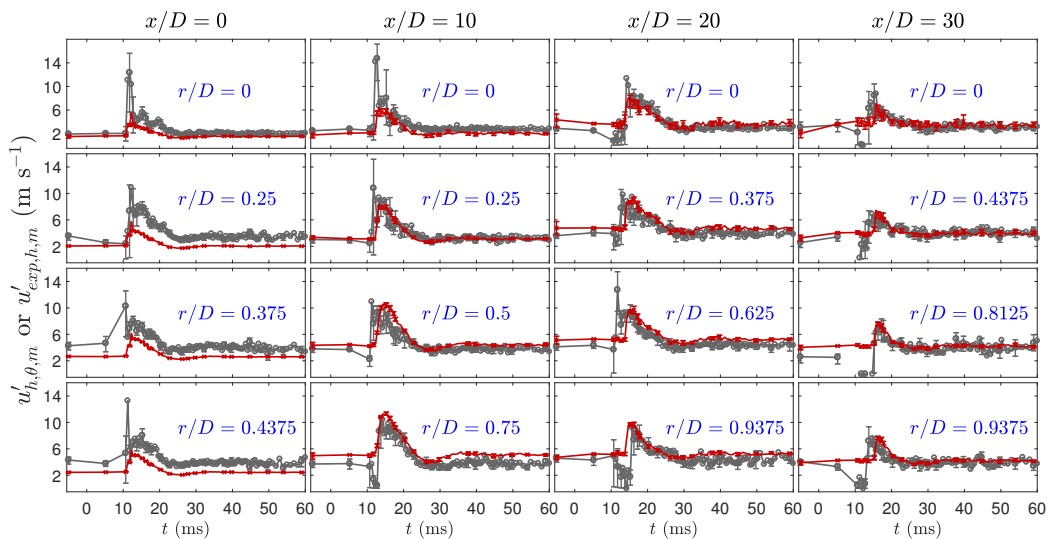


Figure 2.14. Time series of the predicted (dark red solid lines) and measured (grey lines with circles) rms axial velocity at the different axial and radial locations in the pulsed jet flame. The error bars are the 95% confidence intervals.

The time series of the rms axial velocity at the different axial and radial locations are compared directly in Figure 2.14. The error bars are again the 95% confidence intervals. The large measurement uncertainty before and at the beginning of the pulse is also evident from the figure, which again explains the large discrepancy between the predicted and measured rms velocity at time. The rms velocity at the inlet (the specified boundary condition) is smaller than the measurements, which is expected because there is some discrepancy between the old [148] and new [15] measurements of the rms velocity and the forcing used in the inflow boundary condition generation is from the old measurements [148] as discussed in Section 2.5.1. It has been shown that in flame L this error in the inflow rms velocity boundary condition (about 40%) yields much smaller error (up to 5%) in the downstream in Figure 2.4. From Figure 2.14, we can make a similar observation in the turbulent pulsed jet flame. The discrepancy between the predicted and measured rms velocity at the downstream location  $x/D = 30$  is very small despite the large difference between them at the jet inlet  $x/D = 0$ . The models are capable of capturing the transient process of the turbulent fluctuations with reasonable accuracy, including the magnitude of the fluctuation and the timing and duration of the pulse. The discrepancy between the model predictions and the measurements can be attributed to the same reasons used to explain the discrepancy in Figure 2.13. Overall the temporal evolution of the rms axial velocity in the pulsed jet flame is also captured by the current LES/PDF methods satisfactorily.

In summary, a direct comparison of the LES/PDF predictions and measurements of the velocity statistics is made, to provide a sensible understanding of the LES model capability to represent the underlying unsteady physical processes.

### 2.5.5 Experimental validation of combustion field

So far, the focus of previous sections is mainly placed on the flow and turbulence fields of the pulsed jet flame. It has been shown that the LES/PDF method captures the temporal evolution of flow and turbulence fields well. As a response to the evolving flow and turbulence fields, the combustion fields of the pulsed jet flame feature complex bimodal and

statistically transient combustion dynamics involving significant extinction and re-ignition, as reported experimentally in [15]. In the following, we present the combustion fields and examine if the method can capture the measured response of combustion fields to the inflow velocity pulse.

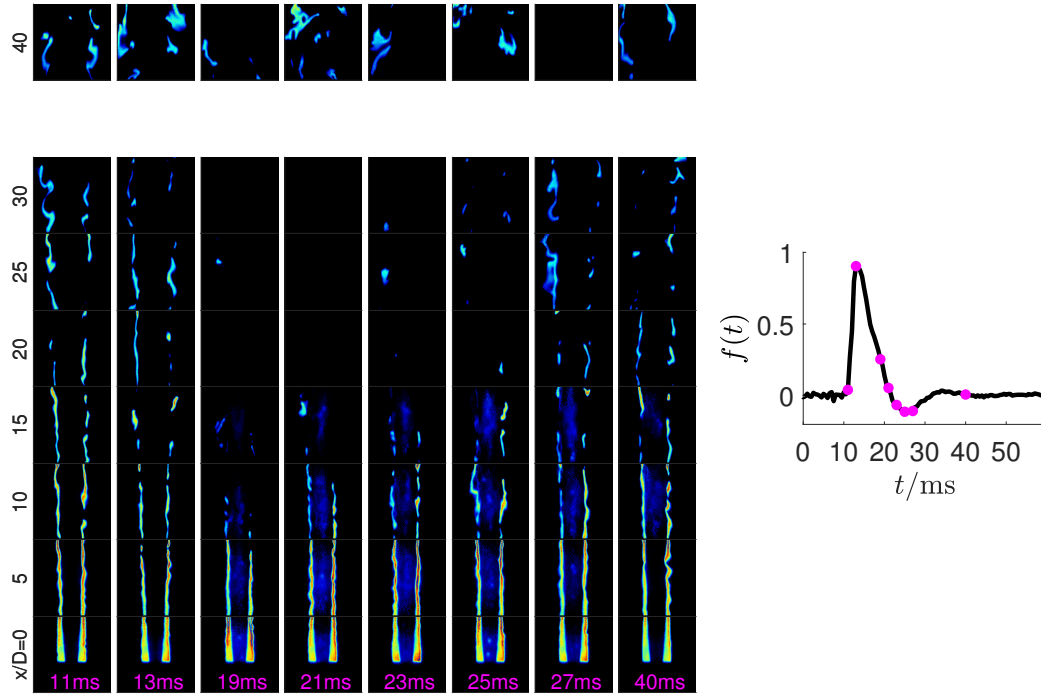


Figure 2.15. Time series of the measured PLIF-OH images [15] at the selected times,  $t = [11, 13, 19, 21, 23, 25, 27, 40]$  ms.

Time series of high-speed PLIF-OH images at 5 kHz are available [15] for the model performance assessment in combustion field prediction. These PLIF-OH images are measured at the axial locations  $x/D = [0, 5, 10, 15, 20, 25, 30, 40]$  simultaneously with an effective area of  $5D \times 5D$ . Combining the PLIF-OH images at all the axial locations together, we get a full view of the jet flame as in Figure 2.15. Figure 2.15 shows an example of the PLIF-OH images at eight selected times  $t = [11, 13, 19, 21, 23, 25, 27, 40]$  ms from left to right. In the measurement, the inflow velocity pulse starts at  $t = 11$  ms and lasts for about 10 ms causing a maximum jet inflow velocity exceeding the extinction threshold of a  $\text{CH}_4/\text{Air}$  jet flame at the current configuration. As a result of the inflow velocity pulse, the flame

experiences a statistically transient combustion process involving significant extinction and re-ignition. The selected eight times in Figure 2.15 cover the whole transient combustion response of the jet flame to the inflow velocity pulse, the locations of which are also shown in the pulse profile as the magenta dots. At  $t = 11$  ms, the flame has not been affected by the velocity pulse yet and exhibits a healthy burning state with a thin flame front represented by the PLIF-OH signal with few discontinuities/holes. With the inflow velocity pulse added, the flame is under intense flow field stretching, exhibits significant local extinction represented by the increased number of discontinuities/holes in the flame front, and is broken into two branches separated by an extinction band shown as a completely black area inside the measured box (e.g., at  $x/D = 20$ ), at  $t = [19, 21, 23, 25]$  ms. The flame is observed to re-establish the healthy burning state at later stages,  $t = [27, 40]$  ms, when the effect of the pulse is fading out. The statistically transient bimodal combustion dynamics shown in Figure 2.15 poses a strong challenge to turbulent combustion models. In the following, we examine if the current LES/PDF models can capture the observed combustion dynamics.

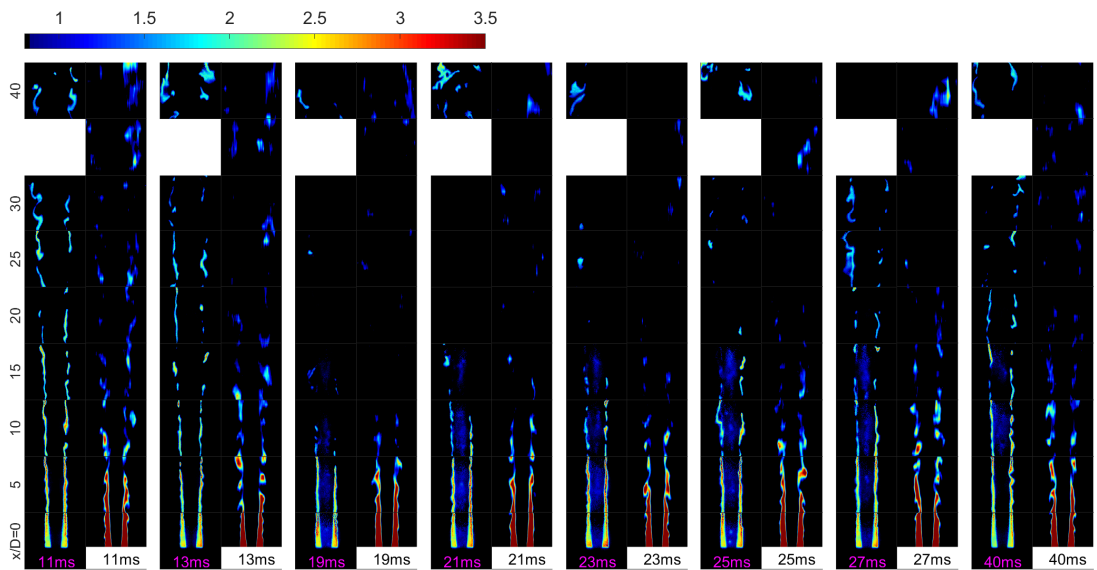


Figure 2.16. Time series of the measured PLIF-OH images (left) [15] and the predicted OH mass fraction contours (right) at the selected times,  $t = [11, 13, 19, 21, 23, 25, 27, 40]$  ms.

Figure 2.16 presents a qualitative comparison of the measured PLIF-OH images from Figure 2.15 with the contour plots of LES/PDF predicted OH mass fraction at the corresponding times. At each time, the plot on the left is the PLIF-OH image and on the right is the contour of OH mass fraction, both of which are frequently used to represent the flame front in experiments and simulations, respectively. In Figure 2.16, different quantities are compared, i.e., PLIF-OH signal intensity from experiment [15] and OH mass fraction from simulation, with different color schemes. The top color bar is for the OH mass fraction only and the PLIF-OH color bar is not shown. At  $t = 11$  ms, the flame shows a healthy burning state both in the simulation and measurement. At later stages, similar levels of extinction and re-ignition are observed in the prediction and the measurement. For example, at  $x/D = 20$ , the measured PLIF-OH image box shows a completely extinguished state from  $t = 19$  ms and starts to exhibit new burning events at  $t = 25$  ms; the predicted OH mass fraction contour plots show the similar temporal evolution process with an extinction duration from 19 ms to 25 ms. The comparison in Figure 2.16 supports that the current models capture the different stages of the statistically transient and bimodal combustion dynamics in the pulsed flame qualitatively well.

Figure 2.16 features a qualitative comparison. In the following, we quantify the extinction events with PDFs of OH mass fraction,  $f_{\phi_{OH}|0.02 < \xi < 0.1}$ , and temperature,  $f_{T|0.02 < \xi < 0.1}$ , around the stoichiometric condition  $\xi_{st} = 0.05$ . Figure 2.17 shows an example of the two PDFs (top for OH mass fraction and bottom for T) at three axial locations  $x/D = [10, 20, 30]$ , and two selected times  $t = [11, 19]$  ms, which represents the healthy burning and the significant extinction stages, respectively. A clear peak shift of the PDFs from high OH mass fraction/temperature at  $t = 11$  ms (red line) to low OH mass fraction/temperature at  $t = 19$  ms (blue line) is observed at all the three locations.

The results in Figures 2.15, 2.16 and 2.17 are at the few selected times. High temporal resolution data are available for both experiment and simulation, from which we can get more temporal evolution information of the flame. The time history of the PDFs of OH mass fraction and temperature,  $f_{\phi_{OH}|0.02 < \xi < 0.1}$  (top row) and  $f_{T|0.02 < \xi < 0.1}$  (bottom row), is shown in Figure 2.18 at three axial locations  $x/D = [10, 20, 30]$ . Valley-shaped PDF

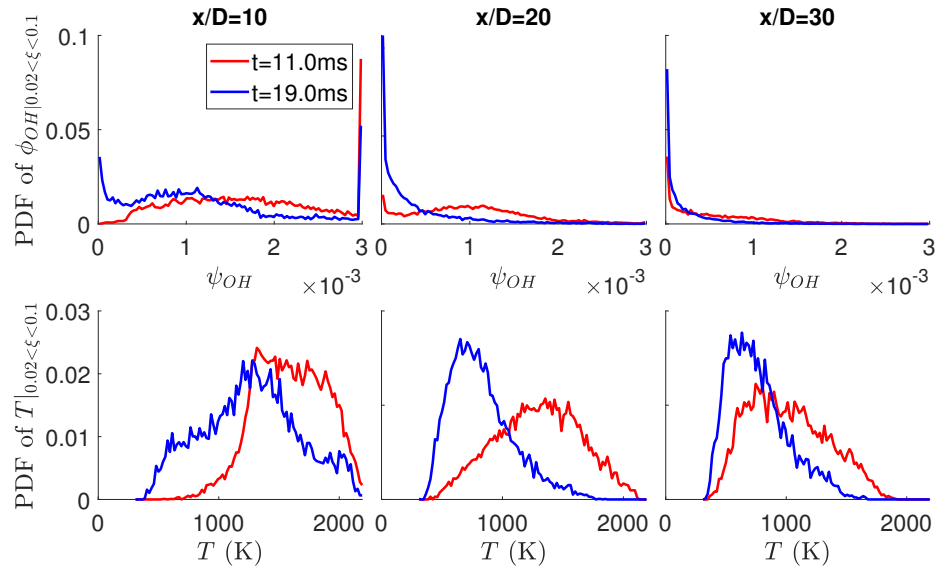


Figure 2.17. PDF profiles of conditional temperature,  $T|_{0.02 < \xi < 0.1}$ , and OH mass fraction,  $\phi_{OH}|_{0.02 < \xi < 0.1}$ , at three locations,  $x/D = [10, 20, 30]$ .

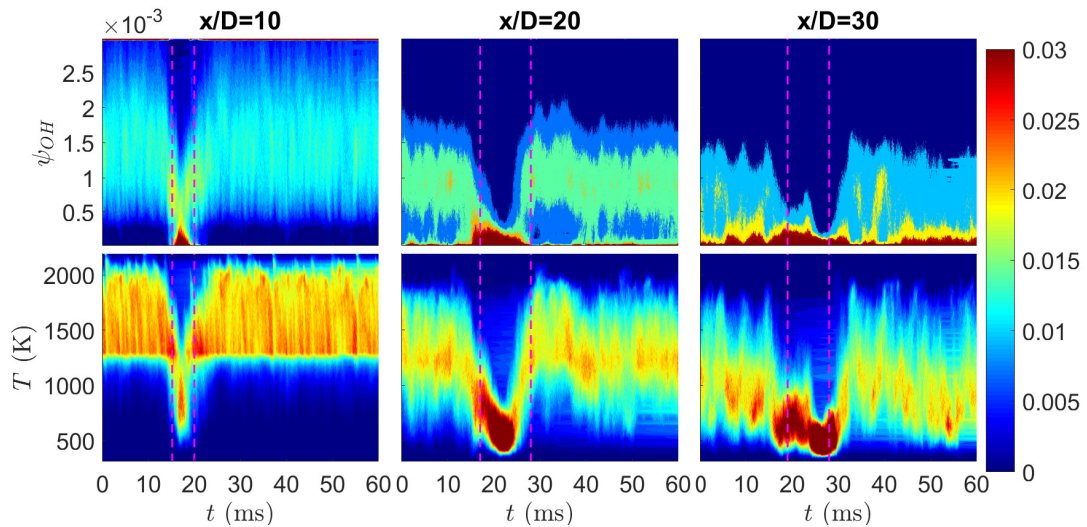


Figure 2.18. Contours of PDF of conditional temperature,  $T|_{0.02 < \xi < 0.1}$ , and OH mass fraction,  $\phi_{OH}|_{0.02 < \xi < 0.1}$ , at three locations,  $x/D = 10, 20, 30$ . The dashed magenta lines indicate the corresponding extinction duration from measurement [15].

distributions are observed in the figure. Before the inflow velocity pulse,  $t < 11$  ms, the flame is burning at a statistically stationary state and a PDF distribution uniform in time is observed. At later times, the peak of PDFs is found to shift toward lower OH mass fractions/temperature due to significant extinction events, which forms a valley. The width of the valley shapes in time represents the extinction duration. The measured extinction duration in [15] at the three axial locations is also shown in Figure 2.18 by the magenta dashed lines. It shows that the predicted time duration of the extinction is approximately close to the measurement, supporting that the current LES/PDF models capture roughly the statistically transient bimodal combustion dynamics reasonably well. Some differences are observed at the downstream location  $x/D = 30$ , where a longer extinction duration is predicted mainly due to the inaccuracy in the prediction of burning re-establishment events.

## 2.6 Conclusions

A combined LES/PDF method is employed to study a turbulent pulsed jet flame which is not statistically stationary, like those in many previous studies. Prediction of the flow, turbulence, and combustion fields is studied. Systematic validation of LES to reproduce the physical temporal evolution of the flow, turbulence and combustion fields is conducted. General assessment approaches for the models to predict statistically transient flames are discussed. New strategies are developed based on multiple averaging approaches for computing the statistics and on a bootstrap method for constructing the confidence intervals. The simulation results are compared extensively with the experimental data. Based on the comparative studies, the following conclusions are drawn:

1. The uncertainty in the measured rms axial velocity can be as high as 40%, but the effect of such uncertainty (when used to specify the inflow boundary conditions) on the flow and flame predictions downstream is negligible (within 5%).
2. A simple scaling approach to specify the time-dependent inflow turbulence boundary condition for the pulsed jet flame is found to be reasonably valid, which is supported by the examination of the underlying assumptions using the experimental data.

3. The sensitivity of the model predictions of the flow and turbulence fields to the mixing parameter  $C_\phi$ , the grid resolution, the inflow turbulence intensity, and the number of IID simulation realisations is examined to confirm the suitability of the adopted model and numerical parameters for the current study.
4. The predictions of the temporal evolution of the mean and rms axial velocity in the turbulent pulsed jet flame by using LES/PDF are found to be mostly within  $\pm 30\%$  deviation from the experimental data.
5. A direct comparison of the time series of the predicted and measured mean and rms axial velocity demonstrates the capability of the employed method to capture the flow and turbulence fields in the pulsed jet flame.
6. A qualitative comparison of the measured PLIF-OH images and the predicted OH mass fraction contours at the selected times shows that the employed method captures the major combustion stages, i.e., healthy burning, significant extinction, two flame branches, and burning re-establishment, related to the statistically transient bimodal combustion dynamics in the pulsed jet flame.
7. A close examination of the time history of conditional PDFs of OH mass fraction and temperature shows that the temporal evolution of the combustion fields is captured reasonably by using the method, with a relatively accurate representation of the measured timings of extinction duration at upstream locations but less accurate at downstream locations mainly due to the inaccuracy in predicting re-ignition events.

In this chapter, we assess the LES/PDF method's performance in the Sydney turbulent pulsed piloted jet flame. The method is found to capture the temporal evolution of flow, turbulence and combustion fields reasonably, which therefore demonstrates its great potential in predicting the statistically transient combustion process in real engines. The pulsed jet flame is designed as the Sydney piloted flame L subject to a fuel jet inflow velocity pulse. Combustion in the turbulent pulsed flame is depicted as exhibiting bimodal

and multi-regime combustion dynamic as discussed in Section 2.1. The facts that its base case, flame L, has been widely studied, and that it exhibits multi-regime combustion, make the turbulent pulsed flame is a good test case to study multi-regime combustion. However, the fact that it is a statistically transient flame with bimodal combustion dynamics brings in additional challenges such as the specification of inflow conditions, largely increased computational cost, and the difficulty in model validation. Besides, limited experimental data is available for the pulsed flame, which prevents an extensive comparison between predicted results with measurements. Hence, another set of combustion problems, consisting of existing turbulent piloted flames, is designed to study multi-regime combustion in the following chapter.

### **3. A UNIFIED VIEW OF PILOT STABILIZED TURBULENT JET FLAMES FOR MODEL ASSESSMENT ACROSS DIFFERENT COMBUSTION REGIMES**

Single-regime turbulent combustion has been the main focus in previous studies. Significant limitations exist in those studies since most practical combustion applications involve multi-regime combustion. Developing and validating multi-regime turbulent combustion models are expected to be an emerging area with significant challenges. To facilitate model assessment across different combustion regimes, we develop a model validation framework by unifying several existing pilot stabilized turbulent jet flames in different combustion regimes. The characteristic similarity and difference of the employed piloted flames are examined, including the Sydney piloted flames L, B, and M, the Sandia piloted flames D, E, and F, a series of piloted premixed Bunsen flames, and the Sydney/Sandia inhomogeneous inlet piloted jet flames. Proper parameterization and a regime diagram are introduced to characterize the pilot stabilized flames covering non-premixed, partially premixed, and premixed flames. A preliminary model assessment is carried out to examine the simultaneous model performance of the large-eddy simulations (LES)/probability density function (PDF) method for the piloted jet flames across different combustion regimes.

#### **3.1 Introduction**

Most studies of turbulent combustion in the past have focused on a problem that is dominated by one regime of combustion. Practical combustion problems, however, are typically not in a single regime, and different regimes of combustion can occur simultaneously in

---

<sup>2</sup>The content of this chapter is from the paper [149] — H. Wang, P. Zhang, A unified view of pilot stabilized turbulent jet flames for model assessment across different combustion regimes. Proceedings of the Combustion Institute, 2017, 36: 1693-1703.

the same combustion field. It is imperative to study multi-regime combustion to provide a detailed understanding of combustion processes that are of practical interest.

Past modeling studies of turbulent combustion have primarily focused on developing and validating models for a specific combustion regime. Typically a model that is suitable for one combustion regime cannot be used directly in another regime without significant modifications. The mixture fraction based models such as flamelet [53] and conditional moment closure (CMC) [54] are applicable to turbulent non-premixed combustion, although the idea of the modeling concept in flamelet and CMC can be borrowed for developing premixed combustion models [150, 151]. The transported probability density function (PDF) model [55] does not embed strong assumptions about combustion regimes in the model when compared to other models such as flamelet, and in theory the model is potentially applicable to all combustion regimes although the current PDF model has been only tested in single regime combustion and some mixing models such as Euclidean Minimum Spanning Tree (EMST) [84] are originally developed for non-premixed flames.

The goal of this work is to establish a systematic framework for validating turbulent combustion models across different combustion regimes. The idea behind this work is largely based on the outcomes of the TNF workshop [2], and it is built upon the seminal work of the pilot stabilized jet flames. The piloted jet flames originate from the early work by Masri and Bilger [9, 152]. The Sydney piloted jet flames L, B, and M [9, 118] are examples of early work. Later, the Sydney burner is used in the Sandia piloted flames D, E, and F [88] which received unprecedented attention from modelers. A similar burner is also used in the study of turbulent premixed Bunsen flames, the flames F1, F2, and F3 [83]. Recently, a series of new flames with inhomogeneous fuel jet inlet [24–26] is developed by introducing another tube that is retractable inside the Sydney pilot burner to produce variable fuel jet inlet conditions. Various combustion regimes can be produced from this series of new flames, ranging from non-premixed to partially premixed flames. The pilot used in the Sydney burner also appears in many other flames, such as the piloted premixed jet burner (PPJB) [153] and the Darmstadt stratified burner [20, 21], which are not covered in the cur-

rent work. In the present paper, the considered burners are limited to those which have methane as fuel issuing from the central fuel jet and cold air as the coflow.

In this work, we examine the similarity of these existing pilot stabilized turbulent jet flames and characterize this similarity through a set of parameters so that all the considered piloted jet flames can be viewed as flames in the same series. By doing so, we expect to be able to provide an innovative framework for validating turbulent combustion models across different combustion regimes. The specific objectives of the work are two folds: to provide a unified view of pilot stabilized turbulent jet flames across different combustion regimes, and to conduct a preliminary assessment of the LES/PDF method [46] in the unified piloted turbulent jet flames.

### 3.2 A unified view of piloted turbulent jet flames

Four cases of piloted turbulent jet flames are considered, including the Sydney piloted flames L, B, and M [9, 118], the Sandia piloted flames D, E, and F [88], the piloted premixed Bunsen flames F1, F2, and F3 [83], and the Sydney/Sandia inhomogeneous inlet jet flames [24–26].

#### 3.2.1 Global characterization of piloted turbulent jet flames

A sketch of the pilot burner is shown in Figure 3.1. For the four cases of piloted turbulent jet flames, Table 3.1 summarizes the dimension of the burner ( $D_f$ : fuel jet pipe diameter;  $D_p$  pilot pipe diameter) and the Reynolds number based on the fuel jet bulk velocity  $Re_{f,b}$ . The flames I1, I2, I3, and I4 denote the Sydney/Sandia inhomogeneous inlet jet flames [24–26] with their additional information summarized in Table 3.2. In these flames, the central tube in Figure 3.1 is used, and it is retractable so that different recession distance  $L$  can be achieved. The central tube supplies  $\text{CH}_4$ , and the annulus supplies air in flames I1-I4. The retraction mechanism provides an adjustable level of partial mixing between  $\text{CH}_4$  and air. The bulk velocities of the central tube  $u_{c,b}$ , of the annulus  $u_{a,b}$ , and of the fuel jet  $u_{f,b}$  in flames I1-I4 are shown in Table 3.2.

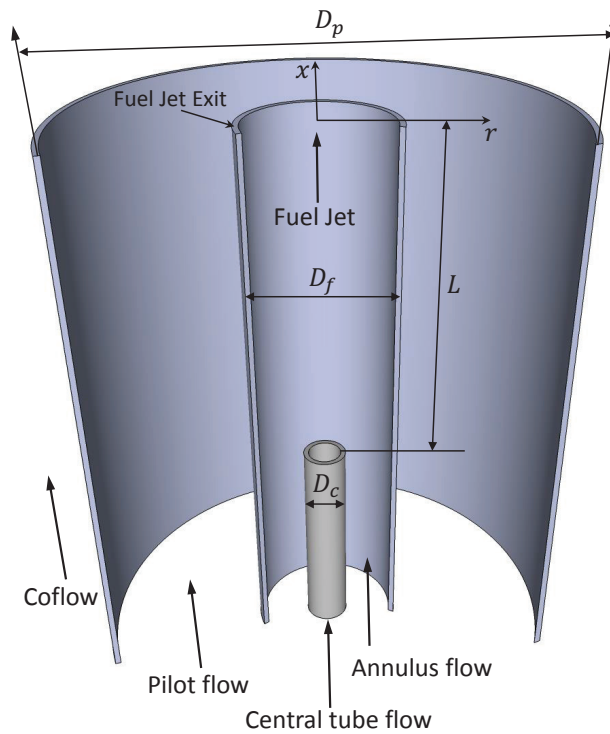


Figure 3.1. The Sydney pilot flame burner [9, 152]. Two concentric tubes are used, the fuel jet tube ( $D_f$ ) and the pilot tube ( $D_p$ ), to separate the fuel jet, the hot pilot flow, and the coflow air. The central tube ( $D_c$ ) is a recent addition to the burner [24–26] to produce different stratifications in composition at the fuel jet exit with varying recession distance  $L$ . More information about the geometric parameters can be found in Tables 3.1 and 3.2.

The above four cases of flames on a pilot burner are from independent studies. In this work we draw the similarity of these different flames and provide a unified view of all these flames as a new series through proper parameterization in the following Section 3.2.2.

### 3.2.2 Parameterization and regime diagram of piloted turbulent jet flames

To provide a unified view of all these different flames, we employ a single definition of mixture fraction with pure  $\text{CH}_4$  as the nominal fuel, based on the Bilger's definition

Table 3.1. Summary of piloted turbulent jet flames.

case	$D_f$ (mm)	$D_p/D_f$	$Re_{f,b}$	$\phi_f$	$\xi_f$	$\theta$
flame L	7.2	2.50	17,900	$\infty$	1.000	1.000
flame B	7.2	2.50	20,400	$\infty$	1.000	1.000
flame M	7.2	2.50	23,800	$\infty$	1.000	1.000
flame D	7.2	2.50	22,400	3.17	0.156	1.000
flame E	7.2	2.50	33,600	3.17	0.156	1.000
flame F	7.2	2.50	44,800	3.17	0.156	1.000
flame F1	12.0	5.67	50,886	1.00	0.055	1.000
flame F2	12.0	5.67	39,143	1.00	0.055	1.000
flame F3	12.0	5.67	23,486	1.00	0.055	1.000
flame I1	7.5	2.40	27,600	4.76	0.217	0.975
flame I2	7.5	2.40	26,800	4.76	0.217	0.664
flame I3	7.5	2.40	37,500	4.76	0.217	0.633
flame I4	7.5	2.40	48,300	4.76	0.217	0.618

Table 3.2. Sydney/Sandia inhomogeneous inlet piloted turbulent jet flames [25]. Volume flow rate ratios of air to fuel  $\text{CH}_4$  for all the four cases are 2:1.

case	case name in [25]	$L$ (mm)	$u_{c,b}$ (m/s)	$u_{a,b}$ (m/s)	$u_{f,b}$ (m/s)
flame I1	FJ200-5GP-Lr300-59	300.0	69.2	61.5	59.0
flame I2	FJ200-5GP-Lr75-57	75.0	67.0	59.5	57.0
flame I3	FJ200-5GP-Lr75-80	75.0	93.8	83.4	80.0
flame I4	FJ200-5GP-Lr75-103	75.0	120.6	107.2	103.0

[154]. With this definition, a unique stoichiometric mixture fraction for all the flames is  $\xi_{st} = 0.055$ , and the mixture fraction of the fuel is not always one, e.g., the mixture fraction of the fuel in flame D is  $\xi_f = 0.156$ . The values of the mixture fraction based on this

definition for the fuel jet,  $\xi_f$ , are summarized in Table 3.1 for the different piloted turbulent jet flames, assuming a fully mixed condition, as well as the equivalence ratio of the fuel,  $\phi_f$ .

With the addition of the central tube in the fuel jet in the pilot burner shown in Figure 3.1, we can view all four piloted turbulent jet flames in Section 3.2.1 as a generalized piloted flame series. Flames L, B, and M can be viewed as a case that there is no annulus air supply and the recession distance  $L \rightarrow \infty$ . Flames D, E, and F can be viewed as a case that has the  $\text{CH}_4$  and air mass flow rates matching the equivalent ratio of flames D, E, and F, and has the recession distance  $L \rightarrow \infty$ . Flames F1, F2, and F3 can be viewed in a similar way. In the following, we introduce a mixedness parameter,  $\theta$ , that quantifies the level of mixing of the mixture at the fuel jet exit.

We first define a mixing parameter,  $\eta$ , at the fuel jet exit plane ( $x/D_f = 0$ ) as shown in Figure 3.1,

$$\eta = \frac{1}{\dot{m}_f} \int_0^{\frac{D_f}{2}} \left( \widetilde{\xi}_e - \widetilde{\xi}_{e,b} \right)^2 \bar{\rho}_e \widetilde{u}_e 2\pi r dr, \quad (3.1)$$

where the tilde represents Favre averaging,  $r$  is the radial distance,  $\widetilde{u}$  is the mean axial velocity,  $\bar{\rho}$  is the mean mixture density,  $\dot{m}_f$  is the mass flow rate from the fuel jet, the subscript "e" denotes the fuel jet exit location, and the subscript "b" denotes a bulk quantity. The bulk mixture fraction  $\widetilde{\xi}_{e,b}$  at the fuel jet exit is obtained from

$$\widetilde{\xi}_{e,b} = \frac{\int_0^{\frac{D_f}{2}} \widetilde{\xi} \bar{\rho} \widetilde{u} 2\pi r dr}{\dot{m}_f} = \frac{\dot{m}_c \times 1 + \dot{m}_a \times 0}{\dot{m}_f} = \frac{\dot{m}_c}{\dot{m}_f} = \frac{\dot{m}_c}{\dot{m}_c + \dot{m}_a}, \quad (3.2)$$

where the conditions of  $\widetilde{\xi} = 1$  for the central  $\text{CH}_4$  tube and  $\widetilde{\xi} = 0$  for the annulus air slot are used,  $\dot{m}_c$  and  $\dot{m}_a$  are the mass flow rates from the central tube and from the annulus, respectively, and  $\dot{m}_f = \dot{m}_a + \dot{m}_c$ . When  $L \rightarrow 0$ , there is no mixing between  $\text{CH}_4$  and air,  $\eta_{L \rightarrow 0} = \left( 1 - \widetilde{\xi}_{e,b} \right)^2 \dot{m}_c / \dot{m}_f + \widetilde{\xi}_{e,b}^2 \dot{m}_a / \dot{m}_f$ , and when  $L \rightarrow \infty$ , the fuel consisting of  $\text{CH}_4$  and air has fully mixed,  $\eta_{L \rightarrow \infty} = 0$ . For a finite length  $L$ ,  $\eta$  is between  $\eta_{L \rightarrow 0}$  and  $\eta_{L \rightarrow \infty}$ . A mixedness parameter,  $\theta$ , can then be defined as

$$\theta = 1 - \left( \frac{\eta - \eta_{L \rightarrow \infty}}{\eta_{L \rightarrow 0} - \eta_{L \rightarrow \infty}} \right)^{\frac{1}{2}}, \quad (3.3)$$

such that  $\theta$  is between 0 and 1, with  $\theta = 0$  meaning no mixing and  $\theta = 1$  meaning full mixing.

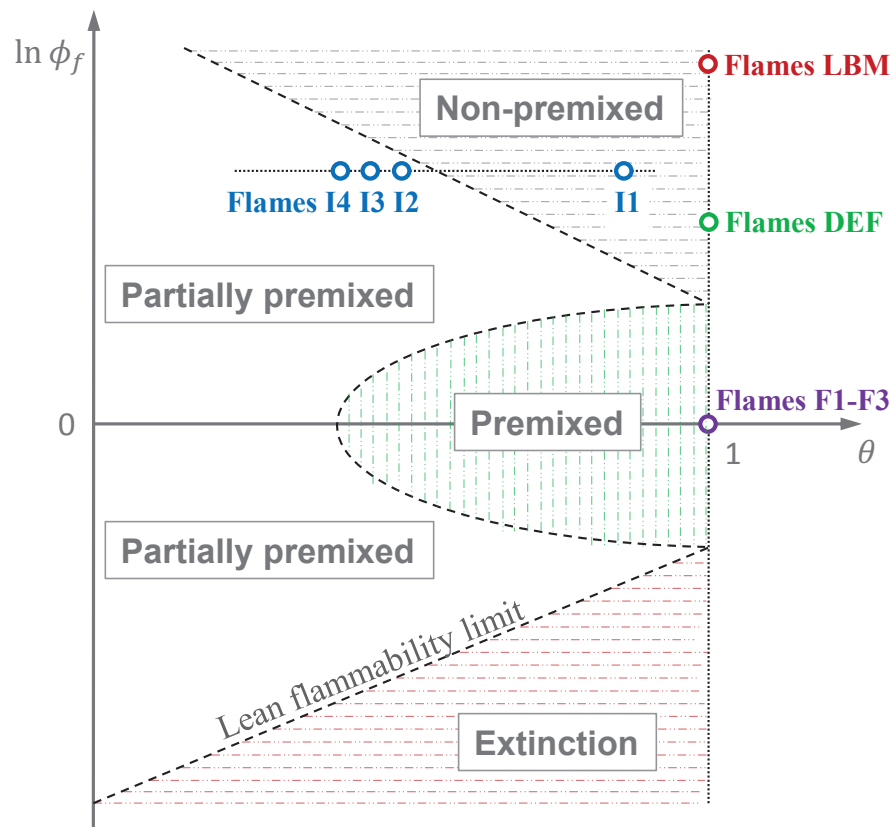


Figure 3.2. A regime diagram for pilot stabilized turbulent jet flames. (The diagram is not to scale.)

With the two parameters,  $\phi_f$  and  $\theta$ , we can introduce a regime diagram for the pilot stabilized turbulent jet flames, as shown in figure 3.2. Different combustion regimes including premixed, non-premixed and partially premixed are covered on the regime diagram. A premixed combustion regime covers a region that is around the condition of  $\theta = 1$  (full mixing) and  $\phi_f = 1$  (stoichiometric condition), and the piloted premixed jet flames F1, F2, and F3 are examples in this regime. A turbulent non-premixed combustion regime is located inside the fuel rich condition ( $\phi_f > 1$ ) as shown in the figure. The non-premixed piloted jet flames, Sydney flames L, B, and M, Sandia flames D, E, and F, and Sydney/Sandia inhomogeneous

inlet jet flame I1, are inside the non-premixed combustion regime on the diagram. The other region on the regime diagram is mainly the partially premixed combustion regime, and the Sydney/Sandia inhomogeneous inlet jet flames I2, I3, and I4 are example flames in this region. An extinction region is expectedly located on the fuel lean side ( $\phi_f < 1$ ) as shown in the figure when the condition is outside of the lean flammability condition. It is noted that the regime diagram is not to scale and the boundaries between different regimes are unknown presently. Additional parameters such as  $Re$  and Damkohler number  $Da$  are needed to fully characterize the flame for each point on the regime diagram. For example, with too high  $Re$  or too low  $Da$ , we can get a extinguished flame. In addition to the information at the fuel jet exit, the pilot inflow conditions including the tube diameter, inflow velocity, and temperature are also required to fully describe each flame. Nevertheless, the regime diagram is very helpful to the understanding of pilot stabilized turbulent jet flames and the different regimes that they can cover. Specifically, the regime diagram has the following potentially applications: (1) to provide a better overview of the existing experiments; (2) to identify zones that have not been covered in existing studies; (3) to enable a more complete model validation over a wide range of flames, as presented in this paper. From the diagram, we can see that the pilot burner is capable of producing different regimes of combustion by simply varying two parameters  $\phi_f$  and  $\theta$  on a single burner. This is extremely valuable for model assessment across different combustion regimes.

### 3.2.3 Examination of unified piloted turbulent jet flames

In this sub-section, we examine the different piloted turbulent jet flames, with the focus on the trend of changes of flame characteristics from one regime to another. Such an examination is helpful to identifying the critical characteristics of the flames in different regimes that will be useful for the later model assessment.

Figure 3.3 depicts the conditional mean temperature and conditional PDF of temperature (conditioning on  $0.02 < \xi < 0.1$ ) from the measurements at a selected downstream location of the pilot stabilized turbulent jet flames (the data for flames F1, F2 and F3 are not

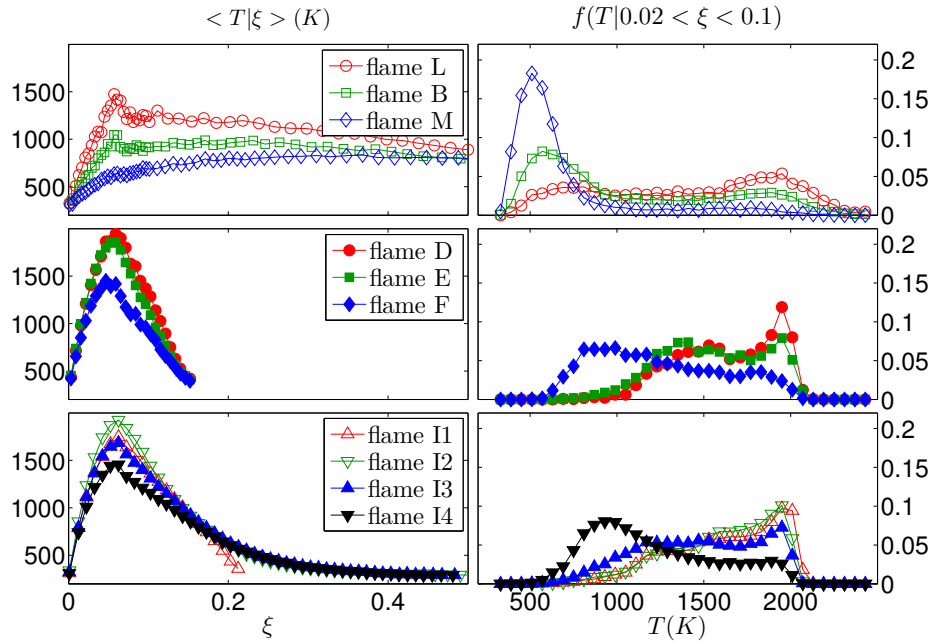


Figure 3.3. The measured conditional mean temperature  $\langle T|\xi \rangle$  (K) and conditional PDF of temperature  $f(T|0.02 < \xi < 0.1)$  against  $\xi$  at  $x/D_f = 20$  in flames L, B, and M [9, 118], and at  $x/D_f = 15$  in flames D, E, and F [88], and flames I1-I4 [25]. (More results are shown in the Supplementary Materials.)

available). The axial locations chosen for showing the measurement data in the different flames are selected based on the criterion that the location is approximately near the flame neck where most local extinction occurs (also not too close to the fuel jet exit). Several observations can be made from Figure 3.3.

- Flames L, B, and M are non-premixed between pure  $\text{CH}_4$  ( $\xi_f = 1$ ) and air ( $\xi = 0$ ), and flames D, E, and F can be viewed as non-premixed flames between premixed  $\text{CH}_4$ /air rich mixture at  $\phi_f = 3.17$  ( $\xi_f = 0.156$ ) and air, as shown in the plots of the conditional mean temperature in Figure 3.3. Flame I1 is close to a non-premixed flame because of its high mixedness parameter ( $\theta = 0.975$ ), between a fuel of  $\text{CH}_4$ /air mixture at  $\phi_f = 4.76$  ( $\xi_f = 0.217$ ) and air in the mixture fraction space.
- Flames I2-I4 are partially premixed flames and their conditional means of temperature are different from the non-premixed flames. They cannot be viewed as a non-

premixed flame between one single fuel and air. As shown in figure 3.3, for  $\xi < 0.1$ , the conditional mean temperature and conditional PDF of flames I2-I4 are similar to those of flame I1 and flames D, E, and F, but, for  $\xi > 0.1$ , the conditional mean temperature of flames I2-I4 is very different from flame I1, suggesting possible partially premixed stratified flames.

- With the increase of  $Re$  (or decrease of  $Da$ ) in the same flame series, i.e., flames L, B, and M, flames D, E, and F, and flames I2, I3, and I4, the conditional mean temperature reduces because of the increased level of local extinction. Correspondingly, the peak conditional PDF shifts towards low temperature.
- Flames M, F, and I4 are close to the flame blow-out limit. Comparing the pure  $\text{CH}_4$  case (flame M) and the diluted  $\text{CH}_4$  cases (flame F and flame I4), we can see that the peak conditional mean temperature in flame M is much lower than that in flames F and I4. The corresponding conditional PDF of temperature in flame M peaks at about 600 K, while this PDF peaks at about 900 K in flame F and flame I4. This indicates that the pure  $\text{CH}_4$  flames L, B, and M are more resistant to flame extinction than flames with the diluted  $\text{CH}_4$  on the pilot burner.

These observations represent the characteristic similarity and difference among the unified piloted turbulent jet flames. It is extremely difficult to accurately reproduce simultaneously all these characteristics with any of the existing models. The unified piloted turbulent jet flames are expected to serve as challenging test cases for modeling multi-regime combustion.

Figure 3.4 shows the radial profiles of the measured mean temperature at the selected axial location in each of the piloted turbulent jet flames. The mean temperature profiles within the same flame series tend to be similar in terms of the shape of the temperature profiles. The temperature peaks at a similar radial location within the same flame series, and the difference is mainly in the magnitude of temperature. This trend is evident in each series of flames (flames L, B, and M, flames D, E, and F, and flames I2, I3, and I4). Flame I1 is an exception in its series (flames I1-I4), and its temperature has a similar profile to

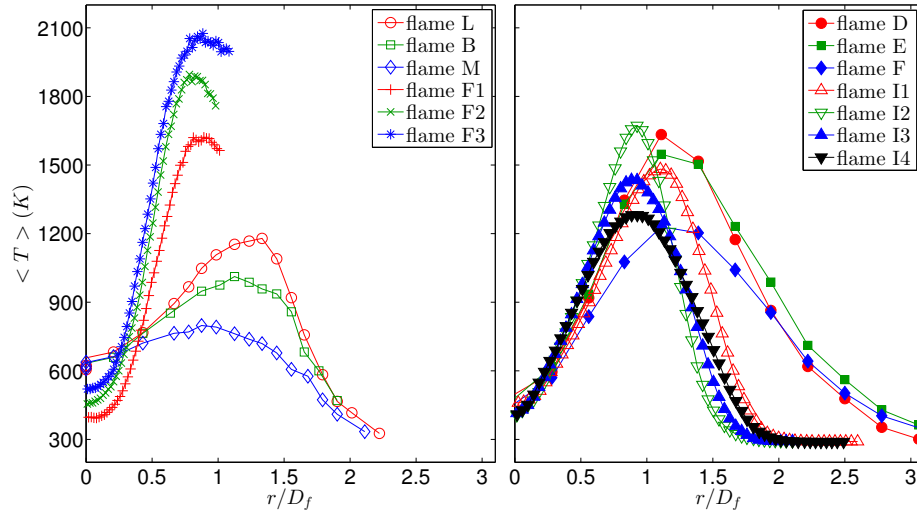


Figure 3.4. The measured radial profiles of the mean temperature  $\langle T \rangle$  (K) at  $x/D_f = 20$  in flames L, B, and M [9, 118], at  $x/D_f = 8.5$  in flames F1, F2, and F3 [83], and at  $x/D_f = 15$  in flames D, E, and F [88], and flames I1-I4 [25]. (More results are shown in the Supplementary Materials.)

flames D, E, and F, which is consistent with the observation that flame I1 is non-premixed. Flames I1 and I2 have a similar  $Re$  and the same  $\phi_f$ . The main difference between them is the mixedness parameter  $\theta$ , and this difference is likely the main reason for the difference of the mean temperature observed between flames I1 and I2 in figure 3.4. Given the different temperature profiles in the different flames resulting from different combustion regimes, it is of great interest to examine whether a turbulent combustion model can reproduce this variation consistently in all these pilot stabilized jet flames in different combustion regimes. In the following Section 3.3, we demonstrate, for the first time, an examination of the LES/PDF method applied to all these flames in the same set of calculations to examine the consistent capability of the model for multi-regime combustion.

### 3.3 Assessment of LES/PDF in unified piloted turbulent jet flames

A preliminary model assessment is performed simultaneously for LES/PDF of the unified set of piloted turbulent jet flames. The same set of models and parameters are used in all

simulations. No attempt is made to optimize the choice of the model parameters to improve predictions for a specific case. Our focus is put on examining the consistency of the model performance across different combustion regimes, instead of focusing on the predictability of the model in a specific regime, which has been done extensively before. The selected set of flames for this model assessment includes flame L, flame E, flame F1, and flames I1-I4.

### 3.3.1 LES/PDF modeling approach

A previously developed LES/PDF modeling framework [46] is employed in this study to model the piloted turbulent jet flames. LES [135] is used to model the flow and turbulence fields, and the transport PDF method [55, 99] is used to model the combustion fields. A mixing model, Euclidean Minimum Spanning Tree (EMST) [84], is used for the closure of the micromixing term in the PDF equation. A fixed constant  $C_\phi = 3.0$  that determines the rate of mixing in the EMST model is used in all the simulations. It is widely known that the value of  $C_\phi$  can significantly influence the modeling results, and it is often found that an improved prediction for a specific test case can be obtained by adjusting  $C_\phi$ . In this work, all model constants are fixed, including  $C_\phi = 3.0$ , when the models are applied to the piloted jet flames across different combustion regimes, to provide a more objective assessment of the models.

Table 3.3. The computational domain and the number of grids in the axial, radial, and azimuthal directions, respectively, used in the LES/PDF simulations of the piloted turbulent jet flames.

case	$[x/D_f] \times [r/D_f] \times [z]$	$n_x \times n_r \times n_z$
flame L	$[0, 60] \times [0, 20] \times [0, 2\pi]$	256×108×48
flame E	$[0, 80] \times [0, 20] \times [0, 2\pi]$	256×128×48
flame F1	$[0, 20] \times [0, 20] \times [0, 2\pi]$	144×128×64
flame I1	$[-40, 60] \times [0, 20] \times [0, 2\pi]$	384×144×64
flames I2-I4	$[-10, 45] \times [0, 20] \times [0, 2\pi]$	256×144×64

For flame L, flame E, and flame F1, the computational domains start at the fuel jet exit plane, and the inflow boundary conditions are directly imposed at the fuel jet exit. For flames I1-I4, the domain extends to the upstream of the fuel jet exit and starts at the central tube exit (see Figure 3.1). The detailed information about the computational domain and grid for the different flames are summarized in Table 3.3. It is noted that different grid resolutions are employed for the different cases. The resolution requirements for the different cases are different. For example, flame L is much "thinner" than flame E, and the length of the interesting regions in flame F1 is much shorter than those in flame L and flame E. A single resolution that is suitable for all cases can be prohibitively expensive to compute. The currently employed grid resolutions for the different cases are based on grid convergence studies and previous studies [14]. (The grid convergence study results of two selected cases (flame L and flame I2) are presented in the Supplementary Materials of this paper.) A separate simulation of a fully developed turbulent pipe flow (and an annulus slot for flames I1-I4) is performed to supply the inflow boundary conditions for all the flame simulations. Other boundary conditions are imposed from the measurements. More details about the simulations can be found in [46].

### **3.3.2 Model assessment across different combustion regimes**

#### **Inflow conditions at the fuel jet exit**

The quality of the inflow condition at the fuel jet exit plane is expected to have a significant effect on the downstream predictions. Here we examine the predictions of the inflow conditions in flames I1-I4. Figure 3.5 shows the radial profiles of the mean and rms of mixture fraction at  $x/D_f = 1$ . The measured mean mixture fractions are predicted accurately in flames I1-I4, while the rms mixture fraction is over-predicted quite significantly. This over-prediction is likely attributed to an inadequate grid resolution inside the fuel jet pipe, as indicated by the grid convergence study results in the Supplementary Materials. We emphasize that the focus of this work is to examine the performance consistency of the same model for different combustion regimes. The current grid specification summarized in Ta-

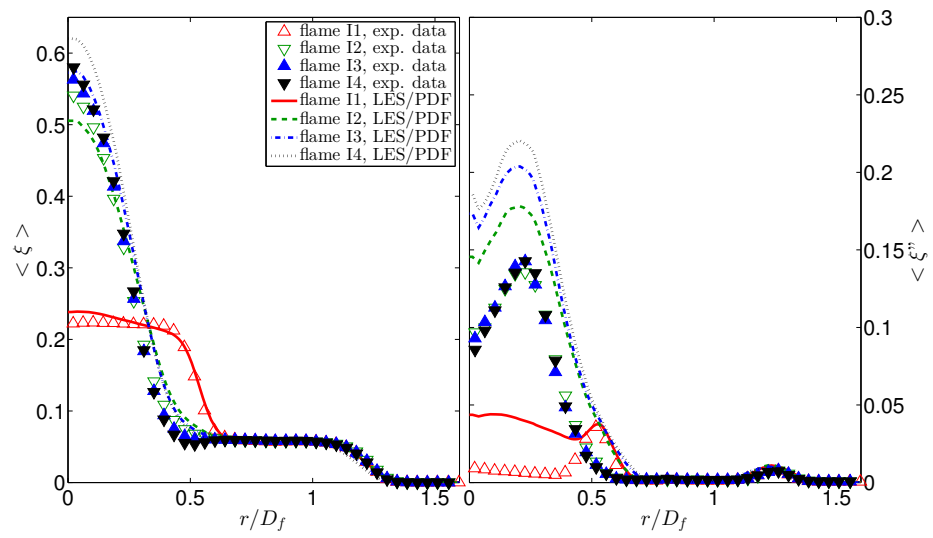


Figure 3.5. Radial profiles of the predicted (lines) and measured (symbols) mean and rms mixture fractions  $\langle \xi \rangle$ ,  $\langle \xi \epsilon \rangle$  at  $x/D_f = 1$  in flames I1-I4 [25].

ble 3.3 is expected to be adequate to serve the purpose of this study. Detailed parametric studies of flames I1-I4, including a grid refinement study, will be conducted in our future work.

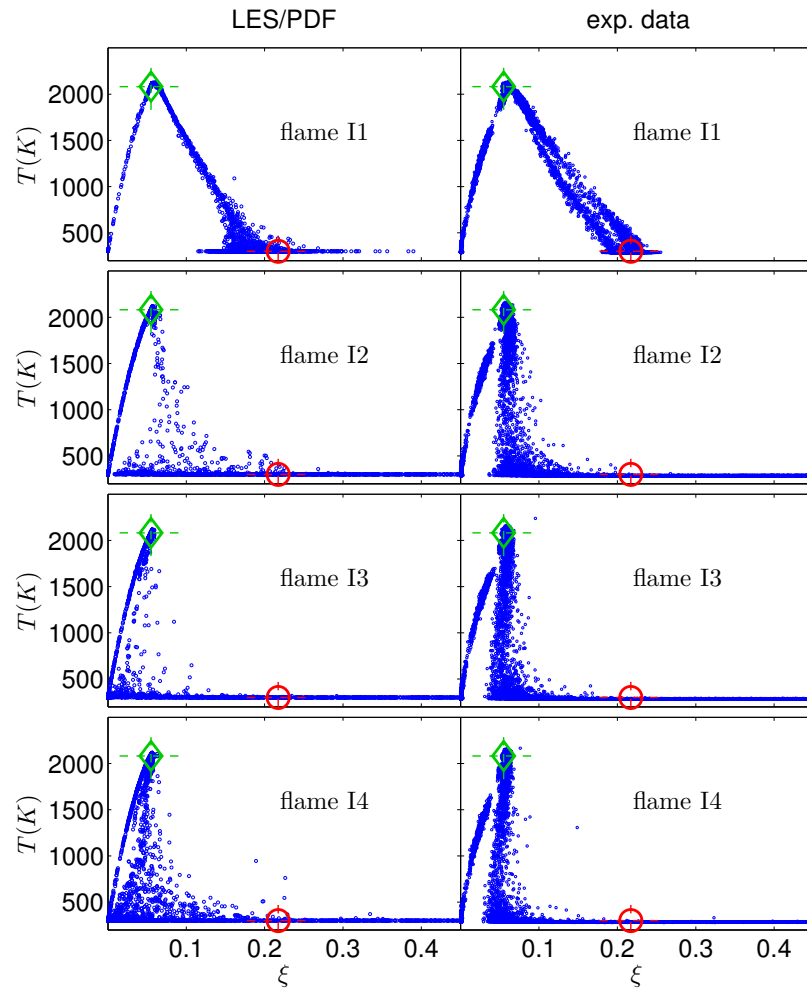


Figure 3.6. Predicted (left) and measured (right) scatter plot of temperature against mixture fractions at  $x/D_f = 1$  in flames I1-I4 [25]. The diamond symbols correspond to the pilot condition, and the circle symbols indicate the theoretically fully mixed condition of the fuel jet.

Figure 3.6 compares qualitatively the particle scatter plot of temperature  $T$  against the mixture fraction  $\xi$  at  $x/D_f = 1$  in flames I1-I4. The diamond symbols in the figure denote

the pilot condition, and the circle symbols denote a theoretically fully mixed condition of the fuel jet (the corresponding value of mixture fraction,  $\xi_f = 0.217$ ). Flame I1 is apparently close to the fully mixed condition at  $x/D_f = 1$  based on the measurement in Figure 3.6, and the model captures this level of mixing very well but with larger variance indicated by a larger particle scattering around the fully mixed condition, which is consistent the over-prediction of the rms mixture fraction by the model in figure 3.5. Flames I2-I4 correspond to stratified mixing with very wide scattering of the particles in the mixture fraction space at the unburnt temperature  $T = 300$  K, at  $x/D_f = 1$ . The LES/PDF predictions show more scattering than the measurements for flames I2-I4 too, especially at the fuel lean condition ( $\xi < 0.03$ ).

Although there is some level of discrepancy between the model predictions of the inflow conditions and the measurements in flames I1-I4, we find no significant difference of the discrepancy of the model predictions from the measurements near the fuel jet exit among the different flames, and overall consistent model performance is observed.

### **Predictions of mixing process**

Next we examine the predictions of the mixing process in the piloted turbulent jet flames by examining the mean and rms mixture fraction at a selected downstream location in each flame, at  $x/D_f = 15$  in flame E and flames I1-I4, at  $x/D_f = 20$  in flame L, and at  $x/D_f = 8.5$  in flame F1. Figure 3.7 shows the comparison of the predicted and measured mean and rms mixture fraction at the selected axial locations in the piloted turbulent jet flames. From the figure, we can see that the model predictions for the mean mixture fraction are in an excellent agreement with the experimental data. Except in flame F1 which does not have experimental data, the rms mixture fractions in all flames in Figure 3.7 are predicted reasonably well by LES/PDF in comparison with the measurements. There is over-prediction of the rms mixture fraction in all flames, except in flame E where the rms mixture fraction is only very slightly over-predicted. Overall, a consistent model performance is observed in the predictions of the mixing process by using the same model in all

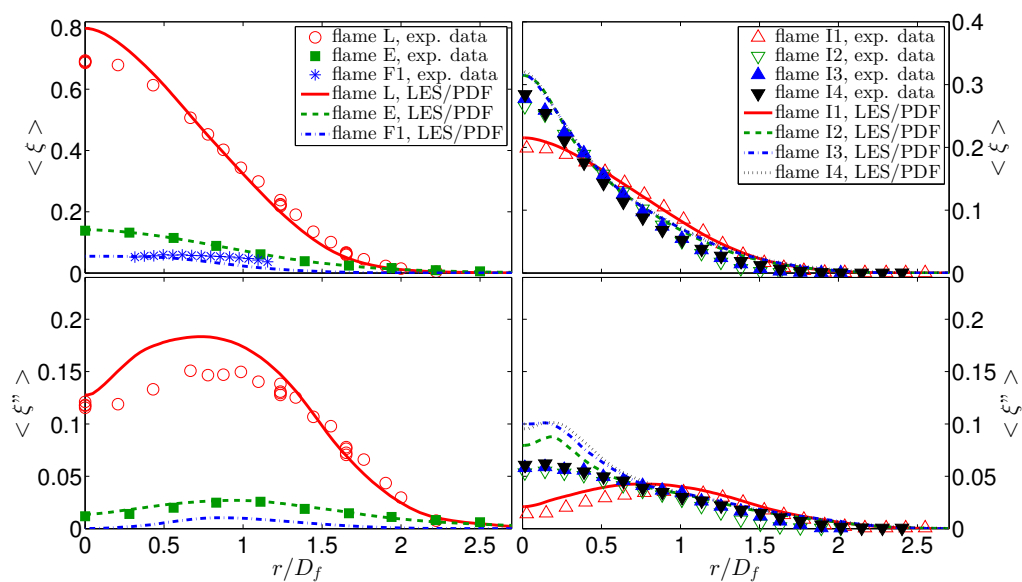


Figure 3.7. Radial profiles of the predicted (lines) and measured (symbols) mean and rms mixture fractions  $\langle \xi \rangle$ ,  $\langle \xi \epsilon \rangle$  at  $x/D_f = 20$  in flame L, at  $x/D_f = 8.5$  in flame F1, at  $x/D_f = 15$  in flame E, and in flames I1-I4. (More results are shown in the Supplementary Materials.)

these different flames, covering non-premixed, partially premixed, and premixed combustion.

### Predictions in the mixture fraction space

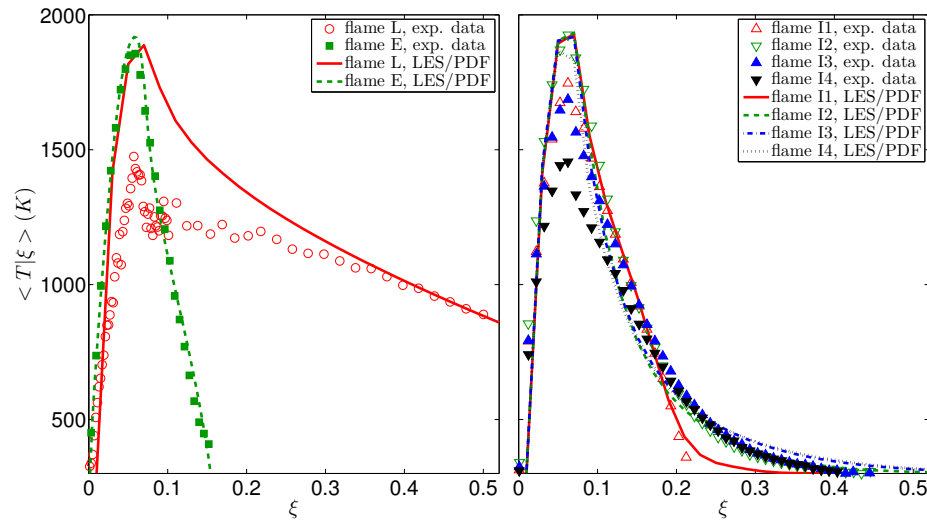


Figure 3.8. Predicted (lines) and measured (symbols) conditional mean temperature  $\langle T|\xi \rangle$  (K) against  $\xi$  at  $x/D_f = 20$  in flame L, at  $x/D_f = 15$  in flame E, and in flames I1-I4. (More results are shown in the Supplementary Materials.)

Figure 3.8 shows the conditional mean temperature against the mixture fraction. In terms of the performance of LES/PDF in the different flames, we can make the following observations:

- Excellent agreement between the simulations and the measurements is observed in flame E and flame I2. In all other flames, the maximum conditional mean temperature is over-predicted;
- The predicted maximum conditional mean temperature in all flames shown in the figure is surprisingly similar, close to 1900 K, while the measured ones are very different in the different flames;

- In the series of flames I1-I4, the predictions are almost indistinguishable between  $\xi = [0, 0.1]$ , as opposed to the very different measurements.

Clearly there is noticeable quantitative performance difference of LES/PDF in these different flames. The model, in its current state, seems limited in adequately reproducing the difference of the different flames observed in the experiments, as suggested by the last two observations above.

### Predictions in the physical space

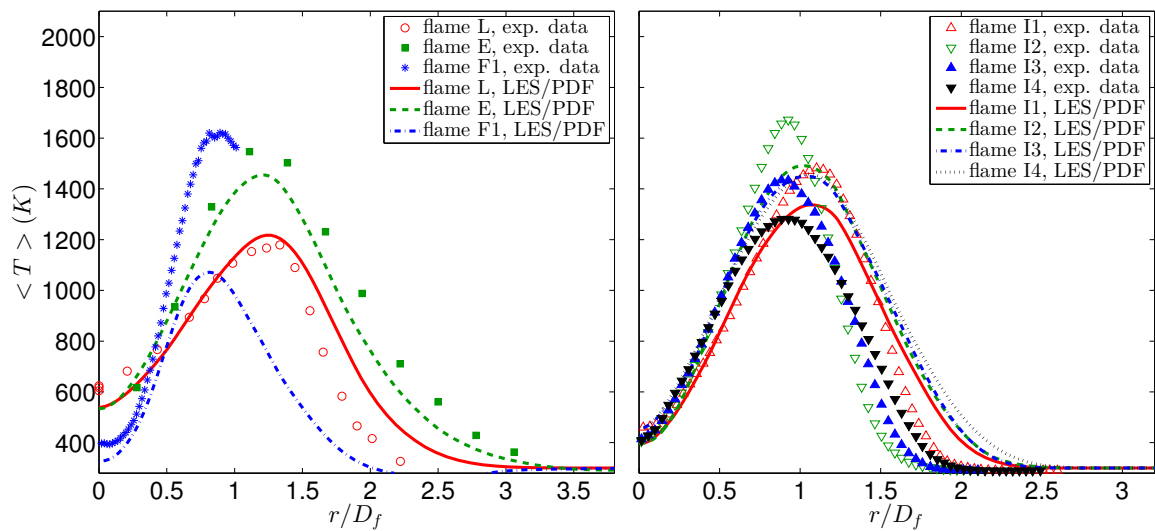


Figure 3.9. Radial profiles of the predicted (lines) and measured (symbols) mean temperature  $\langle T \rangle$  (K) at  $x/D_f = 20$  in flame L, at  $x/D_f = 8.5$  in flame F1, at  $x/D_f = 15$  in flame E, and in flames I1-I4. (More results are shown in the Supplementary Materials.)

The LES/PDF predictions of the radial profiles of the mean temperature in the piloted turbulent jet flames are further examined in Figure 3.9. The measured mean temperature profile is predicted reasonably well in the non-premixed flames L, E, and I1. Significant underprediction of temperature is observed in the premixed flame F1. In the series of flames I1-I4, the predictions capture the overall trend of temperature variations in the radial direc-

tion including the peak temperature location. However, the performance difference of the model predictions in comparison with the measurements in the different flames is significantly different. First, the predicted trend of the temperature variation in the outer mixing layer from one flame to another is in the opposite direction to the trend observed in the measurements. For example, the measurements show that flame I1 is wider than I2 at  $x/D_f = 15$  based on the measured temperature variation, while the model predicts the opposite. Second, the difference among the predictions of flames I1-I4 is much smaller than that from the measurements, especially near the outer mixing layer where the models yield very similar results for the different flames, while the measurements are significantly different in the different flames. This observation is confirmed by examining the results at further downstream locations in the piloted jet flames (results are shown in the Supplementary Materials). This suggests that the LES/PDF model is limited in differentiating the significantly different behaviors in different flames as compared to the measurements, especially in the partially premixed regime. It is noted that the performance difference of the models in the different flames cannot be explained by the difference in the numerical errors caused by the different domain sizes and meshes used in the different flames. The same domain size and mesh are indeed used in flames I2-I4, with which the model still shows very different performance. This performance difference can be best explained by the fundamental difference of the different flames and the limitation of the currently employed LES/PDF model to represent all the flames in different combustion regimes simultaneously.

### 3.4 Conclusions

A unified view of several pilot stabilized turbulent jet flames from independent previous studies is established by proper parameterization of the flames based on the characteristic similarity and difference of the flames. A regime diagram for the turbulent jet flames stabilized on the pilot flame burner is introduced, which covers all three major combustion regimes, non-premixed, partially premixed, and premixed. Comparative studies are performed to examine the trend of changes in the unified piloted turbulent jet flames when

moving from one combustion regime to another. The unified piloted turbulent jet flames provide a challenging model assessment framework for the performance of turbulent combustion models across multi-regime combustion. A preliminary model assessment is carried out for the large eddy simulation (LES)/probability density function (PDF) method in examining the consistency of the model's performance in the different combustion regimes. The applicability of the LES/PDF model to the different combustion regimes is clearly demonstrated in this model assessment. The model is found to be able to reproduce the piloted turbulent jet flames reasonably well. Several limitations of the model are also identified, including the limitation of the model to reproduce the measured difference of the different flames in different regimes. Such limitations are very useful for guiding future improvement of the model.

#### **4. VARIANCE CONSISTENT MEAN SHIFT PARTICLE MODEL FOR TREATING DIFFERENTIAL MOLECULAR DIFFUSION IN TRANSPORTED PDF METHODS FOR TURBULENT REACTIVE FLOWS**

A mean shift (MS) particle model has been developed before to account for molecular diffusion in the transported probability density function (PDF) methods for turbulent reactive flows (McDermott and Pope, *Journal of Computational Physics*, 2007, 226, 947-993). The MS model is superior over the traditional random walk model for its capabilities to incorporate differential molecular diffusion and to yield a consistent DNS limit of scalar variance production/dissipation. The MS model, however, yields inconsistent transport of the scalar variance because of the missing molecular diffusion in the resultant variance transport equation. To yield fully consistent transport of scalar mean and variance, a variance consistent mean shift (VCMS) model is developed in this work. The VCMS model formulations are developed for both a single-scalar system and a multi-scalar system. Boundedness violation of particle scalars exists in both the MS and VCMS models and causes a realizability issue of the models. An correction algorithm (called MP correction by McDermott and Pope) has been developed before to correct the boundedness violation in the MS model. The MP correction is found to produce overcorrection to the particles, resulting in underprediction of the scalar variance. In addition, it is only applicable to the IEM mixing model. In this work, three new boundedness correction algorithms are developed based on the strategies of a least-decay factor (LDF), clipping at scalar bounds (CSB), and clipping with paired mixing (CPM). The accuracy and consistency of the VCMS models are examined and validated thoroughly in a turbulent mixing layer problem. The effectiveness and accuracy of the

---

<sup>3</sup>The content of this chapter is from the paper [155] — P. Zhang, H. Wang. Variance consistent mean shift particle model for treating differential molecular diffusion in transported PDF methods for turbulent reactive flows. *Computers & Fluids*, 2018, 170: 53-76.

different boundedness correction algorithms are also examined and assessed in the mixing layer problem. The applicability of the CPM correction to other mixing models (MCurl and EMST) is also demonstrated.

#### 4.1 Introduction

Multiple physical/chemical/thermal processes, such as fluid convection, multi-component molecular diffusion, multi-phase, chemical reaction, turbulence, radiation, and heat transfer, are involved in turbulent reactive flows found in numerous engineering applications such as gas turbines and gasoline engines. To develop predictive CFD tools for these engineering problems, it is needed to build accurate sub-models for each of these physical/chemical/thermal processes as building blocks. This work mainly concerns with developing accurate and consistent molecular diffusion sub-models in the context of the transported probability density function (PDF) methods [55,99] in conjunction with the Reynolds averaged Navier-Stokes (RANS) simulations or large-eddy simulations (LES) [99].

Historically, in the modeling of turbulent combustion problems (with RANS or LES), molecular diffusion has often been viewed insignificant, and simple models were constructed to treat the effect of molecular diffusion by completely neglecting it or assuming equal diffusivities for all multi-components. These simplifications are common in the modeling of turbulent non-premixed combustion, and many models have the build-in assumption of equal diffusivities [53, 54]. Molecular diffusion, however, has substantial theoretical significance because of the fundamental role of molecular diffusion in multi-component transport problems. The significance of differential molecular diffusion in turbulent combustion, in contrast to the simplified equal molecular diffusion, has been reported in a number of experimental studies [103, 104, 156–159] and direct numerical simulation (DNS) studies [105, 160–164]. In the RANS modeling, the effect of molecular diffusion on the transport of moment fields is arguably small when compared to the diffusive transport that is caused by turbulent eddies. This small effect, however, can cause substantial effect on the combustion modeling due to the highly nonlinear nature of turbulence. Rowinski and

Pope [165] showed that the prediction of the flame width is highly sensitive to molecular diffusion in the PDF modeling of a piloted lean premixed flame [153, 166, 167]. Wang and Kim [168] demonstrated a strong sensitivity of the predicted flame extinction limit to different molecular diffusion models in Sandia flame E [88] by using the PDF method [55]. In LES, the magnitude of the sub-filter scale eddy diffusivity can be comparable to the molecular diffusivities, and hence an accurate treatment of multi-component molecular diffusion is important. Kemenov and Pope [169] found that molecular diffusivity can exceed the sub-filter scale eddy diffusivity in the near field of Sandia flame D [88] in LES. Han et al. [170] showed the strong sensitivity of flame ignition to different molecular diffusion models in the LES/PDF modeling of the Cabra flame [171]. Thus the traditional view of molecular diffusion being insignificant in turbulent combustion is not fully justified, and an accurate account of detailed molecular diffusion as a building block in turbulent combustion modeling is equally important as many other sub-models.

In mixture fraction based combustion models for turbulent non-premixed combustion, the combustion process is assumed to be mixing controlled. This means that an accurate modeling of diffusion and mixing is critical to the prediction accuracy. These combustion models rely on the assumption that the mixture fraction is a conserved scalar whose transport is independent of chemical reaction. It is well known that equal-diffusivity assumption has to be introduced for the mixture fraction to be a conservative scalar, and as a result, highly simplified molecular diffusion treatment is inevitable in the mixture fraction based models such as flamelet models [53] and conditional moment closure (CMC) [54]. Efforts have been made recently to extend these models for treating DMD, *e.g.*, DMD in CMC [172] and DMD in flamelet models [173, 174].

In the transported PDF method which is employed in the current work, the equal-diffusivity assumption has long been practiced as well. In the particle formation of the PDF method [55, 175], molecular diffusion is often treated through a random walk (RW) model in which the effect of molecular diffusion is accounted for by the random walk of particles in the physical space. In the RW model, molecular diffusion of all different components is modeled through the same particle random motion in the physical space, and hence equal molecular

diffusivity has to be used. This creates a significant challenge to extending the RW model for treating DMD. Another challenge with the RW model is that it introduces spurious variance production/dissipation at the DNS limit, as revealed by McDermott and Pope [176] and Viswanathan et al. [177]. This means that the model does not converge correctly to the DNS limit. To remedy these two problems, McDermott and Pope [176] introduced a so-called mean shift (MS) particle model to allow the incorporation of DMD and to ensure the convergence of the model. The MS particle model has been used in several studies (*e.g.*, [61, 70, 165, 170, 177, 178]) and has showed promising performance. There is also an interesting work to combine the RW model and the MS model to take advantages of both models [179].

The MS particle model is an important advancement of the transported PDF method to account for DMD. The model, however, is not flawless, and there are three main issues with the current form of the MS particle model. First, despite the consistent DNS limit of the MS model compared to the RW model, the MS model yields inconsistent transport of the scalar variance because of the missing molecular diffusion term in the variance transport equation. (In the DNS limit, the variance goes to zero and hence this inconsistent transport of scalar variance does not affect the DNS limit). The inconsistency causes spurious diffusion of the scalar variance for practical applications where the scalar variance is not zero. Second, the MS model cannot guarantee the boundedness of scalars. A boundedness correction algorithm has been introduced in [176]. The performance of the correction, its convergence and its impact on the prediction accuracy, however, have not been fully examined. Third, the MS model, in its current form, is applicable only to one mixing model, the Interaction by Exchange with the Mean (IEM) mixing model [85] (or the Linear Mean-Square Estimation (LMSE) model [127]). There are other (and sometimes more attractive) mixing models available, such as the Modified Curl (MCurl) model [82] and the Euclidean Minimum Spanning Tree (EMST) model. It is needed to extend the MS model and correction algorithms to be compatible with other mixing models. The goal of this paper is to address the above three issues with the MS particle model to further advance the transport PDF methods. The objectives are

1. To develop and validate fully consistent mean shift particles models for treating DMD by using the transported PDF methods;
2. To examine and develop boundedness correction algorithms in the mean shift particle models to ensure realizability and to be applicable to other mixing models.

The rest of the paper is organized as follows. Section 4.2 reviews the basics of the transported PDF methods and the models for treating molecular diffusion including the RW model and the MS model. The problems with the current molecular diffusion models are discussed also in Section 4.2. Section 4.3 develops an advanced mean shift particle model that is consistent for the transport of both the scalar mean and variance fields. The new models, called the variance consistent mean shift (VCMS) particle models, are thoroughly examined and validated in Section 4.4. The conclusions are drawn in Section 4.5.

## 4.2 Transported PDF methods and molecular diffusion models

### 4.2.1 Transported PDF methods and Monte Carlo solution method

The transported PDF methods [55,99] were originally developed in the RANS context, and were later extended to LES [180]. The molecular diffusion models discussed in this work can be used in both RANS and LES. To simplify the discussion, we will adopt the RANS terminologies in this paper, and expect the models to be applicable to LES as well.

For a multi-component gas phase reactive flow system with  $n_\phi$  mass fractions ( $n_\phi > 2$ ), the conservation equation of the mass fraction  $\phi_\alpha$  ( $\alpha = 1, \dots, n_\phi$ ) can be written as

$$\frac{\partial \rho \phi_\alpha}{\partial t} + \nabla \cdot (\rho \mathbf{u} \phi_\alpha) = \nabla \cdot (\rho \Gamma_\alpha \nabla \phi_\alpha) + \rho S_\alpha + C_\alpha, \quad (4.1)$$

where  $\mathbf{u}$  is the velocity vector,  $\Gamma_\alpha$  is the molecular diffusivity of species  $\alpha$ , and  $S_\alpha$  is the chemical reaction source term. The chemical reaction source term is kept in the equations for completeness although the test cases we considered in Section 4.4 are non-reacting ( $S_\alpha = 0$ ). Summation rule is not implied over the repeated index in this work. In equation (4.1), the mixture-averaged molecular diffusion [181] is assumed which is widely used for

the modeling of combustion and is reported to be a reasonable model for describing multi-component molecular diffusion [109,182]. A correction term  $C_\alpha$  is needed in equation (4.1) to ensure mass conservation, *i.e.*, all mass fractions sum to one,

$$\sum_{\alpha} \phi_{\alpha} = 1. \quad (4.2)$$

A typical correction can be written as

$$C_{\alpha} = -\nabla \cdot \left( \rho \phi_{\alpha} \sum_{\beta} \Gamma_{\beta} \nabla \phi_{\beta} \right). \quad (4.3)$$

It is noted that the correction  $C_{\alpha}$  is needed only for a multi-scalar system ( $n_{\phi} \geq 3$ ), and is not needed for a single scalar system ( $n_{\phi} = 1$  or 2). Here a single scalar system includes cases with  $n_{\phi} = 1$  (*e.g.*, mixture fraction or enthalpy) or with  $n_{\phi} = 2$  which is a binary diffusion system and has one degree of freedom. By performing Favre averaging on equation (4.1), we can derive the following modeled transport equations for the mean  $\tilde{\phi}_{\alpha}$  and variance  $\widetilde{\phi_{\alpha}''^2}$ ,

$$\frac{\partial \bar{\rho} \tilde{\phi}_{\alpha}}{\partial t} + \nabla \cdot (\bar{\rho} \tilde{\mathbf{u}} \tilde{\phi}_{\alpha}) = \nabla \cdot [\bar{\rho} (\Gamma_t + \Gamma_{\alpha}) \nabla \tilde{\phi}_{\alpha}] + \bar{\rho} \tilde{S}_{\alpha} + \hat{C}_{\alpha}, \quad (4.4)$$

$$\begin{aligned} \frac{\partial \bar{\rho} \widetilde{\phi_{\alpha}''^2}}{\partial t} + \nabla \cdot (\bar{\rho} \tilde{\mathbf{u}} \widetilde{\phi_{\alpha}''^2}) &= \nabla \cdot [\bar{\rho} (\Gamma_t + \Gamma_{\alpha}) \nabla \widetilde{\phi_{\alpha}''^2}] - 2\bar{\rho} \Omega \widetilde{\phi_{\alpha}''^2} \\ &+ 2\bar{\rho} \Gamma_t \nabla \tilde{\phi}_{\alpha} \cdot \nabla \tilde{\phi}_{\alpha} + 2\bar{\rho} (\widetilde{\phi_{\alpha} S_{\alpha}} - \tilde{\phi}_{\alpha} \tilde{S}_{\alpha}), \end{aligned} \quad (4.5)$$

where “ $\bar{\square}$ ” and “ $\widetilde{\square}$ ” denote Reynolds averaging and Favre averaging, respectively. When deriving the above equations (4.4) and (4.5), we have used the following equations or common models,

$$\widetilde{\Gamma_{\alpha} \nabla \phi_{\alpha}} \approx \Gamma_{\alpha} \nabla \tilde{\phi}_{\alpha}, \quad (4.6)$$

$$\mathbf{u} = \tilde{\mathbf{u}} + \mathbf{u}'', \quad \phi_{\alpha} = \tilde{\phi}_{\alpha} + \phi_{\alpha}'', \quad (4.7)$$

$$-\bar{\rho} \widetilde{\mathbf{u}'' \phi_{\alpha}''^m} \approx \bar{\rho} \Gamma_t \nabla \widetilde{\phi_{\alpha}''^m}, \quad (m = 1, 2), \quad (4.8)$$

$$\tilde{C}_{\alpha} \approx \hat{C}_{\alpha} = -\nabla \cdot \left( \bar{\rho} \tilde{\phi}_{\alpha} \sum_{\beta} \Gamma_{\beta} \nabla \tilde{\phi}_{\beta} \right), \quad (4.9)$$

$$\widetilde{\phi_{\alpha} C_{\alpha}} - \tilde{\phi}_{\alpha} \tilde{C}_{\alpha} \approx 0, \quad (4.10)$$

$$2\bar{\rho} \Gamma_{\alpha} \nabla \widetilde{\phi_{\alpha}'' \cdot \nabla \phi_{\alpha}''} = 2\bar{\rho} \Gamma_{\alpha} \nabla \widetilde{\phi_{\alpha} \cdot \nabla \phi_{\alpha}} - 2\bar{\rho} \Gamma_{\alpha} \nabla \tilde{\phi}_{\alpha} \cdot \nabla \tilde{\phi}_{\alpha} = 2\bar{\rho} \Omega \widetilde{\phi_{\alpha}''^2}, \quad (4.11)$$

where the fluctuations in the transport properties are neglected in equation (4.6), the gradient transport model [99] is used in equation (4.8) with  $\Gamma_t$  being the turbulent diffusivity, simple models are used for the terms involving the conservation correction  $C_\alpha$  in equations (4.9) and (4.10), and  $\Omega$  is the mixing frequency in equation (4.11). The two transport equations in (4.4) and (4.5) will be used as references for developing consistent transported PDF models for treating molecular diffusion.

In the transported PDF methods [55, 99], taking  $\Phi = (\phi_1, \phi_2, \dots, \phi_{n_\phi})$  as a random vector, we can define a single-point single-time joint PDF  $f(\Psi; \mathbf{x}, t)$  to represent the random distribution of values taken from the sample space  $\Psi = (\psi_1, \psi_2, \dots, \psi_{n_\psi})$  corresponding to  $\Phi$ . (The terminology for  $f$  in LES is sometimes named filtered density function or FDF [180].) Following Pope [55, 99], a governing equation for  $f(\Psi; \mathbf{x}, t)$  is derived from equation (4.1) as

$$\frac{\partial \bar{\rho} \tilde{f}}{\partial t} + \sum_{\alpha} \frac{\partial}{\partial \psi_{\alpha}} \left[ \bar{\rho} S_{\alpha}(\Psi) \tilde{f} \right] = -\nabla \cdot \left( \bar{\rho} \langle \mathbf{u} | \Psi \rangle \tilde{f} \right) - \sum_{\alpha} \frac{\partial}{\partial \psi_{\alpha}} \left[ \langle \nabla \cdot (\rho \Gamma_{\alpha} \nabla \phi_{\alpha}) + C_{\alpha} | \Psi \rangle \tilde{f} \right], \quad (4.12)$$

in which  $\langle \square | \square \rangle$  is a conditional mean, and  $\tilde{f}$  is the density-weighted PDF. The chemical reaction source term  $S_{\alpha}$  appears in a closed term in the PDF transport equation in (4.12). Both terms on the right-hand side that involve a conditional mean in the PDF transport equation require modeling closure. The effect of molecular diffusion in the last term of equation (4.12) is unclosed and its closure is the focus of this study. The closure of the PDF transport equation is discussed in the later sections.

The transported PDF equation in (4.12) is usually solved by employing the Monte Carlo particle method [55]. The joint PDF  $\tilde{f}$  is represented by an ensemble of particles in each CFD grid cell. Each particle has a set of properties including the particle locations  $\mathbf{X}_p^*$ , mass  $m_p^*$  and scalars  $\Phi_p^*$ , where  $p$  is the particle index,  $p = 1, \dots, n_p$  with  $n_p$  the number of particles in a grid cell and the superscript “\*” denotes that the quantity is evaluated at the particle location  $\mathbf{X}_p^*$ . A set of stochastic differential equations (SDEs) can be developed, and the evolution of these particles following these SDEs represents, in a discrete manner, the evolution of the joint PDF. Once the PDF transport equation is solved numerically for  $\tilde{f}$

(with proper model closure for the unclosed terms in the transport equation), the grid-based  $m$ th moments that are of most practical interest are approximated from ensemble average as

$$\widetilde{\phi}_\alpha^m = \int \psi_\alpha^m \widetilde{f}(\Psi; \mathbf{x}, t) d\Psi \approx \frac{\sum_{p=1}^{n_p} m_p^* \cdot (\phi_{\alpha,p}^*)^m}{\sum_{p=1}^{n_p} m_p^*}. \quad (4.13)$$

#### 4.2.2 Random walk model for equal-diffusivity problems

In the RW model [55, 175], with the assumption of equal-diffusivity  $\Gamma_\alpha = \Gamma$  (and unity Lewis number if the energy equation is included), the PDF equation in (4.12) can be reformulated and closed as

$$\frac{\partial \bar{\rho} \widetilde{f}}{\partial t} + \nabla \cdot (\bar{\rho} \widetilde{\mathbf{u}} \widetilde{f}) + \sum_\alpha \frac{\partial}{\partial \psi_\alpha} [\bar{\rho} S_\alpha(\psi) \widetilde{f}] = \nabla \cdot [\bar{\rho} (\Gamma_t + \Gamma) \nabla \widetilde{f}] + \sum_\alpha \frac{\partial}{\partial \psi_\alpha} [\bar{\rho} \Omega (\psi_\alpha - \widetilde{\phi}_\alpha) \widetilde{f}], \quad (4.14)$$

in which, the following equations or models are used,

$$\langle \mathbf{u} | \Psi \rangle = \widetilde{\mathbf{u}} + \langle \mathbf{u}'' | \Psi \rangle, \quad (4.15)$$

$$-\bar{\rho} \langle \mathbf{u}'' | \Psi \rangle \widetilde{f} = \bar{\rho} \Gamma_t \nabla \widetilde{f}, \quad (4.16)$$

$$-\sum_\alpha \frac{\partial}{\partial \psi_\alpha} [\langle \nabla \cdot (\rho \Gamma \nabla \phi_\alpha) | \Psi \rangle \widetilde{f}] = \nabla \cdot (\bar{\rho} \Gamma \nabla \widetilde{f}) - \bar{\rho} \sum_\alpha \sum_\beta \frac{\partial^2}{\partial \psi_\alpha \partial \psi_\beta} [\langle \Gamma \nabla \phi_\alpha \cdot \nabla \phi_\beta | \Psi \rangle \widetilde{f}], \quad (4.17)$$

$$-\sum_\alpha \sum_\beta \frac{\partial^2}{\partial \psi_\alpha \partial \psi_\beta} [\langle \Gamma \nabla \phi_\alpha \cdot \nabla \phi_\beta | \Psi \rangle \widetilde{f}] = \sum_\alpha \frac{\partial}{\partial \psi_\alpha} [\Omega (\psi_\alpha - \widetilde{\phi}_\alpha) \widetilde{f}]. \quad (4.18)$$

Equation (4.15) is the conditional Favre decomposition [55], equation (4.16) is the gradient diffusion model [99] with  $\Gamma_t$  being the turbulent diffusivity, and equation (4.17) is an equality that can be derived by using the delta function [55, 99]. The last term in the PDF transport equation (4.14) is called the micro-mixing term and is commonly modeled by using mixing models such as the IEM model [85, 127]), the MCurl model [82] and the EMST model [84]. In this work, for most of the discussions, we use the IEM model to close the mixing term in equation (4.18) in which  $\Omega$  is the mixing frequency. The effect of the different mixing models will be commented later in Section 4.4.6. It is noted that the mass conservation correction term is  $C_\alpha = 0$  in equation (4.3) when equal-diffusivity is assumed.

The SDEs corresponding to the closed PDF transport equation (4.14) with the RW model are written as

$$d\mathbf{X}_p^*(t) = \left[ \tilde{\mathbf{u}} + \frac{\nabla[\bar{\rho}(\Gamma_t + \Gamma)]}{\bar{\rho}} \right]^* dt + \sqrt{2(\Gamma_t + \Gamma)^*} d\mathbf{W}, \quad (4.19)$$

$$d\Phi_p^*(t) = -\Omega^* (\Phi_p^* - \tilde{\Phi}^*) dt + \mathbf{S} (\Phi_p^*) dt, \quad (4.20)$$

$$\rho_p^* = \rho (\Phi_p^*), \quad (4.21)$$

where  $\mathbf{W}$  is an isotropic vector-valued Wiener process,  $\mathbf{S} = (S_1, \dots, S_{n_\phi})$  is the chemical reaction source vector, and equation (4.21) is an equation of state that relates density to scalars. In the RW model, the spatial molecular diffusion is modeled by the terms in the particle position equation (4.19) with the molecular diffusivity  $\Gamma$ , and the effect of molecular diffusion is simply added to the turbulent diffusion through random walk.

The governing equations for the mean  $\tilde{\phi}_\alpha$  and variance  $\widetilde{\phi_\alpha'^2}$  based on the RW model can be obtained from the transported PDF equation in (4.14) as

$$\frac{\partial \bar{\rho} \tilde{\phi}_\alpha}{\partial t} + \nabla \cdot (\bar{\rho} \tilde{\mathbf{u}} \tilde{\phi}_\alpha) = \nabla \cdot [\bar{\rho} (\Gamma_t + \Gamma) \nabla \tilde{\phi}_\alpha] + \bar{\rho} \tilde{S}_\alpha, \quad (4.22)$$

$$\begin{aligned} \frac{\partial \bar{\rho} \widetilde{\phi_\alpha'^2}}{\partial t} + \nabla \cdot (\bar{\rho} \tilde{\mathbf{u}} \widetilde{\phi_\alpha'^2}) &= \nabla \cdot [\bar{\rho} (\Gamma_t + \Gamma) \nabla \widetilde{\phi_\alpha'^2}] - 2\bar{\rho} \Omega \widetilde{\phi_\alpha'^2} \\ &+ 2\bar{\rho} (\Gamma_t + \Gamma) \nabla \tilde{\phi}_\alpha \cdot \nabla \tilde{\phi}_\alpha + 2\bar{\rho} (\widetilde{\phi_\alpha S_\alpha} - \tilde{\phi}_\alpha \tilde{S}_\alpha). \end{aligned} \quad (4.23)$$

Comparing the transport equations (4.22) and (4.23) with those equations (4.4) and (4.5), we observe two major problems with the RW model.

1. First, equal diffusivity has to be assumed ( $\Gamma_\alpha = \Gamma$ ) and detailed molecular diffusion with differential diffusion effect cannot be considered.
2. Second, a spurious variance production ( $= 2\bar{\rho}\Gamma\nabla\tilde{\phi}_\alpha \cdot \nabla\tilde{\phi}_\alpha$ ) appears in the variance transport equation (4.23). The spurious variance production leads to an incorrect limiting behavior of the scalar variance at the limit of laminar flows with  $\Gamma_t = 0$  and  $\widetilde{\phi_\alpha'^2} = 0$ .

These two problems have been corrected in the MS model developed in [176], as discussed in the following Section 4.2.3.

### 4.2.3 Mean shift particle model for differential molecular diffusion

In the MS particle model developed by McDermott and Pope [176], the transported PDF equation (4.12) is modeled as

$$\begin{aligned} \frac{\partial \bar{\rho} \tilde{f}}{\partial t} + \nabla \cdot (\bar{\rho} \tilde{\mathbf{u}} \tilde{f}) + \sum_{\alpha} \frac{\partial}{\partial \psi_{\alpha}} \left[ \bar{\rho} S_{\alpha}(\Psi) \tilde{f} \right] &= \nabla \cdot (\bar{\rho} \Gamma_t \nabla \tilde{f}) \\ + \sum_{\alpha} \frac{\partial}{\partial \psi_{\alpha}} \left[ - \left( \nabla \cdot (\bar{\rho} \Gamma_{\alpha} \nabla \tilde{\phi}_{\alpha}) + \hat{C}_{\alpha} \right) \tilde{f} + \bar{\rho} \Omega (\psi_{\alpha} - \tilde{\phi}_{\alpha}) \tilde{f} \right], \end{aligned} \quad (4.24)$$

by using equations (4.7), (4.15), and (4.16) and the following equations or models,

$$\langle \nabla \cdot (\rho \Gamma_{\alpha} \nabla \phi_{\alpha}) | \Psi \rangle = \nabla \cdot (\bar{\rho} \Gamma_{\alpha} \nabla \tilde{\phi}_{\alpha}) + \langle \nabla \cdot (\rho \Gamma_{\alpha} \nabla \phi_{\alpha}'' ) | \Psi \rangle, \quad (4.25)$$

$$\langle C_{\alpha} | \Psi \rangle = \hat{C}_{\alpha} + \langle C_{\alpha} - \hat{C}_{\alpha} | \Psi \rangle \approx \hat{C}_{\alpha}, \quad (4.26)$$

$$- \sum_{\alpha} \frac{\partial}{\partial \psi_{\alpha}} \left[ \langle \nabla \cdot (\rho \Gamma_{\alpha} \nabla \phi_{\alpha}'' ) + C_{\alpha} - \hat{C}_{\alpha} | \Psi \rangle \tilde{f} \right] = \sum_{\alpha} \frac{\partial}{\partial \psi_{\alpha}} \left[ \bar{\rho} \Omega (\psi_{\alpha} - \tilde{\phi}_{\alpha}) \tilde{f} \right]. \quad (4.27)$$

The IEM model is used to close the micro-mixing term in equation (4.27) as in equation (4.18). It is noted that the micro-mixing terms in the PDF equations (4.14) and (4.24) are different, but are modeled with the same mixing model.

The SDEs corresponding to the closed PDF transport equation (4.24) with the MS model are written as [176],

$$d\mathbf{X}_p^*(t) = \left[ \tilde{\mathbf{u}} + \frac{\nabla (\bar{\rho} \Gamma_t)}{\bar{\rho}} \right]^* dt + \sqrt{(2\Gamma_t)^*} d\mathbf{W}, \quad (4.28)$$

$$d\phi_{\alpha,p}^*(t) = -\Omega^* (\phi_{\alpha,p}^* - \tilde{\phi}_{\alpha}^*) dt + \left[ \frac{\nabla \cdot (\bar{\rho} \Gamma_{\alpha} \nabla \tilde{\phi}_{\alpha}) + \hat{C}_{\alpha}}{\bar{\rho}} \right]^* dt + S_{\alpha}(\Phi_p^*) dt. \quad (4.29)$$

In this model, the spatial molecular diffusion is modeled by adding a mean shift term to the particle scalar equation (4.29) (the second term on the right-hand side of the equation).

The governing equations for the mean  $\tilde{\phi}_{\alpha}$  and variance  $\widetilde{\phi_{\alpha}''^2}$  based on the MS model can be obtained from the transported PDF equation (4.24). The equation for the mean  $\tilde{\phi}_{\alpha}$  is found to be the same as equation (4.4), while for the variance  $\widetilde{\phi_{\alpha}''^2}$ , the equation is

$$\frac{\partial \bar{\rho} \widetilde{\phi_{\alpha}''^2}}{\partial t} + \nabla \cdot (\bar{\rho} \tilde{\mathbf{u}} \widetilde{\phi_{\alpha}''^2}) = \nabla \cdot (\bar{\rho} \Gamma_t \nabla \widetilde{\phi_{\alpha}''^2}) - 2\bar{\rho} \Omega \widetilde{\phi_{\alpha}''^2} + 2\bar{\rho} \Gamma_t \nabla \tilde{\phi}_{\alpha} \cdot \nabla \tilde{\phi}_{\alpha} + 2\bar{\rho} (\widetilde{\phi_{\alpha} S_{\alpha}} - \tilde{\phi}_{\alpha} \tilde{S}_{\alpha}). \quad (4.30)$$

From the governing equations (4.4) and (4.30), we can see that the spatial differential molecular diffusion is correctly considered for the mean scalar transport in (4.4). The model also yields consistent limiting behavior for the variance equation (4.30) in laminar flows with  $\Gamma_t = 0$  and  $\widetilde{\phi_\alpha''^2} = 0$ , *i.e.*, no spurious variance production. The two problems encountered by using the RW model in Section 4.2.2 have been successfully resolved by employing the MS model. A new inconsistency, however, is observed in the variance equation (4.30) where the molecular diffusion term in the form of  $\nabla \cdot (\overline{\rho} \Gamma_\alpha \nabla \widetilde{\phi_\alpha''^2})$  is missing and only the turbulent diffusion term is found, when compared to equation (4.5). (More generally, the spatial molecular diffusion for the scalar covariance is also missing in the MS model [176].) This leads to an incorrect variance prediction for any problem of practical relevance (*i.e.*, non-zero variance), even though the MS model has a correct limiting behavior when the variance approaches zero. This inconsistency of the MS model in the variance transport motivated this work, and new models that are fully consistent for both the scalar mean and variance will be developed in Section 4.3.

#### 4.2.4 Boundedness preservation and correction algorithm

In combustion problems, the scalars  $\phi_\alpha$  represent the mass fractions of all chemical species which sum to one as shown in equation (4.2). Combing the fact that  $\phi_\alpha$  is non-negative, we see that all these scalars are bounded,  $\phi_\alpha \in [\phi_{\alpha,min}, \phi_{\alpha,max}]$  where  $\phi_{\alpha,min}$  and  $\phi_{\alpha,max}$  define the scalar bounds. Any scalar values outside of these bounds are not realizable. Preserving the scalar bounds of the particles is thus critically important to develop a realizable and robust molecular diffusion model for combustion. The RW model can be shown to preserve the boundedness of particles, while the MS model discussed in Section 4.2.3 cannot. To preserve the boundedness of particles in the MS model, a correction algorithm is needed. In this work, we are mainly concerned with individual boundedness and correction algorithms to preserve the individual boundedness. There are more concerns related to the realizability of the mean shift models, and the detailed discussions can be referenced in [176]. The scalar bounds  $[\phi_{\alpha,min}, \phi_{\alpha,max}]$  can be defined in different ways, *e.g.*, as a global

maximum and minimum in the whole domain or as fixed global limits  $[0, 1]$ . In this work, we adopt the global limits  $[0, 1]$  as a necessary condition for boundedness, which may not be sufficient to ensure other realizability issues such as joint boundedness [176].

McDermott and Pope [176] introduced a correction algorithm to force the lower limit of mixing frequency  $\Omega$  in the IEM model in equation (4.29) so that the boundedness is strictly preserved. We name this correction algorithm as the MP correction. (To be more precise, the MP algorithm is a boundedness violation avoidance algorithm by altering mixing frequency so that boundedness is preserved. For simplicity, we do not distinguish this subtle difference between a correction algorithm and an avoidance algorithm, and still call it a correction algorithm.) To illustrate the MP correction, we consider a non-reacting problem ( $\mathbf{S}(\Phi) = 0$ ). We march the particle scalar equation (4.29) in the MS model from time step  $t^n$  to  $t^{n+1}$  after a time-step size of  $\Delta t = t^{n+1} - t^n$ ,

$$\phi_{\alpha,p}^{*,n+1} = \phi_{\alpha,p}^{*,n} + c(\Delta t) \left( \tilde{\phi}_\alpha^n - \phi_{\alpha,p}^{*,n} \right) + \left[ \Delta \tilde{\phi}_\alpha(\Delta t) \right]^n, \quad (4.31)$$

where the superscript  $n$  denotes the time step,  $c(\Delta t) = 1 - \exp(-\Omega \Delta t)$  is called a decay-factor [176], and  $\Delta \tilde{\phi}_\alpha(\Delta t)$  is the mean shift defined as

$$\Delta \tilde{\phi}_\alpha(\Delta t) = \frac{\nabla \cdot (\bar{\rho} \Gamma_\alpha \nabla \tilde{\phi}_\alpha) + \hat{C}_\alpha}{\bar{\rho}} \Delta t. \quad (4.32)$$

A simple first-order fractional step scheme is used in equation (4.31) to advance equation (4.29) in time, and a spatially first-order implementation is used since both  $c(\Delta t)$  and  $\left[ \Delta \tilde{\phi}_\alpha \right]^n$  are the same for all the particles in the same grid cell. Second-order accuracy is challenging to achieve and is outside the scope of this work. The second term and third term on the right hand side of equation (4.31) represent the changes to the particles due to the IEM mixing term and the mean shift term, respectively, after a time step  $\Delta t$ . The MP correction limit the decay-factor  $c(\Delta t)$  by the following equation,

$$c(\Delta t) \geq \max_\alpha \left( \frac{\left[ \Delta \tilde{\phi}_\alpha(\Delta t) \right]^n}{\min_{p,x} (\phi_{\alpha,p}^{*,n}) - \tilde{\phi}_\alpha^n}, \frac{\left[ \Delta \tilde{\phi}_\alpha(\Delta t) \right]^n}{\max_{p,x} (\phi_{\alpha,p}^{*,n}) - \tilde{\phi}_\alpha^n} \right). \quad (4.33)$$

The outer operation of maximum in (4.33) is done over all the scalars  $\alpha$  in a grid cell, and the inner minimum/maximum is done over the particles in the whole computational

domain  $\mathbf{x}$ . This algorithm basically increases the mixing rate of the IEM model to prevent the boundedness violation caused by the MS model. This increased mixing by the MP correction is artificial and thus must be minimized. It will be shown later that the MP correction is sufficient to ensure boundedness but not necessary, and improved correction algorithms with reduced artificial mixing will be introduced.

To better understand the MP correction, we consider a case where the mean shift term in equation (4.33) is positive,  $[\Delta\tilde{\phi}_\alpha]^n > 0$ . In this case, only the upper bound of the particle scalar,  $\phi_{\alpha,max}$  can be potentially violated. The idea of the MP correction [176] is to preserve the upper bounds of particles by forcing the maximum particle scalar values at the new time step  $t^{n+1}$  not to exceed the old maximum values at  $t^n$ , *i.e.*,

$$\phi_{\alpha,p}^{*,n+1} \leq \max_{q,\mathbf{x}} \left( \phi_{\alpha,q}^{*,n} \right). \quad (4.34)$$

It is noted that, if we sort particles  $\phi_{\alpha,p}^{*,n}$  at  $t^n$  based on the  $\alpha$ th scalar, the sorted sequence remains unchanged for this scalar after the particle update in equation (4.31). As a result, in order to enforce equation (4.34) for all particles, we just need to ensure the particle that has the maximum scalar value to satisfy (4.34). This can be achieved from equation (4.31) by

$$[\Delta\tilde{\phi}_\alpha]^n \leq c(\Delta t) \left( \max_{p,\mathbf{x}} \left( \phi_{\alpha,p}^{*,n} \right) - \tilde{\phi}_\alpha^n \right). \quad (4.35)$$

A similar analysis can be done for the case of  $[\Delta\tilde{\phi}_\alpha]^n < 0$  to obtain

$$-[\Delta\tilde{\phi}_\alpha]^n \leq c(\Delta t) \left( \tilde{\phi}_\alpha^n - \min_{p,\mathbf{x}} \left( \phi_{\alpha,p}^{*,n} \right) \right). \quad (4.36)$$

Combining equations (4.35) and (4.36), we obtain the MP correction algorithm in equation (4.33).

There are a number of issues with the MP correction algorithm:

1. It can be seen from the above analysis that the enforcement of the boundedness by the MP correction is conservative and is not necessary although sufficient. With the MP correction, it can happen that an unnecessary correction is performed even if there is no boundedness violation, resulting in overcorrection. (Please see Appendix 4.5 for an illustration of the overcorrection issue with the MP correction algorithm);

2. The influence of the correction algorithm on the prediction accuracy of the scalar variance using the MS model is unknown;
3. The impact of the MP correction algorithm on the accuracy of the MS model is also unclear.
4. The MP correction is based on the fact that the particle update does not change the sorting sequence of particles which is true for the employed IEM model. The correction is not effective if a different mixing model is used such as MCurl or EMST.

In this work, the influence of the correction algorithms on the model performance will be thoroughly examined. New and improved correction algorithms will be developed. Extension to other mixing models will also be discussed. These new developments will be discussed in the following Section 4.3 along with the development of the new variance consistent mean shift (VCMS) models.

### 4.3 Variance consistent mean shift particle model for molecular diffusion

An improved MS model, the VCMS model, is targeted in this section to resolve the inconsistency in the variance transport observed in Section 4.2.3 while retaining all other positive features of the MS model [176]. To explore potential strategies for the improvement, we discuss the VCMS model for a single-scalar diffusion system first and then extend it to a multiple-scalar diffusion system.

#### 4.3.1 VCMS model for a single scalar diffusion system

We consider a single conserved independent scalar  $\xi$  which can find many applications such as the mixture fraction ( $n_\phi = 1$ ) defined in the flamelet models [53] or CMC [54] for turbulent non-premixed combustion or a mass fraction in a binary diffusion system ( $n_\phi = 2$ ). The governing equation for  $\xi$  is written as

$$\frac{\partial \rho \xi}{\partial t} + \nabla \cdot (\rho \mathbf{u} \xi) = \nabla \cdot (\rho \Gamma \nabla \xi). \quad (4.37)$$

We seek a fully consistent model for the particle scalar as follows,

$$d\xi_p^*(t) = -(\Omega + \omega)^* (\xi_p^* - \tilde{\xi}^*) dt + \left[ \frac{\nabla \cdot (\bar{\rho} \Gamma \nabla \tilde{\xi})}{\bar{\rho}} \right]^* dt, \quad (4.38)$$

with an added correction  $\omega$  to the mixing frequency  $\Omega$ , such that the particle scalar equation (4.38) along with the particle position equation (4.28) yield the following consistent scalar mean and variance transport equations,

$$\frac{\partial \bar{\rho} \tilde{\xi}}{\partial t} + \nabla \cdot (\bar{\rho} \tilde{\mathbf{u}} \tilde{\xi}) = \nabla \cdot [\bar{\rho} (\Gamma_t + \Gamma) \nabla \tilde{\xi}], \quad (4.39)$$

$$\frac{\partial \bar{\rho} \tilde{\xi}''^2}{\partial t} + \nabla \cdot (\bar{\rho} \tilde{\mathbf{u}} \tilde{\xi}''^2) = \nabla \cdot [\bar{\rho} (\Gamma_t + \Gamma) \nabla \tilde{\xi}''^2] - 2\bar{\rho} \Omega \tilde{\xi}''^2 + 2\bar{\rho} \Gamma_t \nabla \tilde{\xi} \cdot \nabla \tilde{\xi}. \quad (4.40)$$

In contrast to the missing molecular diffusion term in the scalar variance equation (4.30) with the MS model, the VCMS model in equation (4.38) is capable of yielding the correct diffusion terms in the variance equation (4.40) if an appropriate model for the mixing frequency correction  $\omega$  is provided. It can be shown that  $\omega$  needs to be specified as follows in order to yield the transport equations (4.39) and (4.40),

$$\omega = - \frac{\nabla \cdot (\bar{\rho} \Gamma \nabla \tilde{\xi}''^2)}{2\bar{\rho} \tilde{\xi}''^2}. \quad (4.41)$$

Different from  $\Omega$  which is always positive,  $\omega$  can be positive, negative, or zero. With the added  $\omega$  term in equation (4.38), the mean transport equation (4.39) is not altered when compared to the MS model. In the limit of laminar flows with  $\tilde{\xi}''^2 \rightarrow 0$ , there is no spurious production term in variance equation (4.40). The correct limiting behavior of the variance is thus preserved in the VCMS model. In summary, this single-scalar VCMS model successfully resolves the variance inconsistency issue in the MS model discussed in Section 4.2.3 while preserving other desired properties such as the mean conservation and consistent limiting variance behavior.

### 4.3.2 Boundedness correction for single-scalar VCMS model

Scalar values in reactive flows are usually bounded. For example, for a conserved scalar in a mixing layer problem, the values of the scalar are bounded by the boundary values.

Similar to the MS model in Section 4.2.3, the VCMS model for a single scalar system in Section 4.3.1 cannot guarantee scalar boundedness at the particle level because of the added mean shift term, and a correction algorithm is required for the VCMS model to work properly. It is noted that this boundedness issue occurs only at the particle level and does not impact the boundedness of the mean scalars. The MP correction [176] is able to preserve the bounds of  $\xi$  when used, but it causes overcorrection as shown in Section 4.2.4. In this work, we develop a few new correction algorithms and examine their performance in later sections.

To develop new correction algorithms for the single-scalar VCMS model, we march the particle scalar equation (4.38) in the VCMS model from time step  $t^n$  to  $t^{n+1}$ , following the same analysis as in Section 4.2.4,

$$\xi_p^{*,n+1} = \xi_p^{*,n} + c^+(\Delta t) \left( \tilde{\xi}^{*,n} - \xi_p^{*,n} \right) + \left[ \Delta \tilde{\xi}(\Delta t) \right]^n, \quad (4.42)$$

where  $c^+(\Delta t) = 1 - \exp[-(\Omega + \omega)\Delta t]$  is a modified decay-factor that includes the effect of  $\omega$ , and  $\Delta \tilde{\xi}(\Delta t) = \nabla \cdot (\bar{\rho} \Gamma \nabla \tilde{\xi}) \Delta t / \bar{\rho}$ .

### The MP correction for single-scalar VCMS model

As the particle update in equation (4.31) in the MS model, the particle update in equation (4.42) for the single-scalar VCMS model does not change the particle sequence in the scalar space. Thus we can use the same idea to develop the MP correction for the single-scalar VCMS model. The model can be written as, similar to the MP correction in the MS model in equation (4.33),

$$c^+(\Delta t) \geq \max \left( \frac{\left[ \Delta \tilde{\xi}(\Delta t) \right]^n}{\min_{p,x} (\xi_p^{*,n}) - \tilde{\xi}^n}, \frac{\left[ \Delta \tilde{\xi}(\Delta t) \right]^n}{\max_{p,x} (\xi_p^{*,n}) - \tilde{\xi}^n} \right), \quad (4.43)$$

where  $\left[ \min_{p,x} (\xi_p^{*,n}), \max_{p,x} (\xi_p^{*,n}) \right]$  are the minimum and maximum scalar particle values of  $\xi$  at  $t^n$  in the whole computation domain, which in some cases can be different from the global limits  $[\xi_{min}, \xi_{max}] = [0, 1]$ . The MP correction enforces that the maximum and

minimum scalar values of the particles at the  $n$ th time step are not exceeded after the particle time advancement in equation (4.42), which is unnecessary if only the global limits  $[0, 1]$  are of concern. Meanwhile, an unnecessary MP correction can occur even if there is no violation of boundedness. With the MP correction, the scalar mean is not affected, while the variance tends to be underpredicted. The MP correction works only for the IEM mixing model with the single-scalar VCMS model.

### Least decay-factor correction for single-scalar VCMS model

We seek a new correction algorithm that is similar to the MP correction in equation (4.43) by minimizing the correction to the modified decay-factor  $c^+$ , so that the correction is used only when there is boundedness violation. The updated particle scalars in equation (4.42), after a time step  $\Delta t$ , are required to be within the scalar bounds,  $\xi_{min} \leq \xi_p^{*,n+1} \leq \xi_{max}$ . As noted before in Section 4.2.4, the particle update step in equation (4.42) does not change the particle relative position in the scalar space. In another words, if the particles are sorted based on the values of  $\xi_p^{*,n}$  at time  $t^n$ , after one time step, the sorting sequence of the particles remain unchanged based on the values of  $\xi_p^{*,n+1}$  at time  $t^{n+1}$ . That means that if we can ensure the particles with values of  $\max_p(\xi_p^{*,n})$  and  $\min_p(\xi_p^{*,n})$  bounded at the new time, all other particle values will be bounded automatically. By using equation (4.42) for the particles with the maximum and minimum scalar values, we can readily obtain the following algorithm with the least decay-factor (LDF) correction,

$$c^+(\Delta t) \geq \max \left( \frac{\max_p(\xi_p^{*,n}) - \xi_{max} + [\Delta \tilde{\xi}(\Delta t)]^n}{\max_p(\xi_p^{*,n}) - \tilde{\xi}^n}, \frac{\min_p(\xi_p^{*,n}) - \xi_{min} + [\Delta \tilde{\xi}(\Delta t)]^n}{\min_p(\xi_p^{*,n}) - \tilde{\xi}^n} \right). \quad (4.44)$$

This ensures that  $\left[ \max_p(\xi_p^{*,n+1}) \leq \xi_{max} \right]$  and  $\left[ \min_p(\xi_p^{*,n+1}) \geq \xi_{min} \right]$  after the LDF correction. This LDF enforcement is different from the MP enforcement in equation (4.34), and hence represents a fundamental difference between LDF and MP corrections. The LDF correction is performed only when it is needed (e.g., when  $\max_p(\xi_p^{*,n+1}) > \xi_{max}$  occurs after the time advancement without correct), and hence alleviates the unnecessary correction

observed in the MP correction in Section 4.3.2, *i.e.*, the LDF correction is sufficient and necessary. Just like the MP correction, the LDF correction does not affect the mean scalar, while it is expected to improve the underprediction of the variance by the MP correction. The LDF correction works only for the IEM mixing model with the single-scalar VCMS model.

A common issue of the MP correction and the LDF correction is that when there is boundedness violation, the correction is done over all the particles in a grid cell even if the majority of particles are not in violation. This uniform correction strategy imposes significant constraint over new development of correction algorithms. We therefore relax the strategy and introduce non-uniform correction algorithms by performing correction only as needed for the particles in violation in the following Sections 4.3.2 and 4.3.2.

### Clipping at scalar bounds correction for single-scalar VCMS model

In non-uniform correction algorithms, we take a predictor-corrector approach. We first advance equation (4.42) to obtain the particle predictor as  $\xi_p^{*,\hat{n}} = \xi_p^{*,n} + c^+(\Delta t) \left( \tilde{\xi}^{*,n} - \xi_p^{*,n} \right) + [\Delta \tilde{\xi}(\Delta t)]^n$ , followed by a correction step for those particles that violate the scalar bounds, where the superscript  $\hat{n}$  denotes a predictor step. In this case, the correction serves as a postprocessing step. (Because of the postprocessing strategy, non-uniform correction algorithms are not limited to the IEM mixing model anymore.) A simple postprocessing correction is to clip particle scalars at the scalar bounds (CSB) for those violated particles,

$$\xi_p^{*,n+1} = \max \left[ \xi_{min}, \min \left( \xi_{max}, \xi_p^{*,\hat{n}} \right) \right]. \quad (4.45)$$

This is equivalent to the following requirement for the modified decay-factor of each particle

$$[c^+(\Delta t)]_p \geq \max \left( \left( \xi_p^{*,n} - \xi_{max} + [\Delta \tilde{\xi}(\Delta t)]^n \right) \cdot F \left( \xi_p^{*,n} - \tilde{\xi}^n \right), \right. \\ \left. - \left( \xi_p^{*,n} - \xi_{min} + [\Delta \tilde{\xi}(\Delta t)]^n \right) \cdot F \left( \tilde{\xi}^n - \xi_p^{*,n} \right) \right), \quad (4.46)$$

where the function  $F(y)$  is defined as

$$F(y) = \frac{1}{2} \left( \frac{1}{y} + \frac{1}{|y|} \right). \quad (4.47)$$

The CSB correction is non-uniform among all particles (because the modified decay-factor  $[c^+(\Delta t)]_p$  depends on the particle index in equation (4.46)) and only the decay-factors for those particles with boundedness violation are corrected. This correction is expected to be optimal, in some sense, to the particle system to ensure boundedness, which is desired. Its drawback is obvious — it does not conserve the scalar mean.

### Clipping with paired-mixing correction for single-scalar VCMS model

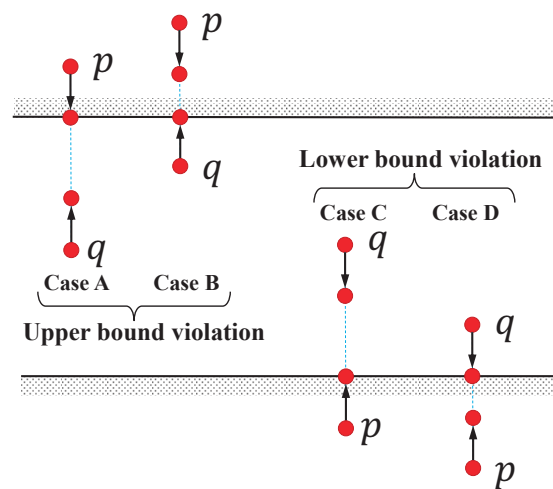


Figure 4.1. Illustration of the clipping with paired-mixing (CPM) correction algorithm

The clipping with paired-mixing (CPM) correction is an improved clipping by randomly selecting a paired particle from the same grid cell to compensate the clipping of the violated particle so that the particle scalar mean is conserved. The algorithm is illustrated in Figure 4.1. To correct a particle  $p$  that violates the scalar bound, if the paired particle  $q$  can compensate the clipping to ensure boundedness of both particles, particle  $p$  is moved to the scalar bound with particle  $q$  to compensate the move to conserve the scalar mean (Case A and Case C in Figure 4.1); Otherwise, particle  $q$  is moved to the scalar bound with particle  $p$  to compensate the move (Case B and Case D in Figure 4.1). In Case B and Case D, the

boundedness violation has not been fully resolved, and another paired-particle will be selected to continue the correction process. The CPM correction algorithm for single-scalar VCMS model is outlined below:

---

Step 1: advance particles in time in a grid cell to obtain a predictor  $\xi_p^{*,\hat{n}} = \xi_p^{*,n} + c^+(\Delta t) \left( \tilde{\xi}^{*,n} - \xi_p^{*,n} \right) + [\Delta \tilde{\xi}(\Delta t)]^n$ ;

Step 2: loop particles in the grid cell to find the first particle  $p$  that violates the scalar bound;

Step 3: find the scalar bound value  $B_a$  that is violated by the particle  $p$ , *i.e.*,  $B = \xi_{max}$  if the upper bound is violated, otherwise  $B = \xi_{min}$ .

Step 4: randomly select another particle  $q$  from the same grid cell that does not violate the same scalar bound as particle  $p$ ;

Step 5: compute the average of the two selected particles,  $\eta = \left( \xi_p^{*,\hat{n}} + \xi_q^{*,\hat{n}} \right) / 2$ ;

Step 6: compute a mixing parameter  $\theta$  as,

$$\theta = \min \left( \frac{B - \xi_p^{*,\hat{n}}}{\eta - \xi_p^{*,\hat{n}}}, \frac{B - \xi_q^{*,\hat{n}}}{\eta - \xi_q^{*,\hat{n}}} \right); \quad (4.48)$$

Step 7: correct the particles,  $\xi_p^{*,\hat{n}} = (1 - \theta) \cdot \xi_p^{*,\hat{n}} + \theta \cdot \eta$  and  $\xi_q^{*,\hat{n}} = (1 - \theta) \cdot \xi_q^{*,\hat{n}} + \theta \cdot \eta$ ;

Step 8: check if the boundedness of particle  $p$  is satisfied. If there is no violation, select the next particle  $p$  that violates the scalar bound, otherwise keep the current particle  $p$ , and go to Step 3.

Step 9: update the final particle scalars,  $\xi_p^{*,n+1} = \xi_p^{*,\hat{n}}$ .

---

Compared to the CSB correction in Section 4.3.2, the CPM correction here involves more particle mixing in order to conserve the scalar mean. The variance prediction by using the CPM correction is expected to be lower than the CSB correction. Both the CSB correction and the CPM correction are considered as non-uniform correction algorithms which

attempt to correct those particles with violation only. This correction strategy is expected to show improvement over the uniform correction algorithms: the MP correction in Section 4.3.2 and the LDF correction in Section 4.3.2. Another advantage of the non-uniform correction algorithms is that they can be incorporated with other mixing models such as MCurl and EMST, while MP and LDF, when combined with the single-scalar VCMS, can only be used with IEM.

In summary, four different boundedness correction algorithms are discussed in this section for the VCMS model for a single scalar system. These correction algorithms will be thoroughly examined in the later discussions in Section 4.4.

### 4.3.3 VCMS model for a multiple-scalar diffusion system

To develop the VCMS model for multiple scalars ( $n_\phi \geq 3$ ), we first try extending the VCMS model for a single scalar in Section 4.3.1. Such an extension, however, does not seem to be able to yield a fully consistent model even after several inconsistency corrections, as illustrated in Appendix 4.5. Thus we seek a different approach and in the following we introduce a systematic approach for developing a fully consistent VCMS model for multiple scalars.

We seek a model as follows with a general correction term  $\check{C}_{\alpha,p}$  added to equation (4.29) in the MS model,

$$d\phi_{\alpha,p}^*(t) = -\Omega^* \left( \phi_{\alpha,p}^* - \tilde{\phi}_\alpha^* \right) dt + \left[ \frac{\nabla \cdot \left( \bar{\rho} \Gamma_\alpha \nabla \tilde{\phi}_\alpha \right) + \hat{C}_\alpha}{\bar{\rho}} \right]^* dt + S_\alpha \left( \Phi_p^* \right) dt + \check{C}_{\alpha,p}^* dt. \quad (4.49)$$

This correction term  $\check{C}_{\alpha,p}$  (to be determined) is added such that the following three constraints are satisfied: (1) particle level consistency; (2) consistency for the mean scalar; (3) consistency for the variance scalar. These constraints can be expressed as the following equations,

$$\sum_\alpha \check{C}_{\alpha,p}^* = 0, \quad (4.50)$$

$$\widetilde{\check{C}}_\alpha = \frac{\sum_{p=1}^{n_p} m_p^* \check{C}_{\alpha,p}^*}{\sum_{p=1}^{n_p} m_p^*} = 0, \quad (4.51)$$

$$\widetilde{\phi}_\alpha \check{C}_\alpha = \frac{\sum_{p=1}^{n_p} m_p^* \phi_{\alpha,p}^* \check{C}_{\alpha,p}^*}{\sum_{p=1}^{n_p} m_p^*} = -\omega_\alpha \widetilde{\phi}_\alpha'^2. \quad (4.52)$$

Equation (4.50) is used to enforce the normalization condition at the particle level ( $\sum_\alpha \phi_{\alpha,p}^* = 1$ ), equation (4.51) is written so that the added correction  $\check{C}_{\alpha,p}^*$  does not affect the particle scalar mean, and equation(4.52) is added to account for the missing molecular diffusion term for the variance equation in the MS model with  $\omega_\alpha$  being the frequency correction defined similar to equation (4.41) for a single-scalar problem as

$$\omega_\alpha = -\frac{\nabla \cdot (\bar{\rho} \Gamma_\alpha \nabla \widetilde{\phi}_\alpha'^2)}{2\bar{\rho} \widetilde{\phi}_\alpha'^2}. \quad (4.53)$$

There are  $n_p$  constraints in equation (4.50) and  $n_\phi$  constraints in each of equations (4.51) and (4.52). In total, there are  $n_p + 2n_\phi$  constraints that can be used to determine the same number of unknowns.

We seek a linear model for the correction  $\check{C}_{\alpha,p}$  in equation (4.49) as follows with  $n_p + 2n_\phi$  unknowns,

$$\check{C}_{\alpha,p} = -\hat{\omega}_\alpha \phi_{\alpha,p} + b_\alpha + d_p, \quad (4.54)$$

where  $\hat{\omega}_\alpha$  is a modified mixing frequency correction,  $b_\alpha$  and  $d_p$  are model parameters. To be determined,  $\hat{\omega}_\alpha$  and  $b_\alpha$  are independent of the particle index  $p$ , and  $d_p$  is independent of the scalar index  $\alpha$ . By using equation (4.51), we can readily find that,

$$b_\alpha = \hat{\omega}_\alpha \tilde{\phi}_\alpha - \tilde{d}, \quad (4.55)$$

in which  $\tilde{d} = \sum_{p=1}^{n_p} m_p^* d_p^* / \sum_{p=1}^{n_p} m_p^*$ . Substituting equation (4.55) to the model in equation (4.54), we have

$$\check{C}_{\alpha,p} = -\hat{\omega}_\alpha (\phi_{\alpha,p} - \tilde{\phi}_\alpha) + (d_p - \tilde{d}). \quad (4.56)$$

Next, we use equation (4.56) in the constraint in equation (4.50) to find that

$$(d_p - \tilde{d}) = \frac{1}{n_\phi} \sum_\beta \hat{\omega}_\beta (\phi_{\beta,p} - \tilde{\phi}_\beta). \quad (4.57)$$

Substituting it into equation (4.56), we obtain a model for  $\check{C}_{\alpha,p}$  that has the unknown  $\hat{\omega}_\alpha$  only,

$$\check{C}_{\alpha,p} = -\hat{\omega}_\alpha (\phi_{\alpha,p} - \tilde{\phi}_\alpha) + \frac{1}{n_\phi} \sum_{\beta} \hat{\omega}_\beta (\phi_{\beta,p} - \tilde{\phi}_\beta). \quad (4.58)$$

Finally, by combining the constraints in (4.52) into equation (4.58), we get the set of linear equations that can be used to determine  $\hat{\omega}_\alpha$ ,

$$n_\phi \widetilde{\phi''^2}_\alpha \hat{\omega}_\alpha - \sum_{\beta} \widetilde{\phi''\phi''}_{\alpha\beta} \hat{\omega}_\beta = n_\phi \omega_\alpha \widetilde{\phi''^2}_\alpha. \quad (4.59)$$

This is a linear system and can be written as

$$\mathcal{A} \hat{\Omega} = \mathbf{B}, \quad (4.60)$$

with

$$\mathcal{A} = \begin{bmatrix} (n_\phi - 1) \widetilde{\phi''^2}_1 & -\widetilde{\phi''\phi''}_1 & \cdots & -\widetilde{\phi''\phi''}_{1n_\phi} \\ -\widetilde{\phi''\phi''}_1 & (n_\phi - 1) \widetilde{\phi''^2}_2 & \cdots & -\widetilde{\phi''\phi''}_{2n_\phi} \\ \cdots & \cdots & \cdots & \cdots \\ -\widetilde{\phi''\phi''}_{1n_\phi} & -\widetilde{\phi''\phi''}_{2n_\phi} & \cdots & (n_\phi - 1) \widetilde{\phi''^2}_{n_\phi} \end{bmatrix}, \quad \hat{\Omega} = \begin{bmatrix} \hat{\omega}_1 \\ \hat{\omega}_2 \\ \cdots \\ \hat{\omega}_{n_\phi} \end{bmatrix}, \quad \mathbf{B} = \begin{bmatrix} n_\phi \omega_1 \widetilde{\phi''^2}_1 \\ n_\phi \omega_2 \widetilde{\phi''^2}_2 \\ \cdots \\ n_\phi \omega_{n_\phi} \widetilde{\phi''^2}_{n_\phi} \end{bmatrix}. \quad (4.61)$$

By solving this linear system, we can obtain the vector  $\hat{\Omega}$ . We thus have a fully consistent VCMS model for multiple scalars by substituting  $\check{C}_{\alpha,p}$  in equation (4.58) into equation (4.49),

$$d\phi_{\alpha,p}^*(t) = -(\Omega + \hat{\omega}_\alpha)^* (\phi_{\alpha,p}^* - \tilde{\phi}_\alpha^*) dt + \frac{1}{n_\phi} \sum_{\beta} \hat{\omega}_\beta^* (\phi_{\beta,p}^* - \tilde{\phi}_\beta^*) + \left[ \frac{\nabla \cdot (\bar{\rho} \Gamma_\alpha \nabla \tilde{\phi}_\alpha) + \hat{C}_\alpha}{\bar{\rho}} \right]^* dt + S_\alpha (\Phi_p^*) dt, \quad (4.62)$$

with  $\hat{\omega}_\alpha$  determined by solving equation (4.60). The solution of  $\hat{\omega}_\alpha$  depends on all the scalars even if equal molecular diffusion is assumed. This unfortunately violates the linear principle of scalar transport in turbulence [176, 183]. The linear principle provides a constraint on model development. Its actual effect on the predictions of DMD here is difficult to measure because the linear principle can only be observed in the limit of equal diffusion. Hence, the violation of this principle will not be discussed further.

It is noted that the VCMS model in equation ((4.62)) cannot be used for a single-scalar case ( $n_\phi = 1$ ) since the normalization condition in (4.50) is not required for a single scalar. Thus the VCMS models for a single scalar in Section 4.3.1 and for multiple scalars here are different models for different cases with no overlap between them, *i.e.*, the single scalar VCMS model is not considered a special case of the multi-scalar VCMS model. In practice, both models are useful for combustion problems since a full set of governing equations for combustion consists of species mass fractions and energy. The species mass fractions can be modeled by using the multi-scalar VCMS model while the energy equation can be modeled by using the single-scalar VCMS model. The single-scalar VCMS model is also useful for binary diffusion problems and for combustion models where a single conserved scalar such as mixture fraction is considered [53, 54].

#### 4.3.4 Boundedness correction for multiple-scalar VCMS model

To develop boundedness correction algorithms for the multiple-scalar VCMS model, we consider a non-reacting case ( $S_\alpha = 0$ ) and advance the particle scalar equation (4.62) for the multi-scalar VCMS model from time step  $t^n$  to  $t^{n+1}$ , using the same scheme in equation (4.31),

$$\phi_{\alpha,p}^{*,n+1} = \phi_{\alpha,p}^{*,n} + c(\Delta t) \left( \tilde{\phi}_\alpha^n - \phi_{\alpha,p}^{*,n} \right) + \left[ \Delta \hat{\phi}_{\alpha,p}(\Delta t) \right]^n, \quad (4.63)$$

with a modified scalar shift term  $\left[ \Delta \hat{\phi}_{\alpha,p}(\Delta t) \right]^n$  defined as follows,

$$\left[ \Delta \hat{\phi}_{\alpha,p}(\Delta t) \right]^n = \hat{c}_\alpha(\Delta t) \left( \tilde{\phi}_\alpha^n - \phi_{\alpha,p}^{*,n} \right) - \frac{1}{n_\phi} \sum_\beta \hat{c}_\beta(\Delta t) \left( \tilde{\phi}_\beta^n - \phi_{\beta,p}^{*,n} \right) + \left[ \Delta \tilde{\phi}_\alpha(\Delta t) \right]^n, \quad (4.64)$$

where  $\hat{c}_\alpha(\Delta t) = 1 - \exp(-\hat{\omega}_\alpha \Delta t)$  is a decay-factor that is based on  $\hat{\omega}_\alpha$  defined in equation (4.59), and  $\Delta \tilde{\phi}_\alpha(\Delta t)$  is defined in equation (4.32). The numerical consistency and the first-order temporal accuracy of scheme (4.63) can be readily verified by performing a Taylor series analysis.

In terms of correction algorithms, a substantial difference between the multi-scalar VCMS model and the models discussed before (such as the MS model and single-scalar VCMS model) is that the multi-scalar VCMS model does not retain the sorting sequence of

particles after the particle update in equation (4.63) even the IEM is used, because of the summation term  $1/n_\phi \cdot \sum_\beta \hat{c}_\beta(\Delta t) \left( \tilde{\phi}_\beta^n - \phi_{\beta,p}^{*,n} \right)$  in equation (4.64). This summation term destroys the sorting sequence of particles and introduces additional challenges to the development of correction algorithms for the multi-scalar VCMS model.

### The MP correction for multi-scalar VCMS model

As discussed in Section 4.2.4, the MP correction in equation (4.33) is effective only if sorted particle sequence remains unchanged after the particle update. Thus it cannot be directly used for the multi-scalar VCMS model. The MP correction requires that the updated values of particle scalars do not exceed the extreme values before the update,  $\min_{q,x} \left( \phi_{\alpha,q}^{*,n} \right) \leq \phi_{\alpha,p}^{*,n+1} \leq \max_{q,x} \left( \phi_{\alpha,q}^{*,n} \right)$ . By using this requirement directly in equation (4.63), we can find a correction to the decay factor  $c$  to ensure scalar boundedness. Unfortunately, this correction can lead to  $c > 1$  for some cases, which contradicts the fact that  $c$  is always between  $[0, 1]$  since  $\Omega \geq 0$ , and also it cannot guarantee boundedness since there is an upper limit for  $c$  even if  $c > 1$  is allowed to ensure boundedness. Thus we have to seek a different approach. Here we take the advancement step in equation (4.63) as a predictor  $\phi_{\alpha,p}^{*,\hat{n}} = \phi_{\alpha,p}^{*,n} + c(\Delta t) \left( \tilde{\phi}_\alpha^n - \phi_{\alpha,p}^{*,n} \right) + \left[ \Delta \tilde{\phi}_{\alpha,p}(\Delta t) \right]^n$ , followed by a corrector step,

$$\phi_{\alpha,p}^{*,n+1} = \phi_{\alpha,p}^{*,\hat{n}} + \check{c} \left( \tilde{\phi}_\alpha^n + \left[ \Delta \tilde{\phi}_\alpha(\Delta t) \right]^n - \phi_{\alpha,p}^{*,\hat{n}} \right), \quad (4.65)$$

where  $\check{c}$  is a new decay-factor introduced for the boundedness correction, and  $\tilde{\phi}_\alpha^n + \left[ \Delta \tilde{\phi}_\alpha(\Delta t) \right]^n$  is the mean of the particle predictor  $\phi_{\alpha,p}^{*,\hat{n}}$ . The decay-factor  $\check{c}$  is determined by imposing the MP requirement to the results from equation (4.65) as

$$\min_{q,x} \left( \phi_{\alpha,q}^{*,n} \right) \leq \phi_{\alpha,p}^{*,\hat{n}} + \check{c} \left( \tilde{\phi}_\alpha^n + \left[ \Delta \tilde{\phi}_\alpha(\Delta t) \right]^n - \phi_{\alpha,p}^{*,\hat{n}} \right) \leq \max_{q,x} \left( \phi_{\alpha,q}^{*,n} \right), \quad (4.66)$$

which can be manipulated to yield the new MP correction for the multi-scalar VCMS model,

$$\check{c} \geq \max_{\alpha,p} \left( \left( \phi_{\alpha,p}^{*,\hat{n}} - \max_{q,x} \left( \phi_{\alpha,q}^{*,n} \right) \right) \cdot F \left( \phi_{\alpha,p}^{*,\hat{n}} - \tilde{\phi}_\alpha^n - \left[ \Delta \tilde{\phi}_\alpha(\Delta t) \right]^n \right), \right. \\ \left. - \left( \phi_{\alpha,p}^{*,\hat{n}} - \min_{q,x} \left( \phi_{\alpha,q}^{*,n} \right) \right) \cdot F \left( \tilde{\phi}_\alpha^n + \left[ \Delta \tilde{\phi}_\alpha(\Delta t) \right]^n - \phi_{\alpha,p}^{*,\hat{n}} \right) \right). \quad (4.67)$$

The maximum operation in equation (4.67) is done over all the species  $\alpha$  and all the particles  $p$ , which is different from the MP correction for the MS model in equation (4.33) and is more expensive to evaluate. With the minimum value of  $\check{c}$  obtained from equation (4.67), we can then formulate a single-step particle advancement, by substituting the particle predictor  $\phi_{\alpha,p}^{*,\hat{n}}$  into equation (4.65),

$$\phi_{\alpha,p}^{*,n+1} = \phi_{\alpha,p}^{*,n} + [1 - (1 - c(\Delta t)) \cdot (1 - \check{c})] \left( \tilde{\phi}_{\alpha}^n - \phi_{\alpha,p}^{*,n} \right) + (1 - \check{c}) \left[ \Delta \hat{\phi}_{\alpha,p}(\Delta t) \right]^n + \check{c} \left[ \Delta \tilde{\phi}_{\alpha}(\Delta t) \right]^n. \quad (4.68)$$

When  $\check{c} = 0$ , the time advancement in equation (4.68) is reduced to the original equation (4.63). The MP correction for the multi-scalar VCMS model enforces that the previous extreme values of each particle scalar are not exceeded after the modified particle update in equation (4.68). After the MP correction, the means of scalars are not affected, while the variances are reduced. It is worthwhile to mention that the MP correction for the multi-scalar VCMS model is quite different from the original MP correction for the MS model, although we name them the same because they are designed to achieve the same effect of preserving the scalar extremes of particles. One particularly noticeable difference is that the MP correction for the multi-scalar VCMS model can be used for other mixing models such as MCurl and EMST too because the correction is served as a post-processing step for the multi-scalar VCMS model.

### Least decay-factor for multi-scalar VCMS model

Following the idea of the LDF correction for the single-scalar VCMS model in Section 4.3.2, we restrict the least decay factor  $\check{c}$  in the multi-scalar VCMS model in equation (4.68) such that the updated scalars remain within scalar bounds,  $\phi_{\alpha,min} \leq \phi_{\alpha,p}^{*,n+1} \leq \phi_{\alpha,max}$ . The LDF correction algorithm can be readily obtained by replacing the scalar extreme values by the scalar bounds in equations (4.66) and (4.67) as

$$\check{c} \geq \max_{\alpha,p} \left( \left( \phi_{\alpha,p}^{*,\hat{n}} - \phi_{\alpha,max} \right) \cdot F \left( \phi_{\alpha,p}^{*,\hat{n}} - \tilde{\phi}_{\alpha}^n - \left[ \Delta \tilde{\phi}_{\alpha}(\Delta t) \right]^n \right), \right. \\ \left. - \left( \phi_{\alpha,p}^{*,\hat{n}} - \phi_{\alpha,min} \right) \cdot F \left( \tilde{\phi}_{\alpha}^n + \left[ \Delta \tilde{\phi}_{\alpha}(\Delta t) \right]^n - \phi_{\alpha,p}^{*,\hat{n}} \right) \right). \quad (4.69)$$

As noted before, the requirement for the LDF correction is less strict than that for the MP correction. The LDF correction also conserves scalar means of particles and reduces variance. Similar to MP for the multi-scalar VCMS model in Section 4.3.4, the LDF correction can be used for other mixing models other than the IEM model. Both the MP and LDF corrections for the multi-scalar VCMS model are done uniformly for all particles, *i.e.*, the same  $\check{c}$  is used for all the particles in the same grid cell. In the following, we further seek non-uniform boundedness correction algorithms for the multi-scalar VCMS model.

### Clipping at scalar bounds correction for multi-scalar VCMS model

To develop non-uniform correction algorithms for the multi-scalar VCMS model, we first advance equation (4.63) to obtain the predictor  $\phi_{\alpha,p}^{*,\hat{n}} = \phi_{\alpha,p}^{*,n} + c(\Delta t) \left( \tilde{\phi}_{\alpha}^n - \phi_{\alpha,p}^{*,n} \right) + \left[ \Delta \hat{\phi}_{\alpha,p}(\Delta t) \right]^n$ , and then perform CSB corrections for those particles that violate the scalar bounds, by using equation (4.65) with

$$[\check{c}]_p \geq \max_{\alpha} \left( \left( \phi_{\alpha,p}^{*,\hat{n}} - \phi_{\alpha,max} \right) \cdot F \left( \phi_{\alpha,p}^{*,\hat{n}} - \tilde{\phi}_{\alpha}^n - \left[ \Delta \tilde{\phi}_{\alpha}(\Delta t) \right]^n \right), \right. \\ \left. - \left( \phi_{\alpha,p}^{*,\hat{n}} - \phi_{\alpha,min} \right) \cdot F \left( \tilde{\phi}_{\alpha}^n + \left[ \Delta \tilde{\phi}_{\alpha}(\Delta t) \right]^n - \phi_{\alpha,p}^{*,\hat{n}} \right) \right). \quad (4.70)$$

The difference between equation (4.70) for the CSB correction and equation (4.69) for the LDF correction is that the operation maximum is done differently. In equation (4.69), it is done over all the particles in the same grid cell, while in equation (4.70), it is only for those particles that are in violation of the scalar bounds after the particle predictor step. Different values of the decay factor  $\check{c}$  are used in the CSB correction for different particles, resulting in non-uniform correction. While the CSB correction introduces least changes to particles, in some sense, the scalar means of particles are not conserved after the correction.

### Clipping with paired-mixing correction for multi-scalar VCMS model

Following the CPM correction for the single-scalar VCMS model in Section 4.3.2, we improve the CSB correction above by randomly selecting a paired particle to compensate the clipping of the corrected particle so that the particle scalar means are fully conserved.

The CPM correction for the single-scalar VCMS model in Section 4.3.2 can be modified for multiple scalars. A significant difference in the CPM correction for multiple scalars in comparison with the CPM correction for single scalar is that, for multiple scalars, a boundedness correction for one scalar of a particle can introduce new violations of boundedness of the other scalars for the same particle. Thus it is useful to track new violations after each correction to avoid too many looping of the particles, and we use a queue  $Q$  in the algorithm to efficiently track particles that need correction. The CPM correction algorithm for multi-scalar VCMS model is outlined below:

- 
- Step 1: advance particles in time in a grid cell to obtain a predictor  $\phi_{\alpha,p}^{*,\hat{n}} = \phi_{\alpha,p}^{*,n} + c(\Delta t) \left( \tilde{\phi}_{\alpha}^n - \phi_{\alpha,p}^{*,n} \right) + \left[ \Delta \hat{\phi}_{\alpha,p}(\Delta t) \right]^n$ ;
- Step 2: initialize a queue  $Q$ , and enter all boundedness violations, in terms of index pairs  $\{p, \alpha\}$ , to  $Q$ ;
- Step 3: dequeuer a particle  $\{p, \alpha\}$  from  $Q$ . If not successful, *i.e.*,  $Q$  is empty, go to Step 10. If the particle scalar  $\phi_{\alpha,p}^{*,\hat{n}}$  is within the scalar bounds, repeat this step.
- Step 4: find the  $\alpha$ th scalar bound value  $B_{\alpha}$  that is violated, *i.e.*,  $B_{\alpha} = \phi_{\alpha,max}$  if the upper bound is violated, otherwise  $B_{\alpha} = \phi_{\alpha,min}$ ;
- Step 5: randomly select another particle  $q$  from the same cell that does not violate the same scalar bound as particle  $p$  for the  $\alpha$ th scalar;
- Step 6: compute the average of the two selected particles,  $\eta_{\beta} = \left( \phi_{\beta,p}^{*,\hat{n}} + \phi_{\beta,q}^{*,\hat{n}} \right) / 2$  for all scalars  $\beta = 1, \dots, n_{\phi}$ ;
- Step 7: compute a mixing parameter  $\theta$  as, based on the  $\alpha$ th scalar,
- $$\theta = \min \left( \frac{B_{\alpha} - \phi_{\alpha,p}^{*,\hat{n}}}{\eta_{\alpha} - \phi_{\alpha,p}^{*,\hat{n}}}, \frac{B_{\alpha} - \phi_{\alpha,q}^{*,\hat{n}}}{\eta_{\alpha} - \phi_{\alpha,q}^{*,\hat{n}}} \right); \quad (4.71)$$
- Step 8: correct the particles,  $\phi_{\beta,p}^{*,\hat{n}} = (1 - \theta) \cdot \phi_{\beta,p}^{*,\hat{n}} + \theta \cdot \eta_{\beta}$  and  $\phi_{\beta,q}^{*,\hat{n}} = (1 - \theta) \cdot \phi_{\beta,q}^{*,\hat{n}} + \theta \cdot \eta_{\beta}$  for all scalars  $\beta = 1, \dots, n_{\phi}$ ;

Step 9: check the boundedness of particles  $p$  and  $q$  for all scalars. Enqueue new violations into  $Q$ , and go to Step 3;

Step 10: update the final particle scalars,  $\phi_{\alpha,p}^{*,n+1} = \phi_{\alpha,p}^{*,\hat{n}}$ , for all particles and all scalars.

---

In summary, four boundedness correction algorithms are discussed in Section 4.3.4 for the VCMS model for a multi-scalar system. These correction algorithms will be thoroughly examined in the later discussions along with the validation of the VCMS models.

The VCMS models for single-scalar systems and multi-scalar systems are developed in Section 4.3. These models preserve some of the positive attributes of the previous MS model (Section 4.2.3) such as yielding consistent DNS limits and capable of treating differential molecular diffusion, while they are able to archive full consistency for the variance transport that is missing from the MS model. Meanwhile, a series of new particle scalar boundedness correction algorithms are developed, including LDF, CSB, and CPM, which are intended to alleviate the overcorrection caused by the previous MP correction. These models and correction algorithms will be thoroughly examined and validated in the following Section 4.4.

#### **4.4 Examination and validation of variance consistent mean shift particle models**

The VCMS models and the boundedness correction algorithms developed in Section 4.3 are examined and validated in this section. Section 4.4.1 describes a turbulent mixing layer problem as the benchmark case for model validation, followed by detailed examinations of different cases in Sections 4.4.2-4.4.5. Section 4.4.6 examines the performance of the VCMS models when combined with the different mixing models. The computational cost of different models is briefly discussed in Section 4.4.7. The model performance under real turbulence conditions is evaluated in Section 4.4.8.

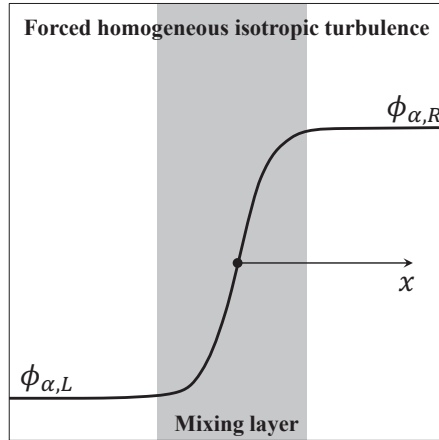


Figure 4.2. A turbulent mixing layer in forced homogeneous isotropic turbulence

#### 4.4.1 A turbulent mixing layer test case

We employ an inert constant density turbulent mixing layer problem [174] in forced homogeneous isotropic turbulence as illustrated in Figure 4.2 as the benchmark case for the model validation. From the RANS viewpoint, the mixing layer problem is statistically one dimensional and is transient, and hence a one-dimensional unsteady RANS simulation can be used for the modeling of the mixing layer problem. The specification of the mixing layer parameters can be determined following [174] and their current specifications are summarized in Table 4.1 for most of the simulations conducted in this work.

The turbulent Reynolds number  $Re_t$  in Table 4.1 is specified to be 100 which corresponds to a low Reynolds number condition in a typical mixing layer experiment [184]. The value of the turbulent mixing frequency  $\Omega$  in Table 4.1 corresponds to a velocity-to-scalar timescale ratio of  $C_\phi = 2\Omega k/\varepsilon \approx 0.01$ . This value of  $C_\phi$  is smaller than the value observed in shear flow problems (typically about 2.0) [185]. It is worthwhile to reiterate that the main purpose of the MS and VCMS models is for modeling the effect of molecular diffusion in turbulent flames which tends to diminish at high Reynolds numbers. Hence it is reasonable to assume a low Reynolds number condition in the test case to effectively isolate

the effect of molecular diffusion from other physics for a focused study of the mathematical consistency and convergence of the models. Additionally, a lowered mixing frequency is used in order to yield less physical mixing such that the errors in the transport of scalar variance can be effectively isolated from other source of errors such as grid discretization errors and statistical errors of the Monte Carlo particle method. The lowered mixing frequency causes the RMS of scalars to double approximately when compared to a typical experimental observation (*e.g.*, [184]). The model performance under real turbulence conditions will be examined in Section 4.4.8.

Table 4.1. Mixing layer parameters and their specifications

Mixing layer parameters	Parameter specification
Density $\bar{\rho}$	$\bar{\rho} = 1.0 \text{ kg/m}^3$
Kinematic viscosity $\nu$	$\nu = 1.6 \times 10^{-5} \text{ m}^2/\text{s}$
Turbulent kinetic energy $k$	$k = 1 \text{ m}^2/\text{s}^2$
Turbulent Reynolds number $Re_t$	$Re_t = 2k^2/(3\nu\epsilon) = 100$
Turbulent kinetic energy dissipation rate $\epsilon$	$\epsilon = 2k^2/(3\nu Re_t) = 416.67 \text{ m}^2/\text{s}^3$
Turbulent eddy viscosity $\nu_t$	$\nu_t = 0.09 \times k^2/\epsilon = 2.16 \times 10^{-4} \text{ m}^2/\text{s}$
Prandtl number $Pr$	$Pr = 0.7$
Turbulent Schmidt number $Sc_t$	$Sc_t = 0.9$
Molecular diffusivity $\Gamma_\alpha$	$\Gamma_\alpha = \nu/(Pr \cdot Le_\alpha)$
Turbulent diffusivity $\Gamma_t$	$\Gamma_t = \nu_t/Sc_t = 2.40 \times 10^{-4} \text{ m}^2/\text{s}$
Turbulent mixing frequency $\Omega$	$\Omega = 2.0 \text{ s}^{-1}$
Simulation end time $t_e$	$t_e = 3.125 \times 10^{-3} \text{ s}$
Thickness of turbulent mixing layer at time $t_e$ , $l_m$	$l_m = 2\sqrt{(\Gamma_t + \Gamma)(t_0 + t_e)} = 3.10 \times 10^{-3} \text{ m}$

Numerical results from both the finite volume (FV) method and the PDF particle method are sought. The FV results serve as the solution reference for the assessment of consistency and accuracy of the particle model results. The FV results can be obtained by solving the

mean and variance transport equations (4.4) and (4.5) directly (reduced to one-dimensional unsteady equations with the mean velocity  $\tilde{\mathbf{u}} = 0$  and the chemical reaction  $S_\alpha = 0$  for the current inert mixing layer). The initial conditions of the mean and variance of scalars at  $t = 0$  s are specified as follows

$$\tilde{\xi} = \frac{\tilde{\xi}_R - \tilde{\xi}_L}{2} \left[ 1 + \operatorname{erf} \left( \frac{x}{2\sqrt{(\Gamma_t + \Gamma) t_0}} \right) \right] + \tilde{\xi}_L, \quad (4.72)$$

$$\tilde{\xi}''^2 = 0.8 \times (\tilde{\xi} - \xi_{min}) (\xi_{max} - \tilde{\xi}), \quad (4.73)$$

$$\tilde{\phi}_\alpha = \frac{\tilde{\phi}_{\alpha,R} - \tilde{\phi}_{\alpha,L}}{2} \left[ 1 + \operatorname{erf} \left( \frac{x}{2\sqrt{(\Gamma_t + \Gamma_\alpha) t_0}} \right) \right] + \tilde{\phi}_{\alpha,L}, \quad (\alpha = 1, \dots, n_\phi - 1), \quad (4.74)$$

$$\tilde{\phi}_\alpha''^2 = 0.8 \times (\tilde{\phi}_\alpha - \phi_{\alpha,min}) (\phi_{\alpha,max} - \tilde{\phi}_\alpha), \quad (\alpha = 1, \dots, n_\phi - 1), \quad (4.75)$$

where equations (4.72) and (4.73) are for a single-scalar system and equations (4.74) and (4.75) are for a multi-scalar system, the subscripts ‘‘L’’ and ‘‘R’’ denote the left and right boundaries, respectively,  $\operatorname{erf}(\cdot)$  is the error function,  $t_0 = 2 \times 10^{-3}$  s is a reference time, and equations (4.73) and (4.75) specify the initial variance to be 80% of the maximum possible variance given that the scalars are bounded between  $[\xi_{min}, \xi_{max}]$  or  $[\phi_{\alpha,min}, \phi_{\alpha,max}]$ . The initial variance is non-zero only inside the mixing layer. For the multi-scalar case, the initial conditions for the first  $n_\phi - 1$  scalars are specified from equations (4.74) and (4.75), and the last scalar  $\phi_{n_\phi}$  is initialized by using equation (4.2). In the FV method, equations (4.4) and (4.5) are discretized by using a second-order accurate central difference scheme and a second-order time integration scheme. The computational domain is specified to be  $x \in [-5.6l_m, 5.6l_m]$ , where  $l_m$  is the thickness of the turbulent mixing layer at the end of the simulation time at  $t = t_e = 3.125 \times 10^{-3}$  s,  $l_m = 2\sqrt{(\Gamma_t + \Gamma)(t_0 + t_e)}$ . A uniform grid is used for the FV solution and 1000 grid cells are used to obtain adequate spatial accuracy, and the time step size is specified to be  $\Delta t = 3.125 \times 10^{-7}$  s for the FV method, corresponding to the CFL number about 0.12. These FV results with high grid resolution and small time step size are used as accurate references for the particle model results validation.

The PDF particle results are obtained by tracking an ensemble of particles initially distributed uniformly in the one-dimensional physical space in  $x$ . The particle scalars are initialized by using a presumed  $\beta$ -PDF independent for each scalar based on their mean and variance in equations (4.72) and (4.73) (or equations (4.74) and (4.75)). The same domain size as in the FV method is used in the particle method. A uniform grid of 400 cells and the time step size  $\Delta t = 3.125 \times 10^{-6}$  s are used for the particle method. Different numbers of particles per grid cell  $n_{pc}$  are used for the simulations, ranging from  $n_{pc} = 50$  to  $n_{pc} = 5000$ . The particles advance in time according to the SDEs for the different models, *e.g.*, equations (4.19) and (4.20) for the RW model in Section 4.2.2, by using a first-order accurate time advancement scheme. The mean and variance of scalars from the particle method are then calculated from the particles by using equation (4.13).

Multiple-trial PDF particle simulations of the mixing layer are conducted to reduce the statistical error [55] involved in the PDF statistical results. The numerical solutions from the fine-grid FV method are used to measure the statistical and bias errors involved in the particle method, as well as the model error. A local error for a quantity  $Y$  from the  $k$ th particle simulation trial is defined as

$$e_{Y,k}(\mathbf{x}, t) = Y_{PT,k}(\mathbf{x}, t) - Y_{FV}(\mathbf{x}, t), \quad (4.76)$$

where the subscripts ‘‘FV’’ and ‘‘PT’’ denote a result from the FV method and the PDF particle method, respectively. Given a finite number of particles and a finite number of realizations, the error  $e_{Y,k}$  is random. A bias-free estimate of the expectation of  $e_{Y,k}$ ,  $E_Y \approx \langle e_{Y,k} \rangle$ , and the standard deviation  $\sigma_Y$ , can be obtained from a total of  $n_t$  simulation trials as [186],

$$E_Y = \sqrt{\frac{n_t}{n_t - 1} \left( \langle e_{Y,k} \rangle_t^2 - \frac{1}{n_t} \langle e_{Y,k}^2 \rangle_t \right)}, \quad (4.77)$$

$$\sigma_Y = \sqrt{\frac{n_t}{n_t - 1} \left( \langle e_{Y,k}^2 \rangle_t - \langle e_{Y,k} \rangle_t^2 \right)}, \quad (4.78)$$

where  $\langle \cdot \rangle_t$  denotes the average of the results from different simulation trials,  $\langle \cdot \rangle_t = \sum_{i=1}^{n_t} (\cdot) / n_t$ . The 95% confidence interval for estimating  $E_Y$  can be then constructed as  $[E_Y - 1.96 \times \sigma_Y, E_Y + 1.96 \times \sigma_Y]$ .

#### 4.4.2 Single scalar without boundedness correction

We first consider a single-scalar mixing layer problem to validate the consistency of the VCMS model developed in Section 4.3.1. The boundedness of the scalar for particles is not enforced in this study, so that we can focus on the mathematical consistency of the VCMS model first. The effect of boundedness correction on the single-scalar VCMS model will be examined in Section 4.4.3. It is noted that although the particle scalar boundedness is not guaranteed, the scalar mean is bounded. Two previous models, the RW model in Section 4.2.2 and the MS model in Section 4.2.3, are also considered to show various consistency issues involved in those models and the advantages of using the new VCMS model. The RW model for the single-scalar mixing layer is obtained by solving the particle equations (4.19) and (4.20) with  $n_\phi = 1$  and  $S_\alpha = 0$ . The MS model is implemented by solving the particle equations (4.28) and (4.29) with  $n_\phi = 1$ ,  $S_\alpha = 0$ , and the conservation correction  $\hat{C}_\alpha = 0$ . For a single-scalar system, the normalization condition in equation (4.2) is not applicable, and hence the correction for conservation is removed ( $C_\alpha = 0$ ). In the VCMS model, the particle equations (4.28) and (4.38) are solved with the correction to the mixing frequency  $\omega$  determined from equation (4.41). The parameters of the single-scalar mixing layer test case are summarized in Table 4.1, and the Lewis number is specified to be  $Le = 0.1$  for the testing. The boundary conditions are specified to be  $[\tilde{\xi}_L, \tilde{\xi}_R] = [1, 0]$  in equation (4.72).

Figure 4.3 shows the simulation results of the scalar mean  $\tilde{\xi}$ , the scalar root mean square (RMS)  $\xi_{RMS} = \sqrt{\widetilde{\xi'^2}}$ , and their errors  $E_{\tilde{\xi}}$  and  $E_{\xi_{RMS}}$  (defined in equation (4.77)) against  $x/l_m$  at the end of the simulation time  $t = t_e$  in the single-scalar turbulent mixing layer. In the simulations, the number of particles per cell is specified to be  $n_{pc} = 5000$ , and  $n_t = 30$  simulation trials are performed to construct the 95% confidence intervals shown as the error bars in the figure. This large value of  $n_{pc} = 5000$  is purposely chosen to reduce the statistical and bias errors [55, 187, 188] involved in the simulations in order to isolate the errors involved in the different models from the numerical errors for a focused study of model errors. In practical applications, however, only a small number of particles per cell can be afforded (say  $n_{pc} \leq 100$ ), which can lead to significant statistical errors in evaluating

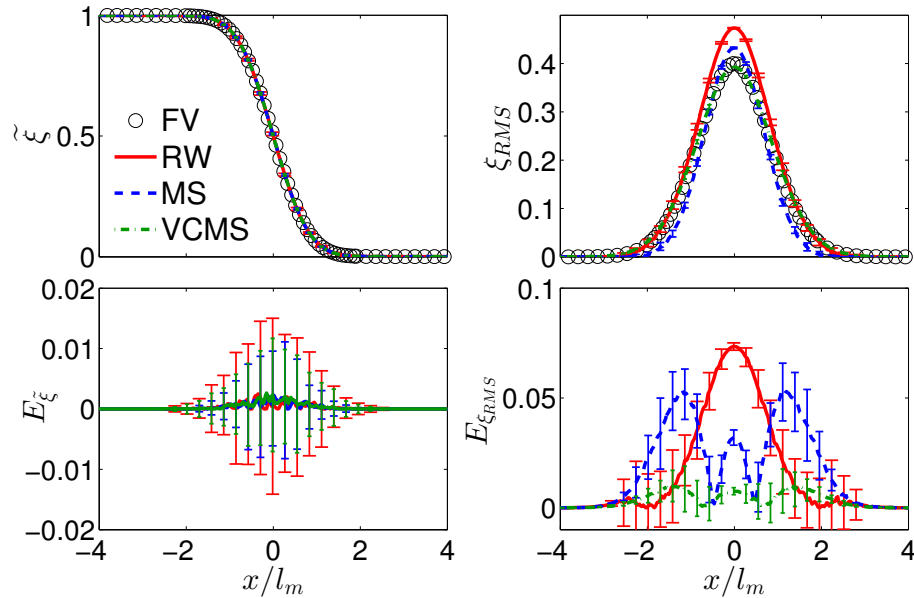


Figure 4.3. The profiles of the scalar mean  $\tilde{\xi}$ , the scalar RMS  $\xi_{RMS}$ , and their errors  $E_{\tilde{\xi}}$  and  $E_{\xi_{RMS}}$  against  $x/l_m$  in the single-scalar turbulent mixing layer with the RW, MS, and VCMS models (without boundedness correction). The error bars are the 95% confidence intervals estimated from multi-trial simulations.

the statistics from particles and the gradients of statistics (e.g., the examination of  $\omega$  in equation (4.41)). There exist several techniques to reduce the statistical errors such as time-averaging [189] and smoothing [177]. These techniques are not used here because of the large value of  $n_{pc}$ . From Figure 4.3, we can see that all three models (the RW, MS, and VCMS models) yield very similar results for the scalar mean  $\tilde{\xi}$  that are close to the reference FV results shown as circles. This is consistent with the fact that all three models yield identical conservation equations for  $\tilde{\xi}$ . The error  $E_{\tilde{\xi}}$  is relatively small from all three models, and the error bars for the results of the RW model appear to be slightly larger than the other two models. (The error bars for the different models can be distinguished by their cap size, e.g., the RW model results have the largest cap size for the error bars than the other two models.) The predictions of the scalar RMS  $\xi_{RMS}$  by the different models are significantly different. The scalar RMS predicted by the RW model appears to be consistently larger than the FV reference and this can be attributed to the spurious variance production in the

variance transport equation (4.23) from the RW model (see Section 4.2.2). The scalar RMS profile predicted by the MS model is steeper in gradient when compared to the FV reference, which is consistent with the missing molecular diffusion term for the variance transport equation (4.30) in the MS model (see Section 4.2.3). The RMS results from the VCMS model are in an excellent agreement with the FV results, indicating the consistency of the model for the predictions of variance. The errors for the scalar RMS predictions,  $E_{\xi_{RMS}}^{\xi}$ , are also shown in the figure. The magnitude of error in the MS model in predicting scalar RMS can reasonably justify the effort of developing the consistent VCMS models in this paper: (1) the error  $E_{\xi_{RMS}}^{\xi}$  by the MS model due to the missing variance molecular diffusion is only slightly lower than that by the RW model caused by a spurious production which has been treated as an important issue [176, 177]; (2) the relative error in predicting  $\xi_{RMS}$  is about 10% in Figure 4.3, which generally is viewed as non-negligible in applications; (3) the maximum error  $E_{\xi_{RMS}}^{\xi}$  is about 0.05 in Figure 4.3 which is comparable to the magnitude of differential molecular diffusion quantified by the RMS of difference in mixture fractions observed in DNS of flames [109].

Non-zero errors  $E_{\xi_{RMS}}^{\xi}$  are present in the results from all three models in Figure 4.3. In general, the errors  $E_{\xi_{RMS}}^{\xi}$  consist of two types of errors: the model consistency error and the numerical error (primarily the bias error [55, 187, 188] in the particle method). It is speculated that both model error and numerical error contribute to  $E_{\xi_{RMS}}^{\xi}$  in the RW and MS models, while no model error is present in the VCMS model. To confirm this speculation, we perform convergence analysis to identify the different types of errors involved in each model by varying the number of particles per cell from 50 to 5000 in the single-scalar mixing layer problem. The grid size and time step size have been purposely chosen to be small enough such that the numerical errors associated with the spatial and temporal discretization errors are negligible when compared to the bias error [55, 187, 188] associated with a finite number of particles per cell. In general, in the PDF particle method, the error  $E_Y$  in equation (4.77) can be modelled as [55, 188]

$$E_Y = \left| C_{e1} + \frac{C_{e2}}{n_{pc}} \right|, \quad (4.79)$$

where  $C_{e1}$  and  $C_{e2}$  are model constants, the first term  $C_{e1}$  denotes the combined model error and numerical error such as spatial discretization error that are independent of  $n_{pc}$ , and the second term  $C_{e2}/n_{pc}$  is the bias error involved in the particle method that is inversely proportional to  $n_{pc}$  [55, 187, 188]. When  $n_{pc} \rightarrow \infty$ , the error  $E_Y$  approaches  $|C_{e1}|$ . When a model is mathematically consistent,  $|C_{e1}| = 0$  is expected. By performing a convergence test by varying  $n_{pc}$ , we can estimate  $C_{e1}$  and  $C_{e2}$ , which enables us to examine if a model is consistent or not. In practical simulations,  $|C_{e1}|$  cannot reach zero even if a model is mathematically consistent because of the errors arising from the truncation errors due to spatial and temporal discretization. For the current PDF particle simulations, the errors due to the numerical truncation are estimated to be about  $E_{tr}(\tilde{\xi}) \sim \mathcal{O}(10^{-3})$  for the scalar mean and  $E_{tr}(\xi_{RMS}) \sim \mathcal{O}(10^{-4})$  for the scalar RMS, based on a numerical grid convergence study.

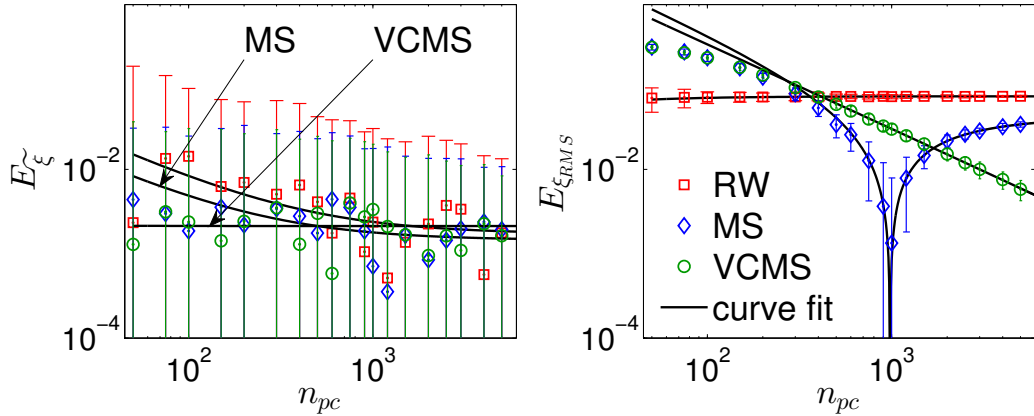


Figure 4.4. The convergence of the PDF particle prediction errors for the scalar mean  $E_{\tilde{\xi}}$  and RMS  $E_{\xi_{RMS}}$  at  $x/l_m = 0$  against  $n_{pc}$  in the single-scalar turbulent mixing layer with the RW, MS, and VCMS models (without boundedness correction). The error bars are the 95% confidence intervals estimated from multi-trial simulations. The solid lines are the curve fits by using the model equation (4.79).

The convergence of  $E_{\tilde{\xi}}$  and  $E_{\xi_{RMS}}$  based on the results at  $x/l_m = 0$  from the PDF modeling of the single-scalar mixing layer with the RW, MS, and VCMS models is shown in Figure 4.4, where the curve fits based on the model of error in equation (4.79) are also shown

as solid lines. For the current mixing layer test case, the bias errors involved in the scalar mean  $\tilde{\xi}$  are relatively small as can be seen in Figures 4.3 and 4.4, and the confidence intervals of estimating the errors is large. The values of errors  $|C_{e1}|$  corresponding to  $n_{pc} \rightarrow \infty$  based on equation (4.79) are tabulated in Table 4.2 for the different cases. From the table, we can see that the errors  $|C_{e1}|$  without boundedness correction are on the order of  $\mathcal{O}(10^{-3})$  which is the same as  $E_{tr}(\tilde{\xi}) \sim \mathcal{O}(10^{-3})$  mentioned above. This indicates that the errors in the predictions of the scalar mean by the three models (RW, MS, and VCMS) are free of model errors, which confirms that the three models are consistent for the predictions of the scalar mean. For the convergence of errors  $E_{\xi_{RMS}}$  in Figure 4.4, we can clearly see the different convergence behaviors. When  $n_{pc} \rightarrow \infty$ , the error  $E_{\xi_{RMS}}$  in the RW model approaches a non-zero constant  $|C_{e1}(\xi_{RMS})| \approx 7.4 \times 10^{-2}$  as shown in Table 4.2, which is much greater than  $E_{tr}(\xi_{RMS}) \sim \mathcal{O}(10^{-4})$ . The significant difference between  $|C_{e1}(\xi_{RMS})|$  and  $E_{tr}(\xi_{RMS})$  shows that the RW model involves a model error for the scalar RMS prediction, which is consistent with the spurious variance production in the RW model discussed in Section 4.2.2. Similarly, it is shown that the MS model is not convergent as well in terms of  $E_{\xi_{RMS}}$  with  $|C_{e1}(\xi_{RMS})| \approx 4.3 \times 10^{-2} \gg E_{tr}(\xi_{RMS})$  (see Table 4.2), which is also consistent with the missing molecular diffusion in the variance transport discussed in the MS model in Section 4.2.3. The new VCMS model introduced in this work, shows an evident convergence trend in Figure 4.4 with  $|C_{e1}(\xi_{RMS})| \approx 1.1 \times 10^{-4}$  (see Table 4.2) on the same order as  $E_{tr}(\xi_{RMS})$ , which implies that there is no model error in the VCMS model for variance prediction. This strongly supports the claim that the single-scalar VCMS model is consistent for both the scalar mean and the scalar RMS in Section 4.3.1.

In summary, we examined the accuracy and consistency of the three different PDF particle models (RW, MS, and VCMS) in a single-scalar turbulent mixing layer. The inconsistency in the RW and MS models for the scalar variance transport is clearly demonstrated through the convergence tests. The consistency of the VCMS model is also clearly shown from the convergence results. This confirms that the VCMS model introduced in this work resolves the inconsistency issue of the missing molecular diffusion in the variance transport

Table 4.2. The values of errors  $|C_{e1}|$  for  $\tilde{\xi}$  and  $\xi_{RMS}$  corresponding to  $n_{pc} \rightarrow \infty$  in equation (4.79) from the simulations of the single-scalar turbulent mixing layer with the different models (RW, MS, and VCMS) and the different boundedness correction algorithms at  $x/l_m = 0$  (or 0.6).

Model	Boundedness Correction Algorithm	$x/l_m$	$ C_{e1}(\tilde{\xi}) $	$ C_{e1}(\xi_{RMS}) $
RW		0	$1.7 \times 10^{-3}$	$7.4 \times 10^{-2}$
MS	w/o correction	0	$1.4 \times 10^{-3}$	$4.3 \times 10^{-2}$
VCMS	w/o correction	0	$2.1 \times 10^{-3}$	$1.1 \times 10^{-4}$
VCMS	MP	0	$1.3 \times 10^{-3}$	$2.1 \times 10^{-1}$
VCMS	LDF	0	$1.8 \times 10^{-3}$	$6.0 \times 10^{-2}$
VCMS	CSB	0.6	$1.2 \times 10^{-2}$	$1.2 \times 10^{-2}$
VCMS	CPM	0	$2.2 \times 10^{-3}$	$1.3 \times 10^{-2}$

while retaining other positive features of the MS model such as yielding a consistent DNS limit (*i.e.*, no spurious variance production that is observed in the RW model).

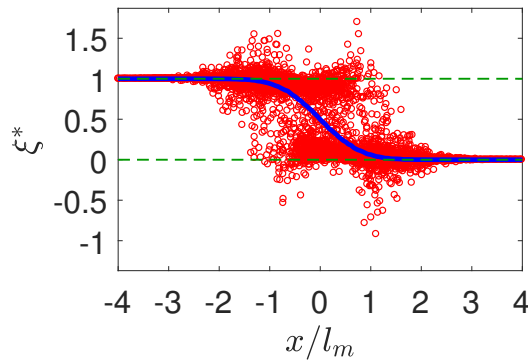


Figure 4.5. The particle scalar values  $\xi^*$  against  $x/l_m$  in the single-scalar turbulent mixing layer predicted by the VCMS model without boundedness correction. (Circles: the particle scalar values  $\xi^*$ ; solid line: the scalar mean  $\tilde{\xi}$ ; dashed lines: the scalar upper and lower bounds.)

Although the single-scalar VCMS model is shown to be consistent as shown above, the particle scalar bounds ( $[\xi_{min}, \xi_{max}] = [0, 1]$ ) are exceeded in the simulations. Figure 4.5

shows the particle scalar values  $\xi^*$  from the VCMS model (at time  $t = t_e$ ) to demonstrate the violation of the particle scalar bounds. To enforce the particle scalar bounds, a correction algorithm is needed. McDermott and Pope [176] has developed a correction algorithm (the MP correction in Section 4.2.4) for this purpose. The enforcement of particle scalar bounds potentially jeopardizes the accuracy and convergence of the VCMS model. The effect of applying the correction has not been examined before. The effect of using the MP correction and the new boundedness correction algorithms in Section 4.3.2 in the single-scalar VCMS model is examined in the following Section 4.4.3.

#### 4.4.3 Single scalar with boundedness correction

Simulations of the single-scalar turbulent mixing layer with the conditions the same as those in Figure 4.3 are performed by using the VCMS model with the four different boundedness correction algorithms in Section 4.3.2 (MP, LDF, CSB, and CPM). The particle scalar values  $\xi^*$ , after employing the different boundedness correction algorithms, are shown in Figure 4.6. All four correction algorithms are able to enforce the particle scalar bounds effectively. Meanwhile, the impact of employing the different correction algorithms on the distribution of particle scalars is different. The MP and LDF correction algorithms yield much more changes to the particle scalars than CSB and CPM, in comparison with the results without correction in Figure 4.5. The aforementioned overcorrection by the MP algorithm [176] in Section 4.3.2 is clearly seen. The new correction algorithms developed in this work alleviate the overcorrection by the MP correction to different degrees. The correction to the particles potentially compromises the accuracy and convergence of the VCMS model. Thus it is desired to have minimum correction to the particles while enforcing particle scalar bounds.

The effect of the boundedness correction algorithms on the accuracy of the model for the single scalar turbulent mixing layer is examined in Figure 4.7. The correction algorithms MP, LDF, and CPM have no effect on the predictions of the scalar mean since they all conserve scalar mean as discussed in Section 4.3.2. The CSB correction yields slightly

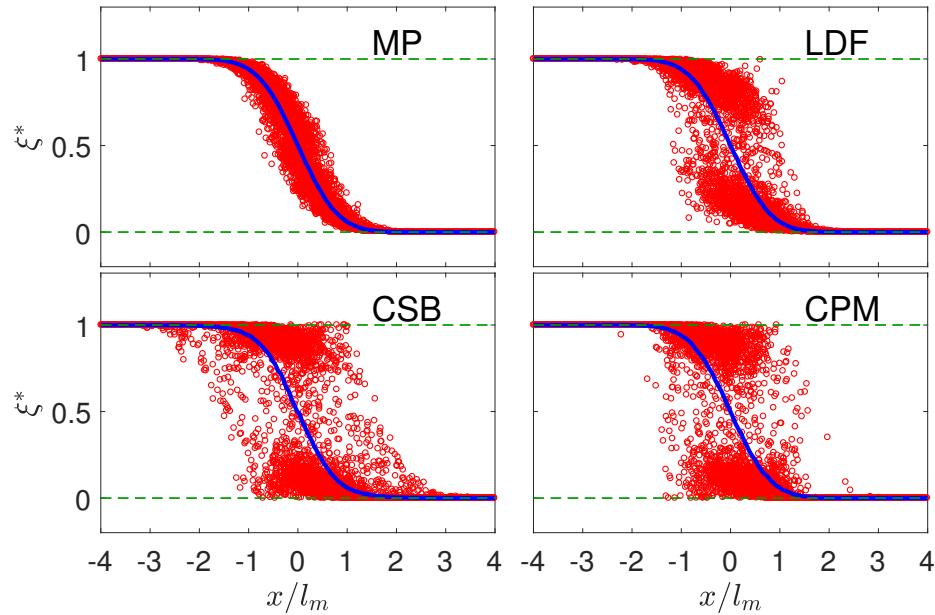


Figure 4.6. The particle scalar values  $\xi^*$  against  $x/l_m$  in the single-scalar turbulent mixing layer predicted by the VCMS model with the four different boundedness correction algorithms, MP, LDF, CSB, and CPM. (Circles: the particle scalar values  $\xi^*$ ; solid line: the scalar mean  $\xi$ ; dashed lines: the scalar upper and lower bounds.)

larger error  $E_{\xi}$  in Figure 4.7 because the CSB correction does not conserve the scalar mean as discussed in Section 4.3.2. All the correction algorithms tend to underpredict the scalar RMS  $\xi_{RMS}$  because of the increased mixing introduced by the correction algorithms, and this level of underprediction by the different correction algorithms is different as shown in Figures 4.6 and 4.7. The MP correction causes severe underprediction of  $\xi_{RMS}$  for the mixing layer as shown in Figure 4.7, and reduces  $\xi_{RMS}$  by about 56% in comparison with the results without boundedness correction in Figure 4.3. The LDF correction has some improvement over the MP correction, and reduces  $\xi_{RMS}$  by about 25% after the correction is introduced. The CSB and CPM perform similarly for the predictions of  $\xi_{RMS}$  and reduce  $\xi_{RMS}$  by about only 10% in comparison with the uncorrected results. Overall, the non-uniform correction algorithms (CSB and CPM) are superior over the uniform correction (MP and LDF) and result in less underprediction of  $\xi_{RMS}$ . The CPM correction performs

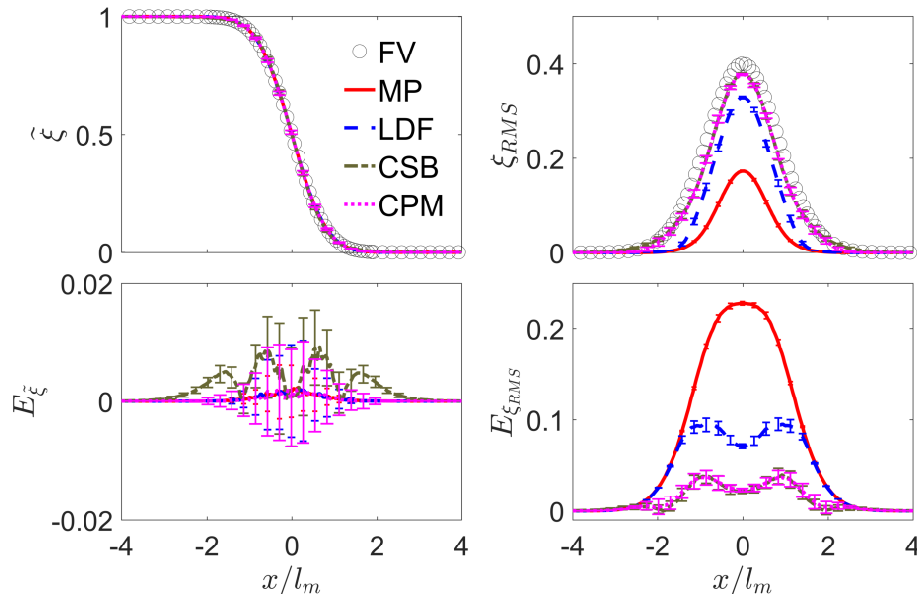


Figure 4.7. The profiles of the scalar mean  $\tilde{\xi}$ , the scalar RMS  $\xi_{RMS}$ , and their errors  $E_{\tilde{\xi}}$  and  $E_{\xi_{RMS}}$  against  $x/l_m$  in the single-scalar turbulent mixing layer with the VCMS model and the four different boundedness correction algorithms (MP, LDF, CSB, and CPM). The error bars are the 95% confidence intervals estimated from multi-trial simulations.

best in terms of conserving the scalar mean and yielding less underprediction of  $\xi_{RMS}$  while preserving the particle scalar bounds.

The MP, LDF, and CPM correction algorithms are mathematically consistent in the predictions of the scalar mean in the single-scalar VCMS model as confirmed by the obtained error values  $\left|C_{e1}(\tilde{\xi})\right| \approx 1 \times 10^{-3}$  shown in Table 4.2. The convergence of  $E_{\tilde{\xi}}$  by these correction algorithms is very close to that without boundedness correction in Figure 4.4 (results are not shown). The CSB correction, however, affects the scalar mean due to the lack of the conservation of the scalar mean. The convergence of  $E_{\tilde{\xi}}$  at  $x/l_m = 0.6$  in the turbulent mixing layer with the CSB correction is shown in Figure 4.8. The location of  $x/l_m = 0.6$  is near the location of maximum error  $E_{\tilde{\xi}}$  observed in Figure 4.7. Obviously, the results do not show a convergent behavior. The level of the particle-number-independent error  $\left|C_{e1}(\tilde{\xi})\right| \approx 1.2 \times 10^{-2}$  (see Table 4.2) from the CSB correction with the VCMS

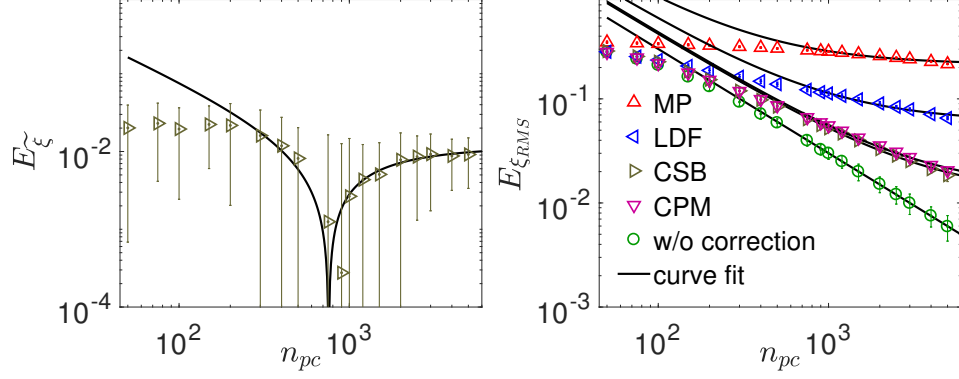


Figure 4.8. The convergence of the PDF particle prediction errors for the scalar mean  $E_{\tilde{\xi}}$  and RMS  $E_{\xi_{RMS}}$  at  $x/l_m = 0$  against  $n_{pc}$  in the single-scalar turbulent mixing layer with the VCMS model and the different correction algorithms (MP, LDF, CSB, and CMP). The error bars are the 95% confidence intervals estimated from multi-trial simulations. The solid lines are the curve fits by using the model equation (4.79). The errors are evaluated at the mixing layer center  $x/l_m = 0$  except  $E_{\tilde{\xi}}$  with the CSB correction which is evaluated at  $x/l_m = 0.6$  (for  $E_{\tilde{\xi}}$ , only the results from CSB are shown).

model (at  $x/l_m = 0.6$ ) is much greater than  $E_{tr}(\tilde{\xi}) \sim \mathcal{O}(10^{-3})$ , indicating that CSB is an inconsistent correction algorithm for the scalar mean.

Figure 4.8 also examines the effect of applying the boundedness correction algorithms to the single-scalar VCMS model on the convergence of  $E_{\xi_{RMS}}$  in the turbulent mixing layer. Without correction, the error  $E_{\xi_{RMS}}$  (circles in Figure 4.8, also shown in Figure 4.4) exhibits evident convergence with the scaling as  $n_{pc}^{-1}$ . After applying the different particle boundedness correction algorithms, we can see that the errors  $E_{\xi_{RMS}}$  deviate from the results without correction. The deviation is different for the different correction algorithms, with the MP correction having the most deviation, the LDF the next, and CSB and CPM the least deviation. This deviation implies that the consistency of the single-scalar VCMS model has been compromised and a model error has been introduced. The model errors  $|C_{e1}(\xi_{RMS})|$  estimated from the model fits in equation (4.79) are  $2.1 \times 10^{-1}$ ,  $6.0 \times 10^{-2}$ ,  $1.2 \times 10^{-2}$ , and  $1.3 \times 10^{-2}$  for MP, LDF, CSB, and CMP, respectively, as shown in Table 4.2. The new correction algorithms introduced in this work (LDF, CSB, and CMP) perform much better

than the MP correction developed before, especially the non-uniform corrections (CSB and CMP).

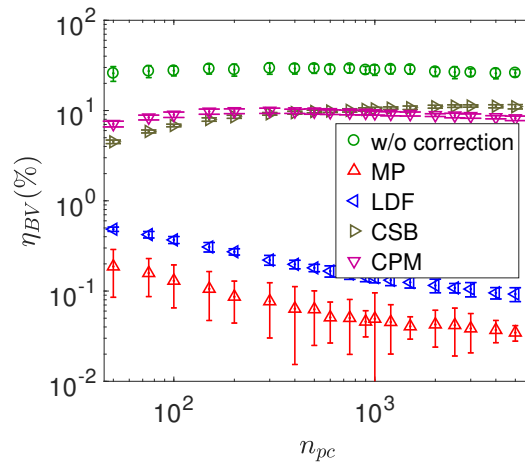


Figure 4.9. The percentage  $\eta_{BV}$  of the number of particles that violate the scalar bounds among the total number of particles used in the simulations of the single-scalar turbulent mixing layer by using the VCMS model and with or without boundedness correction. The error bars are the 95% confidence intervals estimated from multi-trial simulations.

To gain more insights into the role of the correction algorithms, we track the total number of violations of particle scalar bounds in the whole simulations of the single-scalar turbulent mixing layer from  $t = 0$  to  $t = t_e$ , and calculate the percentage,  $\eta_{BV}$ , of particles with scalar bounds violation among the total number of particles. The variations  $\eta_{BV}$  against  $n_{pc}$  with the different correction algorithms and without correction are shown in Figure 4.9. For the current employed test case with the single-scalar VCMS model without correction,  $\eta_{BV}$  (circles in Figure 4.9) is approximately 25% and this value is approximately constant when  $n_{pc}$  is changed. This implies that the violation of particle scalar bounds does not disappear at the limit of  $n_{pc} \rightarrow \infty$ , and at the limit, the correction algorithms employed in this work cannot yield the right convergence limit. Nevertheless, the correction algorithms are necessary to ensure realizability of particle scalars for reactive flow simulations. Expectedly, the correction algorithms can reduce the number of particle boundedness violations. The CSB and CMP correction algorithms reduce the values of  $\eta_{BV}$  to about 10%, and the MP and

LDF correction algorithms reduce the values of  $\eta_{BV}$  below 1%. The significant reduction of  $\eta_{BV}$  by the MP and LDF correction algorithms is consistent with their aggressive correction shown in Figures 4.6, 4.7, and 4.8.

In summary, we examined the effect of the different boundedness correction algorithms on the accuracy and convergence of the single-scalar VCMS model. The different correction algorithms do not affect the convergence of the scalar mean, except the CSB correction. The convergence of the VCMS model for the scalar RMS, however, is compromised by the correction algorithms. The performance of the different correction algorithms (MP, LDF, CSB, and CPM) is compared in detail. The MP correction is found to be too aggressive and reduces the scalar RMS and  $\eta_{BV}$  significantly, while newly introduced correction algorithms are found to improve the results to various degrees. Among the four correction algorithms, CPM is found to perform the best overall. A single-scalar system is considered so far to validate the single-scalar VCMS model and the corresponding boundedness correction algorithms. In the following Sections 4.4.4 and 4.4.5, a multi-scalar system is considered to validate the multi-scalar VCMS model and the correction algorithms.

#### 4.4.4 Multiple scalars without boundedness correction

A turbulent mixing layer with  $n_\phi = 4$  scalars is considered here to examine and validate the multi-scalar VCMS model developed in Section 4.3.3. The boundedness of the particle scalars is not enforced here and the focus is put on the mathematical consistency of the multi-scalar VCMS model. The effect of boundedness correction for the multi-scalar VCMS model will be investigated in the next Section 4.4.5. The RW and MS models are also considered here for comparison. The parameters of the multi-scalar mixing layer test case are summarized in Table 4.1, and the Lewis numbers  $Le_\alpha$  are specified to be [0.1, 0.2, 1, 5] for the four scalars in the testing. These Lewis numbers are chosen to represent typical combustion problems where the Lewis number is typically found to be between 0.1 and 5. It is noted that the current models are applicable to any Lewis number. The boundary conditions are specified to be  $\tilde{\Phi}_L = [0, 0.2, 0.2, 0.6]$  and  $\tilde{\Phi}_R = [0.1, 0, 0.1, 0.8]$  in equation

(4.74). The RW model for the multi-scalar mixing layer is obtained by solving the particle equations (4.19) and (4.20) with  $S_\alpha = 0$  (no chemical reaction). The RW model is unable to treat different Lewis numbers, and hence the assumption of  $Le_\alpha = 1$  has to be introduced in the RW model for the multi-scalar mixing layer test case. The MS model is implemented by solving the particle equations (4.28) and (4.29) with  $S_\alpha = 0$ . For the multi-scalar system, the normalization condition in equation (4.2) is enforced through the conservation correction  $\hat{C}_\alpha$  in equation (4.29). In the VCMS model, the particle equations (4.28) and (4.62) are solved with the modified mixing frequency correction  $\hat{\omega}_\alpha$  determined by solving equation (4.60).

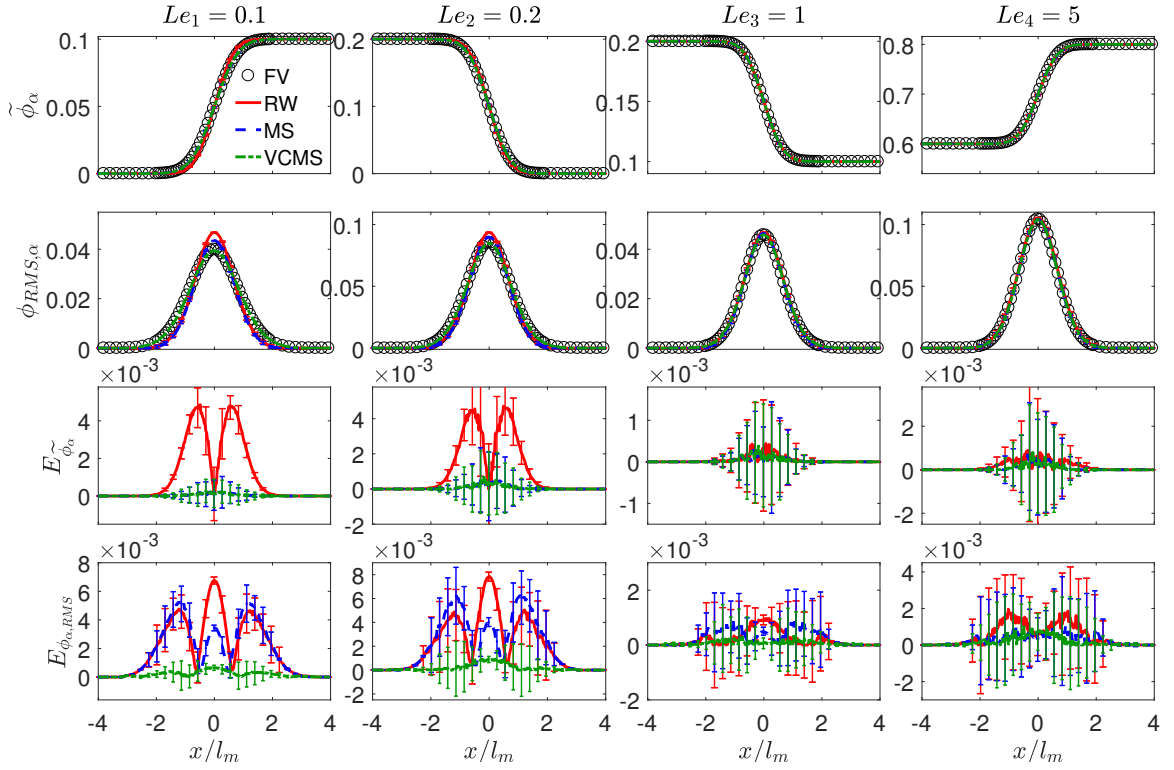


Figure 4.10. The profiles of the scalar mean  $\tilde{\Phi}$  (vector), the scalar RMS  $\Phi_{RMS}$ , and their errors  $E_{\tilde{\Phi}}$  and  $E_{\Phi_{RMS}}$  against  $x/l_m$  for the different scalars in the multi-scalar turbulent mixing layer with the RW, MS, and VCMS models (without boundedness correction). The error bars are the 95% confidence intervals estimated from multi-trial simulations.

Figure 4.10 shows the simulation results of the mean  $\tilde{\Phi}$ , the RMS  $\Phi_{RMS}$ , and their errors  $E_{\tilde{\Phi}}$  and  $E_{\Phi_{RMS}}$  (defined in equation (4.77)) against  $x/l_m$  at the end of the simulation time  $t = t_e$  for the four scalars in the multi-scalar turbulent mixing layer. In the simulations, the number of particles per cell is specified to be  $n_{pc} = 5000$ , and  $n_t = 30$  simulation trials are performed to construct the 95% confidence intervals shown as the error bars in the figure. For the predictions of  $\tilde{\Phi}$  in the figure, we can see that the RW model results are in some deviation from the FV reference results, while both MS and VCMS model results are in good agreement with the FV results. The errors  $E_{\tilde{\Phi}}$  with the RW model are substantially larger than the results with MS and VCMS, especially for the scalars with the smaller Lewis number. This significant error in the RW model is caused by the assumption of  $Le_\alpha = 1$  in the RW model. Both MS and VCMS models predict differential molecular diffusion accurately in terms of the mean scalars in the multi-scalar turbulent mixing layer. For the predictions of  $\Phi_{RMS}$ , the RW model also yields significant deviation from the FV results and relatively large errors  $E_{\Phi_{RMS}}$  as shown in Figure 4.10. This level of errors in the RW model consists of two sources of model errors: one from the assumption of unity Lewis numbers and the other from the spurious variance production discussed in Section 4.2.2. The MS model also yields relatively large errors for the predictions of  $\Phi_{RMS}$ , and the errors are expectedly caused by the inconsistency of the model due to the missing molecular diffusion effect in the variance equation (4.30) (see Section 4.2.3). The newly developed multi-scalar VCMS model yields the results of  $\Phi_{RMS}$  in excellent agreement with the FV results with the relative errors much smaller than those from the RW and MS models. This supports the fact that the multi-scalar VCMS model is fully consistent for the scalar mean and RMS, as discussed in Section 4.3.3.

Convergence tests are performed by varying the number of particles per cell from 50 to 5000 in the multi-scalar mixing layer problem to examine the convergence of the different models. Figure 4.11 shows the convergence of  $E_{\tilde{\Phi}}$  and  $E_{\Phi_{RMS}}$  from the PDF modeling of the multi-scalar mixing layer with the RW, MS, and VCMS models. The results from the mixing layer center at  $x/l_m = 0$  are shown for most of the results except  $E_{\tilde{\Phi}}$  with the RW model at  $x/l_m = 0.6$ . The error  $E_{\tilde{\Phi}}$  with the RW model reaches maximum approxi-

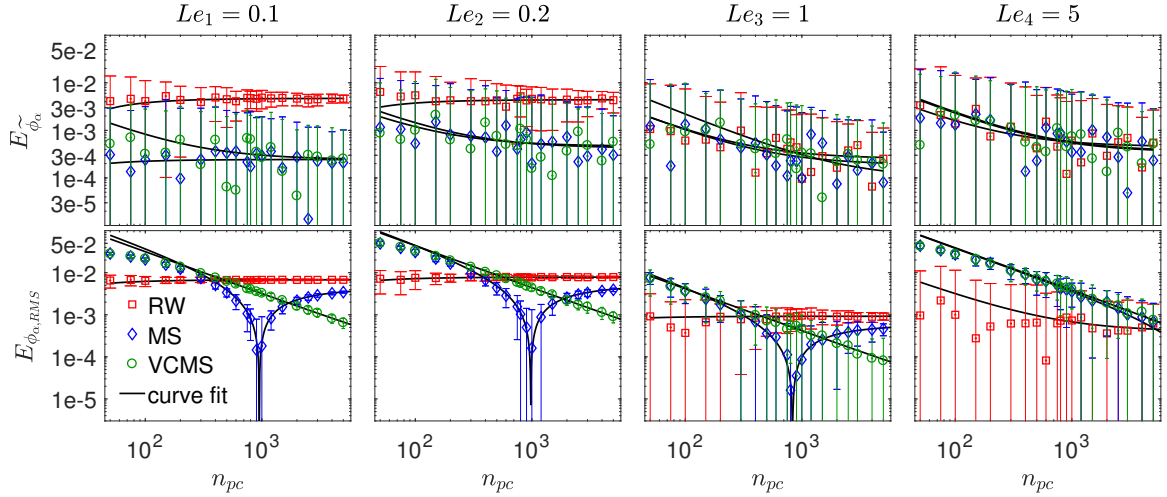


Figure 4.11. The convergence of the PDF particle prediction errors for the mean  $E_{\tilde{\Phi}}$  and RMS  $E_{\Phi_{RMS}}$  against  $n_{pc}$  for the different scalars in the multi-scalar turbulent mixing layer with the RW, MS, and VCMS models (without boundedness correction). The error bars are the 95% confidence intervals estimated from multi-trial simulations. The solid lines are the curve fits by using the model equation (4.79). The errors are evaluated at the mixing layer center  $x/l_m = 0$  except  $E_{\tilde{\Phi}}$  with the RW model which is evaluated at  $x/l_m = 0.6$ .

mately at  $x/l_m = 0.6$  as shown in Figure 4.10. The errors  $\left| C_{e1}(\Phi_{RMS}) \right|$  estimated from the model in equation (4.79) are tabulated in Table 4.3 for the multi-scalar mixing layer. For the convergence results of  $E_{\tilde{\Phi}}$  in Figure 4.11, we can clearly see the non-convergent behavior of the RW model. For the MS and VCMS model models, although the convergence is not clear either, but the estimated errors  $\left| C_{e1}(\tilde{\Phi}) \right|$  which are independent of  $n_{pc}$  in equation (4.79) are much less than those from the RW model, as shown in Table 4.3. This suggests that  $E_{\tilde{\Phi}}$  from the MS and VCMS models in Figure 4.11 are the truncation errors  $E_{tr}(\tilde{\Phi})$  which is  $\mathcal{O}(10^{-4})$  based on a convergence test of the multi-scalar mixing layer, while the RW model involves model errors caused by the unity Lewis number assumption in the RW model. For the convergence of  $E_{\Phi_{RMS}}$  in Figure 4.11, both RW and MS results show non-convergent behaviors, while the VCMS model demonstrates evident convergence for  $n_{pc}$  up to 5000. For VCMS model, Table 4.3 shows that the values of  $\left| C_{e1}(\Phi_{RMS}) \right|$  are approximately on the same order as the truncation errors  $E_{tr}(\Phi_{RMS})$  which are estimated

to be  $\mathcal{O}(10^{-5})$  for the multi-scalar mixing layer. This confirms that the multi-scalar VCMS model is fully consistent for the transport of scalar variance as discussed in Section 4.3.3. For the RW and MS models, model errors are present for the variance predictions according to the non-convergent behaviors shown in Figure 4.11 as well as the larger magnitudes of  $|C_{e1}(\Phi_{RMS})|$  than  $E_{tr}(\Phi_{RMS})$  in Table 4.3.

Table 4.3. The values of errors  $|C_{e1}|$  for  $\tilde{\Phi}$  and  $\Phi_{RMS}$  corresponding to  $n_{pc} \rightarrow \infty$  in equation (4.79) from the simulations of the multi-scalar turbulent mixing layer with the different models (RW, MS, and VCMS) without boundedness correction at  $x/l_m = 0$  (or 0.6).

Model	$x/l_m$	Quantity	$ C_{e1}(\tilde{\Phi}) $ or $ C_{e1}(\Phi_{RMS}) $
RW	0.6	$\tilde{\Phi}$	$[4.7 \times 10^{-3}, 4.4 \times 10^{-3}, 2.5 \times 10^{-4}, 4.5 \times 10^{-4}]$
MS	0	$\tilde{\Phi}$	$[2.4 \times 10^{-4}, 4.2 \times 10^{-4}, 1.9 \times 10^{-4}, 3.5 \times 10^{-4}]$
VCMS	0	$\tilde{\Phi}$	$[2.4 \times 10^{-4}, 4.6 \times 10^{-4}, 9.8 \times 10^{-5}, 3.6 \times 10^{-4}]$
RW	0	$\Phi_{RMS}$	$[6.8 \times 10^{-3}, 7.9 \times 10^{-3}, 9.2 \times 10^{-4}, 4.0 \times 10^{-4}]$
MS	0	$\Phi_{RMS}$	$[4.3 \times 10^{-3}, 5.0 \times 10^{-3}, 5.9 \times 10^{-4}, 2.8 \times 10^{-4}]$
VCMS	0	$\Phi_{RMS}$	$[4.1 \times 10^{-5}, 2.3 \times 10^{-5}, 4.0 \times 10^{-6}, 3.0 \times 10^{-5}]$

To sum up, we examined the accuracy and consistency of three PDF particle models (RW, MS, and VCMS) in a multi-scalar turbulent mixing layer. The RW model is unable to treat differential molecular diffusion and yields large errors in the predictions of both the scalar mean and variance in a multi-scalar turbulent mixing layer. The MS model is capable of capturing differential molecular diffusion in terms of the predictions of the scalar mean but fails to yield consistent predictions for the scalar variance. The multi-scalar VCMS model developed in Section 4.3.3 is confirmed to be fully consistent for the predictions of both the mean and variance of scalars.

#### 4.4.5 Multiple scalars with boundedness correction

Although the multi-scalar VCMS model is fully consistent for the transport of both the scalar mean and variance, the particles can exceed their scalar bounds which results in a serious realizability issue in practical simulations for combustion since the scalars in combustion are bounded. To resolve the issue, different correction algorithms have been discussed in Section 4.3.4 for the multi-scalar VCMS model. Here we examine the effect of the correction algorithms on the accuracy and convergence of the multi-scalar VCMS model. The scalar bounds for the multi-scalar system are defined to be  $[\phi_{\alpha,min}, \phi_{\alpha,max}] = [0, 1]$ ,  $\alpha = 1, \dots, n_\phi$ . In another words, we are enforcing the global scalar bounds, and individual scalars can possibly exceed their boundary values  $[\tilde{\Phi}_L, \tilde{\Phi}_R]$ . This helps minimize the artificial “mixing” introduced by the boundedness correction algorithms.

Simulations of the multi-scalar turbulent mixing layer with the conditions the same as those in Section 4.4.4 are performed by using the multi-scalar VCMS model with the four different boundedness correction algorithms in Section 4.3.4 (MP, LDF, CSB, and CPM). The particle scalar values  $\Phi^*$ , without boundedness correction and with correction, are shown in Figure 4.12. All four correction algorithms are able to enforce the particle scalar bounds effectively. The effect of the different correction algorithms on the particles in the multi-scalar mixing layer is similar to that in the single-scalar mixing layer shown in Figure 4.6. The MP correction shows a trend of overcorrection in Figure 4.12, even for some particles that are within the scalar bounds. The new correction algorithms developed in Section 4.3.4 (LDF, CSB, and CPM) show different levels of improvement to the MP correction. The particle values in the scalar space are shown in a triangular coordinate in Figure 4.13, to illustrate the evolution of joint scalar statistics of particles at the end of the simulation  $t = t_e$ . The scalars  $\phi_3$  and  $\phi_4$  are combined to show the four-scalar particles on the triangular coordinate. The subtracted  $2/3$  from  $\phi_3^* + \phi_4^*$  is to make the particles near the center of the triangle. The initial particles reside in a parallelogram shown as the dashed lines in the first subplot of Figure 4.13. This parallelogram defines a joint boundedness constraint [176] for the multi-scalar diffusion system, *i.e.*, the particles need to remain in the parallelogram

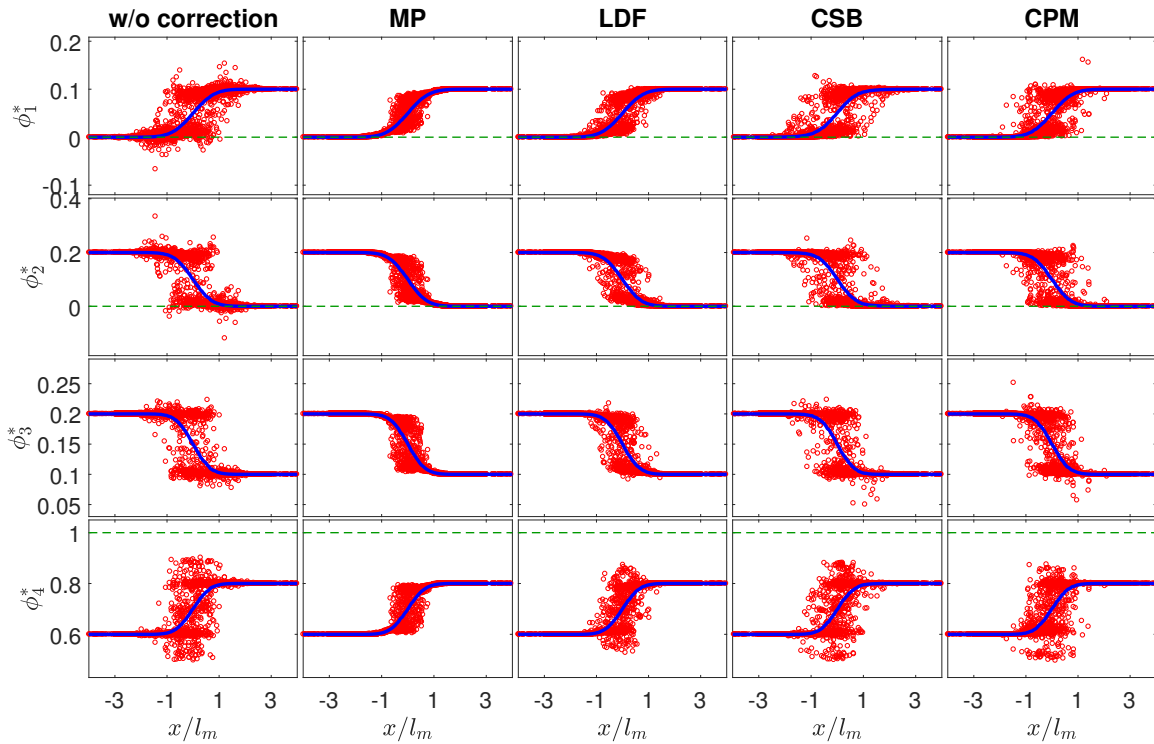


Figure 4.12. The particle scalar values  $\Phi^*$  against  $x/l_m$  in the multi-scalar turbulent mixing layer predicted by the VCMS model with the four different boundedness correction algorithms, MP, LDF, CSB, and CPM. (Circles: the particle scalar values  $\Phi^*$ ; solid line: the scalar mean  $\tilde{\Phi}$ ; dashed lines: the scalar upper and lower bounds.)

at later times. The current correction algorithms do not impose such a stringent realizable constraint, and instead only individual boundedness [176] is enforced. After 1000 time steps, without boundedness correction, the particles can move away from the parallelogram region, violating both individual boundedness and joint boundedness. With the MP correction and LDF correction, the particles seem to be confined inside the parallelogram to be consistent with the individual boundedness and joint boundedness, but at the cost of significant artificial mixing. For CSB and CPM, the particles satisfy the individual boundedness so that no particles can move above the triangle in Figure 4.13, but evidently they violate the joint boundedness by moving outside of the parallelogram region.

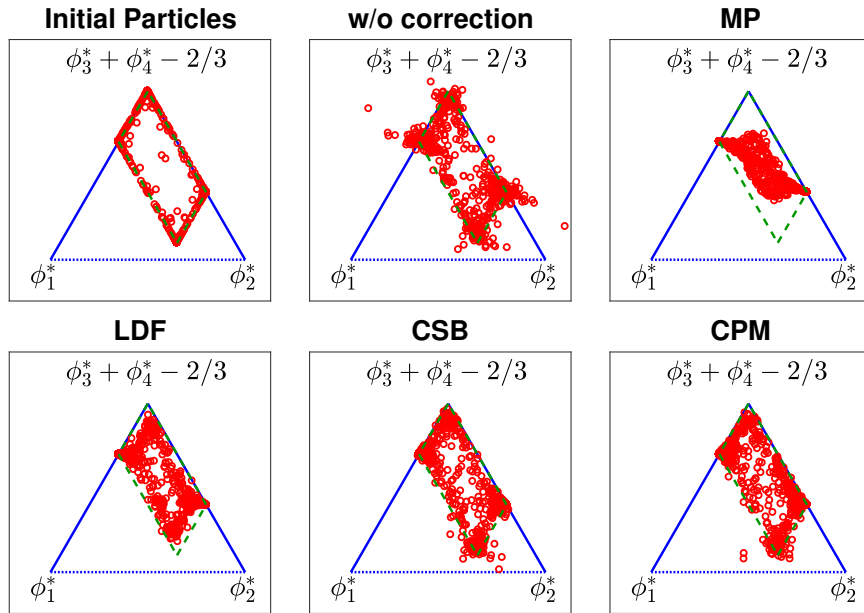


Figure 4.13. The particle values in the scalar space shown in a triangular coordinate system. (The scalars  $\phi_3$  and  $\phi_4$  are combined to show the four-scalar particles on the triangular coordinate. First subplot shows the initial particles, second subplot shows the updated particles at  $t = t_e$  without boundedness correction, and all the other subplots show the updated particles with the different correction algorithms.)

The effect of the boundedness correction algorithms on the accuracy of the multi-scalar VCMS model is examined in Figure 4.14. The correction algorithms MP, LDF, and CPM have no effect on the predictions of the scalar mean since they all conserve scalar mean as discussed in Section 4.3.4. The CSB correction yields slightly larger error  $E_{\tilde{\Phi}}$  in Figure 4.14 because the CSB correction does not conserve the scalar mean as discussed in Section 4.3.4. All the correction algorithms tend to underpredict  $\Phi_{RMS}$  because of the increased mixing caused by the correction algorithms, and this level of underprediction by the different correction algorithms is different as shown in Figure 4.14. The MP correction underpredicts  $\Phi_{RMS}$  by about 60% at  $x/l_m = 0$  when compared with the FV results. The LDF correction performs better than MP and underpredicts  $\Phi_{RMS}$  by about 17%. The CSB and CPM underpredict  $\Phi_{RMS}$  by about 3% and 7%, respectively. The performance difference of the

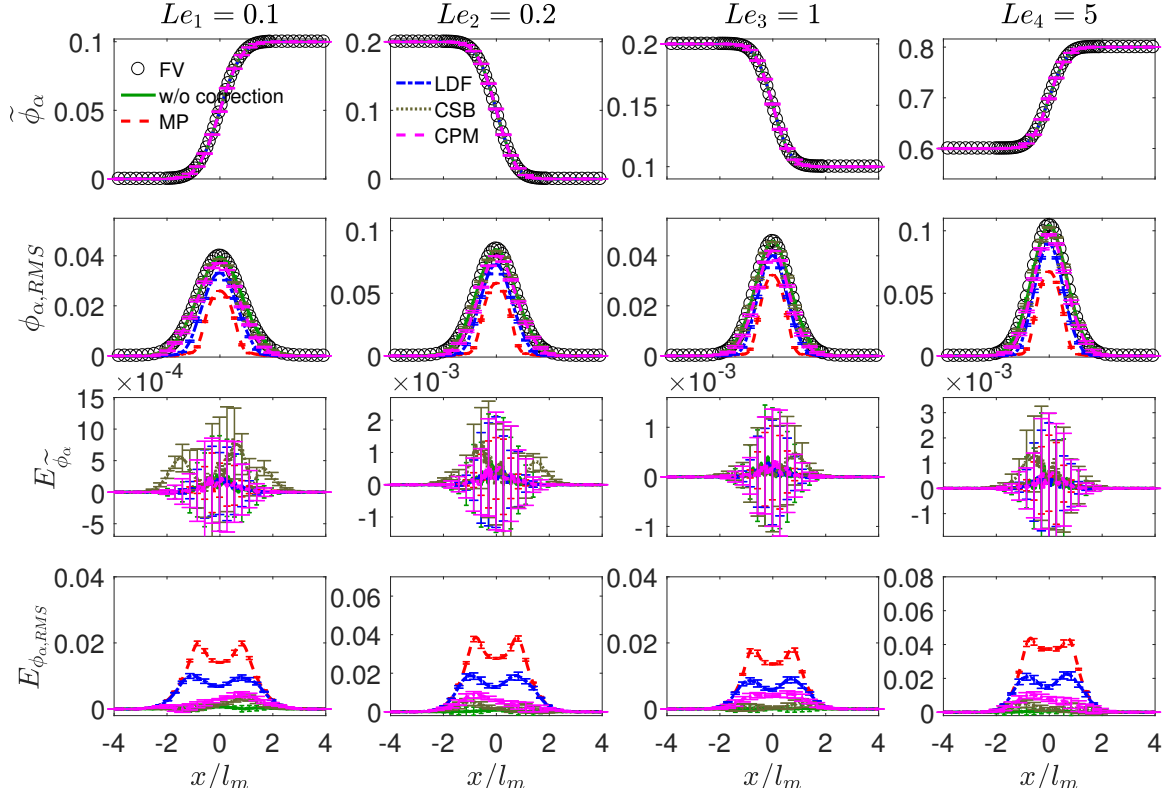


Figure 4.14. The profiles of the scalar mean  $\tilde{\Phi}$  (vector), the scalar RMS  $\Phi_{RMS}$ , and their errors  $E_{\tilde{\Phi}}$  and  $E_{\Phi_{RMS}}$  against  $x/l_m$  for the different scalars in the multi-scalar turbulent mixing layer with the VCMS model and the different boundedness correction algorithms (MP, LDF, CSB, and CPM). The error bars are the 95% confidence intervals estimated from multi-trial simulations.

CSB and CPM in the multi-scalar VCMS models seems larger than that in the single-scalar VCMS model discussed in Section 4.4.3.

The effect of the correction algorithms on the convergence of the multi-scalar VCMS model for the mixing layer is examined in Figure 4.15. The errors  $|C_{e1}|$  estimated from the model in equation (4.79) are tabulated in Table 4.4 based on the convergence results for the multi-scalar mixing layer. The MP, LDF, and CPM correction algorithms are mathematically consistent in the predictions of the scalar mean in the multi-scalar VCMS model as confirmed by the obtained error values  $|C_{e1}(\tilde{\Phi})| \sim \mathcal{O}(10^{-4})$  shown in Table 4.4 which is the same as the truncation error  $E_{tr}(\tilde{\Phi})$ . The convergence of  $E_{\tilde{\Phi}}$  by these correction algo-

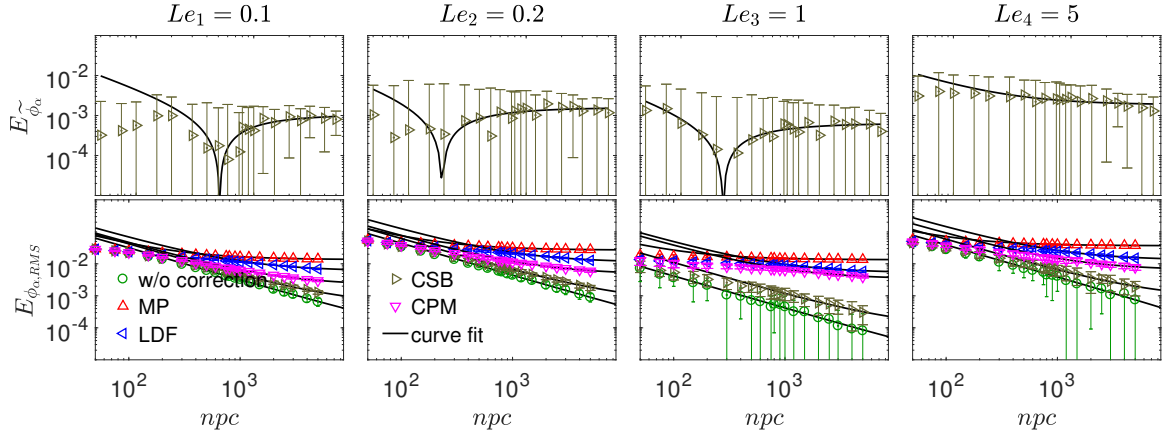


Figure 4.15. The convergence of the PDF particle prediction errors for the mean  $E_{\tilde{\Phi}}$  and RMS  $E_{\Phi_{RMS}}$  against  $n_{pc}$  for the different scalars in the multi-scalar turbulent mixing layer with the VCMS model and the different correction algorithms (MP, LDF, CSB, and CPM). The error bars are the 95% confidence intervals estimated from multi-trial simulations. The solid lines are the curve fits by using the model equation (4.79). The errors are evaluated at the mixing layer center  $x/l_m = 0$  except  $E_{\tilde{\Phi}}$  with the CSB correction which is evaluated at  $x/l_m = 0.6$  or  $-0.6$ .

gorithms (MP, LDF, and CPM) is very close to that without boundedness correction in Figure 4.11 (results are not shown). The CSB correction does not conserve scalar mean and hence yields a model error in the order of  $(10^{-3})$  as shown in Table 4.4 that is much greater than the truncation error  $E_{tr}(\tilde{\Phi})$ . The convergence of  $E_{\tilde{\Phi}}$  is shown in Figure 4.15 at  $x/l_m = 0.6$  for the turbulent mixing layer with the CSB correction. Evidently, the results do not show a convergent behavior, confirming that CSB is an inconsistent correction algorithm for the scalar mean. The convergence of  $E_{\Phi_{RMS}}$  with the different correction algorithms is shown in Figure 4.15. The correction algorithms compromise the convergence achieved by the multi-scalar VCMS model without correction, and a model error  $|C_{e1}(\Phi_{RMS})|$  is introduced with the order of magnitude about  $\mathcal{O}(10^{-2})$  for MP and LDF, and  $\mathcal{O}(10^{-3})$  for CSB and CPM, as shown in Table 4.4, in contrast with the truncation error  $E_{tr}(\Phi_{RMS}) \sim \mathcal{O}(10^{-5})$  for the multi-scalar mixing layer. The new correction algorithms introduced in this work perform better than the MP correction, especially the non-uniform corrections (CSB and CPM).

Overall, the non-uniform correction algorithms (CSB and CPM) are superior over the uniform correction (MP and LDF) and result in less reduction of  $\Phi_{RMS}$ . The CPM correction seems to perform best in terms of conserving the scalar mean and yielding less underprediction of  $\Phi_{RMS}$ , while preserving the particle scalar bounds.

Table 4.4. The values of errors  $|C_{e1}|$  for  $\tilde{\Phi}$  and  $\Phi_{RMS}$  corresponding to  $n_{pc} \rightarrow \infty$  in equation (4.79) from the simulations of the multi-scalar turbulent mixing layer with the multi-scalar VCMS model and with the different boundedness correction algorithms (MP, LDF, CSB, or CPM) at  $x/l_m = 0, 0.6, \text{ or } -0.6$ .

Model	$x/l_m$	Quantity	$ C_{e1}(\tilde{\Phi}) $ or $ C_{e1}(\Phi_{RMS}) $
MP	0	$\tilde{\Phi}$	$[1.2 \times 10^{-4}, 3.1 \times 10^{-4}, 2.0 \times 10^{-4}, 4.3 \times 10^{-4}]$
LDF	0	$\tilde{\Phi}$	$[2.0 \times 10^{-4}, 3.7 \times 10^{-4}, 3.4 \times 10^{-4}, 6.3 \times 10^{-4}]$
CSB	0.6 or -0.6	$\tilde{\Phi}$	$[1.1 \times 10^{-3}, 1.6 \times 10^{-3}, 6.3 \times 10^{-4}, 1.9 \times 10^{-3}]$
CPM	0	$\tilde{\Phi}$	$[1.8 \times 10^{-4}, 4.3 \times 10^{-4}, 2.3 \times 10^{-4}, 6.1 \times 10^{-4}]$
MP	0	$\Phi_{RMS}$	$[1.4 \times 10^{-2}, 2.7 \times 10^{-2}, 1.3 \times 10^{-2}, 3.7 \times 10^{-2}]$
LDF	0	$\Phi_{RMS}$	$[5.9 \times 10^{-3}, 1.1 \times 10^{-2}, 5.2 \times 10^{-3}, 1.3 \times 10^{-2}]$
CSB	0	$\Phi_{RMS}$	$[5.0 \times 10^{-4}, 6.3 \times 10^{-4}, 1.0 \times 10^{-4}, 8.3 \times 10^{-4}]$
CPM	0	$\Phi_{RMS}$	$[2.1 \times 10^{-3}, 4.7 \times 10^{-3}, 3.4 \times 10^{-3}, 6.4 \times 10^{-3}]$

The percentage,  $\eta_{BV}$ , of particles with scalar bounds violation among the total number of particles is examined in Figure 4.16 for the multi-scalar VCMS model. For the multi-scalar mixing layer test case with VCMS without boundedness correction,  $\eta_{BV}$  (circles in Figure 4.16) is approximately 17% and this value remains the same when  $n_{pc}$  is increased. This suggests that the violation of particle scalar bounds exists even when  $n_{pc} \rightarrow \infty$ . The correction algorithms, on the other hand, are necessary for ensuring realizability of particle scalars for simulations of problems like turbulent combustion. The CSB and CPM correction algorithms reduce the value of  $\eta_{BV}$  to about 5% in the multi-scalar mixing layer, the LDF correction algorithm reduces the value of  $\eta_{BV}$  below 0.1% when  $n_{pc} > 200$ , and the MP

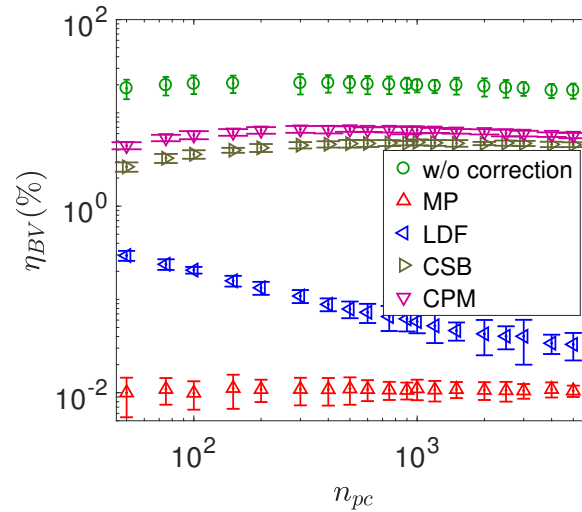


Figure 4.16. The percentage  $\eta_{BV}$  of the number of particles that violate the scalar bounds among the total number of particles used in the simulations of the multi-scalar turbulent mixing layer by using the VCMS model and with or without boundedness correction. The error bars are the 95% confidence intervals estimated from multi-trial simulations.

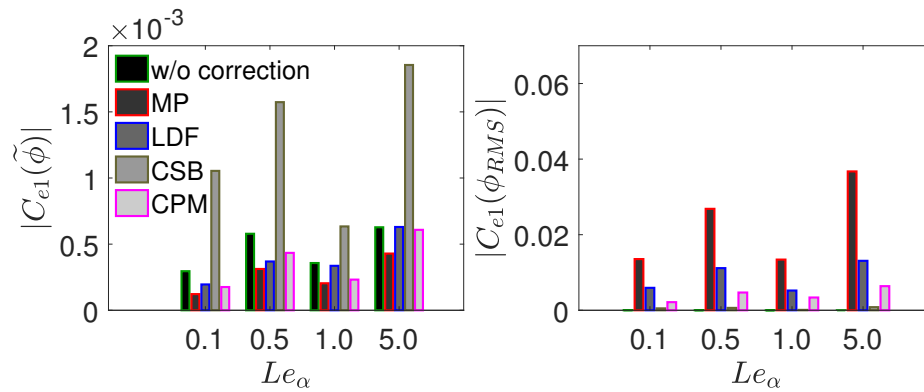


Figure 4.17. The errors  $|C_{e1}|$  involved in the different correction algorithms (MP, LDF, CSB, and CPM) combined with the multi-scalar VCMS model for the predictions of the scalar mean  $\tilde{\Phi}$  (left) and the scalar RMS  $\Phi_{RMS}$  (right) in the multi-scalar turbulent mixing layer.

correction decreases  $\eta_{BV}$  to 0.01%. The significant reduction of  $\eta_{BV}$  by the MP correction is consistent with its aggressive correction.

Although the correction algorithms to the boundedness violation of the particle scalars introduce model errors to the VCMS models, they are required in order to ensure realizability of scalar values in practical combustion simulations. The boundedness issue is not completely resolved in this work, while the newly developed correction algorithms have shown substantial improvement to the previously developed MP correction [176]. Such improvement is highlighted further in Figure 4.17 where the errors  $|C_{e1}|$  involved in the correction algorithms are compared for the predictions of the scalar mean  $\tilde{\Phi}$  and scalar RMS  $\Phi_{RMS}$  in the multi-scalar mixing layer problem discussed in Section 4.4.5. The new correction algorithms (LDF, CSB, CPM) reduce the error  $|C_{e1}(\Phi_{RMS})|$  substantially when compared with the MP correction.

Although we advocate the advantages of VCMS model (an improvement to the MS model) and the new correction algorithms in this paper, we do not diminish the importance of the RW model. The RW model is still the most widely used model for the Lagrangian PDF particle method and it does not have any realizability issue despite the inconsistency issue discussed in Section 4.1. There is a work to suggest that the RW model is numerically more stable than the MS model [179]. Both types of models (RW and MS) are expected to be useful and serve well for different purposes. When the modeling of DMD is concerned, the MS and VCMS models are the only suitable choices because RW assumes equal molecular diffusivities. In the multi-scalar case, it has been demonstrated that the MS and VCMS models yield errors for the predictions of scalar mean up to one-order of magnitude smaller than that from the RW model (as shown in Figures 4.10 and 4.14, and Tables 4.3 and 4.4). It is also noticed that the VCMS combined with CPM yields error for the predictions of scalar RMS smaller than or comparable to the RW model (as shown in Figures 4.10 and 4.14, and Tables 4.3 and 4.4) because of the realizability issue. It is worthwhile to mention that the boundedness correction in the multi-scalar case can cause more error than the single scalar case because of the need to ensure boundedness of every scalar. The correction of one scalar requires simultaneous correction of all the other scalars of the same particle even if they do not violate scalar bounds. For this reason, the realizability issue of the MS and VCMS models for multiple scalars has not been completely resolved. Nevertheless, the new

correction algorithms introduced in this work are a significant improvement to the existing MP correction.

In summary, we examined the effect of the boundedness correction algorithms on the accuracy and convergence of the multi-scalar VCMS model. The different correction algorithms do not affect the convergence of the scalar mean, except the CSB correction, and the convergence of the VCMS model for the scalar RMS is compromised by employing the correction. The performance of the different correction algorithms (MP, LDF, CSB, and CPM) is compared in detail. The MP correction is found to be too aggressive and reduces the scalar RMS and  $\eta_{BV}$  significantly, and the newly introduced correction algorithms (LDF, CSB, and CMP) are found to be able to yield improved results to various degrees.

#### 4.4.6 Effect of different mixing models

Another issue with the MP correction (when combined with the MS model) is that it can be used only with the IEM mixing model. The IEM mixing model is less attractive for modeling turbulent flames with local extinction [132]. In the newly developed multi-scalar VCMS model, the four correction algorithms can be combined with any mixing models, as mentioned in Section 4.3.4. Two more mixing models (MCurl and EMST) are examined with the CPM correction algorithms for the multi-scalar mixing layer to illustrate the compatibility of the new correction algorithms with different mixing models. When using a new mixing model, we only use the mixing model for the micro-mixing term (the term involving  $\Omega$  in equation (4.62)) and still use the IEM formulation for the variance correction (the terms involving  $\hat{\omega}_\alpha$ ). Figure 4.18 shows the particle scatter plots obtained with the MCurl and EMST mixing models (with the CPM correction), and the comparison of the predictions of the scalar mean and RMS with the different mixing models. The results show little difference among the different mixing models in the predictions of the mixing layer test case, and confirm the effectiveness of the CPM correction when combined with the different mixing models.

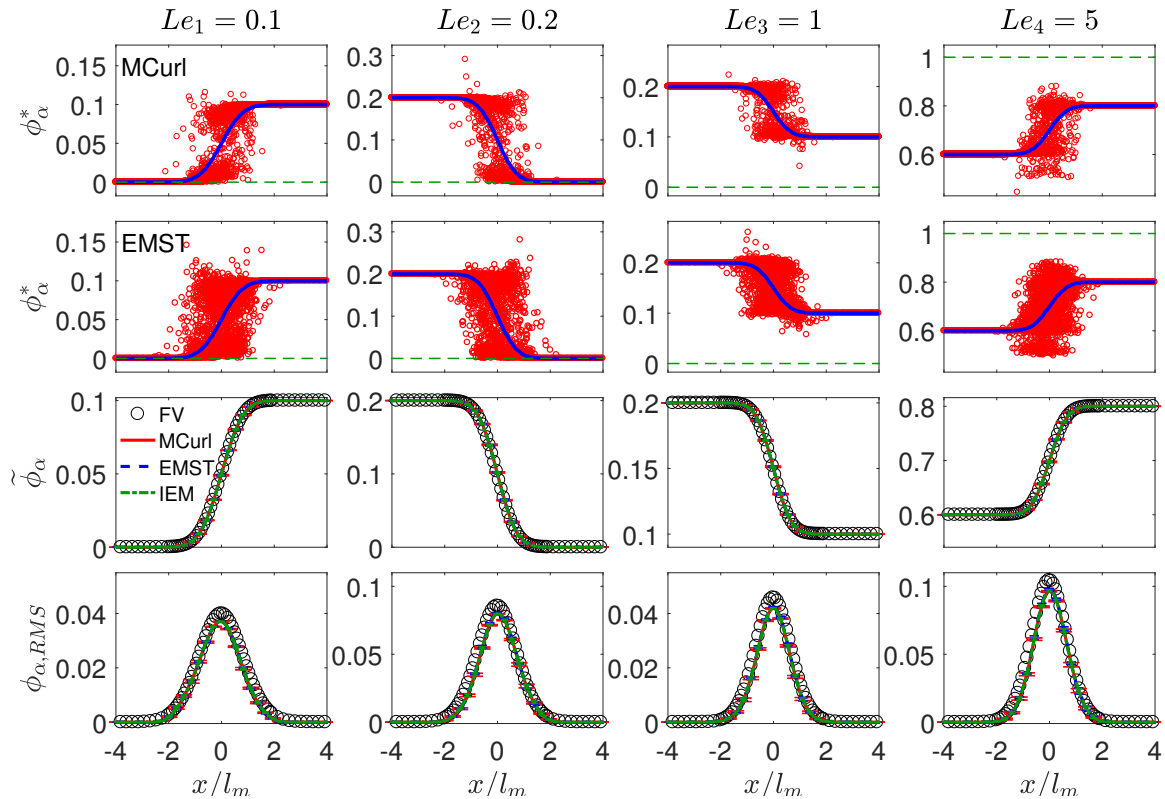


Figure 4.18. The particle scalar values  $\Phi^*$  against  $x/l_m$  in the multi-scalar turbulent mixing layer predicted by the VCMS model with the CPM correction and with the MCurl mixing model (the first row) and the EMST mixing model (the second row). The profiles of the scalar mean  $\tilde{\Phi}$  against  $x/l_m$  with the different mixing models are shown in the third row, and the profiles of the scalar RMS  $\Phi_{RMS}$  in the last row. The error bars are the 95% confidence intervals estimated from multi-trial simulations.

#### 4.4.7 Comparison of computational cost

The computational cost of the VCMS model is higher than the MS model. The implementation of the multi-scalar VCMS model requires  $O(n_p n_\phi^2)$  operations to form the linear system in equation ((4.60)) and another  $O(n_\phi^3)$  to solve the system. Nevertheless, the cost of the VCMS model still scales linearly with  $n_p$ . Although the cost of solving the linear system in ((4.60)) can be expensive, this cost can still be relatively small when a combustion problem is concerned where the calculation of finite-rate chemistry is usually the dominant

cost. Additionally, the matrix  $\mathcal{A}$  in equation ((4.61)) may become diagonally dominant when  $n_\phi \gg 1$ , which makes the solution less expensive than  $O(n_\phi^3)$ . The computational cost of the different particle models and the correction algorithms has been compared in the multi-scalar mixing layer problem. No substantial difference has been found in their cost. For example, the relative cost ratio of using MP, LDF, CSB, and CPM in the VCMS model is about 5:5:5:4, and the ratio of using MS, RW, and VCMS models is about 10:13:22.

#### 4.4.8 Model performance under real turbulence conditions

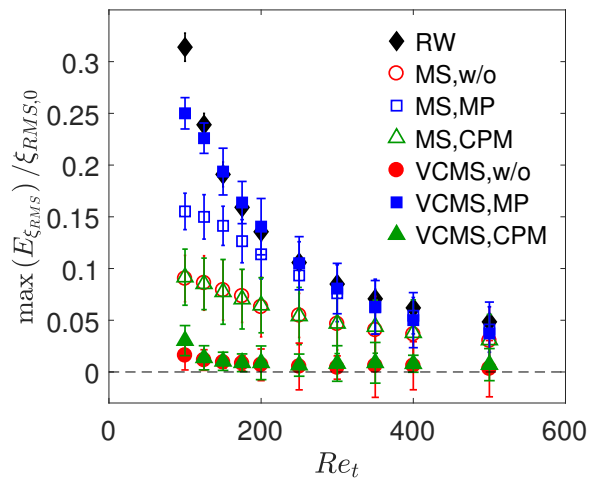


Figure 4.19. The predicted maximum error of  $\xi_{RMS}$ ,  $\max(E_{\xi_{RMS}}) / \xi_{RMS,0}$ , against  $Re_t$  in the single-scalar turbulent mixing layer test case with the RW model, the MS model and the VCMS model, and three boundedness correction options: without correction, with the MP correction, and with the CPM correction. The error bars are the estimated 95% confidence intervals estimated from multi-trial simulations.

The extensive discussions above are based on a turbulent mixing layer test case in Section 4.4.1. The test case is manufactured and is arguably to be not representative to realistic turbulence conditions. In particular, the  $Re_t = 100$  is relatively low, and the velocity-to-scalar timescale ratio  $C_\phi \approx 0.01$  is lower than a realistic value. These parameters are intentionally chosen to isolate the effect of molecular diffusion for a focused study of the

mathematical consistency and convergence of the molecular diffusion models. In the above discussions, we focus mainly on the relative performance difference of the different models and the boundedness correction algorithms. Here, we extend the mixing layer test case in Section 4.4.1 to more realistic turbulence conditions by employing  $C_\phi = 2$  according to an experiment (*e.g.* [185]), to assess the performance of the different models under realistic conditions. A range of the values of  $Re_t$  is specified to examine the model performance under real turbulence conditions,  $Re_t \in [100, 500]$ . The estimated turbulent  $Re_t$  (defined in Table 4.1) in several realistic cases (in experiments or DNS) is summarized in Table 4.5. From the table we can see that,  $Re_t = 100$  is near the lower end of turbulence conditions in realistic problems. The examined range of  $Re_t = [100, 500]$  is expected to be able to represent a range of realistic problems with relatively low Re, with which the effect of molecular diffusion is expected to be evident.

For the turbulent mixing layer test case (with  $C_\phi = 2$  and  $Re_t \in [100, 500]$ ), the predicted maximum relative error of  $\xi_{RMS}$ ,  $\max(E_{\xi_{RMS}}) / \xi_{RMS,0}$ , where  $\xi_{RMS,0}$  is the RMS at the center of the mixing layer, against  $Re_t$  is depicted in Figure 4.19. Both the MS and VCMS models are considered, and the RW model is also included as a reference. Three cases for MS and VCMS are simulated, without boundedness correction, with the MP correction, and with the CPM correction. The yielded relative error by the MS model without correction (open circle) at  $Re_t = 100$  (with  $C_\phi = 2$ ) is about 10%, which is the same as the relative error observed in Figure 4.3 with the same  $Re_t$  but with  $C_\phi \approx 0.01$ . This indicates that the model relative error and inconsistency in the MS model discussed in this work does not have a strong dependence on  $C_\phi$ . Comparing the MS model and the VCMS model without boundedness correction, we can see a clear difference of the error levels. The error involved in the VCMS model case is negligibly small and is mostly independent of  $Re_t$  (caused by other sources of errors such as grid error). The error in the MS model is greater than that in VCMS due to the MS model inconsistency and decreases when  $Re_t$  increased as expected. Within the considered range of  $Re_t$ , the MS error due to the missing spatial transport of scalar variance is between 10% at  $Re_t = 100$  and 3% at  $Re_t = 500$ . The MP correction combined with the MS model raises the relative error to about 16% at  $Re_t = 100$ ,

Table 4.5. Estimated range of turbulent  $Re_t$  in a few laboratory-scale experiments or DNS.

Experiments or DNS	Cases	Estimated range of $Re_t$
Thermal mixing layer in grid turbulence by Ma and Warhaft [184]	$x_0/M = 60.0$ (where $x_0$ refers to the position of the mandoline from the grid and $M$ is the grid size of grid turbulence generator).	[87, 137]
	$x_0/M = 20.0$	[94, 204]
	$x_0/M = 2.0$	[98, 472]
Sandia temporally evolving jet CO/H <sub>2</sub> DNS flames [190]	Case L: $Re_0 = 2510$ (where $Re_0$ is the fuel jet bulk Reynolds number.)	(0, 70]
	Case M: $Re_0 = 4478$	(0, 125]
	Case H: $Re_0 = 9079$	(0, 214]
Premixed flames experiment [191]	Case with mass flow rate 10 kg/h: $Re_0 = 4871$ , where $Re_0$ is the jet bulk Reynolds number	$\sim 87$
	Case with mass flow rate 18 kg/h: $Re_0 = 8768$	$\sim 134$
Sandia piloted jet flame D [88]	$Re_0 = 22400$ (where $Re_0$ is the fuel jet bulk Reynolds number.)	(0, 1130], around [120, 650] near the non-premixed flame front

and 5% at  $Re_t = 500$ . This illustrates that the issues raised in this paper due to the inconsistency of MS and the overcorrection of MP are relevant even at not small Reynolds number

turbulence conditions, say  $Re_t \geq 300$  (with relative error greater than 10%). This range of  $Re_t$  covers most of the experimental conditions shown in Table 4.5, and hence demonstrates the relevance of the current study to realistic problems. The MP correction when combined with the VCMS model significantly degrades the simulation results of the consistent model and causes the relative error to be even higher than the MS model with MP correction and close to the error from the RW model for this single-scalar case. This demonstrates the need to develop new correction algorithms to be combined with the new VCMS models. With the newly developed CPM correction, the MS model and VCMS model yield results very close to the results without boundedness correction, indicating the superior performance of the CPM correction over the entire range of  $Re_t$  that is examined in Figure 4.19. In summary, the issues raised in this paper related to the inconsistency of MS and the overcorrection of MP are shown to be evident even under realistic turbulence conditions. The performance of the newly introduced models (the VCMS model and CPM correction) is further demonstrated under these conditions, and hence the new work presented in this paper represents an important advancement to the transport PDF method for treating differential molecular diffusion consistently and accurately. The results shown in Figure 19 are for a single-scalar case for which the RW model performs mostly worse than MS and VCMS with different correction algorithms, for the predictions of scalar RMS. The same trend is expected to be true for the predictions of scalar mean (if unit Lewis number is used in RW). As discussed in Section 4.4.5, the performance of the correction algorithms in multi-scalar cases deteriorates for the predictions of scalar RMS, and the best combination with VCMS and CPM may reach the same order of magnitude of error as the RW model for some scalars. Nevertheless, the VCMS model with CPM can reduce the error of RW for the scalar mean by one-order of magnitude and it represents a significant improvement to the existing MS model with MP correction.

The conclusions obtained from this paper is highly expected to be extensible to simulations of actual two dimensional or three-dimensional turbulence and combustion problems. Those simulations will be conducted in our future work to further demonstrate the capability of the new models and correction algorithms.

To summarize, we examined and validated the VCMS models developed in Section 4.3 in detail in this section. The mathematical consistency of the VCMS models is verified. The performance difference of the different correction algorithms is compared in detail, and the new correction algorithms show superior performance over the MP correction. The effect of the correction algorithms on model convergence is also examined thoroughly to provide a detailed understanding of the different models. The compatibility of the new correction algorithms with different mixing models other than the IEM model is also examined and confirmed. The relevance of the model issues and model advancement to realistic problems is established.

## 4.5 Conclusions

This work aims at resolving the inconsistent transport of the scalar variance by the MS model for treating DMD in the transported PDF methods for turbulent reactive flows. Fully consistent models called VCMS models are developed to resolve the issue of the MS model while retaining other positive features of the MS model. The single-scalar VCMS model is developed first by introducing a correction to the mixing to account for the missing molecular diffusion for the scalar variance in the MS model. The single-scalar VCMS model cannot be extended straightforwardly to a multi-scalar system. A systematic strategy is introduced to develop a fully consistent multi-scalar VCMS model. In conjunction with the VCMS model development, new boundedness correction algorithms (LDF, CSB, and CPM) are introduced to enforce realizability of the particle scalars in addition to extending the conventional MP correction to the VCMS models. The mathematical consistency and accuracy of the VCMS models are validated in a turbulent mixing layer problem. The performance of the different boundedness correction algorithms is examined in detail in the mixing layer problem when combined with the VCMS models. The new correction algorithms, especially CPM, show significant improvement when compared to the MP correction. The effect of the correction algorithms on the model consistency is also evaluated thoroughly. All correction algorithms lead to a model error, while the magnitudes of errors

for the different correction algorithms are very different. The assessment of the correction algorithms provides a guideline for choosing the algorithms for applications. The incorporation of other mixing models with the VCMS model is also explored, and the results are very promising, while in the MS model, only IEM can be used when combined with the MP correction. These results signify an important advancement to the transported PDF methods for treating detailed molecular diffusion accurately and robustly in turbulent combustion problems.

## Appendices

### An illustration of the overcorrection by the MP correction algorithm

We use a simple example to illustrate the overcorrection by the MP correction algorithm [176] [176]. A single scalar system with a number of  $n_p = 20$  particles is considered with the initial particle scalar values uniformly distributed between  $[\xi_s, \xi_e]$ , *i.e.*, the initial particle values at time  $t = t^n$  are  $\xi_p^n = \xi_s + (p - 1)(\xi_e - \xi_s)/(n_p - 1)$ , ( $p = 1, \dots, n_p$ ). A single particle time step advancement is performed to obtain the new particle values  $\xi_p^{n+1}$  at time  $t = t^{n+1}$  by using equation (4.31). The value of  $c$  in equation (4.31) is specified to be  $c = 0.1$  and the mean shift  $\Delta\tilde{\xi} = -0.3$  in this illustration. Since  $\Delta\tilde{\xi}$  is negative, the lower bound violation at  $\xi = 0$  is of concern here. Three cases with different values of  $[\xi_s, \xi_e]$  are considered, and the new particle values  $\xi_p^{n+1}$  against  $\xi_p^n$  are shown in Figure 4.20 for the three cases. For the first case  $[\xi_s, \xi_e] = [0, 0.7]$ , one initial particle (shown as circles) is exactly on the scalar lower bound  $\xi = 0$ . After the particle step, without correction, the lower bound is clearly violated (shown as squares). With the MP correction, the lower bound is enforced and the particle that is on the bound initially stays on the lower bound (shown as triangles), which is expected. For the second case  $[\xi_s, \xi_e] = [0.1, 0.8]$ , the initial particles are not on the lower bound. After the particle step, the lower bound violation is seen without correction. Now, with the MP correction, the lower bound is enforced but unfortunately no updated particles are on the lower bound, represents an example of overcorrection by the MP correction algorithm. For the third case  $[\xi_s, \xi_e] = [0.3, 1]$ , no particle bound violation

occurs after the particle update without correction. However, in this case, the MP algorithm still yields correction that is obviously unnecessary, and this represents a second example of overcorrection by the MP correction algorithm.

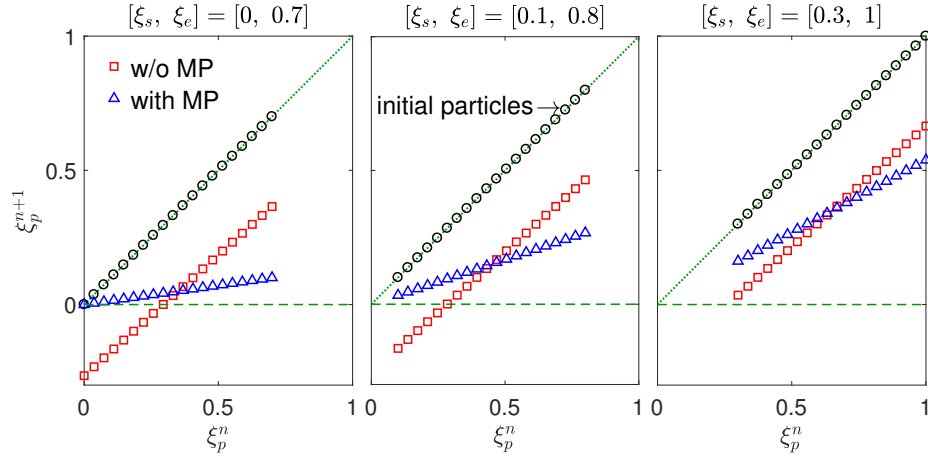


Figure 4.20. Updated particle values  $\xi_p^{n+1}$  against the initial particles  $\xi_p^n$  after one particle time step for the three different cases with different values of  $[\xi_s, \xi_e]$  to illustrate the overcorrection caused by the MP correction algorithm.

### Direct extension of single-scalar VCMS model to multiple scalars

The single-scalar VCMS model developed in Section 4.3.1 can be easily extended to multiple scalars, by modifying the particle scalar equation (4.29) in the MS model into

$$d\phi_{\alpha, p}^*(t) = -(\Omega + \omega_\alpha)^* (\phi_{\alpha, p}^* - \tilde{\phi}_\alpha^*) dt + \left[ \frac{\nabla \cdot (\bar{\rho} \Gamma_\alpha \nabla \tilde{\phi}_\alpha) + \hat{C}_\alpha}{\bar{\rho}} \right]^* dt + S_\alpha (\Phi_p^*) dt, \quad (4.5.80)$$

where  $\omega_\alpha$  is the added correction mixing frequency defined in equation (4.53), following equation (4.41) for the single-scalar case, to account for the missing molecular diffusion term in the variance equation (4.30) by the MS model. Obviously,  $\omega_\alpha$  has to be specified differently for the different scalars. With the model in (4.5.80), the corresponding mean and

variance scalar equations can be derived and are found to be fully consistent with the model equations (4.4) and (4.5). This extension of the single-scalar VCMS model in Section 4.3.1 to multiple scalars seems to be able to successfully improve the MS model to yield consistent transport equations for both the scalar mean and the variance. Unfortunately, however, the model in (4.5.80) is not consistent at the particle level even the first two moments (the mean and variance) are consistent. This can be shown by summing (4.5.80) over all scalars, and the normalization condition in equation (4.2) is not satisfied because of the dependency of  $\omega_\alpha$  in equation (4.5.80) on the scalars. It is possible to introduce a correction to satisfy the particle normalization condition, *e.g.*,

$$d\phi_{\alpha,p}^*(t) = -(\Omega + \omega_\alpha)^* (\phi_{\alpha,p}^* - \tilde{\phi}_\alpha^*) dt + \tilde{\phi}_\alpha^* \sum_\beta \omega_\beta^* (\phi_{\beta,p}^* - \tilde{\phi}_\beta^*) dt + \left[ \frac{\nabla \cdot (\bar{\rho} \Gamma_\alpha \nabla \tilde{\phi}_\alpha) + \hat{C}_\alpha}{\bar{\rho}} \right]^* dt + S_\alpha (\Phi_p^*) dt, \quad (4.5.81)$$

in which the second-term on the right-hand side is added to enforce the normalization condition in equation (4.2). This correction leads immediately to an undesired source term in the following corresponding variance equation (the last term on the right-hand side) when compared to equation (4.5),

$$\frac{\partial \bar{\rho} \widetilde{\phi_\alpha''^2}}{\partial t} + \nabla \cdot (\bar{\rho} \widetilde{\mathbf{u}} \widetilde{\phi_\alpha''^2}) = \nabla \cdot \left[ \bar{\rho} (\Gamma_t + \Gamma) \nabla \widetilde{\phi_\alpha''^2} \right] - 2\bar{\rho} \Omega \widetilde{\phi_\alpha''^2} + 2\bar{\rho} \Gamma_t \nabla \tilde{\phi}_\alpha \cdot \nabla \tilde{\phi}_\alpha + 2\bar{\rho} (\widetilde{\phi_\alpha S_\alpha} - \tilde{\phi}_\alpha \tilde{S}_\alpha) + 2\bar{\rho} \tilde{\phi}_\alpha \sum_\beta \omega_\beta \widetilde{\phi_\alpha'' \phi_\beta''}. \quad (4.5.82)$$

It looks like that one correction to an inconsistency will always lead to another inconsistency. Thus, the simple extension of the single-scalar VCMS to multiple scalars does not seem to be able to yield a fully consistent model.

## **5. AN A PRIORI EXAMINATION OF A POWER-LAW MIXING TIME SCALE MODEL FOR TRANSPORTED PDF METHOD IN A HIGH-KARLOVITZ NUMBER TURBULENT PREMIXED DNS FLAME**

DNS of a high-Karlovitz number turbulent premixed jet flame has been reported recently (Wang et al., Proc. Combust. Inst., 2017, 36, 2045-2053). The DNS flame features an intense interaction between the turbulence and flame structures in the broken reaction zone regime as suggested by the DNS dimensionless parameters. In this work, we analyze the DNS results to gain insights into the modeling of sub-filter scale mixing in the context of large-eddy simulations (LES) and probability density function (PDF) method. A sub-filter scale mixing time scale is analyzed with respect to the filter size to examine the validity of a power-law scaling model for the mixing time scale in LES/PDF. The results show remarkable agreement with a simple power-law scaling when the filter size is sufficiently large. A detailed examination of the power-law fitting parameters in space and among different scalars finds that the power parameter is approximately constant except in the area near the jet exit, while the other parameter related to the flame length scale shows a clear spatial and scalar dependence. A new model for the mixing time scale is proposed based on the DNS observation, and has been demonstrated to represent the mean and instantaneous mixing time scale reasonably well in a priori assessment.

### **5.1 Introduction**

Practical combustion configurations in transportation and propulsion applications have been pushed toward extreme conditions such as high speed, high pressure, compact combustor size, and lean burning. Understanding combustion under extreme conditions is thus

imperative for the development of predictive models for combustion problems that are relevant to practical applications. Ultra-lean burning is an extreme combustion condition that is highly desired in many applications like automobile engines and gas turbines due to the environmental concerns and government regulations. Ultra-lean turbulent premixed combustion is characterized by a high Karlovitz (Ka) number, which is defined as the time-scale ratio between a characteristic chemical time scale,  $\tau_C$ , and the Kolmogorov turbulence time scale,  $\tau_\eta$ , *i.e.*,  $Ka = \tau_C/\tau_\eta$ . Under very high-Ka conditions, small-scale turbulent eddies penetrate a premixed flame front and push the combustion towards the distributed reaction regime. The chemical scales are tightly entangled with the spectrum of turbulence scales and create a strong turbulence-chemistry coupling that makes the predictive modeling of high-Ka turbulent premixed combustion a highly challenging task. It is critically needed to develop a thorough understanding of the characteristics and scaling of high-Ka turbulent premixed combustion for the development of accurate turbulent combustion models.

Because of its importance, high-Ka turbulent premixed combustion has received significant attentions. Examples of existing work include the experimental studies [153, 166, 167, 192–198] and the direct numerical simulation (DNS) studies [32–41, 199]. These studies have helped gain deep insights into the combustion physics and inspired new modifications to the traditional regime diagrams of turbulent premixed combustion, such as the Borghi diagram [150, 200]. The experimental study in [195] found that, with increasing turbulence intensity, the measured preheat zone is broadened as indicated by the Borghi diagram but no broadened reaction zone is observed even with  $Ka > 100$ , which is contradictory to the Borghi diagram. Similar observations with thin reaction zones with  $Ka > 100$  have also been reported in other experimental [192–194] and DNS [32] studies. In contrast, however, the broadened reaction zones were observed experimentally by Dunn et al. [153, 166] and Zhou et al. [196–198]. It was speculated that the contradictory observations are caused by the different configurations used in the different studies, although the exact cause is yet to be found. Besides, the measured boundary between the broadened preheat thin reaction zone regime and flamelet regime in [195] is not at  $Ka = 1$ , which is not consistent with the Borghi diagram. A new diagram based on the measurements was then proposed with up-

dated boundaries between the flamelet regime and thin reaction zone regime, and between the thin reaction zone regime and distributed reaction regime.

DNS has become an extremely important tool to study fundamental combustion physics, but its use in practical combustion problems is still very limited. Statistical models are still needed to provide feasible engineering solutions. Among many existing turbulent combustion statistical models, the transported probability density function (PDF) method (or filtered-density function (FDF) method) is attractive for its intrinsic closure for the sub-filter scale chemical reaction effect. It provides a highly useful tool for modeling turbulent combustion that is not mixing controlled. The transported PDF method has been largely tested in non-premixed combustion which is mostly mixing controlled. Both Reynolds-averaged Navier-Stokes (RANS) modeling [58,59,201–203] and large-eddy simulation (LES) modeling [70,117,149,168,204–207] have been conducted by using the transported PDF method. In these existing transported PDF studies of non-premixed combustion, the target cases range from early canonical Sydney piloted jet flames L, B, and M [9,118] and Sandia piloted jet flames D, E, and F [88], to more recent Sydney/Sandia inhomogeneous inlet piloted jet flames [25,26,208]. The overall performance of the transported PDF method in non-premixed combustion is demonstrated to be reasonable, including the predictions of low-probability combustion scenarios like local extinction and re-ignition [14,59].

The transported PDF method has also been applied to partially premixed and premixed combustion, although the effort is much less than non-premixed combustion. A frequently modeled premixed flame case is the turbulent premixed Bunsen jet flames F1, F2, and F3 [83]. LES/PDF studies of flame F3 were reported in [209] and of flame F1 were reported in [149]. Wang and Zhang [149] evaluated the performance of LES/PDF in predicting combustion across different combustion regimes including premixed and partially premixed. More recent premixed combustion cases are the piloted premixed jet burner (PPJB) [153,166] and turbulent counterflow premixed jet flames (TCF) [87,210]. Rowinski and Pope [165,211] studied the PPJB flames using transported PDF method in both RANS and LES contexts. LES/PDF studies of the TCF flames were reported in [212,213]. Despite these efforts of applying the transported PDF method to partially premixed and premixed

combustion, they are less comprehensive than the efforts for non-premixed combustion. In most of these existing PDF modeling of partially premixed and premixed combustion, the same sub-models that are developed for the non-premixed combustion are used directly, including the micro-scale mixing models. Turbulent premixed combustion, however, is fundamentally different from non-premixed combustion and is usually not mixing controlled as observed in many non-premixed combustion problems. The coupling between chemical reaction and molecular diffusion in premixed combustion is tighter when compared to non-premixed combustion, which yields additional modeling challenges for modeling premixed combustion [214]. Most of the existing mixing models for the transported PDF method are developed based on mixing-controlled problems like non-premixed combustion. The rate of mixing is determined purely by turbulence and the small-scale coupling between mixing and chemical reaction is neglected. It is thus needed to assess the new challenges of mixing modeling in turbulent premixed combustion and develop new or improved mixing models to accurately describe the coupling between mixing and reaction in premixed combustion.

There have been a few attempts to develop mixing models in the transported PDF method for turbulent premixed combustion. Pope and Anand [215] developed models for mixing in two extreme combustion regimes, *i.e.*, distributed reaction and flamelet regimes. In the distributed reaction regime, turbulent mixing is dominant and the molecular transport effect is treated as that in the inert mixing case. The scalar mixing time scale is modeled as proportional to the turbulent time scale with a model constant,  $C_\phi$ . In the flamelet regime, the flame is assumed locally to be an undistributed laminar flame and then the molecular diffusion can be tabulated from the corresponding laminar flames. Recently, Kuron et al. [216] combined the two mixing models for the two extreme combustion regimes into a hybrid model. The new model is able to treat the transition from one mixing limit to the other. For inert mixing or turbulent dominant mixing process, large scale properties dominate and small scales effects are often negligible, while in flamelet regime of premixed combustion, the effects of small scale properties, such as chemical reaction and Kolmogorov eddies, on mixing are significant and need to be considered. Linstedt and Vaos [79] developed a mixing time scale model to incorporate the effects of small scale properties (the Kolmogorov

and local flame propagation velocities) and examined the model performance in flames F1 and F3. In the aforementioned models [79, 215, 216] for the mixing time scale, a model constant,  $C_\phi$ , needs to be pre-specified. A large variation in  $C_\phi$  values has been observed in different studies [167, 211]. To avoid the uncertainty in specifying constant  $C_\phi$  values, Stöllinger and Heinz [217] developed a model based on a transport equation that can be used for the mixing time scale in the thickened flame regime. They combined the transport equation based mixing time scale model for the thickened flame regime with an algebraic model by Kolla et al. [218] for the flamelet regime, and introduced a linear blending model for the mixing time scale which is believed to be more general and applicable to different regimes of turbulent premixed combustion. The aforementioned new developments of premixed combustion mixing models are all in the RANS modeling context. Recently, Wang et al. [219] developed a sub-filter scale mixing time scale model, called locally enhanced mixing by reaction (LER) model, in the LES modeling context for premixed combustion. The LER model is developed to incorporate the chemical kinetic effects on the sub-filter scale scalar mixing process. It models the sub-filter scale scalar mixing frequency as a power law of the LES filter size and this power-law scaling is supported by previous DNS studies [220]. Despite these recent developments, more efforts are still needed to examine and improve the transported PDF method for mixing modeling in turbulent premixed combustion.

The application of the PDF method to high-Ka number premixed combustion is even more limited. To the best of our knowledge, only few transported PDF studies of premixed combustion at high Ka numbers are reported in the literature. Dunn et al. [167] presented RANS/PDF calculations of the PPJB flames with  $Ka = 100 \sim 3500$  (defined as  $Ka = \tau_f / (\sqrt{15}\tau_\eta)$  in [153] and  $\tau_f$  is the unstrained laminar flame time scale) and studied the effects of constant  $C_\phi$  values with the EMST mixing model. Rowinski and Pope [165, 211] applied RANS/PDF and LES/PDF methods to study the PPJB flames. In these modeling studies, essentially the same set of sub-models were used for modeling the high-Ka turbulent premixed combustion as that used for non-premixed [206]. No work has been reported on developing mixing models that are suitable for high-Ka premixed combustion. This work

aims to advance the transported PDF method by developing and assessing mixing models for extreme combustion conditions with a high Ka number.

The modeling of sub-filter scale mixing for high-Ka combustion is fundamentally challenging. In particular, there is a significant gap in the understanding of the characteristics and scaling of high-Ka number combustion. A fundamental question to be answered is how the rate of sub-filter scale mixing depends on the LES filter size. Without a clear understanding of this dependence, it is difficult to develop regime-consistent mixing models. Wang et al. [219] formulated a power-law scaling of the mixing time scale based on existing DNS studies [220] and developed the LER model. The LER model is the first model of its kind for modeling the sub-filter scale mixing time scale in the transported PDF method for turbulent premixed combustion. The model has been examined in low or moderate Ka numbers. Its applicability to high-Ka combustion has not been examined so far. This work aims to gain fundamental scaling of high-Ka combustion by conducting an *a priori* examination of the power-law scaling model for the mixing time scale. Existing DNS database for high-Ka turbulent premixed flames will be used for the *a priori* study.

There have been several DNS studies reported on high-Ka combustion [32–41, 199]. Among these studies, the DNS flames in [32–37] are all limited to statistically one dimensional planar flames in homogeneous isotropic turbulence. Recently, the first non-trivial configuration in a high-Ka DNS jet flame was reported [38–41]. The DNS flame features an intense interaction between the turbulence and flame structures with  $Ka = 250$  at the jet exit and belongs to the distributed reaction zone regime in the Borghi diagram. In this work, we perform an *a priori* examination in the high-Ka DNS flame in terms of the sub-filter mixing time scale modeling in the LES/transported PDF method. The objective is to evaluate the extensibility of the LER model for the sub-filter mixing time to high-Ka combustion cases.

The rest of the paper is organized as follows. Section 5.2 discusses the LES/PDF method with a focus on the micro-mixing process modeling. Section 5.3 reports the examination results of sub-filter mixing time scale in the high-Ka DNS jet flame. Section 5.3.1 briefly summarizes the case conditions. Section 5.3.2 reports the DNS observations of the scaling

factor. Section 5.3.3 develops a new model, and compares the performance of the new model with existing models in an a priori examination. Finally, the conclusions are drawn in Section 5.4.

## 5.2 LES/PDF modeling of turbulent combustion

A combined LES/PDF methodology is chosen in this work as the baseline model for the study of the sub-filter scale mixing. The modeling approach is briefly reviewed in Section 5.2.1. The sub-filter scale mixing models are discussed in Section 5.2.2. The discussion on the modeling of the time scale for the sub-filter scale mixing is presented in Section 5.2.3.

### 5.2.1 LES/PDF method

In the combined LES/PDF method [206], the flow and turbulence fields are solved by using the LES method [135], and the combustion fields are described statistically by using the joint composition transported PDF method [206, 221]. Details about the combined LES/PDF model can be found in [117, 206] and previous applications of LES/PDF can be found in [14, 70, 117, 149, 206]. This work mainly focuses on the transported PDF model and we briefly summarize the method in the following.

In the transported PDF method, a single-point single-time joint composition PDF,  $f_\phi(\boldsymbol{\psi}; \mathbf{x}, t)$ , is used to represent the sub-filter scale distribution of random combustion fields  $\boldsymbol{\phi}(\mathbf{x}, t)$  at a spatial location  $\mathbf{x}$  and time  $t$ . The composition vector  $\boldsymbol{\phi} = \{\phi_\alpha, \alpha = 1, \dots, n_\phi\}$  consists of the mass fractions of species and the enthalpy, and  $\boldsymbol{\psi}$  is the corresponding composition sample space vector. The transport equation of the density-weighted sub-filter scale composition PDF,  $\tilde{f}_\phi(\boldsymbol{\psi}; \mathbf{x}, t)$ , is

$$\frac{\partial \bar{\rho} \tilde{f}}{\partial t} + \nabla \cdot (\bar{\rho} \tilde{\mathbf{u}} \tilde{f}) + \sum_\alpha \frac{\partial}{\partial \psi_\alpha} (\bar{\rho} S_\alpha(\boldsymbol{\psi}) \tilde{f}) = \nabla \cdot (\bar{\rho} \Gamma_t \nabla \tilde{f}) - \sum_\alpha \frac{\partial}{\partial \psi_\alpha} (\overline{(D_\alpha + C_\alpha)} | \boldsymbol{\psi} \bar{\rho} \tilde{f}), \quad (5.2.1)$$

where  $\overline{\square}$  and  $\tilde{\square}$  denote volume filtering and density-weighted filtering, respectively,  $\rho$  is density,  $D_\alpha = \frac{1}{\rho} \nabla \cdot (\rho \Gamma_\alpha \nabla \phi_\alpha)$  with  $\Gamma_\alpha$  is the molecular diffusivity of the  $\alpha$ th composition,

$S_\alpha$  is the chemical source term, and the summation rule is not implied here by the repeated indices in this work. In Eq. (5.2.1),  $C_\alpha = -\frac{1}{\rho} \nabla \cdot \left( \rho \sum_{\beta=1}^{n_{spec}} \Gamma_\beta \nabla \phi_\beta \right) \delta_{\alpha n_{spec}}$  is a correction term to ensure mass conservation in a multi-scalar diffusion system, where  $\delta_{\alpha n_{spec}}$  is the Kronecker delta implying all the mass correction is distributed to the last species, *i.e.*,  $N_2$ . In the current examination work,  $N_2$  is not considered and hence we only report the contribution of  $D_\alpha$  to the sub-filter scale mixing in the following. In Eq. (5.2.1),  $\tilde{\mathbf{u}} = \{\tilde{u}_i, i = 1, 2, 3\}$  is the resolved velocity vector, and the sub-filter scale part of the convection term is modeled by using the gradient model [99] with  $\Gamma_t$  being the sub-filter scale turbulent diffusivity and shown as the first term in the right-hand side of Eq. (5.2.1). The terms on the left-hand side are closed, including the highly nonlinear chemical source term, which is the most attractive feature of the transported PDF methods. The last term on the right-hand side is the conditional molecular diffusion term,  $\overline{D_\alpha | \boldsymbol{\psi}}$ , which is unclosed and requires modeling.

The conditional molecular diffusion term,  $\overline{D_\alpha | \boldsymbol{\psi}}$ , acting as a convective velocity in the high dimensional composition space in Eq. (5.2.1), represents the effects of molecular diffusion on the evolution of the joint PDF distribution of combustion fields. Molecular diffusion is a fundamentally important physical process in turbulent combustion, which enables chemical reaction by transporting the fresh reactants and the combustion products around the flame front and mixing them at the molecular scale. The rate of the molecular diffusion process depends on the molecular diffusivity as well as the scalar gradient distribution which is highly dependent on turbulence and chemical reaction, especially in and near the flame front. From the computational perspective, molecular diffusion occurs at the molecular scale and cannot be resolved in LES, and hence modeling is required. Besides, the driving force of molecular diffusion is the spatial non-uniformity, while the single-point PDF contains no sub-filter scale spatial gradient information, and therefore a model is required for the conditional molecular diffusion term in the LES/PDF method. The assessment and development of models for the unclosed conditional molecular diffusion term are the focus of this work.

## 5.2.2 Mixing models for conditional molecular diffusion

To model the conditional molecular diffusion term  $\overline{D_\alpha|\boldsymbol{\psi}}$  in Eq. (5.2.1), two different modeling strategies [99, 155, 175, 176] are usually adopted as shown in the following equations (5.2.2) and (5.2.3).

$$-\sum_{\alpha} \frac{\partial}{\partial \psi_{\alpha}} \left( \overline{\tilde{\rho} \tilde{f} D_{\alpha}|\boldsymbol{\psi}} \right) \approx \nabla \cdot \left( \overline{\tilde{\rho} \Gamma \nabla \tilde{f}} \right) - \sum_{\alpha} \sum_{\beta} \frac{\partial^2}{\partial \psi_{\alpha} \partial \psi_{\beta}} \left[ \overline{\tilde{\rho} \tilde{f} \Gamma \nabla \phi_{\alpha} \cdot \nabla \phi_{\beta}|\boldsymbol{\psi}} \right] \quad (5.2.2)$$

$$-\sum_{\alpha} \frac{\partial}{\partial \psi_{\alpha}} \left( \overline{\tilde{\rho} \tilde{f} D_{\alpha}|\boldsymbol{\psi}} \right) \approx -\sum_{\alpha} \frac{\partial}{\partial \psi_{\alpha}} \left[ \tilde{f} \nabla \cdot \left( \overline{\tilde{\rho} \Gamma_{\alpha} \nabla \tilde{\phi}_{\alpha}} \right) + \overline{\tilde{\rho} \tilde{f} \frac{1}{\rho} \nabla \cdot \left( \rho \Gamma_{\alpha} \nabla \phi_{\alpha}'' \right) |\boldsymbol{\psi}} \right] \quad (5.2.3)$$

In the first strategy in Eq. (5.2.2) [99, 175], the conditional molecular diffusion term in Eq. (5.2.1), is split into two parts, the molecular diffusion of the joint PDF in the physical space,  $\nabla \cdot \left( \overline{\tilde{\rho} \Gamma \nabla \tilde{f}} \right)$ , and the conditional dissipation term in the composition space,  $-\sum_{\alpha} \sum_{\beta} \frac{\partial^2}{\partial \psi_{\alpha} \partial \psi_{\beta}} \left[ \overline{\tilde{\rho} \tilde{f} \Gamma \nabla \phi_{\alpha} \cdot \nabla \phi_{\beta}|\boldsymbol{\psi}} \right]$ . In this modeling strategy, equal molecular diffusivity for different species  $\alpha$  has to be assumed  $\Gamma_{\alpha} = \Gamma$  and hence it cannot treat differential molecular diffusion (DMD). The random walk model [175] has been frequently used to treat the diffusion of the PDF with equal molecular diffusivity. The conditional dissipation term in Eq. (5.2.2) is not closed and requires modeling. The importance of DMD, however, is not diminished in many cases [103–109]. In the second modeling strategy in Eq. (5.2.3), McDermott and Pope [176] proposed a new model called the mean shift (MS) model where the conditional molecular diffusion term is split into a resolved part,  $\frac{1}{\tilde{\rho}} \nabla \cdot \left( \overline{\tilde{\rho} \Gamma_{\alpha} \nabla \tilde{\phi}_{\alpha}} \right)$ , and a sub-filter scale part,  $\overline{\frac{1}{\rho} \nabla \cdot \left( \rho \Gamma_{\alpha} \nabla \phi_{\alpha}'' \right) |\boldsymbol{\psi}}$ , to account for the spatial effect of DMD. The resolved part is closed and can be treated by the mean shift model, and the second part is not closed and requires modeling.

The second terms on the right-hand side of Eqs. (5.2.2) and (5.2.3) are not closed. They are typically referred as the sub-filter scale mixing term and are modeled in the same way although they are not identical. Different sub-filter scale mixing models are available, such as the interaction by exchange with the mean (IEM) model [85], the modified Curl model [82], the Euclidean minimum spanning tree (EMST) model [84], and the shadow

position mixing model (SPMM) [222]. The IEM model formulation is shown in Eqs. (5.2.4) and (5.2.5),

$$-\sum_{\alpha} \sum_{\beta} \frac{\partial^2}{\partial \psi_{\alpha} \partial \psi_{\beta}} \left[ \overline{\tilde{\rho} \tilde{f} \Gamma \nabla \phi_{\alpha} \cdot \nabla \phi_{\beta} | \Psi} \right] \approx \sum_{\alpha} \frac{\partial}{\partial \psi_{\alpha}} \left[ \Omega_{\alpha} \left( \psi_{\alpha} - \tilde{\phi}_{\alpha} \right) \tilde{\rho} \tilde{f} \right], \quad (5.2.4)$$

$$-\sum_{\alpha} \frac{\partial}{\partial \psi_{\alpha}} \left[ \overline{\tilde{\rho} \tilde{f} \frac{1}{\rho} \nabla \cdot (\rho \Gamma_{\alpha} \nabla \phi_{\alpha}'' | \Psi} \right] \approx \sum_{\alpha} \frac{\partial}{\partial \psi_{\alpha}} \left[ \Omega_{\alpha} \left( \psi_{\alpha} - \tilde{\phi}_{\alpha} \right) \tilde{\rho} \tilde{f} \right], \quad (5.2.5)$$

where  $\Omega_{\alpha}$  is the mixing frequency of  $\alpha$ th scalar for the sub-filter scale mixing process, representing the rate of mixing process. Determining the rate of mixing is critically important for turbulent combustion modeling. This work focuses on the modeling of the mixing frequency for turbulent premixed combustion with a high Ka number.

### 5.2.3 Models for sub-filter scale mixing frequency

The sub-filter scale mixing causes the decaying of the sub-filter scale scalar variance in turbulent combustion, the contribution of which is illustrated in a simple pure mixing process as follows,

$$\frac{d \overline{\tilde{\rho} \phi_{\alpha}''^2}}{dt} = -\bar{\rho} \chi_{\alpha} = -2\bar{\rho} \Omega_{\alpha} \overline{\tilde{\rho} \phi_{\alpha}''^2}, \quad (5.2.6)$$

which is derived from the transported PDF equation (5.2.1) with a sub-filter scale mixing model, e.g., Eq. (5.2.4) or (5.2.5), and  $\bar{\rho} \chi_{\alpha} = \overline{2\rho \Gamma_{\alpha} \nabla \phi_{\alpha} \cdot \nabla \phi_{\alpha}} - 2\bar{\rho} \overline{\Gamma_{\alpha} \nabla \tilde{\phi}_{\alpha} \cdot \nabla \tilde{\phi}_{\alpha}}$ .

A widely used model is

$$\Omega_{\alpha} = \frac{C_{\phi} \Gamma_t}{2\Delta^2}, \quad (5.2.7)$$

where  $\Delta$  is the LES filter size,  $C_{\phi}$  is the model constant, and a commonly used value  $C_{\phi} = 3.0$  [117] is specified in this study as well as a much larger value  $C_{\phi} = 30.0$ . The mixing frequency model in Eq. (5.2.7) assumes equal sub-filter scale mixing frequency for all the scalars,  $\Omega_{\alpha} = \Omega$ , as in most of previous PDF studies. In current work, we consider the dependence of sub-filter scale mixing frequency  $\Omega_{\alpha}$  on different scalars  $\alpha$  and further examine the sub-filter scale DMD effects.

The mixing frequency model in Eq. (5.2.7) has been widely used in LES modeling of turbulent non-premixed combustion. Wang et al. [219] questioned the general applicability

of the model to turbulent premixed combustion and developed the LER model that is suitable for both turbulent premixed and non-premixed combustion. The model is proposed based on DNS observations [220] and capable of incorporating the dependence of mixing frequency on the LES filter size and the characteristic flame length scale hence chemical effects on mixing. The LER model is

$$\Omega_\alpha = \frac{C_\phi \Gamma_t}{2\Delta^2} \left[ 1 - \vartheta + \vartheta \cdot F \left( \frac{\Delta}{\delta_{th}} \right) \right], \quad (5.2.8)$$

where  $\vartheta$  is the flame index and  $F(\Delta/\delta_{th})$  is the scaling factor introduced in

$$\bar{\rho} \chi_\alpha = 2\bar{\rho} \widetilde{\Gamma}_\alpha \left( \frac{\partial \widetilde{\phi}_\alpha}{\partial x_i} \right)^2 \cdot (F - 1), \quad (5.2.9)$$

and it is modeled as a piecewise function in the LER model as

$$F \left( \frac{\Delta}{\delta_{th}} \right) = \begin{cases} \left( \frac{\Delta}{\delta_{th}} \right)^a & \text{if } \Delta > \delta_{th}, \\ 1 & \text{if } \Delta \leq \delta_{th}, \end{cases} \quad (5.2.10)$$

where  $\delta_{th}$  is unstrained laminar flame thermal thickness, and  $a$  is a model constant and specified to be  $a = 2$  in [219]. It is worth noting that in the work we deal with the sub-filter scale mixing process and  $\chi_\alpha$  in Eq. (5.2.9) is the sub-filter scale scalar dissipation rate, and therefore we have minus one here to be consistent with the  $F$  definition in [219]. At the DNS limit,  $\Delta \rightarrow 0$ , mixing at all scales is resolved, and therefore  $F = 1$  and  $\Omega_\alpha = 0$ . The piecewise formula of  $F$  in Eq. (5.2.10) in LER model is supported by the data from a DNS turbulent premixed flame at  $Ka \approx 10$  [220]. The flame index  $\vartheta$  is introduced in Eq. (5.2.8) to have a general model suitable for multi-regime combustion, both non-premixed and premixed. It is equal to zero for turbulent non-premixed combustion and as a result, the LER model in Eq. (5.2.8) is equivalent to the conventional model in Eq. (5.2.7); it is equal to one for turbulent premixed combustion and the scaling factor model in Eq. (5.2.10) is employed to incorporate the dependence of mixing frequency on the LES filter size and the characteristic flame length scale hence chemical effects on mixing in turbulent premixed combustion.

The LER model in Eq. (5.2.8) has been applied to predict turbulent premixed flames F1 and F3 in [219], and shows improved prediction accuracy compared with the conventional model in Eq. (5.2.7). However, flames F1 and F3 are at relatively low Ka numbers, as well as the previous DNS support in [220]. A model that is suitable for sub-filter scale mixing frequency in high-Ka combustion is still missing.

In this work, we perform an a priori examination of sub-filter scale mixing frequency scaling in a high-Ka DNS jet flame [38–41], and assess if the existing models are able to reproduce the observed scaling behaviors of the DNS data. In the following, Section 5.3.1 briefly summarizes the configuration of the high-Ka DNS jet flame and presents an overview of the sub-filter scale mixing in the high-Ka DNS jet flame. The observations of the sub-filter scale mixing frequency in the DNS flame are reported in Section 5.3.2, and the model assessment results are presented in Section 5.3.3.

### 5.3 Examination of sub-filter scale mixing frequency modeling in DNS flames

#### 5.3.1 A high-Ka turbulent premixed DNS jet flame

A three-dimensional (3-D) high-Ka turbulent premixed DNS jet flame [38–41] is selected for the examination of sub-filter scale mixing frequency. The DNS flame is calculated by using a compressible 3-D DNS code, S3D [223]. The detailed case configuration and DNS results have been reported in [38–41]. In this work, we briefly summarize the case setup and focus on the sub-filter scale mixing frequency analysis.

The flame is a two-stream  $\text{CH}_4/\text{air}$  jet flame. Fresh  $\text{CH}_4/\text{air}$  mixture stream at  $\Phi = 0.7$  and  $T_j = 300$  K comes out of the round jet with a bulk velocity  $U_b = 110$  m/s. The diameter of the jet is  $D = 1.5$  mm. The corresponding bulk Reynolds number is  $\text{Re}_b = 10,500$ . A high temperature ( $T_c = 1800$  K) laminar coflow stream, which is composed of the combustion products of  $\text{CH}_4/\text{air}$  mixture at  $\Phi_c = 0.9$ , at a velocity  $U_c = 1.8$  m/s is used to stabilize the flame. The experimental measurement of a series of flames with similar configuration can be found in [196–198]. In DNS simulations, a reduced GRI-Mech 3.0 mechanism [224] is used to describe the chemistry. The mechanism has 268 elementary

reactions and 44 species, 16 of which are determined with the quasi-steady state assumption. The transport of the other 28 species is solved directly with constant Lewis numbers.

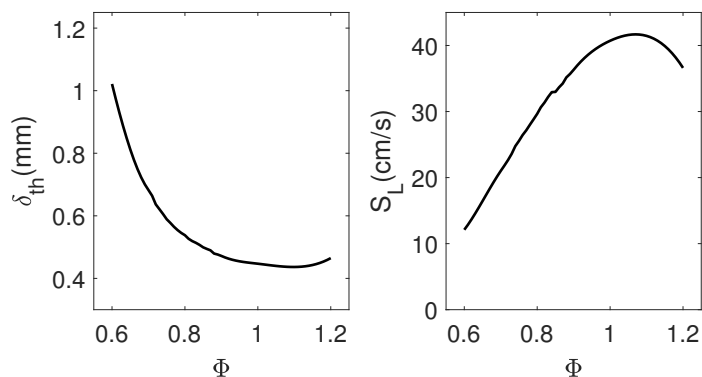


Figure 5.1. Laminar flame thermal thickness and laminar flame speed,  $\delta_{th}$  and  $S_L$ , of  $\text{CH}_4/\text{air}$  mixtures at different equivalence ratios  $\Phi$  and at  $T = 300$  K and  $P = 1$  atm.

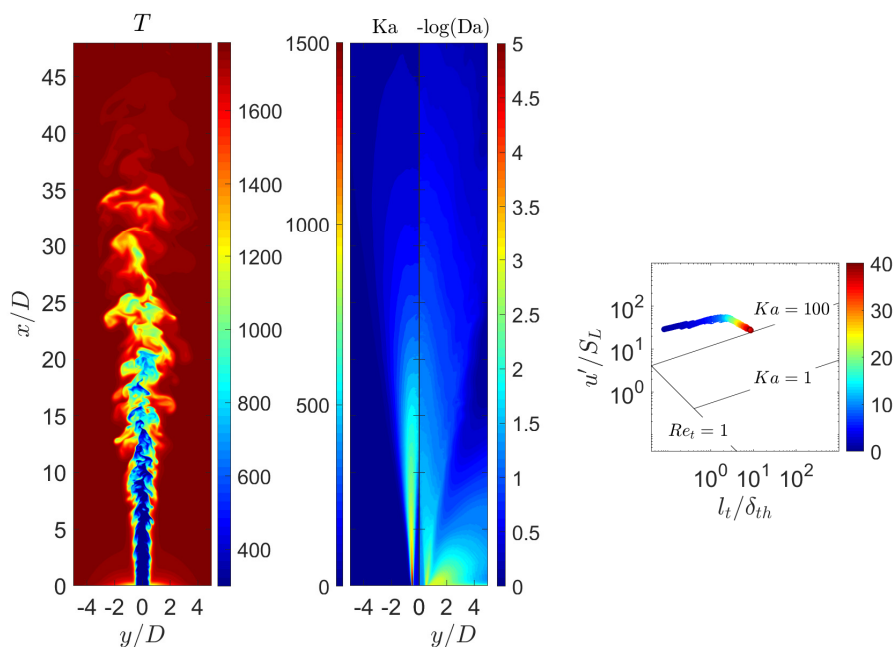


Figure 5.2. Contours of instantaneous temperature  $T$ ,  $Ka$  and  $-\log(Da)$  in the DNS flame, and the location of the DNS flame in the Borghi diagram.

The inflow velocity of the central jet is prescribed as a mean velocity distribution plus a turbulence field. The mean velocity is approximated as a power-law profile. The turbulence field is obtained from a prescribed Passot-Pouquet energy spectrum with a turbulent velocity  $u' = 4$  m/s and an integral length scale  $l_t = 0.75$  mm. A hyperbolic tangent function profile is used to specify the inflow conditions of temperature and species for both jet and coflow streams. More details can be found in [38–41]. The computational domain is  $48D \times 36D \times 36D$  in  $x$  (streamwise),  $y$  (lateral), and  $z$  (lateral) directions. The corresponding numbers of grid cells in the three directions are 2400, 900, and 900, respectively. The grid distribution is uniform in  $x$ -direction with a cell size  $\Delta x = 0.02D$ . In the other two directions, the grid cell size is uniform from  $-5D$  to  $5D$  with  $\Delta y (\Delta z) = 0.02D$  and then stretching outside.

Dimensionless numbers,  $Ka = \tau_C/\tau_\eta$ ,  $Re_t = u'l_t/\nu$  and  $Da = \tau_t/\tau_C$ , are typically used to describe the interactions between turbulence and flame structures in turbulent premixed flame. Here  $\tau_t$  is the integral time scale,  $\tau_t = l_t/u'$ . The Komolgorov time scale is defined as  $\tau_\eta = \sqrt{\nu/\epsilon}$ , and the chemical time scale is defined as  $\tau_C = \delta_{th}/S_L$ , where the laminar flame thermal thickness is  $\delta_{th} = (T_{ad} - T_0)/\max(\partial T/\partial x)$ , and  $S_L$  is the laminar flame speed. The profiles of  $\delta_{th}$  and  $S_L$  for  $CH_4$ /air mixtures at varying  $\Phi$  are shown in Fig. 5.1. The three dimensionless variables are related via  $Re_t = Ka^2 Da^2$ , two of which are therefore usually used to describe the flame. In this flame, we have  $Ka = 250$  and  $Da = 0.054$  based on the jet inflow turbulence and the laminar flame conditions. At the other flame locations,  $Ka$  varies between  $100 \sim 1500$  and  $Da$  varies between  $10^{-3} \sim 10^{-1}$ , as shown in Fig. 5.2. This suggests the flame locates in the distributed/broken reaction zone in the Borghi diagram, which is also shown in Fig. 5.2 and the data points are taken from the maximum radial gradient of mean temperature location along the axial direction. The diagram plot is adjusted following [41,225] due to the different laminar flame thicknesses  $\delta_{th}$  used here and in the original Borghi diagram work where  $\delta_L = \nu/S_L$ .

In LES studies of turbulent combustion, models are needed to describe the unresolved sub-filter scale physical processes including the sub-filter scale mixing. Fig. 5.3 shows the filtered temperature  $\tilde{T}$  and the sub-filter scale RMS temperature,  $\sqrt{T''^2}$ , at  $\Delta = 21\Delta_{DNS}$  in the DNS flame.  $\Delta_{DNS}$  is the DNS grid resolution. The relative sub-filter scale temperature

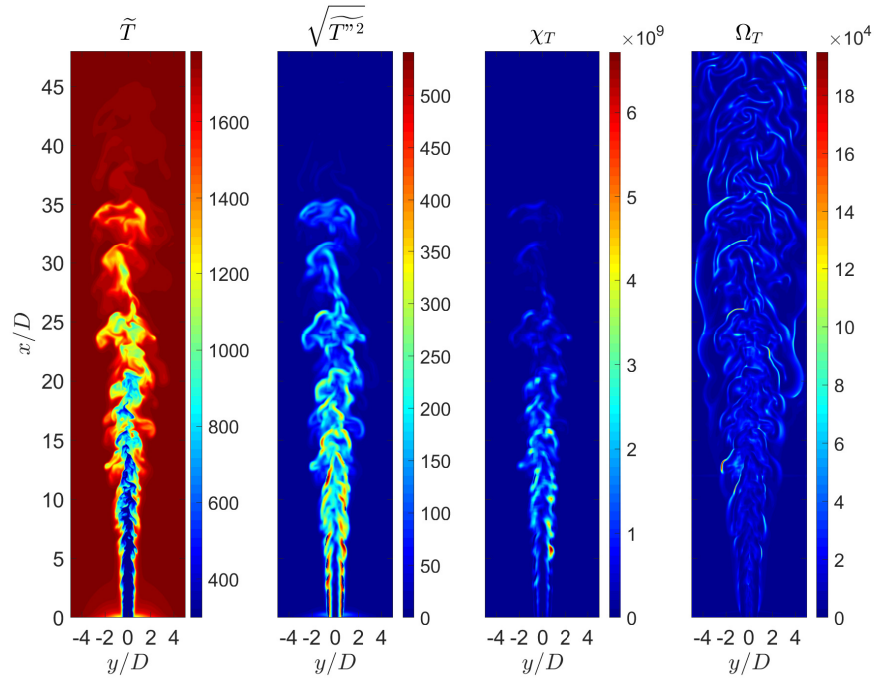


Figure 5.3. Contours of the filtered temperature, the sub-filter scale RMS temperature  $\sqrt{T''^2}$ , the sub-filter scale scalar dissipation rate  $\chi_T$ , and the sub-filter scale mixing time scale  $\Omega_T$  in the DNS flame at a filter size  $\Delta = 21\Delta_{DNS}$ .

fluctuation is around 30%, which implies the non-negligible contribution of the sub-filter scale processes. In the sub-filter scale mixing process, the sub-filter scale fluctuations decay due to sub-filter scale molecular and turbulence transport. The decaying rate of the sub-filter scale fluctuations can be represented by a sub-filter scale scalar dissipation rate,  $\chi_\alpha$ , or a sub-filter scale mixing frequency,  $\Omega_\alpha$ , as in Eq. (5.2.6), which are also shown in Fig. 5.3 for temperature,  $\alpha = T$ . In turbulent non-premixed combustion, the sub-filter scale mixing rate is largely determined by turbulent mixing and the mixing frequency model in Eq. (5.2.7) usually performs well. In turbulent premixed combustion, however, chemical reaction can have significant effects on the sub-filter scale mixing process which is highly dependent on the relative magnitudes of  $\delta_{th}$  and  $\Delta$ . Besides, in LES practices, nonuniform LES filter sizes, also varying from case to case, are typically used. Then a fundamentally and practically important question to ask is how the sub-filter scale mixing frequency  $\Omega_\alpha$  varies

with the LES filter size  $\Delta$ . In the following section, we answer this question by examining the statistical scaling of the sub-filter scale mixing frequency in the high-Ka DNS jet flame, and aim to provide implications for the future sub-filter scale mixing modeling in high-Ka combustion. Box filtering is applied in this work with 25 filter widths uniformly varying in the range  $\Delta \in [\Delta_{DNS}, 49\Delta_{DNS}]$ , where  $\Delta = 49\Delta_{DNS} = 0.98D$  is about  $1.5\delta_{th}(\phi = 0.7)$ .

### 5.3.2 Examination of sub-filter scale mixing frequency

#### Statistical views

In previous DNS studies [220, 226] of statistically one-dimensional planar turbulent premixed flames, the power-law scaling is observed for the scaling factor of the filtered scalar dissipation rate from a volume-averaged,  $\langle \cdot \rangle_V$ , statistical view,

$$\Xi_\alpha = \frac{\langle \widetilde{\rho\chi}_\alpha \rangle_V}{\left\langle 2\widetilde{\rho}\widetilde{\Gamma}_\alpha \left( \frac{\partial \widetilde{\phi}_\alpha}{\partial x_i} \right)^2 \right\rangle_V} = \left( \frac{\Delta}{\delta_{th}} \right)^a. \quad (5.3.1)$$

The power-law scaling observation in Eq. (5.3.1) has been borrowed in the LER model [219] in Eq. (5.2.8) for the modeling of sub-filter scale mixing frequency at turbulent premixed combustion with relatively small Ka numbers. In the current examination of the sub-filter scale mixing frequency in high-Ka combustion, we follow the statistical view as,

$$F_\alpha = \frac{\langle \Omega_\alpha \rangle_{\mathbf{X}}}{\langle \Omega_{\alpha,ref} \rangle_{\mathbf{X}}} + 1, \quad (5.3.2)$$

where  $\Omega_{\alpha,ref} = \frac{2\widetilde{\rho}\widetilde{\Gamma}_\alpha \left( \frac{\partial \widetilde{\phi}_\alpha}{\partial x_i} \right)^2}{2\widetilde{\rho}\widetilde{\phi}_\alpha'^2}$  is the reference mixing frequency based on resolved quantities, and  $\langle \cdot \rangle_{\mathbf{X}}$  represents averaging operation in  $\mathbf{X}$  dimensions. Previously [220], a single value of  $a$  as in Eq. (5.2.10) is obtained from the volume-averaged view, *i.e.*,  $\langle \cdot \rangle_{\mathbf{X}} = \langle \cdot \rangle_{x,r,\theta,t}$ , where  $(x, r, \theta, t)$  represent axial, radial, azimuthal spatial directions, and time, respectively. It has been found that the power-law scaling model with a single global  $a$  is insufficient to represent the local flame properties [220, 226] and therefore Gao et al. [226] proposed a dynamic procedure to obtain the model constant  $a$  which allows for spatial variations. In

this work, we examine the spatial dependence of sub-filter scale mixing frequency in the DNS data and aim to provide useful observations for future modeling. To observe local variations, the statistics in Eq. (5.3.2) are calculated by performing average in time,  $t$ , and the statistically homogeneous direction,  $\theta$ , *i.e.*,  $\langle \cdot \rangle_{\mathbf{X}} = \langle \cdot \rangle_{\theta,t}$ . In turbulent premixed jet flames, the interactions between turbulence and flame structures vary significantly along the axial direction. For example, it has been shown that eddies have an accumulating effect in flame structures [193]. By examining the sub-filter scale mixing frequency in a local view,  $\langle \cdot \rangle_{\theta,t}$ , useful implications can be made for the future sub-filter scale mixing frequency modeling to incorporate the streamwise effects.

### DNS observations of the scaling factor

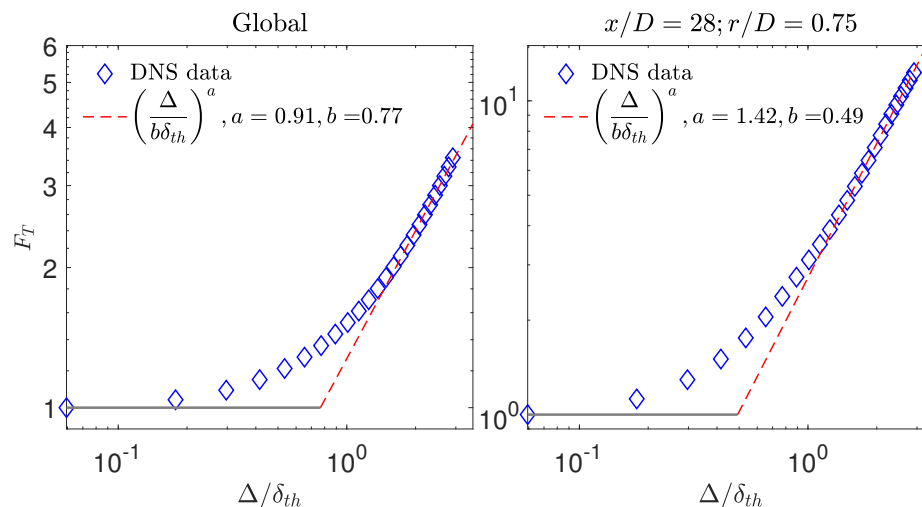


Figure 5.4. Sub-filter scale mixing scaling factor for temperature  $F_T$  from a global view (left), and a local view (right) at  $x/D = 28$ ,  $r/D = 0.75$ .

Following the definition in Eq. (5.3.2), Fig. 5.4 shows the sub-filter scale mixing scaling factor of temperature,  $F_T$ , against the normalized LES-filter size  $\Delta/\delta_{th}$ . The left subplot shows the global volume-averaged ( $\langle \cdot \rangle_{x,r,\theta,t}$ ) results, and the right subplot shows the local-averaged ( $\langle \cdot \rangle_{\theta,t}$ ) results at a spatial location  $x/D = 28$  and  $r/D = 0.75$ . It is observed

that in both cases, when  $\Delta/\delta_{th}$  is large, the DNS data points are clustered along a straight line on the log-log plot, which suggests that the DNS scaling factor  $F_T$  follows a power-law scaling of  $\Delta/\delta_{th}$ . This observation, consistent with previous observations in the DNS flames at relatively low Ka numbers and with simple geometries [220, 226], suggests that a simple power-law scaling model can be used to represent the statistical relationship between the sub-filter scale mixing frequency and the LES-filter size. Also observed in Fig. 5.4 is that when  $\Delta$  is approaching 0, the scaling factor  $F_T$  is approaching 1 as expected since at the limit of  $\Delta \rightarrow 0$ , *i.e.*, DNS limit, turbulence and flame structures are resolved hence no sub-filter scale mixing modeling is required. Apart from the similarities, a difference is observed in the inner cutoff scale of the power-law fitting between the current study and previous studies. In [220, 226], the inner cutoff scale is  $\delta_{th}$ , while the inner cutoff scale of the power-law fitting curve in Fig. 5.4 is  $b\delta_{th}$  with a parameter  $b < 1$ . Parameter  $b$  is related to the local flame length scale, more discussions on which are provided later in the paper.

The power-law scaling observed in Fig. 5.4 is for a specific scalar,  $T$ , at a specific spatial location,  $x/D = 28$  and  $r/D = 0.75$ . In the following, we present a more thorough examination to explore if similar observations can be made at other spatial locations and for more scalars.

Fig. 5.5 shows the scaling factor of temperature  $F_T$  from DNS data against  $\Delta/\delta_{th}$  at more spatial locations. Four axial locations ( $x/D = 4, 16, 28, 40$ ) and 12 radial locations ( $r/D = 0.01 \sim 3.49$ ) are selected covering the whole flame. The DNS data points at large  $\Delta/\delta_{th}$  values are generally observed to cluster around the straight lines in the log-log plots indicating a power-law distribution. Some differences are observed at the upstream location shown as the red circles and red lines,  $x/D = 4$ , where the influence of inflow boundary condition is still significant. Another interesting observation is that the scaling factors at three axial locations ( $x/D = 16, 28, 40$ ) are getting closer as moving away from the centerline. The observation suggests a spatial dependence of the scaling factor which is examined further in Figs. 5.7 and 5.8. Similar observations are made for other scalars (not shown here). It is also observed that the current piecewise fitting in Figs. 5.4 and 5.5 is a good fitting for the DNS data points in two limits, *i.e.*,  $\Delta \rightarrow 0$  and  $\Delta > \delta_{th}$ , but not for

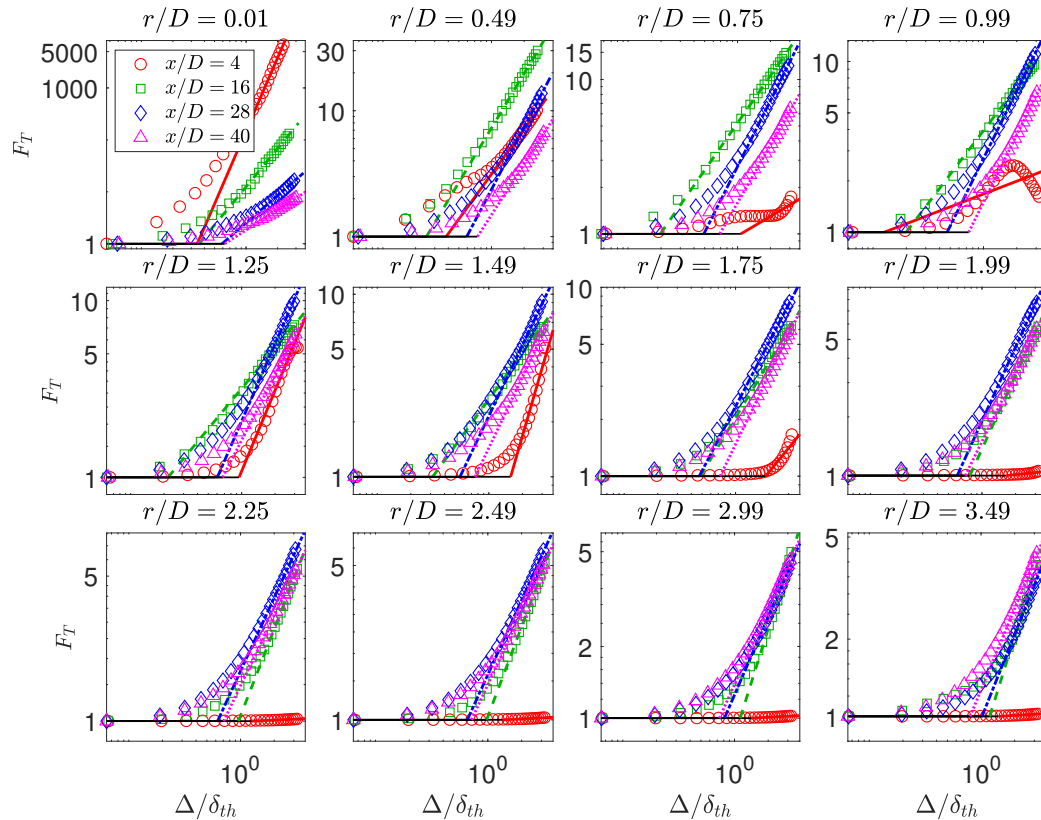


Figure 5.5. Sub-filter scale mixing scaling factor for temperature  $F_T$  at multiple spatial points (symbols: DNS data; lines: power-law fitting curves).

the DNS data points in between. In an attempt to represent these intermediate data points, a blending fitting curve in the form of  $1 + [\Delta/(b\delta_{th})]^a$  is introduced. Fig. 5.6 shows the scaling factor  $F_\alpha$  for species mass fractions and the new curve fitting results at the same axial locations as in Fig. 5.5 and a single radial location at  $r/D = 0.75$  which is near the flame front. It is seen that the DNS data points can be fitted well into the power-law based blending function.

The observed nice fitting of the scaling factor  $F_\alpha$  on  $\Delta/\delta_{th}$  in Figs. 5.4, 5.5 and 5.6 suggests that the sub-filter scale mixing frequency can potentially be represented well by a power-law based model with two parameters,  $a$  and  $b$ , in the high-Ka DNS jet flame. It is also seen in Figs. 5.5 and 5.6 that the distribution of  $F_\alpha$  varies at different locations and among different scalars. It is important to measure the spatial and scalar dependence

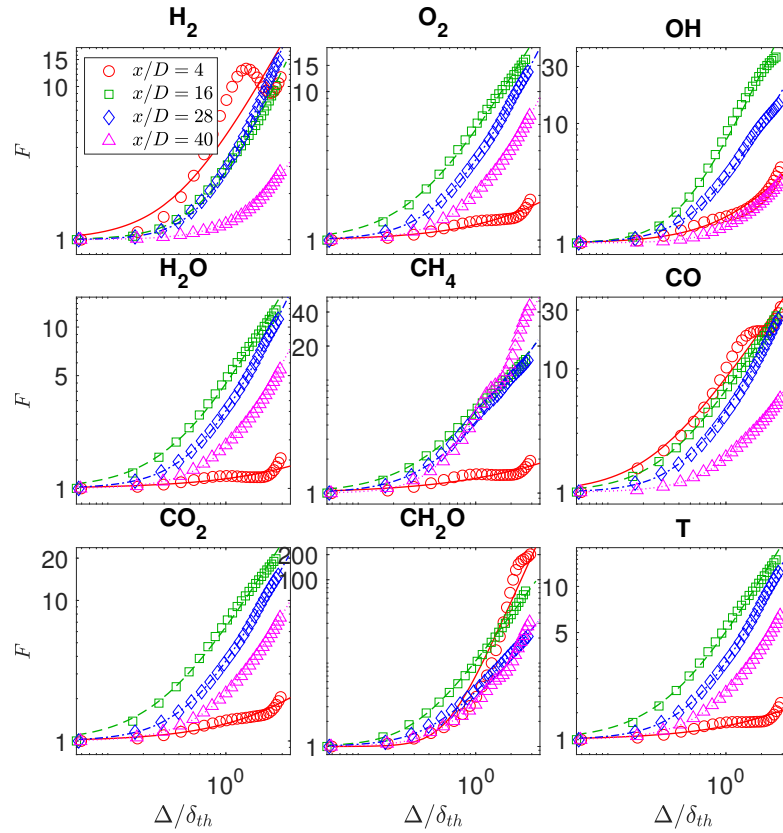


Figure 5.6. Sub-filter scale mixing scaling factor for multiple scalars at multiple spatial points (symbols: DNS data; lines: power-law based fitting curves  $1 + [\Delta/(b\delta_{th})]^a$ ).

quantitatively for future modeling studies. In the following, we examine the dependence by looking at the distributions of parameters  $a$  and  $b$  of the power-law fitting curves in space and among different scalars.

Figs. 5.7 and 5.8 show the radial profiles of parameters  $a$  and  $b$  at four axial locations ( $x/D = 4, 16, 28, 40$ ) and for nine scalars (mass fractions of  $\text{CH}_4$ ,  $\text{O}_2$ ,  $\text{H}_2$ ,  $\text{H}_2\text{O}$ ,  $\text{CO}$ ,  $\text{CO}_2$ ,  $\text{OH}$  and  $\text{CH}_2\text{O}$ , and temperature  $T$ ). Parameters  $a$  and  $b$  are from the power-law based fitting curve  $1 + [\Delta/(b\delta_{th})]^a$  of the DNS data, as these in Fig. 5.6. Only the data at the flame region are shown in the figures, which is represented by the mean temperature as  $\langle T \rangle_{\theta,t} - \langle T \rangle_{\theta,t}^{\min} \leq 0.95 \cdot (\langle T \rangle_{\theta,t}^{\max} - \langle T \rangle_{\theta,t}^{\min})$ . The radial profiles of  $\langle T \rangle_{\theta,t}$  are shown in the middle subplot of Fig. 5.9. Parameter  $a$  in Fig. 5.7 is found to significantly in the

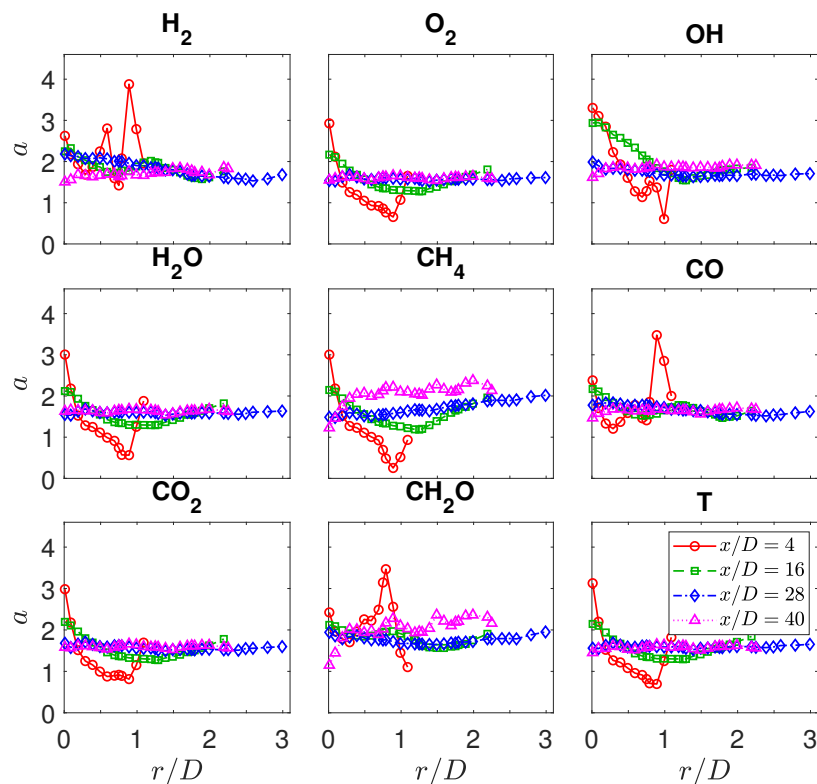


Figure 5.7. Radial profiles of the fitting parameter  $a$  at four axial locations  $x/D = [4, 16, 28, 40]$  for multiple scalars.

radial direction at the upstream location ( $x/D = 4$ ). The radial variation of  $a$  decreases at the downstream locations and  $a$  approaches to a constant,  $a \approx 1.5$ , at  $x/D = 28$  and  $x/D = 40$ , the value of which is similar among the different scalars. Parameter  $b$  in Fig. 5.8 is found to vary between 0 and 4 among all the scalars and at the flame region. The spatial variation of parameter  $b$  is also decaying along the streamwise direction; however, a relatively larger radial variation in parameter  $b$  is observed, compared to  $a$ . Parameter  $b$  is related to the local flame length scale  $\delta_{th}$ . There exist multiple ways of defining flame length scale. The difference in these definitions can cause the difference in parameter  $b$ . In this work, it is defined as the unstrained thermal laminar flame thickness in Fig. 5.1 at the local mean equivalence ratio  $\langle \Phi \rangle_{\theta,t}$ ,  $\delta_{th} = \delta_{th}(\langle \Phi \rangle_{\theta,t})$ , to consider the local variation of the flame length scale due to the compositional stratification. Radial profiles of  $\langle \Phi \rangle_{\theta,t}$

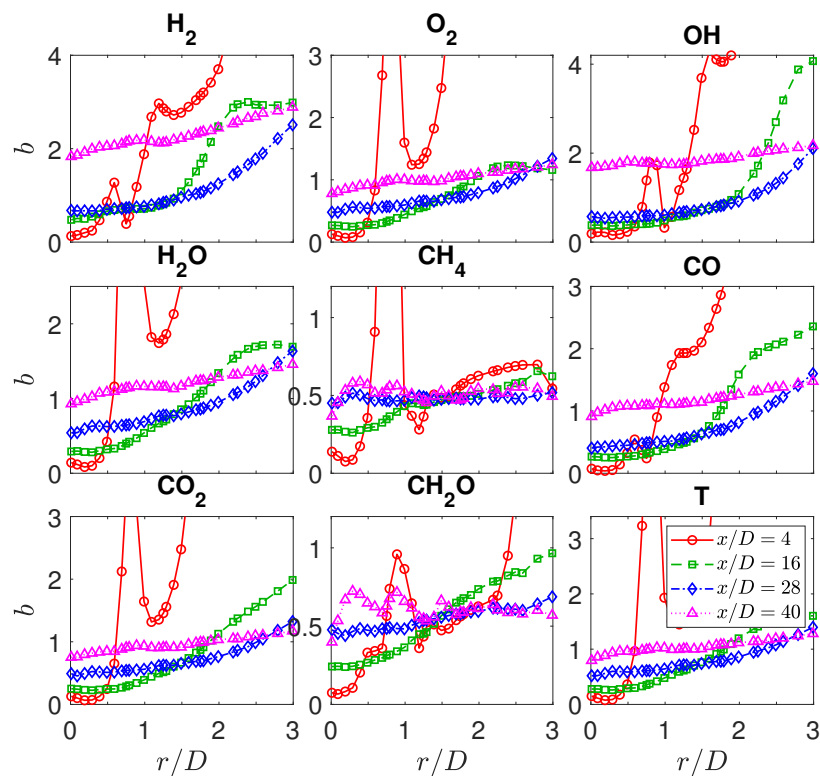


Figure 5.8. Radial profiles of the fitting parameter  $b$  at four axial locations  $x/D = [4, 16, 28, 40]$  for multiple scalars.

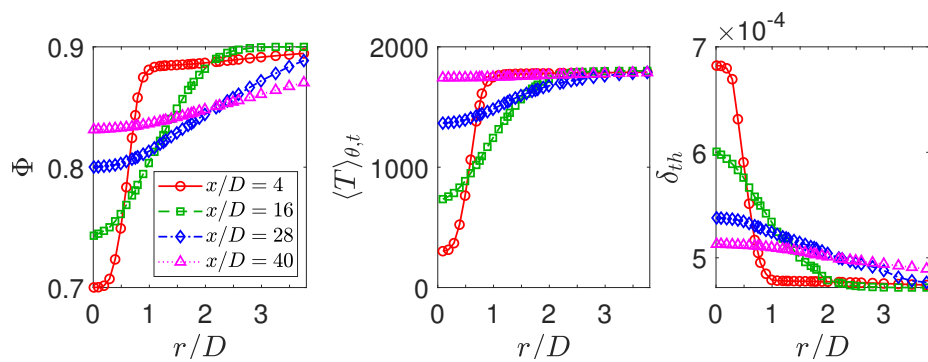


Figure 5.9. Radial profiles of the mean equivalence ratio  $\Phi$ , mean temperature  $\langle T \rangle_{\theta,t}$ , and local flame length scale  $\delta_{th}(\Phi)$ , at four axial locations  $x/D = [4, 16, 28, 40]$ .

and  $\delta_{th}$  are shown in Fig. 5.9. However, in the high-Ka jet flame, the coflow mixtures at  $\Phi = 0.9$  are the combustion products instead of fresh reactants; as a result, the flame length scale is unclear, which suggests a potential direction to improve the local flame length scale definition in future. Also, a clear difference among the scalars is observed in  $b$  distribution, which implies the scaling dependence of  $b$  on the characteristic flame length scale related to individual scalars. Further explorations on parameter  $b$  are needed in future work.

### 5.3.3 Assessment of sub-filter scale mixing frequency models

In the previous section, we examine the statistical scaling of the sub-filter mixing scaling factor  $F_\alpha$  in LES filter size for different scalars and at different spatial locations. The scaling factor results are found to follow a power-law scaling at large  $\Delta$  values and approach one at  $\Delta \rightarrow 0$ , and fit into a blending power-law based fitting curve of the two limits well for all the  $\Delta$ . In this section, we examine if these statistical behaviors can be represented by existing models, propose new models based on the observation, and conduct an *a priori* evaluation of the new models.

#### The scaling factor

We start with the models for the sub-filter scale mixing scaling factor. The model evaluated first is the piecewise function in Eq. (5.2.10) of the LER model. Fig. 5.10 shows the scaling factor of temperature  $F_T$  from DNS data and LER model with the model parameter  $a = 2$ . The left subplot shows the global view result and the right subplot shows the result from a single spatial location at  $x/D = 28$  and  $r/D = 0.75$ . In both cases, the LER model shown as the blue dash-dotted lines is largely deviated from the DNS data. The gray pattern shaded area represents the LER model with the parameter  $a$  varying from 1 to 10. None of these lines is close to the DNS data. This suggests that the LER model with a single model constant  $a$  can not represent the statistical scaling of the scaling factor  $F_T$  in this high-Ka DNS jet flame well. We know from the previous section that the data points

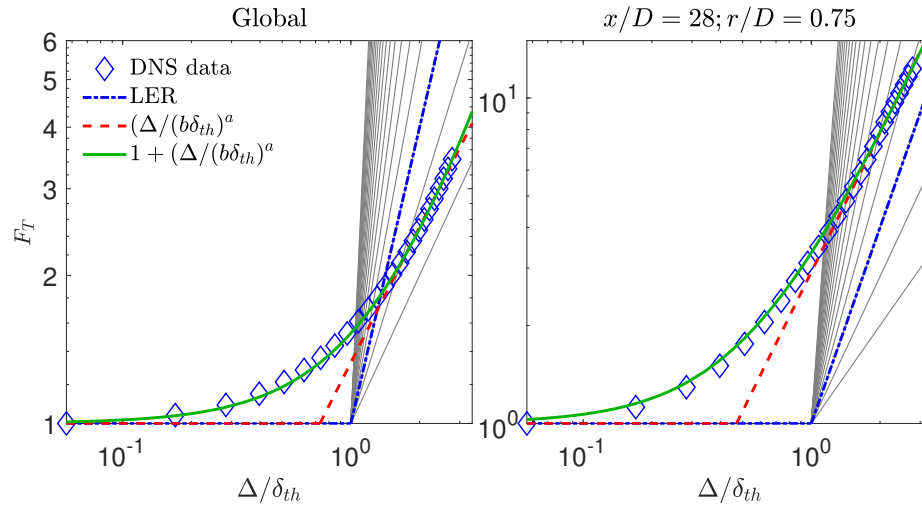


Figure 5.10. Comparisons of the sub-filter scale mixing scaling factor for temperature from DNS data and models.

can be fitted into  $[\Delta/(b\delta_{th})]^a$  with an additional parameter  $b$ . A new piecewise function is proposed based on the observation,

$$F = \begin{cases} \left(\frac{\Delta}{b\delta_{th}}\right)^a & \text{if } \Delta > b\delta_{th}, \\ 1 & \text{if } \Delta \leq b\delta_{th}. \end{cases} \quad (5.3.3)$$

Furthermore, from the previous section, we know that the piecewise fitting function can represent the DNS data points well in the two limits, while large modeling errors are expected when an intermediate LES filter size is used in simulations. Another model for the scaling factor is then proposed based on the observation as well,

$$F = 1 + \left(\frac{\Delta}{b\delta_{th}}\right)^a. \quad (5.3.4)$$

We call the models,  $\Omega_\alpha = \Omega_{\alpha,ref} \cdot (F - 1)$ , with  $F$ s from Eqs. (5.3.3) and (5.3.4), LER-A and LER-B model, respectively. From Fig. 5.7 and 5.8, we observe that  $a \approx 1.5$ , while  $b$  varies considerably in space and among different scalars, the specification of which requires further exploration. In the following model examination,  $a = 1.5$  is used and  $b$  is taken from the curve fitting result unless otherwise stated.

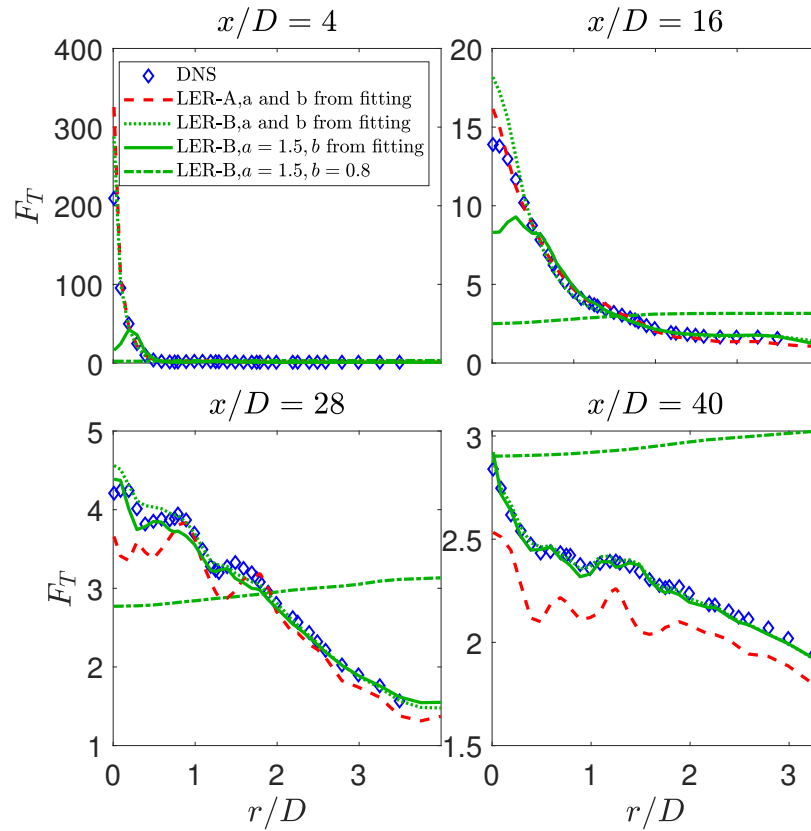


Figure 5.11. Radial profiles of the sub-filter scale mixing scaling factor for temperature from DNS data and models at  $\Delta = 21\Delta_{DNS}$  at four axial locations  $x/D = [4, 16, 28, 40]$ .

Fig. 5.11 shows the radial profiles of the scaling factor  $F_T$  at  $\Delta = 12\Delta_{DNS}$  from DNS data, the piecewise function in Eq. 5.3.3 from the LER-A model with model constants  $a$  and  $b$  from fitting, the blending function in Eq. (5.3.4) from LER-B model with three different sets of model constants  $a$  and  $b$ . The first set values of  $a$  and  $b$  are from the curve fitting, the modeling results of which are shown as the green dotted lines. Similar results for the model in Eq. (5.3.3) with model constants from fitting are also shown in Fig. 5.11 as red dashed lines. These results represent the best performance that the models in Eqs. (5.3.3) and (5.3.4) can achieve. It is observed that the blending function from LER-B represents the DNS data satisfactorily, while the piecewise function from LER-A represents the DNS data less satisfactorily with a slightly lower value. In the following, we only examine the LER-B

model. In the second set of model results shown as the green solid lines, we continue to take  $b$  values from the curve fitting results, while a constant value from observation is used for model parameter  $a = 1.5$ . The green solid lines are in good agreement with the DNS symbols, which implies that  $a = 1.5$  is a good choice. In the third set of results shown as green dash-dotted lines, in addition to constant  $a = 1.5$ , we take a constant value for parameter  $b = 0.8$  as well, which is a very rough approximation as indicated in Fig. 5.8. The significant deviations of the modeling results from the DNS data suggest that a constant  $b$  value is inadequate to describe the scaling factor. The specification of parameter  $b$  is very challenging as aforementioned. More work on this will be conducted in future work. In the current work, we take  $b$  values from the fitting results.

### Mixing frequency

In previous sections, we examine the scaling factor  $F_\alpha$  in DNS data, and the function in Eq. (5.3.4) from the LER-B model is found to represent the scaling factor  $F_\alpha$  well. Besides, the function formula in Eq. (5.3.4) is based on a statistical observation of time/volume-averaged behavior,  $\langle \cdot \rangle_{\mathbf{x}}$ , while in LES modeling, a model for the instantaneous sub-filter scale mixing frequency is desired. Hence, in this section, we examine the LER-B model performance in the sub-filter scale mixing frequency directly, to see if the model could represent the mean and instantaneous sub-filter scale mixing frequency in high-Ka the DNS flame. The results reported in this part are at  $\Delta = 21\Delta_{DNS}$ .

Fig. 5.12 shows the radial profiles of mean mixing frequency of temperature  $\langle \Omega_T \rangle_{\theta,t}$  from the DNS data (blue diamonds) and the LER-B model (green solid lines) at four different axial locations  $x/D = [4, 16, 28, 40]$ . The conventional model results in Eq. (5.2.7) are also shown here as a reference. For the conventional model, it is highly dependent on  $C_\phi$ , which is usually set to be 3 in turbulent combustion modeling studies. In Fig. 5.12, the model result with  $C_\phi = 3.0$  is shown as black dashed lines, which is significantly smaller than the DNS data. Only with a larger  $C_\phi = 30$ , the conventional model can generate comparable mixing frequency values to the DNS data, which is also shown in the figure

as the black dotted lines. Compared to the conventional model, the LER-B model shows a clear improved performance.

The radial profiles of mean mixing frequency  $\langle \Omega_\alpha \rangle_{\theta,t}$  for more scalars  $\alpha = [\text{H}_2, \text{O}_2, \text{OH}, \text{H}_2\text{O}, \text{CH}_4, \text{CO}, \text{CO}_2, \text{CH}_2\text{O}, \text{T}]$  are shown in Fig. 5.13. The symbols represent the DNS results and the lines represent the LER-B model results with  $a = 1.5$  and  $b$  from fitting. It is seen that the LER-B model is able to represent the mean mixing frequency in the DNS jet flame well for the different scalars and spatial locations.

So far, we have examined the model performance in representing the mean mixing frequency  $\langle \Omega_\alpha \rangle_{\theta,t}$ . In LES/PDF simulations, models for instantaneous sub-filter scale mixing frequency are directly needed. Fig. 5.14 show the scatter plots of instantaneous sub-filter scale mixing frequency  $\Omega_\alpha$  at  $\Delta = 21\Delta_{DNS}$  against radial locations for multiple scalars and at four axial locations. The DNS results are shown as blue symbols and the LER-B model results are shown as the red symbols. The blue and red solid lines represent the corresponding mean DNS results and mean LER-B model results at the same color. From Fig.5.14, it is observed that the LER-B model can represent the mean values of mixing frequency well as having been observed in Figs. 5.12 and 5.13. For the instantaneous mixing frequency, the DNS and model results are also quite close at upstream locations, while at downstream locations, the LER-B model results are found to be less scattering than the DNS results.

## 5.4 Conclusions

An *a priori* examination of the sub-filter scale mixing frequency is performed in a high-Ka turbulent premixed DNS jet flame. In particular, the examination focuses on the scaling of mixing frequency scaling factor to LES filter size. An assessment of existing models is reported in terms of the scaling factor and sub-filter scale mixing frequency. This study provides useful implications for future mixing modeling in turbulent premixed combustion under extreme conditions. The conclusions based on the current study are drawn as follows.

- The mixing frequency scaling factor  $F_\alpha$  is found to follow a power-law scaling of LES filter size,  $[\Delta/(b\delta_{th})]^a$  when  $\Delta > \delta_{th}$ , and  $F_\alpha \rightarrow 1$  when  $\Delta \rightarrow 0$ .

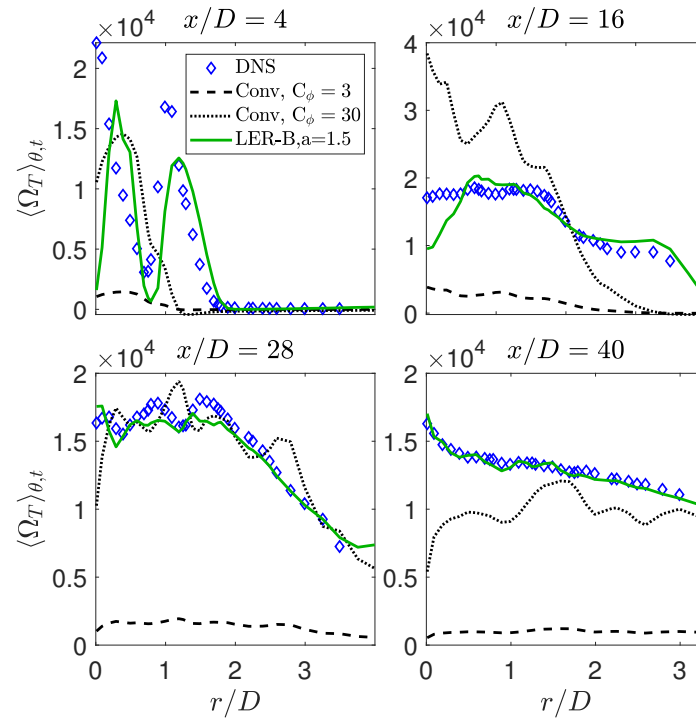


Figure 5.12. Radial profiles of mean mixing frequency  $\Omega_T$  for temperature from DNS data and models.

- A more general fitting curve,  $1 + [\Delta/(b\delta_{th})]^a$ , suitable for all the  $\Delta$ , is found for  $F_\alpha$ .
- The fitting parameters,  $a$  and  $b$ , show different behaviors. Parameter  $a$  varies around a constant value  $a \approx 1.5$  except near the jet exit area for all the scalars, while parameter  $b$  shows a clear spatial and scalar dependence, which requires more examinations.
- The piecewise function model for the scaling factor from the previous LER model with a single model parameter  $a$  is found inadequate to represent the scaling as well.
- Two LER-derived models, LER-A and LER-B, are proposed based on the DNS observations.
- To generate comparable mean mixing frequency with the DNS data, a much larger  $C_\phi$  value,  $C_\phi = 30$ , in the widely used conventional mixing frequency model is required.

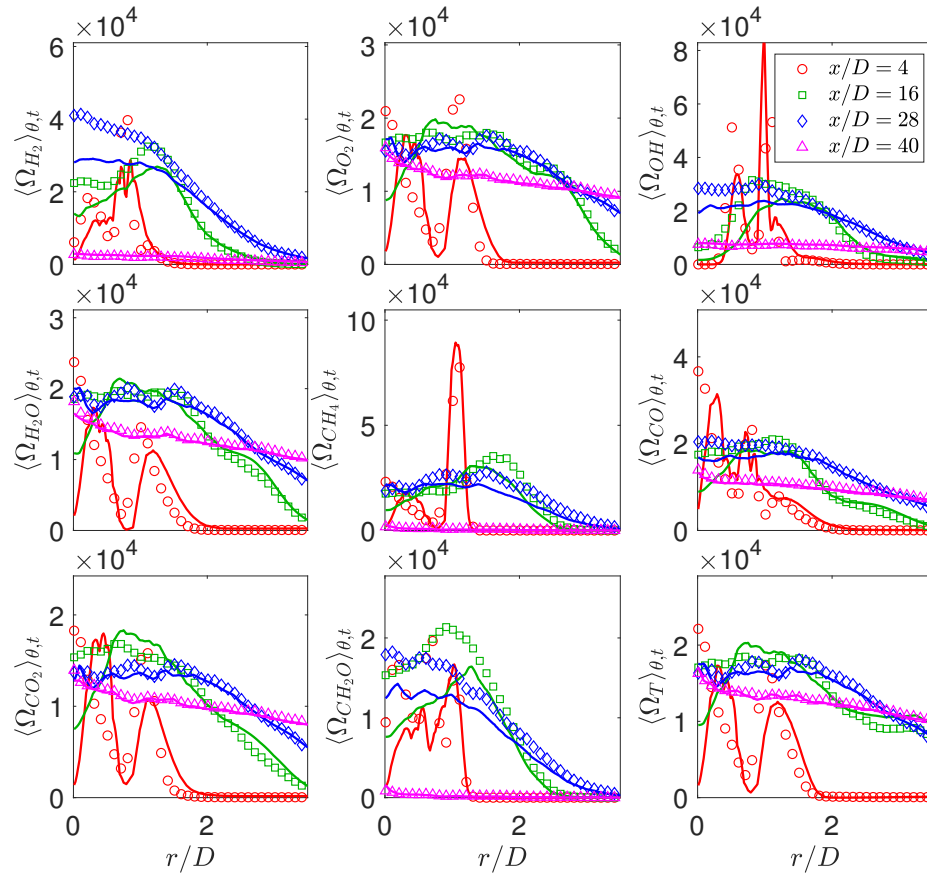


Figure 5.13. Comparison of mean mixing frequency  $\langle \Omega_\alpha \rangle_{\theta,t}$  from DNS and from LER-B model with  $a = 1.5$  and  $b$  from fitting for multiple scalars at four axial locations  $x/D = [4, 16, 28, 40]$ .

- LER-B model with model constant  $a = 1.5$  and  $b$  from fitting is found to represent the mean and instantaneous sub-filter scale mixing frequency well. The specification of model parameter  $b$  in LER-B model requires further work.

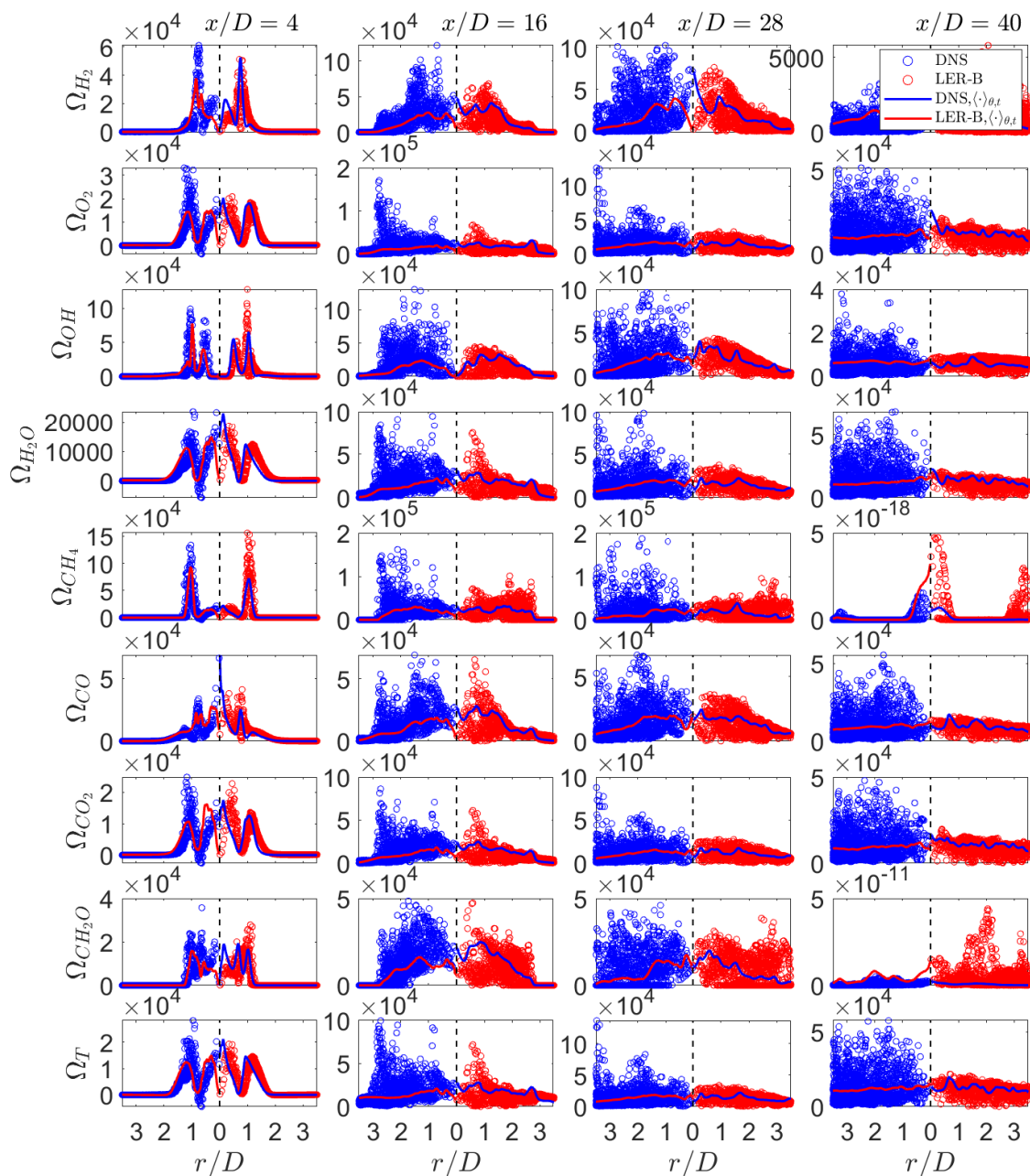


Figure 5.14. Comparison of instantaneous mixing frequency  $\Omega_\alpha$  from DNS and from LER-B model with  $a = 1.5$  and  $b$  from fitting for multiple scalars at four axial locations  $x/D = [4, 16, 28, 40]$ .

## 6. CONCLUSIONS AND FUTURE WORK

In this dissertation, we assess and improve the performance of the LES/PDF method in turbulent combustion modeling. The major conclusions and contributions are summarized as follows.

In Chapter 2, we examine the performance of the LES/PDF method in the Sydney turbulent pulsed piloted jet flame which features statistically transient bimodal combustion dynamics. The method is found to predict the temporal evolution of the flow and turbulence fields satisfactorily, as well as the major combustion stages, *i.e.*, healthy burning, significant extinction, two flame branches and the re-establishment of healthy burning, in the statistically transient combustion process. The method also captures the extinction and re-ignition timings at upstream locations well but fails to capture the re-ignition timing at downstream locations in the pulsed flame. In the assessment study, mixing models that are originally developed for non-premixed combustion are used, while at the downstream locations of the pulsed flame premixed combustion dominates. The inaccuracy of the re-ignition timing prediction suggests the inadequacy of the direct application of mixing models for non-premixed combustion in premixed combustion and the need to advance mixing modeling in premixed combustion. In this study, we extend the model assessment framework from the conventional statistically stationary process to the statistically transient process, demonstrate the method's potential in predicting the statistically transient combustion in real engines, and provide useful information for the future modeling improvement related to the downstream re-ignition prediction in particular.

In Chapter 3, we establish a systematic model assessment framework and perform a preliminary assessment of the LES/PDF method's performance in turbulent combustion across different combustion regimes including non-premixed, premixed and partially premixed combustion. This assessment study is useful for the application of the method to combustion predictions in real engines. The LES/PDF method is found to capture the differ-

ent combustion regimes well, but is limited in reproducing the measured difference among the flames from different combustion regimes. The measured maximum temperature, in particular, varies largely among different flames while the predicted maximum temperature is quite similar. In this study, we demonstrate the method's potential in predicting multi-regime combustion real engines and observe the method's limitations which could serve as a possible direction for the future model improvement. A regime diagram is proposed in this study, on which there are still many uncovered zones currently and which can potentially be used to guide the future design of turbulent piloted jet flames in both experimental and computational studies.

Chapters 4 and 5 focus on advancing the modeling of the molecular transport effects in transported PDF methods. Chapter 4 aims to deal with differential molecular diffusion (DMD) modeling in turbulent combustion. In this study, we develop the variance consistent mean shift (VCMS) model which is able to treat the DMD effects consistently for the prediction of scalar mean and variance. The mathematical consistency and convergence of the VCMS model are demonstrated in the mixing layer test case. We also introduce new boundedness correction algorithms (LDF, CSB, and CPM) to enforce realizability of the particle scalars, and demonstrate their improved performance in the mixing layer test case compared to the conventional MP correction. This study advances the DMD modeling in transported PDF methods for turbulent combustion problems.

Chapter 5 deals with the sub-filter scale mixing modeling in the LES/PDF method for high-Ka turbulent premixed combustion. In this study, we examine the database of a high-Ka DNS jet flame with a focus on the scaling of the mixing frequency scaling factor in LES filter size. The DNS results are found to fit into a power-law scaling well when the filter size is sufficiently large. We propose a new model for the sub-filter scale mixing frequency based on the DNS observations, and conduct an *a priori* assessment of its performance. This study advances our knowledge of the sub-filter scale mixing process in high-Ka combustion, and improves in particular the modeling of mixing frequency in the LES/PDF method.

Our long-term goal in computational turbulent combustion studies is to understand combustion physics and develop accurate and fast computational methods for predicting turbulent combustion in practical combustion systems. This dissertation work demonstrates a significant accomplishment in the subject area. At the same time, it is recognized that more efforts are still needed to fully accomplish the long-term goal. Based on the dissertation work, the following potential future work directions are suggested.

Following the model assessment work, further efforts to assess the LES/PDF method's performance in modern engines are recommended. The LES/PDF method has been demonstrated to be capable of capturing statistically transient bimodal and multi-regime combustion dynamics reasonably in turbulent flames with simple configurations, and it is promising to capture the complex combustion dynamics in real engines. However, this has not been verified yet. More work is still needed to fill in the gap between the practical need and the current combustion modeling.

Furthermore, some performance limitations of the LES/PDF are identified in the model assessment work, such as the limitations in capturing the re-establishment timing of the healthy burning state at the downstream location in the pulsed jet flame and reproducing the measured difference among the flames across the different combustion regimes. Future model development work to overcome these limitations is recommended.

Regarding the model advancement, the current dissertation work mainly focuses on improving the model accuracy. We have developed new models and demonstrated their superiority in simple test cases or via an *a priori* examination of a DNS database, as the first step. The next steps would be to assess the models' performance in the predictions of turbulent flames, and eventually in combustion predictions of real engines.

In addition to the model accuracy, another important aspect in the model advancement work is the computational cost, which in some cases is the major reason that prevents the applications of state-of-the-art turbulent combustion models in engineering problems. Computational power of supercomputers has increased steadily in the past few decades. The current world's fastest supercomputer, Summit, has reached 1.8 exaFLOPS [227]. New

computational methods that are suitable to the exascale systems would greatly reduce the computational cost and allow for advanced combustion predictions in real applications.

## REFERENCES

- [1] U.S. Energy Information Administration, *International Energy Outlook 2017*. [Online]. Available: <http://www.eia.gov/forecasts/ieo/index.cfm>
- [2] *International workshop on measurement and computation of turbulent nonpremixed flames*, <http://www.sandia.gov/TNF/abstract.html>.
- [3] *International Workshop on Premixed Turbulent Flames*, <https://sites.google.com/a/umich.edu/premix-turbulent-flame>.
- [4] D. L. Siebers and B. Higgins, "Flame lift-off on direct-injection diesel sprays under quiescent conditions," SAE Technical Paper, Tech. Rep., 2001.
- [5] P. A. M. Kalt, Y. M. Al-Abdell, A. R. Masri, and R. S. Barlow, "Swirling turbulent non-premixed flames of methane: flow field and compositional structure," *Proceedings of the Combustion Institute*, vol. 29, no. 2, pp. 1913–1919, 2002.
- [6] B. Dally, D. Fletcher, and A. Masri, "Flow and mixing fields of turbulent bluff-body jets and flames," *Combustion Theory and Modelling*, vol. 2, no. 2, pp. 193–219, 1998.
- [7] R. S. Barlow, G. J. Fiechtner, C. D. Carter, and J.-Y. Chen, "Experiments on the scalar structure of turbulent CO/H<sub>2</sub>/N<sub>2</sub> jet flames," *Combustion and Flame*, vol. 120, no. 4, pp. 549–569, 2000.
- [8] R. S. Barlow and C. D. Carter, "Raman/Rayleigh/LIF measurements of nitric oxide formation in turbulent hydrogen jet flames," *Combustion and Flame*, vol. 97, no. 3, pp. 261–280, 1994.
- [9] A. R. Masri, R. W. Dibble, and R. S. Barlow, "The structure of turbulent nonpremixed flames revealed by Raman-Rayleigh-LIF measurements," *Progress in Energy and Combustion Science*, vol. 22, no. 4, pp. 307–362, 1996.
- [10] V. Bergmann, W. Meier, D. Wolff, and W. Stricker, "Application of spontaneous Raman and Rayleigh scattering and 2D LIF for the characterization of a turbulent CH<sub>4</sub>/H<sub>2</sub>/N<sub>2</sub> jet diffusion flame," *Applied Physics B*, vol. 66, no. 4, pp. 489–502, 1998.
- [11] V. Sick, "High speed imaging in fundamental and applied combustion research," *Proceedings of the Combustion Institute*, vol. 34, no. 2, pp. 3509–3530, 2013.
- [12] B. Böhm, C. Heeger, R. L. Gordon, and A. Dreizler, "New perspectives on turbulent combustion: multi-parameter high-speed planar laser diagnostics," *Flow, turbulence and combustion*, vol. 86, no. 3-4, pp. 313–341, 2011.
- [13] M. Juddoo and A. Masri, "High-speed OH-PLIF imaging of extinction and re-ignition in non-premixed flames with various levels of oxygenation," *Combustion and Flame*, vol. 158, no. 5, pp. 902–914, 2011.

- [14] H. Wang, M. Juddoo, S. H. Starner, A. R. Masri, and S. B. Pope, "A novel transient turbulent jet flame for studying turbulent combustion," *Proceedings of the Combustion Institute*, vol. 34, no. 1, pp. 1251–1259, 2013.
- [15] M. Juddoo, A. Kourmatzis, and A. R. Masri, "An experimental study of transient effects in a pulsed, piloted, non-premixed turbulent jet flame," in *9th Asia-Pacific Conference on Combustion, Gyeongju Hilton*, 2013.
- [16] A. R. Masri and M. Juddoo, "Characteristics of turbulent piloted flames with different levels of stratification," *Proceedings of the European Combustion Meeting*, 2015.
- [17] N. Jiang, R. A. Patton, W. R. Lempert, and J. A. Sutton, "Development of high-repetition rate CH PLIF imaging in turbulent nonpremixed flames," *Proceedings of the Combustion Institute*, vol. 33, no. 1, pp. 767–774, 2011.
- [18] B. Böhm, C. Heeger, I. Boxx, W. Meier, and A. Dreizler, "Time-resolved conditional flow field statistics in extinguishing turbulent opposed jet flames using simultaneous highspeed piv/oh-plif," *Proceedings of the Combustion Institute*, vol. 32, no. 2, pp. 1647–1654, 2009.
- [19] J. R. Osborne, S. A. Ramji, C. D. Carter, S. Peltier, S. Hammack, T. Lee, and A. M. Steinberg, "Simultaneous 10 kHz TPIV, OH PLIF, and CH<sub>2</sub>O PLIF measurements of turbulent flame structure and dynamics," *Experiments in Fluids*, vol. 57, no. 5, pp. 1–19, 2016.
- [20] B. Böhm, J. Frank, and A. Dreizler, "Temperature and mixing field measurements in stratified lean premixed turbulent flames," *Proceedings of the Combustion Institute*, vol. 33, no. 1, pp. 1583–1590, 2011.
- [21] F. Seffrin, F. Fuest, D. Geyer, and A. Dreizler, "Flow field studies of a new series of turbulent premixed stratified flames," *Combustion and Flame*, vol. 157, no. 2, pp. 384–396, 2010.
- [22] M. S. Sweeney, S. Hochgreb, M. J. Dunn, and R. S. Barlow, "The structure of turbulent stratified and premixed methane/air flames I: Non-swirling flows," *Combustion and flame*, vol. 159, no. 9, pp. 2896–2911, 2012.
- [23] M. S. Sweeney, S. Hochgreb, M. J. Dunn, and R. S. Barlow, "The structure of turbulent stratified and premixed methane/air flames II: Swirling flows," *Combustion and Flame*, vol. 159, no. 9, pp. 2912–2929, 2012.
- [24] S. Meares and A. R. Masri, "A modified piloted burner for stabilizing turbulent flames of inhomogeneous mixtures," *Combustion and Flame*, vol. 161, no. 2, pp. 484–495, 2014.
- [25] R. S. Barlow, S. Meares, G. Magnotti, H. Cutcher, and A. R. Masri, "Local extinction and near-field structure in piloted turbulent CH<sub>4</sub>/air jet flames with inhomogeneous inlets," *Combustion and Flame*, vol. 162, no. 10, pp. 3516–3540, 2015.
- [26] S. Meares, V. N. Prasad, G. Magnotti, R. S. Barlow, and A. R. Masri, "Stabilization of piloted turbulent flames with inhomogeneous inlets," *Proceedings of the Combustion Institute*, vol. 35, no. 2, pp. 1477–1484, 2015.
- [27] D. Cecere, E. Giacomazzi, N. M. Arcidiacono, and F. R. Picchia, "Direct numerical simulation of a turbulent lean premixed CH<sub>4</sub>/H<sub>2</sub>-Air slot flame," *Combustion and Flame*, vol. 165, pp. 384 – 401, 2016.

- [28] C. Bruno, V. Sankaran, H. Kolla, and J. H. Chen, "Impact of multi-component diffusion in turbulent combustion using direct numerical simulations," *Combustion and Flame*, vol. 162, no. 11, pp. 4313 – 4330, 2015.
- [29] G. Bansal, A. Mascarenhas, and J. H. Chen, "Direct numerical simulations of autoignition in stratified dimethyl-ether (DME)/air turbulent mixtures," *Combustion and Flame*, vol. 162, no. 3, pp. 688 – 702, 2015.
- [30] Y. Minamoto, H. Kolla, R. W. Grout, A. Gruber, and J. H. Chen, "Effect of fuel composition and differential diffusion on flame stabilization in reacting syngas jets in turbulent cross-flow," *Combustion and Flame*, vol. 162, no. 10, pp. 3569 – 3579, 2015.
- [31] A. Attili, F. Bisetti, M. E. Mueller, and H. Pitsch, "Effects of non-unity lewis number of gas-phase species in turbulent nonpremixed sooting flames," *Combustion and Flame*, vol. 166, pp. 192 – 202, 2016.
- [32] A. J. Aspden, M. S. Day, and J. B. Bell, "Turbulence-flame interactions in lean premixed hydrogen: transition to the distributed burning regime," *Journal of Fluid Mechanics*, vol. 680, pp. 287–320, 2011.
- [33] A. J. Aspden, M. S. Day, and J. B. Bell, "Towards the distributed burning regime in turbulent premixed flames," *arXiv preprint arXiv:1806.09865*, 2018.
- [34] B. Savard, B. Bobbitt, and G. Blanquart, "Structure of a high Karlovitz n-C<sub>7</sub>H<sub>16</sub> premixed turbulent flame," *Proceedings of the Combustion Institute*, vol. 35, no. 2, pp. 1377–1384, 2015.
- [35] B. Savard and G. Blanquart, "Broken reaction zone and differential diffusion effects in high Karlovitz n-C<sub>7</sub>H<sub>16</sub> premixed turbulent flames," *Combustion and flame*, vol. 162, no. 5, pp. 2020–2033, 2015.
- [36] S. Lapointe, B. Savard, and G. Blanquart, "Differential diffusion effects, distributed burning, and local extinctions in high Karlovitz premixed flames," *Combustion and flame*, vol. 162, no. 9, pp. 3341–3355, 2015.
- [37] H. Carlsson, R. Yu, and X.-S. Bai, "Flame structure analysis for categorization of lean premixed CH<sub>4</sub>/air and H<sub>2</sub>/air flames at high Karlovitz numbers: Direct numerical simulation studies," *Proceedings of the Combustion Institute*, vol. 35, no. 2, pp. 1425–1432, 2015.
- [38] H. Wang, E. R. Hawkes, and J. H. Chen, "Turbulence-flame interactions in DNS of a laboratory high Karlovitz premixed turbulent jet flame," *Physics of Fluids*, vol. 28, no. 9, p. 095107, 2016.
- [39] H. Wang, E. R. Hawkes, J. H. Chen, B. Zhou, Z. Li, and M. Aldén, "Direct numerical simulations of a high Karlovitz number laboratory premixed jet flame—an analysis of flame stretch and flame thickening," *Journal of Fluid Mechanics*, vol. 815, pp. 511–536, 2017.
- [40] H. Wang, E. R. Hawkes, and J. H. Chen, "A direct numerical simulation study of flame structure and stabilization of an experimental high Ka CH<sub>4</sub>/air premixed jet flame," *Combustion and Flame*, vol. 180, pp. 110–123, 2017.

- [41] H. Wang, E. R. Hawkes, B. Savard, and J. H. Chen, "Direct numerical simulation of a high Ka  $\text{CH}_4$ /air stratified premixed jet flame," *Combustion and Flame*, vol. 193, pp. 229–245, 2018.
- [42] A. Y. Klimenko and R. W. Bilger, "Conditional moment closure for turbulent combustion," *Progress in energy and combustion science*, vol. 25, no. 6, pp. 595–687, 1999.
- [43] V. Zimont, W. Polifke, M. Bettelini, and W. Weisenstein, "An efficient computational model for premixed turbulent combustion at high Reynolds numbers based on a turbulent flame speed closure," in *ASME 1997 International Gas Turbine and Aeroengine Congress and Exhibition*. American Society of Mechanical Engineers, 1997, pp. V002T06A054–V002T06A054.
- [44] M. Ihme and H. Pitsch, "Prediction of extinction and reignition in nonpremixed turbulent flames using a flamelet/progress variable model: 1. A priori study and presumed PDF closure," *Combustion and Flame*, vol. 155, no. 1–2, pp. 70 – 89, 2008.
- [45] H. Zhang and E. Mastorakos, "Prediction of global extinction conditions and dynamics in swirling non-premixed flames using LES/CMC modelling," *Flow, Turbulence and Combustion*, vol. 96, no. 4, pp. 863–889, 2016.
- [46] H. Wang and S. B. Pope, "Large eddy simulation/probability density function modeling of a turbulent  $\text{CH}_4/\text{H}_2/\text{N}_2$  jet flame," *Proceedings of the Combustion Institute*, vol. 33, no. 1, pp. 1319–1330, 2011.
- [47] V. Moureau, B. Fiorina, and H. Pitsch, "A level set formulation for premixed combustion LES considering the turbulent flame structure," *Combustion and Flame*, vol. 156, no. 4, pp. 801 – 812, 2009.
- [48] B. Thornber, R. W. Bilger, A. R. Masri, and E. R. Hawkes, "An algorithm for LES of premixed compressible flows using the Conditional Moment Closure model," *Journal of Computational Physics*, vol. 230, no. 20, pp. 7687 – 7705, 2011.
- [49] R. R. Tirunagari and S. B. Pope, "An investigation of turbulent premixed counter-flow flames using large-eddy simulations and probability density function methods," *Combustion and Flame*, vol. 166, pp. 229 – 242, 2016.
- [50] P. Trisjono, K. Kleinheinz, H. Pitsch, and S. Kang, "Large eddy simulation of stratified and sheared flames of a premixed turbulent stratified flame burner using a flamelet model with heat loss," *Flow, Turbulence and Combustion*, vol. 92, no. 1, pp. 201–235, 2014.
- [51] B. Coriton, M. Zendejdel, S. Ukai, A. Kronenburg, O. T. Stein, S.-K. Im, M. Gamba, and J. H. Frank, "Imaging measurements and LES-CMC modeling of a partially-premixed turbulent dimethyl ether/air jet flame," *Proceedings of the Combustion Institute*, vol. 35, no. 2, pp. 1251 – 1258, 2015.
- [52] T. Brauner, W. P. Jones, and A. J. Marquis, "LES of the Cambridge Stratified Swirl Burner using a Sub-grid pdf Approach," *Flow, Turbulence and Combustion*, vol. 96, no. 4, pp. 965–985, 2016.
- [53] N. Peters, "Laminar diffusion flamelet models in non-premixed turbulent combustion," *Progress in energy and combustion science*, vol. 10, no. 3, pp. 319–339, 1984.

- [54] R. W. Bilger, "Conditional moment closure for turbulent reacting flow," *Physics of Fluids A: Fluid Dynamics (1989-1993)*, vol. 5, no. 2, pp. 436–444, 1993.
- [55] S. B. Pope, "PDF methods for turbulent reactive flows," *Progress in Energy and Combustion Science*, vol. 11, no. 2, pp. 119–192, 1985.
- [56] V. Saxena and S. B. Pope, "PDF calculations of major and minor species in a turbulent piloted jet flame," in *Symposium (International) on Combustion*, vol. 27, 1998, pp. 1081–1086.
- [57] P. Jenny, S. B. Pope, M. Muradoglu, and D. A. Caughey, "A hybrid algorithm for the joint PDF equation of turbulent reactive flows," *Journal of Computational Physics*, vol. 166, no. 2, pp. 218–252, 2001.
- [58] R. Lindstedt, S. Louloudi, and E. Váos, "Joint scalar probability density function modeling of pollutant formation in piloted turbulent jet diffusion flames with comprehensive chemistry," *Proceedings of the Combustion Institute*, vol. 28, no. 1, pp. 149 – 156, 2000.
- [59] J. Xu and S. B. Pope, "PDF calculations of turbulent nonpremixed flames with local extinction," *Combustion and Flame*, vol. 123, no. 3, pp. 281 – 307, 2000.
- [60] I. Dodoulas and S. Navarro-Martinez, "Large eddy simulation of premixed turbulent flames using the probability density function approach," *Flow, turbulence and combustion*, vol. 90, no. 3, pp. 645–678, 2013.
- [61] J. Kim and S. B. Pope, "Effects of combined dimension reduction and tabulation on the simulations of a turbulent premixed flame using a large-eddy simulation/probability density function method," *Combustion Theory and Modelling*, vol. 18, no. 3, pp. 388–413, 2014.
- [62] W. Jones, A. Marquis, and F. Wang, "Large eddy simulation of a premixed propane turbulent bluff body flame using the Eulerian stochastic field method," *Fuel*, vol. 140, pp. 514–525, 2015.
- [63] A. M. Kempf, C. Schneider, A. Sadiki, and J. Janicka, "Large eddy simulation of a highly turbulent methane flame: application to the DLR standard flame," in *TSFP DIGITAL LIBRARY ONLINE*. Begel House Inc., 2001.
- [64] M. Mitani, Y. Ito, and N. Yamasaki, "Large eddy simulation of methane non-premixed flame using the laminar flamelet model," *Journal of Thermal Science*, vol. 20, no. 6, pp. 534–542, 2011.
- [65] A. R. Masri and R. W. Bilger, "Turbulent diffusion flames of hydrocarbon fuels stabilized on a bluff body," in *Symposium (International) on Combustion*, vol. 20, 1985, pp. 319–326.
- [66] V. Raman and H. Pitsch, "Large-eddy simulation of a bluff-body-stabilized non-premixed flame using a recursive filter-refinement procedure," *Combustion and flame*, vol. 142, no. 4, pp. 329–347, 2005.
- [67] A. Kempf, R. Lindstedt, and J. Janicka, "Large-eddy simulation of a bluff-body stabilized nonpremixed flame," *Combustion and flame*, vol. 144, no. 1, pp. 170–189, 2006.

- [68] A. Triantafyllidis, E. Mastorakos, and R. L. G. M. Eggels, "Large eddy simulations of forced ignition of a non-premixed bluff-body methane flame with conditional moment closure," *Combustion and Flame*, vol. 156, no. 12, pp. 2328–2345, 2009.
- [69] V. N. Prasad, M. Juddoo, A. R. Masri, W. P. Jones, and K. H. Luo, "Investigation of extinction and re-ignition in piloted turbulent non-premixed methane–air flames using LES and high-speed OH-LIF," *Combustion Theory and Modelling*, vol. 17, no. 3, pp. 483–503, 2013.
- [70] Y. Yang, H. Wang, S. B. Pope, and J. H. Chen, "Large-eddy simulation/probability density function modeling of a non-premixed CO/H<sub>2</sub> temporally evolving jet flame," *Proceedings of the Combustion Institute*, vol. 34, no. 1, pp. 1241 – 1249, 2013.
- [71] R. Borghi, "On the structure and morphology of turbulent premixed flames," in *Recent advances in the aerospace sciences*. Springer, 1985, pp. 117–138.
- [72] N. Peters, "The turbulent burning velocity for large-scale and small-scale turbulence," *Journal of Fluid Mechanics*, vol. 384, pp. 107–132, 4 1999.
- [73] T. D. Butler and P. J. O'rourke, "A numerical method for two dimensional unsteady reacting flows," in *Symposium (International) on Combustion*, vol. 16, 1977, pp. 1503–1515.
- [74] O. Colin, F. Ducros, D. Veynante, and T. Poinso, "A thickened flame model for large eddy simulations of turbulent premixed combustion," *Physics of Fluids (1994-present)*, vol. 12, no. 7, pp. 1843–1863, 2000.
- [75] S. Menon and W.-H. Jou, "Large-eddy simulations of combustion instability in an axisymmetric ramjet combustor," *Combustion Science and Technology*, vol. 75, no. 1-3, pp. 53–72, 1991.
- [76] A. Hosseinzadeh, A. Sadiki, and J. Janicka, "Assessment of the dynamic SGS wrinkling combustion modeling using the thickened flame approach coupled with FGM tabulated detailed chemistry," *Flow, Turbulence and Combustion*, vol. 96, no. 4, pp. 939–964, 2016.
- [77] F. Proch and A. Kempf, "Modeling heat loss effects in the large eddy simulation of a model gas turbine combustor with premixed flamelet generated manifolds," *Proceedings of the Combustion Institute*, vol. 35, no. 3, pp. 3337–3345, 2015.
- [78] G. Kuenne, A. Ketelheun, and J. Janicka, "LES modeling of premixed combustion using a thickened flame approach coupled with FGM tabulated chemistry," *Combustion and Flame*, vol. 158, no. 9, pp. 1750–1767, 2011.
- [79] R. P. Lindstedt and E. M. Vaos, "Transported PDF modeling of high-Reynolds-number premixed turbulent flames," *Combustion and Flame*, vol. 145, no. 3, pp. 495–511, 2006.
- [80] M. Stöllinger and S. Heinz, "Evaluation of scalar mixing and time scale models in PDF simulations of a turbulent premixed flame," *Combustion and Flame*, vol. 157, no. 9, pp. 1671 – 1685, 2010.
- [81] R. R. Tirunagari and S. B. Pope, "LES/PDF for premixed combustion in the DNS limit," *Combustion Theory and Modelling*, pp. 1–32, 2016.

- [82] J. Janicka, W. Kolbe, and W. Kollmann, "Closure of the transport equation for the probability density function of turbulent scalar fields," *Journal of Non-Equilibrium Thermodynamics*, vol. 4, no. 1, pp. 47–66, 1979.
- [83] Y.-C. Chen, N. Peters, G. A. Schneemann, N. Wruck, U. Renz, and M. S. Mansour, "The detailed flame structure of highly stretched turbulent premixed methane-air flames," *Combustion and flame*, vol. 107, no. 3, pp. 223–IN2, 1996.
- [84] S. Subramaniam and S. B. Pope, "A mixing model for turbulent reactive flows based on Euclidean minimum spanning trees," *Combustion and Flame*, vol. 115, no. 4, pp. 487–514, 1998.
- [85] J. Villermaux and J. C. Devillon, "Représentation de la coalescence et de la redispersion des domaines de ségrégation dans un fluide par un modèle d'interaction phénoménologique," in *Proceedings of the 2nd International symposium on chemical reaction engineering*, vol. 26. Elsevier New York, 1972, pp. 1–13.
- [86] W. P. Jones, F. di Mare, and A. J. Marquis, "LES-BOFFIN: users guide," *Mechanical Engineering Department, Imperial College London, London*, 2002.
- [87] B. Coriton, J. H. Frank, and A. Gomez, "Effects of strain rate, turbulence, reactant stoichiometry and heat losses on the interaction of turbulent premixed flames with stoichiometric counterflowing combustion products," *Combustion and Flame*, vol. 160, no. 11, pp. 2442–2456, 2013.
- [88] R. S. Barlow and J. H. Frank, "Effects of turbulence on species mass fractions in methane/air jet flames," *Symposium (International) on Combustion*, vol. 27, no. 1, pp. 1087–1095, 1998.
- [89] Y. Marzouk, A. Ghoniem, and H. Najm, "Dynamic response of strained premixed flames to equivalence ratio gradients," *Proceedings of the Combustion Institute*, vol. 28, no. 2, pp. 1859–1866, 2000.
- [90] B. Fiorina, R. Mercier, G. Kuenne, A. Ketelheun, A. Avdić, J. Janicka, D. Geyer, A. Dreizler, E. Alenius, C. Duwig, P. Trisjono, K. Kleinheinz, S. Kang, H. Pitsch, F. Proch, F. Cavallo Marincola, and A. Kempf, "Challenging modeling strategies for LES of non-adiabatic turbulent stratified combustion," *Combustion and Flame*, vol. 162, no. 11, pp. 4264–4282, 2015.
- [91] R. Mercier, P. Auzillon, V. Moureau, N. Darabiha, O. Gicquel, D. Veynante, and B. Fiorina, "LES modeling of the impact of heat losses and differential diffusion on turbulent stratified flame propagation: Application to the TU Darmstadt stratified flame," *Flow, turbulence and combustion*, vol. 93, no. 2, pp. 349–381, 2014.
- [92] P. Trisjono, K. Kleinheinz, H. Pitsch, and S. Kang, "Large eddy simulation of stratified and sheared flames of a premixed turbulent stratified flame burner using a flamelet model with heat loss," *Flow, Turbulence and Combustion*, vol. 92, no. 1-2, pp. 201–235, 2014.
- [93] F. C. Marincola, T. Ma, and A. Kempf, "Large eddy simulations of the Darmstadt turbulent stratified flame series," *Proceedings of the Combustion Institute*, vol. 34, no. 1, pp. 1307–1315, 2013.

- [94] O. R. Darbyshire and N. Swaminathan, "A presumed joint PDF model for turbulent combustion with varying equivalence ratio," *Combustion Science and Technology*, vol. 184, no. 12, pp. 2036–2067, 2012.
- [95] S. Nambully, P. Domingo, V. Moureau, and L. Vervisch, "A filtered-laminar-flame PDF sub-grid-scale closure for LES of premixed turbulent flames: II. application to a stratified bluff-body burner," *Combustion and Flame*, vol. 161, no. 7, pp. 1775–1791, 2014.
- [96] F. Proch and A. M. Kempf, "Numerical analysis of the Cambridge stratified flame series using artificial thickened flame LES with tabulated premixed flame chemistry," *Combustion and Flame*, vol. 161, no. 10, pp. 2627–2646, 2014.
- [97] R. Mercier, T. Schmitt, D. Veynante, and B. Fiorina, "The influence of combustion SGS submodels on the resolved flame propagation. Application to the LES of the Cambridge stratified flames," *Proceedings of the Combustion Institute*, vol. 35, no. 2, pp. 1259–1267, 2015.
- [98] T. Brauner, W. P. Jones, and A. J. Marquis, "LES of the Cambridge stratified swirl burner using a sub-grid pdf approach," *Flow, Turbulence and Combustion*, vol. 96, no. 4, pp. 965–985, 2016.
- [99] S. B. Pope, *Turbulent Flows*. Cambridge University Press, 2000.
- [100] T. Lu and C. K. Law, "Toward accommodating realistic fuel chemistry in large-scale computations," *Progress in Energy and Combustion Science*, vol. 35, no. 2, pp. 192 – 215, 2009.
- [101] T. Lu and C. K. Law, "A directed relation graph method for mechanism reduction," *Proceedings of the Combustion Institute*, vol. 30, no. 1, pp. 1333 – 1341, 2005.
- [102] H. Wang and D. A. Sheen, "Combustion kinetic model uncertainty quantification, propagation and minimization," *Progress in Energy and Combustion Science*, vol. 47, pp. 1 – 31, 2015.
- [103] R. W. Dibble and M. B. Long, "Investigation of differential diffusion in turbulent jet flows using planar laser Rayleigh scattering," *Combustion and Flame*, vol. 143, no. 4, pp. 644–649, 2005.
- [104] R. S. Barlow, M. J. Dunn, M. S. Sweeney, and S. Hochgreb, "Effects of preferential transport in turbulent bluff-body-stabilized lean premixed CH<sub>4</sub>/air flames," *Combustion and Flame*, vol. 159, no. 8, pp. 2563–2575, 2012.
- [105] F. Bisetti, J. Y. Chen, J. H. Chen, and E. R. Hawkes, "Differential diffusion effects during the ignition of a thermally stratified premixed hydrogen–air mixture subject to turbulence," *Proceedings of the Combustion Institute*, vol. 32, no. 1, pp. 1465–1472, 2009.
- [106] D. Frederick and J. Y. Chen, "Effects of differential diffusion on predicted autoignition delay times inspired by H<sub>2</sub>/N<sub>2</sub> jet flames in a vitiated coflow using the linear eddy model," *Flow, Turbulence and Combustion*, vol. 93, no. 2, pp. 283–304, Sep 2014.
- [107] M. Matalon, "Intrinsic flame instabilities in premixed and nonpremixed combustion," *Annual Review of Fluid Mechanics*, vol. 39, pp. 163–191, 2007.

- [108] C. Han and H. Wang, “Reynolds-number power-law scaling of differential molecular diffusion in turbulent nonpremixed combustion,” *Physical Review Fluids*, vol. 3, no. 10, p. 103201, 2018.
- [109] C. Han, D. O. Lignell, E. R. Hawkes, J. H. Chen, and H. Wang, “Examination of the effect of differential molecular diffusion in DNS of turbulent non-premixed flames,” *International Journal of Hydrogen Energy*, vol. 42, no. 16, pp. 11 879–11 892, 2017.
- [110] D. Veynante and L. Vervisch, “Turbulent combustion modeling,” *Progress in energy and combustion science*, vol. 28, no. 3, pp. 193–266, 2002.
- [111] H. Yamashita, M. Shimada, and T. Takeno, “A numerical study on flame stability at the transition point of jet diffusion flames,” in *Symposium (International) on Combustion*, vol. 26, 1996, pp. 27–34.
- [112] E. Knudsen and H. Pitsch, “A general flamelet transformation useful for distinguishing between premixed and non-premixed modes of combustion,” *Combustion and flame*, vol. 156, no. 3, pp. 678–696, 2009.
- [113] E. Knudsen and H. Pitsch, “Capabilities and limitations of multi-regime flamelet combustion models,” *Combustion and Flame*, vol. 159, no. 1, pp. 242–264, 2012.
- [114] P.-D. Nguyen, L. Vervisch, V. Subramanian, and P. Domingo, “Multidimensional flamelet-generated manifolds for partially premixed combustion,” *Combustion and Flame*, vol. 157, no. 1, pp. 43–61, 2010.
- [115] B. Fiorina, O. Gicquel, L. Vervisch, S. Carpentier, and N. Darabiha, “Approximating the chemical structure of partially premixed and diffusion counterflow flames using FPI flamelet tabulation,” *Combustion and flame*, vol. 140, no. 3, pp. 147–160, 2005.
- [116] P. Domingo, L. Vervisch, and D. Veynante, “Large-eddy simulation of a lifted methane jet flame in a vitiated coflow,” *Combustion and Flame*, vol. 152, no. 3, pp. 415–432, 2008.
- [117] P. Zhang, A. R. Masri, and H. Wang, “Studies of the flow and turbulence fields in a turbulent pulsed jet flame using LES/PDF,” *Combustion Theory and Modelling*, vol. 21, no. 5, pp. 897–924, 2017.
- [118] A. R. Masri, R. W. Bilger, and R. W. Dibble, “The local structure of turbulent non-premixed flames near extinction,” *Combustion and flame*, vol. 81, no. 3-4, pp. 260–276, 1990.
- [119] J.-Y. Chen, W. Kollmann, and R. Dibble, “PDF modeling of turbulent nonpremixed methane jet flames,” *Combustion Science and Technology*, vol. 64, no. 4-6, pp. 315–346, 1989.
- [120] N. Peters and R. Kee, “The computation of stretched laminar methane-air diffusion flames using a reduced four-step mechanism,” *Combustion and Flame*, vol. 68, no. 1, pp. 17–29, 1987.
- [121] C. Dopazo, “Relaxation of initial probability density functions in the turbulent convection of scalar fields,” *The Physics of Fluids*, vol. 22, no. 1, pp. 20–30, 1979.
- [122] A. R. Masri and S. B. Pope, “PDF calculations of piloted turbulent nonpremixed flames of methane,” *Combustion and Flame*, vol. 81, no. 1, pp. 13–29, 1990.

- [123] S. B. Pope, "An improved turbulent mixing model," *Combustion Science and Technology*, vol. 28, no. 3-4, pp. 131–145, 1982.
- [124] S. B. Pope, "Computationally efficient implementation of combustion chemistry using in situ adaptive tabulation," *Combustion Theory and Modelling*, vol. 1, no. 1, pp. 41–63, 1997.
- [125] V. Saxena and S. B. Pope, "PDF simulations of turbulent combustion incorporating detailed chemistry," *Combustion and Flame*, vol. 117, no. 1-2, pp. 340–350, 1999.
- [126] B. Yang and S. B. Pope, "An investigation of the accuracy of manifold methods and splitting schemes in the computational implementation of combustion chemistry," *Combustion and Flame*, vol. 112, no. 1-2, pp. 16–32, 1998.
- [127] C. Dopazo and E. E. O'Brien, "An approach to the autoignition of a turbulent mixture," *Acta Astronaut.*, vol. 1, no. 9-10, pp. 1239–1266, 1974.
- [128] W. Jones and M. Kakhi, "PDF modeling of finite-rate chemistry effects in turbulent nonpremixed jet flames," *Combustion and Flame*, vol. 115, no. 1-2, pp. 210–229, 1998.
- [129] E. E. O'Brien, "The probability density function (PDF) approach to reacting turbulent flows," in *Turbulent reacting flows*. Springer, 1980, pp. 185–218.
- [130] M. Juddoo, A. R. Masri, and S. B. Pope, "Turbulent piloted partially-premixed flames with varying levels of  $O_2/N_2$ : Stability limits and PDF calculations," *Combustion Theory and Modelling*, vol. 15, no. 6, pp. 773–793, 2011.
- [131] H. Wang and S. B. Pope, "PDF investigations of turbulent non-premixed jet flames with thin reaction zones," in *APS Meeting Abstracts*, 2012.
- [132] J. Xu and S. B. Pope, "PDF calculations of turbulent nonpremixed flames with local extinction," *Combustion and Flame*, vol. 123, no. 3, pp. 281–307, 2000.
- [133] M. Ihme, C. M. Cha, and H. Pitsch, "Prediction of local extinction and re-ignition effects in non-premixed turbulent combustion using a flamelet/progress variable approach," *Proceedings of the Combustion Institute*, vol. 30, no. 1, pp. 793–800, 2005.
- [134] A. C. Davison and D. V. Hinkley, *Bootstrap methods and their application*. Cambridge university press, 1997, vol. 1.
- [135] C. D. Pierce and P. Moin, "Progress-variable approach for large-eddy simulation of non-premixed turbulent combustion," *Journal of Fluid Mechanics*, vol. 504, pp. 73–97, 2004.
- [136] S. B. Pope, "Self-conditioned fields for large-eddy simulations of turbulent flows," *Journal of Fluid Mechanics*, vol. 652, pp. 139–169, 2010.
- [137] J. Smagorinsky, "General circulation experiments with the primitive equations: I. the basic experiment," *Monthly weather review*, vol. 91, no. 3, pp. 99–164, 1963.
- [138] D. K. Lilly, "A proposed modification of the Germano subgrid-scale closure method," *Physics of Fluids A: Fluid Dynamics (1989-1993)*, vol. 4, no. 3, pp. 633–635, 1992.
- [139] C. D. Pierce, "Progress-variable approach for large-eddy simulation of turbulent combustion," Ph.D. dissertation, Stanford University, 2001.

- [140] R. R. Cao, H. Wang, and S. B. Pope, "The effect of mixing models in PDF calculations of piloted jet flames," *Proceedings of the combustion institute*, vol. 31, no. 1, pp. 1543–1550, 2007.
- [141] A. Kazakov and M. Frenklach, "Reduced reaction sets based on gri-mech 1.2," *University of California at Berkeley, Berkeley, CA*, <http://www.me.berkeley.edu/drm>, 1994.
- [142] M. Frenklach, H. Wang, C.-L. Yu, M. Goldenberg, C. T. Bowman, R. K. Hanson, D. F. Davidson, E. J. Chang, G. P. Smith, D. M. Golden, W. C. Gardiner, and V. Lissianski, [http://www.me.berkeley.edu/gri\\_mech/](http://www.me.berkeley.edu/gri_mech/).
- [143] M. Frenklach, H. Wang, M. Goldenberg, G. P. Smith, D. M. Golden, C. T. Bowman, R. K. Hanson, W. C. Gardiner, and V. Lissianski, "Gri-mech—an optimized detailed chemical reaction mechanism for methane combustion," Gas Research Institute, Tech. Rep., 1995.
- [144] M. Muradoglu, S. B. Pope, and D. A. Caughey, "The hybrid method for the PDF equations of turbulent reactive flows: consistency conditions and correction algorithms," *Journal of Computational Physics*, vol. 172, no. 2, pp. 841–878, 2001.
- [145] E. Merzari, W. Pointer, and P. Fischer, "Numerical simulation and proper orthogonal decomposition of the flow in a counter-flow t-junction," *Journal of Fluids Engineering*, vol. 135, no. 9, p. 091304, 2013.
- [146] P. J. Schmid, "Dynamic mode decomposition of numerical and experimental data," *Journal of Fluid Mechanics*, vol. 656, pp. 5–28, 2010.
- [147] M. Rosenblatt, "A central limit theorem and a strong mixing condition," *Proceedings of the National Academy of Sciences*, vol. 42, no. 1, pp. 43–47, 1956.
- [148] *Sydney flame database*. [Online]. Available: <http://sydney.edu.au/engineering/aeromech/thermofluids/piloted.htm>
- [149] H. Wang and P. Zhang, "A unified view of pilot stabilized turbulent jet flames for model assessment across different combustion regimes," *Proceedings of the Combustion Institute*, vol. 36, no. 2, pp. 1693 – 1703, 2017.
- [150] N. Peters, *Turbulent combustion*. Cambridge University Press, 2000.
- [151] S. Amzin, N. Swaminathan, J. W. Rogerson, and J. H. Kent, "Conditional moment closure for turbulent premixed flames," *Combustion Science and Technology*, vol. 184, no. 10-11, pp. 1743–1767, 2012.
- [152] A. Masri and R. Bilger, "Turbulent non-premixed flames of hydrocarbon fuels near extinction: Mean structure from probe measurements," in *Symposium (International) on Combustion*, vol. 21, 1988, pp. 1511–1520.
- [153] M. J. Dunn, A. R. Masri, and R. W. Bilger, "A new piloted premixed jet burner to study strong finite-rate chemistry effects," *Combustion and Flame*, vol. 151, no. 1-2, pp. 46–60, 2007.
- [154] R. Bilger, S. Stårner, and R. Kee, "On reduced mechanisms for methane-air combustion in nonpremixed flames," *Combustion and Flame*, vol. 80, no. 2, pp. 135–149, 1990.

- [155] P. Zhang and H. Wang, "Variance consistent mean shift particle model for treating differential molecular diffusion in transported PDF methods for turbulent reactive flows," *Computers & Fluids*, vol. 170, pp. 53–76, 2018.
- [156] W. Meier, R. S. Barlow, Y. Chen, and J. Chen, "Raman/Rayleigh/LIF measurements in a turbulent  $\text{CH}_4/\text{H}_2/\text{N}_2$  jet diffusion flame: experimental techniques and turbulence–chemistry interaction," *Combustion and Flame*, vol. 123, no. 3, pp. 326–343, 2000.
- [157] W. Bilger and R. W. Dibble, "Differential molecular diffusion effects in turbulent mixing," *Combustion Science and Technology*, vol. 28, no. 3-4, pp. 161–172, 1982.
- [158] L. L. Smith, R. W. Dibble, L. Talbot, R. S. Barlow, and C. D. Carter, "Laser Raman scattering measurements of differential molecular diffusion in turbulent nonpremixed jet flames of  $\text{H}_2/\text{CO}_2$  fuel," *Combustion and Flame*, vol. 100, no. 1, pp. 153–160, 1995.
- [159] M. M. Tacke, S. Linow, S. Geiss, E. P. Hassel, J. Janicka, and J. Y. Chen, "Experimental and numerical study of a highly diluted turbulent diffusion flame close to blowout," *Proceedings of the Combustion Institute*, vol. 27, no. 1, pp. 1139–1148, 1998.
- [160] V. Nilsen and G. Kosály, "Differential diffusion in turbulent reacting flows," *Combustion and Flame*, vol. 117, no. 3, pp. 493–513, 1999.
- [161] O. Gicque, D. Thévenin, and N. Darabiha, "Influence of differential diffusion on super-equilibrium temperature in turbulent non-premixed hydrogen/air flames," *Flow, Turbulence and Combustion*, vol. 73, no. 3-4, pp. 307–321, 2005.
- [162] R. Hilbert and D. Thévenin, "Influence of differential diffusion on maximum flame temperature in turbulent nonpremixed hydrogen/air flames," *Combustion and Flame*, vol. 138, no. 1, pp. 175–187, 2004.
- [163] H. G. Im and J. H. Chen, "Preferential diffusion effects on the burning rate of interacting turbulent premixed hydrogen-air flames," *Combustion and Flame*, vol. 131, no. 3, pp. 246–258, 2002.
- [164] N. Malik, T. Løvås, and F. Mauss, "The effect of preferential diffusion on the soot initiation process in ethylene diffusion flames," *Flow, Turbulence and Combustion*, vol. 87, no. 2-3, pp. 293–312, 2011.
- [165] D. H. Rowinski and S. B. Pope, "Computational study of lean premixed turbulent flames using RANSPDF and LESPDF methods," *Combustion Theory and Modelling*, vol. 17, no. 4, pp. 610–656, 2013.
- [166] M. J. Dunn, A. R. Masri, R. W. Bilger, R. S. Barlow, and G.-H. Wang, "The compositional structure of highly turbulent piloted premixed flames issuing into a hot coflow," *Proceedings of the combustion institute*, vol. 32, no. 2, pp. 1779–1786, 2009.
- [167] M. J. Dunn, A. R. Masri, R. W. Bilger, and R. S. Barlow, "Finite rate chemistry effects in highly sheared turbulent premixed flames," *Flow, Turbulence and Combustion*, vol. 85, no. 3-4, pp. 621–648, 2010.
- [168] H. Wang and K. Kim, "Effect of molecular transport on PDF modeling of turbulent non-premixed flames," *Proceedings of the Combustion Institute*, vol. 35, no. 2, pp. 1137–1145, 2015.

- [169] K. A. Kemenov and S. B. Pope, "Molecular diffusion effects in LES of a piloted methane-air flame," *Combustion and Flame*, vol. 158, no. 2, pp. 240–254, 2011.
- [170] W. Han, V. Raman, and Z. Chen, "LES/PDF modeling of autoignition in a lifted turbulent flame: Analysis of flame sensitivity to differential diffusion and scalar mixing time-scale," *Combustion and Flame*, vol. 171, pp. 69–86, 2016.
- [171] R. Cabra, J. Chen, R. Dibble, A. Karpetis, and R. S. Barlow, "Lifted methane-air jet flames in a vitiated coflow," *Combustion and Flame*, vol. 143, no. 4, pp. 491–506, 2005.
- [172] A. Kronenburg and R. W. Bilger, "Modelling differential diffusion in nonpremixed reacting turbulent flow: model development," *Combustion Science and Technology*, vol. 166, no. 1, pp. 195–227, 2001.
- [173] H. Pitsch and N. Peters, "A consistent flamelet formulation for non-premixed combustion considering differential diffusion effects," *Combustion and Flame*, vol. 114, no. 1, pp. 26–40, 1998.
- [174] H. Wang, "Consistent flamelet modeling of differential molecular diffusion for turbulent non-premixed flames," *The Physics of Fluids*, vol. 28, no. 3, p. 035102, 2016.
- [175] M. S. Anand and S. B. Pope, "Diffusion behind a line source in grid turbulence," in *Turbulent Shear Flows 4*. Springer, 1985, pp. 46–61.
- [176] R. McDermott and S. B. Pope, "A particle formulation for treating differential diffusion in filtered density function methods," *Journal of Computational Physics*, vol. 226, no. 1, pp. 947–993, 2007.
- [177] S. Viswanathan, H. Wang, and S. B. Pope, "Numerical implementation of mixing and molecular transport in LES/PDF studies of turbulent reacting flows," *Journal of Computational Physics*, vol. 230, no. 17, pp. 6916–6957, 2011.
- [178] D. H. Rowinski and S. B. Pope, "An investigation of mixing in a three-stream turbulent jet," *The Physics of Fluids*, vol. 25, no. 10, p. 105105, 2013.
- [179] P. Gerlinger, "Lagrangian transported MDF methods for compressible high speed flows," *Journal of Computational Physics*, vol. 339, pp. 68–95, 2017.
- [180] S. B. Pope, "Computations of turbulent combustion: progress and challenges," *Proceedings of the Combustion Institute*, vol. 23, no. 1, pp. 591–612, 1991.
- [181] R. J. Kee, M. E. Coltrin, and P. Glarborg, *Chemically reacting flow: theory and practice*. John Wiley & Sons, 2005.
- [182] C. Bruno, V. Sankaran, H. Kolla, and J. H. Chen, "Impact of multi-component diffusion in turbulent combustion using direct numerical simulations," *Combustion and Flame*, vol. 162, no. 11, pp. 4313–4330, 2015.
- [183] S. B. Pope, "Consistent modeling of scalars in turbulent flows," *The Physics of Fluids*, vol. 26, no. 2, pp. 404–408, 1983.
- [184] B.-K. Ma and Z. Warhaft, "Some aspects of the thermal mixing layer in grid turbulence," *The Physics of Fluids*, vol. 29, no. 10, pp. 3114–3120, 1986.

- [185] C. Béguier, I. Dekeyser, and B. E. Launder, “Ratio of scalar and velocity dissipation time scales in shear flow turbulence,” *The Physics of Fluids*, vol. 21, no. 3, pp. 307–310, 1978.
- [186] H. Wang, P. P. Popov, and S. B. Pope, “Weak second-order splitting schemes for Lagrangian Monte Carlo particle methods for the composition PDF/FDF transport equations,” *Journal of Computational Physics*, vol. 229, no. 5, pp. 1852–1878, 2010.
- [187] J. Xu and S. B. Pope, “Assessment of numerical accuracy of PDF/Monte-Carlo methods for turbulent reactive flows,” *Journal of Computational Physics*, vol. 152, pp. 192–230, 1999.
- [188] M. Muradoglu, P. Jenny, S. B. Pope, and D. A. Caughey, “A consistent hybrid finite-volume/particle method for the PDF equations of turbulent reactive flows,” *Journal of Computational Physics*, vol. 154, no. 2, pp. 342–371, 1999.
- [189] H. Wang and S. B. Pope, “Time-averaging strategies in the finite-volume/particle hybrid algorithm for the joint PDF equation of turbulent reactive flows,” *Combustion Theory and Modelling*, vol. 12, no. 3, pp. 529–544, 2008.
- [190] E. R. Hawkes, R. Sankaran, J. C. Sutherland, and J. H. Chen, “Scalar mixing in direct numerical simulations of temporally evolving plane jet flames with skeletal CO/H<sub>2</sub> kinetics,” *Proceedings of the Combustion Institute*, vol. 31, no. 1, pp. 1633 – 1640, 2007.
- [191] A. Soika, F. Dinkelacker, and A. Leipertz, “Measurement of the resolved flame structure of turbulent premixed flames with constant reynolds number and varied stoichiometry,” *Proceedings of the Combustion Institute*, vol. 27, no. 1, pp. 785 – 792, 1998.
- [192] A. W. Skiba, T. M. Wabel, J. Temme, and J. F. Driscoll, “Experimental assessment of premixed flames subjected to extreme turbulence,” in *54th AIAA Aerospace Sciences Meeting*, 2016, p. 1454.
- [193] T. M. Wabel, A. W. Skiba, J. E. Temme, and J. F. Driscoll, “Measurements to determine the regimes of premixed flames in extreme turbulence,” *Proceedings of the Combustion Institute*, vol. 36, no. 2, pp. 1809–1816, 2017.
- [194] T. M. Wabel, A. W. Skiba, and J. F. Driscoll, “Evolution of turbulence through a broadened preheat zone in a premixed piloted bunsen flame from conditionally-averaged velocity measurements,” *Combustion and Flame*, vol. 188, pp. 13–27, 2018.
- [195] A. W. Skiba, T. M. Wabel, C. D. Carter, S. D. Hammack, J. E. Temme, and J. F. Driscoll, “Premixed flames subjected to extreme levels of turbulence part I: Flame structure and a new measured regime diagram,” *Combustion and Flame*, vol. 189, pp. 407–432, 2018.
- [196] B. Zhou, C. Brackmann, Q. Li, Z. Wang, P. Petersson, Z. Li, M. Aldén, and X.-s. Bai, “Distributed reactions in highly turbulent premixed methane/air flames: Part I. flame structure characterization,” *Combustion and Flame*, vol. 162, no. 7, pp. 2937–2953, 2015.
- [197] B. Zhou, C. Brackmann, Z. Li, M. Aldén, and X.-S. Bai, “Simultaneous multi-species and temperature visualization of premixed flames in the distributed reaction zone regime,” *Proceedings of the Combustion Institute*, vol. 35, no. 2, pp. 1409–1416, 2015.

- [198] B. Zhou, C. Brackmann, Z. Wang, Z. Li, M. Richter, M. Aldén, and X.-S. Bai, "Thin reaction zone and distributed reaction zone regimes in turbulent premixed methane/air flames: scalar distributions and correlations," *Combustion and Flame*, vol. 175, pp. 220–236, 2017.
- [199] H. Wang, E. R. Hawkes, B. Zhou, J. H. Chen, Z. Li, and M. Aldén, "A comparison between direct numerical simulation and experiment of the turbulent burning velocity-related statistics in a turbulent methane-air premixed jet flame at high Karlovitz number," *Proceedings of the Combustion Institute*, vol. 36, no. 2, pp. 2045–2053, 2017.
- [200] R. Borghi, "Turbulent combustion modelling," *Progress in energy and combustion science*, vol. 14, no. 4, pp. 245–292, 1988.
- [201] J.-Y. Chen, W. Kollmann, and R. W. Dibble, "Pdf modeling of turbulent nonpremixed methane jet flames," *Combustion Science and Technology*, vol. 64, no. 4-6, pp. 315–346, 1989.
- [202] A. R. Masri and S. B. Pope, "PDF calculations of piloted turbulent nonpremixed flames of methane," *Combustion and Flame*, vol. 81, no. 1, pp. 13 – 29, 1990.
- [203] M. Juddoo, A. R. Masri, and S. B. Pope, "Turbulent piloted partially-premixed flames with varying levels of  $O_2/N_2$ : stability limits and PDF calculations," *Combustion Theory and Modelling*, vol. 15, no. 6, pp. 773–793, 2011.
- [204] P. J. Colucci, F. A. Jaber, P. Givi, and S. B. Pope, "Filtered density function for large eddy simulation of turbulent reacting flows," *Physics of Fluids*, vol. 10, no. 2, pp. 499–515, 1998.
- [205] W. P. Jones and V. N. Prasad, "Large eddy simulation of the Sandia flame series (D-F) using the Eulerian stochastic field method," *Combustion and Flame*, vol. 157, no. 9, pp. 1621 – 1636, 2010.
- [206] H. Wang and S. B. Pope, "Large eddy simulation/probability density function modeling of a turbulent  $CH_4/H_2/N_2$  jet flame," *Proceedings of the Combustion Institute*, vol. 33, no. 1, pp. 1319 – 1330, 2011.
- [207] M. Rieth, J.-Y. Chen, S. Menon, and A. M. Kempf, "A hybrid flamelet finite-rate chemistry approach for efficient LES with a transported FDF," *Combustion and Flame*, vol. 199, pp. 183 – 193, 2019.
- [208] S. Meares and A. R. Masri, "A modified piloted burner for stabilizing turbulent flames of inhomogeneous mixtures," *Combustion and Flame*, vol. 161, no. 2, pp. 484–495, 2014.
- [209] S. L. Yilmaz, M. Nik, P. Givi, and P. A. Strakey, "Scalar filtered density function for large eddy simulation of a bunsen burner," *Journal of Propulsion and Power*, vol. 26, no. 1, pp. 84–93, 2010.
- [210] B. Coriton, J. H. Frank, A. G. Hsu, M. D. Smooke, and A. Gomez, "Effect of quenching of the oxidation layer in highly turbulent counterflow premixed flames," *Proceedings of the Combustion Institute*, vol. 33, no. 1, pp. 1647–1654, 2011.
- [211] D. H. Rowinski and S. B. Pope, "PDF calculations of piloted premixed jet flames," *Combustion Theory and Modelling*, vol. 15, no. 2, pp. 245–266, 2011.

- [212] R. R. Tirunagari and S. B. Pope, “An investigation of turbulent premixed counterflow flames using large-eddy simulations and probability density function methods,” *Combustion and flame*, vol. 166, pp. 229–242, 2016.
- [213] R. R. Tirunagari and S. B. Pope, “Characterization of extinction/reignition events in turbulent premixed counterflow flames using strain-rate analysis,” *Proceedings of the Combustion Institute*, vol. 36, no. 2, pp. 1919–1927, 2017.
- [214] S. B. Pope, “Small scales, many species and the manifold challenges of turbulent combustion,” *Proceedings of the Combustion Institute*, vol. 34, no. 1, pp. 1–31, 2013.
- [215] S. B. Pope and M. S. Anand, “Flamelet and distributed combustion in premixed turbulent flames,” *Symposium (International) on Combustion*, vol. 20, no. 1, pp. 403 – 410, 1985.
- [216] M. Kuron, Z. Ren, E. R. Hawkes, H. Zhou, H. Kolla, J. H. Chen, and T. Lu, “A mixing timescale model for TPDF simulations of turbulent premixed flames,” *Combustion and Flame*, vol. 177, pp. 171–183, 2017.
- [217] M. Stöllinger and S. Heinz, “Evaluation of scalar mixing and time scale models in PDF simulations of a turbulent premixed flame,” *Combustion and Flame*, vol. 157, no. 9, pp. 1671–1685, 2010.
- [218] H. Kolla, J. Rogerson, N. Chakraborty, and N. Swaminathan, “Scalar dissipation rate modeling and its validation,” *Combustion Science and Technology*, vol. 181, no. 3, pp. 518–535, 2009.
- [219] H. Wang, T. Pant, and P. Zhang, “LES/PDF modeling of turbulent premixed flames with locally enhanced mixing by reaction,” *Flow, Turbulence and Combustion*, vol. 100, no. 1, pp. 147–175, 2018.
- [220] T. D. Dunstan, Y. Minamoto, N. Chakraborty, and N. Swaminathan, “Scalar dissipation rate modelling for large eddy simulation of turbulent premixed flames,” *Proceedings of the Combustion Institute*, vol. 34, no. 1, pp. 1193–1201, 2013.
- [221] S. B. Pope, “PDF methods for turbulent reactive flows,” *Progress in Energy and Combustion Science*, vol. 11, no. 2, pp. 119 – 192, 1985.
- [222] S. B. Pope, “A model for turbulent mixing based on shadow-position conditioning,” *Physics of Fluids*, vol. 25, no. 11, p. 110803, 2013.
- [223] J. H. Chen, A. Choudhary, B. De Supinski, M. DeVries, E. R. Hawkes, S. Klasky, W.-K. Liao, K.-L. Ma, J. Mellor-Crummey, N. Podhorszki, R. Sankaran, S. Shende, and C. S. Yoo, “Terascale direct numerical simulations of turbulent combustion using S3D,” *Computational Science & Discovery*, vol. 2, no. 1, p. 015001, 2009.
- [224] T. Lu and C. K. Law, “A criterion based on computational singular perturbation for the identification of quasi steady state species: A reduced mechanism for methane oxidation with NO chemistry,” *Combustion and Flame*, vol. 154, no. 4, pp. 761–774, 2008.
- [225] E. R. Hawkes, O. Chatakonda, H. Kolla, A. R. Kerstein, and J. H. Chen, “A petascale direct numerical simulation study of the modelling of flame wrinkling for large-eddy simulations in intense turbulence,” *Combustion and flame*, vol. 159, no. 8, pp. 2690–2703, 2012.

- [226] Y. Gao, N. Chakraborty, and N. Swaminathan, “Dynamic closure of scalar dissipation rate for large eddy simulations of turbulent premixed combustion: A direct numerical simulations analysis,” *Flow, Turbulence and Combustion*, vol. 95, no. 4, pp. 775–802, 2015.
- [227] J. Hines, *Genomics code exceeds exaops on Summit supercomputer*, 2018. [Online]. Available: <https://www.olcf.ornl.gov/2018/06/08/genomics-code-exceeds-exaops-on-summit-supercomputer>